

***Investigations of Metal nanoparticles,  
nanocarbons including graphene, and  
artificial photosynthesis***

*A Thesis Submitted for the Degree of*

**Doctor of Philosophy**

*By*

**Urmimala Maitra**



Chemistry and Physics of Materials Unit  
Jawaharlal Nehru Centre for Advanced Scientific Research  
(A Deemed University)  
Bangalore, India.

**January 2014**



*Dedicated to my family*



# DECLARATION

I hereby declare that the matter embodied in this thesis entitled “**Investigations of Metal nanoparticles, nanocarbons including graphene, and artificial photosynthesis**” is the result of investigations carried out by me under the supervision of Prof. C. N. R. Rao, FRS at the Chemistry and Physics of Materials Unit, JNCASR, Bangalore, India and that it has not been submitted elsewhere for the award of any degree or diploma.

In keeping with the general practice in reporting scientific observations, due acknowledgement has been made whenever the work described is based on the findings of other investigators.

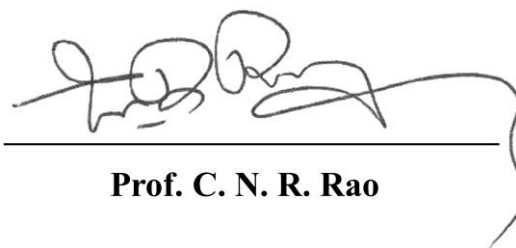
---

(Urmimala Maitra)



# CERTIFICATE

I hereby certify that the matter embodied in this thesis entitled **“Investigations of Metal nanoparticles, nanocarbons including graphene, and artificial photosynthesis”** has been carried out by Ms. Urmimala Maitra at the Chemistry and Physics of Materials Unit, Jawaharlal Nehru Centre for Advanced Scientific Research, Bangalore, India under my supervision and it has not been submitted elsewhere for the award of any degree or diploma.



---

**Prof. C. N. R. Rao**

(Research Supervisor)





## Acknowledgements

At the very onset, I take my opportunity to express deep sense of gratitude to **Prof. C. N. R. Rao, FRS, my research supervisor**, for introducing me to the fascinating field of Nanoscience. It was his enthusiasm that instigated in me the desire to pursue science and has continued to inspire me ever since. I acquired most, if not all, my scientific knowledge from him. His innovative ideas and ability to handle any problem in the simplest of the ways has been the strength behind the completion of this work. It has been a fulfilling experience to work under his encouraging and full spirited guidance. I shall remain ever indebted to him for bearing with me throughout the course of the work. He has not only been instrumental in shaping up my research, my career but my entire personality, my outlook towards life as a whole. I consider myself extremely lucky to receive all the love and care that he has bestowed me with. I do not have words to thank him; I express my deepest gratitude to him.

My sincere thanks to my collaborators; Dr. Subi George, Dr. Ranjan Datta, Prof. A. Sundaresan, Prof. U. V. Waghmare, Prof, U. Ramamurthy for valuable discussions and help during the course of the experiments.

I use this opportunity to thank Dr. A. Govindaraj for helping me in innumerable ways in experimental and official work.

My work would have been incomplete without the help of my co-workers - Dr. Gomathi, Dr. K. S. Subrahmanyam, Dr. K. Biswas, Dr. Panchakarla, Dr. S. Ghosh, Dr. Late, Dr. B. Das, Dr. Matte, Dr. Naidu, Dr. Narendra, Dr. Mrinmoy, Nitesh, Ankit, Uttam and Dr. K. Eswaraprasad who helped me with different problems. Special thanks to them all. I shall remain ever thankful to all my seniors for their valuable suggestions. It has been a wonderful experience working with all my past and present labmates and I thank them for the help in various occasions and for always keeping a amicable and enjoyable atmosphere in lab.

I thank the following faculties namely Prof. G. U. Kulkarni, Prof. S. Balasubramanian, Prof. A. Sundaresan, Prof. S. M. Shivaprasad, Prof. N. Chandrabhas, Dr. T. K. Maji, Dr. Eswaramoorthy and Prof. K. S. Narayan of CPMU, Dr. T. Govindaraju and Dr. S. J. George of NCU, Prof. S. K. Pati, Prof. Umesh V. Waghmare, Prof. S. Narasimhan and Dr. N. S. Vidhyadhiraja of TSU and Prof. S. Ranganathan of Materials Engineering( IISc) for all the illuminating courses and discussions.

I thank the timely help of the technical staff namely Ms. N. R. Selvi (for FESEM), Mrs. T. Usha (for TEM), Mr. Vasu (for UV, PL, IR, TGA), Mr. Anil (for XRD), Mr. Srinath, Mr. Srinivasa Rao and Mr. Srinivas (for technical assistance). The assistance provided by Mr. Arokianathan and Mr. Moorthy is also appreciated. I thank Mrs. Shashi, Mrs. Sudha, Mr. Gowda and Mr. Victor for their help in various aspects.

I thank JNCASR and IISc for extending course work and research facilities. The hostel, the admin, academic staff and Dhanwantari for all their help during my stay here.

I take this opportunity to thank Mrs. Indumati Rao for all the affection and love I have received from her. Her enthusiasm age not withstanding has been a source of inspiration for me. She has been pampering all of us with the gracious and sumptuous dinners, cakes, sweets ever so often. I consider myself blessed to have received all these care and more than everything the wise words of advice every now and then.

Thanks to all my Int. PhD. batch mates with whom I started my life at this centre and whose cheerful company made these six years of life so cherishable. I thank all my friends for their cheerful and often encouraging company.

Finally, I thank my family. It was my father who inculcated in me the love for science. But for him I would not have been here. Thanks to my mother and grandmother who are always ready with their encouraging words and definitely to my sister, times spent with whom has been few of the best times of my life. Thank you all for being what you are. This thesis is a humble offering to you.

# Contents

Declaration	iii
Certificate	v
Acknowledgements	vii
Contents	ix
<b>A Brief introduction to the thesis</b>	<b>1</b>
<b>Part I. Investigations of metal nanoparticles</b>	<b>11</b>
<b>Chapter I.1 <i>Scaling behaviour of plasmon coupling in Au nanoparticles incorporated in polymer matrices</i></b>	
Summary	17
1. Introduction	18
2. Scope of the present investigations	20
3. Experimental Section	21
Synthesis of composites	21
Characterization	22
4. Results and discussion	22
5. Conclusions	30
<b>Chapter I.2 <i>SERS on nanocrystalline Au and Ag films formed at the organic-aqueous</i></b>	
Summary	33
1. Introduction	34
2. Scope of the present investigations	35
3. Experimental Section	36
Preparation of nanocrystalline films of Au and Ag	36
Raman Measurements	37
4. Results and discussion	38
SERS of Pyridine on Au films	38

SERS of Pyridine of Ag films	41
SERS of Rhodamine 6G on Ag films	43
5. Conclusions	44
<b>Chapter I.3 <i>Ferromagnetism of noble metal nanoparticles</i></b>	
Summary	51
1. Introduction	52
2. Scope of the present investigations	53
3. Experimental Section	54
4. Results and discussion	56
5. Conclusions	65
<b>Part II. Investigations of nanodiamond, graphene and related 2D materials</b>	<b>69</b>
<b>Chapter II.1 <i>Covalently and non-covalently functionalized nanodiamond and its covalently linked composites</i></b>	
Summary	95
1. Introduction	96
2. Scope of the present investigations	98
3. Experimental Section	101
Surface homogenization of nanodiamond	101
Functionalization with organotin and organosilane reagent	101
Functionalization with surfactants	102
Functionalization with octyl amine and OPV amine	102
Preparation of covalent binary conjugates of nanocarbons	104
4. Results and discussion	106
Solubilization by covalent and non-covalent functionalization	106
Covalent conjugates of ND with OPV	113
Covalently linked binary conjugates of ND with graphene and carbon nanotubes	118
5. Conclusions	123

## **Chapter II.2 *Mechanical properties of polymer nanocomposites of nanodiamond and other nanocarbons***

Summary	129
1. Introduction	130
2. Scope of the present investigations	131
3. Experimental Section	132
Functionalization of nanofillers	132
Preparation of composites	133
Characterization	133
Mechanical properties	134
4. Results and discussion	134
PVA-nanodiamond composites	135
Binary composites	139
5. Conclusions	148

## **Chapter II.3 *Birch reduction of carbon nanotubes and graphene nanoribbons for chemical H<sub>2</sub> storage***

Summary	151
1. Introduction	152
2. Scope of the present investigations	153
3. Experimental Section	156
Synthesis of single, double and multi-walled nanotubes	156
Synthesis of graphene nanoribbons	157
Birch Reduction	158
Characterization	158
H <sub>2</sub> release studies	159
4. Results and discussion	159
5. Conclusions	169

## **Chapter II.4 *Temperature effects on the Raman spectra of graphene and graphene nanoribbons***

Summary	173
1. Introduction	174

2. Scope of the present investigations	177
3. Experimental Section	178
Synthesis of single and few-layer graphene and graphene nanoribbons	178
Raman studies	179
4. Results and discussion	180
5. Conclusions	189

**Chapter II.5 *Nanoribbons and nanoscrolls of graphene and graphene analouges of BN and MoS<sub>2</sub>***

Summary	193
1. Introduction	194
2. Scope of the present investigations	198
3. Experimental Section	201
Synthesis of graphene analouges of BN and MoS <sub>2</sub>	201
Potassium intercalation and exfoliation	202
Synthesis of MoS <sub>2</sub> and WS <sub>2</sub> nanoscrolls by microwave irradiation	202
Magnetic measurements	203
4. Results and discussion	203
Nanoribbons and nanoscrolls of graphene and graphene analogues of BN and MoS <sub>2</sub> by potassium intercalation	203
MoS <sub>2</sub> and WS <sub>2</sub> nanoscrolls by sudden expansion of liquid N <sub>2</sub> in microwave	211
Magnetic properties of nanoribbons of graphene, BN and MoS <sub>2</sub> , observation of exchange-bias effect	215
5. Conclusions	221

**Part III. Artificial photosynthesis to generate hydrogen and oxygen 227**

**Chapter III.1 *Photochemical oxidation of water catalysed by nanoparticles of Mn and Co oxides; the importance of e<sub>g</sub><sup>1</sup> configuration***

Summary	239
1. Introduction	240

2. Scope of the present investigations	241
3. Experimental Section	242
Synthesis	242
Oxygen evolution measurements	243
4. Results and discussion	244
5. Conclusions	261
<b>Chapter III.2 <i>Highly efficient visible-light induced H<sub>2</sub> generation by single layer 1T-MoS<sub>2</sub> and the nanocomposite of few-layer 2H-MoS<sub>2</sub> with heavily nitrogenated graphene</i></b>	
Summary	265
1. Introduction	266
2. Scope of the present investigations	267
3. Experimental Section	269
Synthesis	269
Characterization	271
Photocatalytic measurements	271
4. Results and discussion	272
5. Conclusions	289
Appendix : Instrumentation and Techniques for characterization	295





## ***Brief introduction to the thesis***

The study of nanomaterials has emerged as a very important field in modern science and technology. The term nanoscience is employed to describe creation and exploitation of materials with dimensions between atoms and bulk materials. Nanomaterials are materials with at least one dimension in the nanometre ( $1\text{nm} = 10^{-9}\text{m}$ ) range. Confining materials to such small dimensions causes them to exhibit properties quite different from the bulk. Quantum phenomena begin to play its role and several new phenomena and properties begin to appear. Suitable control of the properties of nano structures can lead to new science as well as new products, devices and technologies. The foundation of modern colloidal science was laid down by Michael Faraday.<sup>1</sup> At its inception, the science of colloids did not quite catch popular fancy and remained the domain of a few individuals. For example, Ostwald's 1915 book on colloids is titled "The world of neglected dimensions".<sup>2</sup> Thus, successful predictions of optical properties and electronic structure of metal particles by Mie,<sup>3</sup> Gans<sup>4,5</sup> Kubo<sup>6</sup> and Einstein's success in relating Brownian motion to diffusion coefficient<sup>7</sup> did not receive deserved attention. It was Feynman who gave an essential idea when he stated "*There is Plenty of room at the bottom*"<sup>8</sup> and thus heralded a gradual revival of the science of colloids in 1980s which soon became popular as nanoscience. Nanomaterials research was initially motivated by an effort to understand the evolution of bulk structural and electronic properties from molecular scale. The past couple of decades have witnessed an exponential growth of activities in this field worldwide, driven both by the excitement of understanding new science and by the potential hope for applications and economic impacts.

Nanomaterials are defined based on their dimensionalities as **(3-*n*)** dimensional where *n* defines the number of dimensions in nano-regime. Accordingly, nanomaterials are 0D (nanocrystals;  $n=3$ ), 1D (nanorods, nanotubes;  $n=2$ ) and 2D (nanofilms, nanosheets and nanowalls;  $n=1$ ). Table 1 lists the typical nanomaterials of different dimensions.<sup>9</sup>

## ***Brief introduction to the thesis***

**Table 1 Examples of nanomaterials of different dimensionalities:**

	<i>Size (approx.)</i>	<i>Materials</i>
0D-Nanocrystals and clusters (quantum dots)	Diam 1-10 nm	Metals, semiconductors, magnetic materials
Other nanoparticles	Diam 1-100 nm	Ceramic oxides, pnictides
1D-Nanowires	Diam 1-100 nm	Metals, semiconductors, oxides, sulphides, nitrides
Nanotubes	Diam 1-100	Carbon-nanotubes, Layered metal chalcogenide
Nanoporous solids	Pore diam 0.5-10 nm	Zeolites, phosphates etc.
2-D arrays of nanoparticles	Several nm <sup>2</sup> - μm <sup>2</sup>	Metals, semiconductors, magnetic materials.
Surfaces and thin films	Thickness 1-1000nm	Variety of materials –oxides, sulphides, metals etc.
Nanosheets	Single-few layers	Graphene, layered metal oxides and chalcogenides
3-D structures and superlattices	Several nm in three dimensions	Metals, semiconductors, magnetic materials.

Much of the fascination in nanoscience is due to the fact that nanocrystals and other nano-objects such as tubes and wires possess properties that depend on the size of the system. Size plays a crucial role in determining the electronic, chemical, optical and magnetic properties of nanomaterials. Nanocrystals measure a few nanometres in diameter and could contain up to few hundred of atoms. Electrons suffer quantum confinement in such small clusters and cause the nanocrystal to behave in a manner distinct from both the constituting atoms and the corresponding bulk. Moreover, because of such small sizes they possess high surface to volume ratio, (which can reach upto 0.9 for a 1nm) which considerably alters their properties.

Extensive work has been carried out on 0D inorganic nanoparticles specially those of metals and semiconducting oxides, chalcogenides and pnictides.<sup>10</sup> Nanoparticles are generally prepared by chemical methods typical of them being reduction of salts, solvothermal synthesis and decomposition of molecular precursors. Metal nanoparticles are generally prepared by the first method whereby a mild reducing agent is used to reduce the metal salt often in the presence of some capping agents. Capping agents not only limit the particles to nanodimensions but also direct the shape of the crystalline nanoparticle. Metal oxide nanoparticles are generally prepared from metal acetates, acetylacetonates and cupfferonates under solvothermal conditions. Precipitation of metal salts with bases and sol-gel synthesis are other popular techniques. Nictides and Chalcogenides nanocrystals are obtained by the reaction of metal salts with a chalcogen

or pnictogen source or the decomposition of single source precursors under solvothermal or thermolysis conditions.<sup>10,11</sup> Despite the impressive possibility of manipulating individual nanoparticles, engineering of nanomaterials into high performance devices often requires organized assembly of nanoparticles. Decades of work has demonstrated that nanoparticles can assemble by itself driven by interparticle attractive and repulsive forces or can be guided to form assemblies by various techniques.<sup>12</sup> Such assemblies are interesting because they retain the properties of individual nanoparticles with often, emergence of new properties.

Optical and electronic properties of nanomaterials are determined by the electronic energy levels and density of states. Metals when in bulk possess a partially filled electronic band and their ability to conduct electrons is due to the availability of a continuum of energy levels above the Fermi energy,  $E_F$ . However, at nanoscale the continuum of electronic states breaks down making the material insulating. In the case of semiconductors in bulk state, the  $E_F$  is in between the filled and the unfilled levels. Thus, excitation induces the formation of an electron and a hole, which are delocalized over a number of atoms or ions constituting the material. The distance between the hole and the electron is known as the Bohr radius and is on the nanometer length scale. When the size of the semiconductor material becomes smaller than the Bohr radius, it would decrease the space in which the charge carriers move and thus confine their motion, exhibiting quantum confinement. Metal nanoparticles, are well known for their strong interactions with visible light through the resonant excitations of the collective oscillations of the conduction electrons within the particles. As a result, local electromagnetic fields near the particle can be many orders of magnitude higher than the incident fields and the incident light around the resonant-peak wavelength is scattered very strongly. Not only size but shape too plays a role in determining optical property. In case of semiconductor nanocrystals, discrete optical transitions along with band gap opening with size variation are observed in the absorption spectra. Size effects were perhaps first noticed in magnetic measurements carried out on the so called “fine particles” - particles with diameters in the 10-100 nm range.<sup>13</sup> Magnetism of nanoparticles attracts attention due to their single domain nature, which simplifies the theoretical treatment and leads to experimental understanding. Superparamagnetism is one feature that originates because of this single

domain nature. Many metal oxides nanoparticles show evidence for the presence of ferromagnetic interactions at low temperatures specially those of antiferromagnetic oxides.<sup>14,15</sup> Recently, room-temperature ferromagnetism has been observed in nanocrystals of otherwise nonmagnetic materials such as CeO<sub>2</sub>, Al<sub>2</sub>O<sub>3</sub>, ZnO, In<sub>2</sub>O<sub>3</sub> and SnO<sub>2</sub>.<sup>16</sup>

This thesis, dealing with several aspects of nanomaterials, is organized into three parts and discusses properties of nanomaterials of different dimensionalities. Of all the zero dimensional nanomaterials, metal nanoparticles are the most studied. **Part I** of the thesis discusses optical and magnetic properties of metal nanoparticles and is composed of three chapters. Nanoparticles of metals, especially those of Au and Ag, show unique optical properties with emergence of surface plasmon on reduction to diameter below the mean free path of electrons in these materials. On bringing two metal nanoparticles in proximity to each other their surface plasmon couples resulting in a shift in the plasmon absorption band. In **Chapter I. 1** we discuss the scaling behavior of plasmon coupling in a 3-dimensional assembly of gold nanoparticles embedded in polymer matrix. **Chapter I. 2** presents the use of nanoparticulate films of Au and Ag prepared at the aqueous-organic interface as an effective Surface Enhanced Raman Scattering (SERS) substrates for detection of molecules such as Rhodamine 6G and pyridine. It has been recently demonstrated that all inorganic materials when reduced to nanoscale show very weak ferromagnetism. In particular, ferromagnetism in Au nanoparticles is believed to arise from surface capping agents. **Chapter I. 3** discusses the effect of various factors on ferromagnetism of metal nanoparticles and demonstrate that these nanoparticles show weak ferromagnetism even in the absence of any surface capping agent.

Anisotropic nanomaterials are a class of nanomaterials whose properties are direction dependent. 1D nanowires and nanotubes and 2D nanosheets constitute the most common anisotropic nanomaterials.<sup>13-16</sup> Since the discovery of carbon nanotubes in 1991,<sup>17</sup> the study on one-dimensional systems gained impetus. Nanowires and nanotubes of inorganic oxides, sulfides and pnictides were synthesized and their properties studied.<sup>10,18</sup> Nanowires have been prepared by vapour phase methods such as vapour–liquid–solid

growth, vapour–solid growth, oxide-assisted growth and the use of carbothermal reactions. Solution methods for the synthesis of nanowires include seed-assisted growth and oriented attachment.<sup>10</sup> Nanotubes or inorganic layered materials such as BN and transition metal di-chalcogenides are among the most popular inorganic nanotubes. Nanotubes of MoS<sub>2</sub> and other transition metal di-chalcogenides are generally prepared by decomposition of corresponding metal trisulfides and ammonium thiometallate or selenometallate.<sup>19,20</sup> Solvothermal and hydrothermal methods often in the presence of surfactants yield nanotubes specially of metal-oxides. Arc discharge, laser ablation chemical vapour deposition are common methods that yield BN nanotubes.<sup>19,20</sup> Template based synthesis is the most commonly employed technique to prepare nanotubes of metals and metal oxides and involve solution based or electrochemical deposition of metal in the porous membranes of alumina or polycarbonate followed by removal of the template.<sup>20</sup> Carbon nanotubes are one of the strongest and lightest materials and find extensive applications in miniaturization of electronics, mechanical strengthening of polymer composites, gas storage to name a few.<sup>21,22</sup> Metal, metal oxide, chalcogenides and pnictide nanotubes and nanowires have been extensively utilized for sensors, detectors, electrical circuits, FETs, solar cells, Li-ion batteries, supercapacitors.<sup>23-25</sup> The discovery of nanotubes has not only revolutionized the chemistry and physics of 1D nanomaterials but has given impetus to the development of other 1D nanostructures like nanoscrolls, nanoribbons, nanobelts and many more.<sup>26,27</sup>

While two decades of research has established carbon nanotubes and nanotubes and nanowires of inorganic materials as frontier field of study in nanotechnology, two-dimensional systems have been brought to limelight with the advent of unique, unusual properties and fascinating applications of graphene.<sup>28-31</sup> Although nanofilms<sup>32-35</sup> and two dimensional heterostructures<sup>36,37</sup> have been studied for years, the discovery of Graphene gave an impulse to the study of two dimensional nanosheets of inorganic layered materials. Two dimensional nanosheets of transition metal dichalcogenides, layered metal oxides and BN not only exhibit interesting properties but are now finding astonishing applications in FETs, catalysis, Li-ion batteries and many more.<sup>38-40</sup>

**Part II** of the thesis deals with nanocarbons of different dimensionalities namely 0D nanodiamond, 1D carbon nanotubes, graphene nanoribbons, nanoscrolls and 2D graphene; along with graphene analogues of inorganic layered materials. This part is divided into five chapters. A brief introduction to synthesis of carbon nanotubes, graphene and graphene analogues of MoS<sub>2</sub> and BN has been provided in this part. **Chapter II.1** presents covalent and non-covalent surface functionalization of nanodiamond to make them soluble in organic and aqueous medium. Covalent functionalization was used to prepare chromophore-functionalized fluorescent nanodiamond and binary conjugates of nanodiamond with carbon nanotubes and graphene. Mechanical properties of poly(vinyl alcohol)-matrix (PVA) reinforced with nanocarbons as nano-fillers are examined in **Chapter II.2**. Even small addition of nanodiamond leads to significant enhancement in the hardness and elastic modulus of the polymer. When binary combinations of nanodiamond with few-layer graphene, and single-walled nanotubes were reinforced in PVA, the mechanical properties of the resulting composites show extraordinary synergy, improving the stiffness and hardness. In **Chapter II.3**, Birch reduction of the carbon nanotubes has been studied to achieve chemical storage of H<sub>2</sub> in carbon nanotubes and graphene nanoribbons. Chemical storage of hydrogen in these nanocarbons via Birch reduction creates binding strength of hydrogen sufficient to store H<sub>2</sub> at room temperature and release it by heating it to slightly high temperature. Raman spectroscopy has emerged as a unique tool to characterize graphene. In **Chapter II. 4**, the temperature dependence of different Raman modes of graphene has been studied and their temperature coefficients have been determined. The effect of number of layers, doping, functional groups and defects on the temperature coefficients has been explored. Hydrogen storage through formation of reversible chemical bonds provides advantage of having just the right interaction strength needed for a material to be used in vehicular transport. **Chapter II.5** deals with the synthesis of nanoscrolls and nanoribbons of graphene and graphene analogues of BN and MoS<sub>2</sub>. Exfoliation via potassium intercalation or microwave irradiation was used to prepare these nanostructures. The chapter also discusses the emergence of magnetism in these nanostructures.

Sustainable low carbon energy supplies are the most demanding problems of today. Artificial photosynthesis for solar water splitting to generate hydrogen is envisaged as the ultimate path to renewable and clean source of energy. In natural photosynthesis sunlight is captured and converted into energy of chemical bonds in glucose and other organic molecules. Chlorophylls absorb light and generate an electron that travels via a cascade of downhill steps to finally reduce a proton. Artificial photosynthesis thus involves three steps : i) Absorption of solar energy to generate an electron-hole pair, ii) separation of the electron-hole pair and iii) reduction of proton and/or oxidation of H<sub>2</sub>O. Years of effort has been put to increase the efficiency of each of these steps and integrate them to achieve low cost efficient catalysts for photocatalytic hydrogen generation. Traditionally, H<sub>2</sub> is generated from water using Pt electrodes. H<sub>2</sub> is generated at the Pt electrode and O<sub>2</sub> at the counter electrode. Though hydrogen is envisioned as the fuel of future, it is the oxidation of water that is the more difficult step in photosynthesis since it involves transfer for 4 electron. In our effort to find out low-cost, efficient catalysts composed of earth abundant elements, we have studied oxygen evolution with Mn and Co oxide nanoparticles and H<sub>2</sub> evolution with two dimensional-MoS<sub>2</sub> in **Part III** of the thesis. A brief introduction to artificial photosynthesis and its relation to natural photosynthesis has been provided in this part. Oxygen evolution activity of different Mn and Co oxides has been studied in detail in **Chapter III. 1** and it has been found that electronic structure of the transition metal and not the crystal structure of the oxide determines its activity for photo-catalytic water oxidation. All transition metal oxides containing trivalent Co and Mn ions with single electron in the e<sub>g</sub> orbital show good activity. In **Chapter III. 2**, it has been shown that composites of MoS<sub>2</sub> with heavily nitrogen doped graphene show very high catalytic activity with N-doped graphene acting as a good electron donor to p-type MoS<sub>2</sub>. In the same lines it was found that making MoS<sub>2</sub> itself metallic improves the H<sub>2</sub> evolution catalytic activity manifold.

## **References**

1. C. N. R. Rao, A. Mueller and A. K. Cheetham, . *The Chemistry of Nanomaterials*; **Wiley-VCH**, : Weinheim, **2004**.
2. W. Ostwald *Die Welt Der Vernachlassigten Dimensions*; **Steinkopf**: Dresden, **1915**.
3. G. Mie. *Ann. Phys.* **1908**, 330, 377.
4. R. Gans. *Ann. Phys.* **1912**, 342, 881.
5. R. Gans. *Ann. Phys.* **1915**, 352, 270.
6. R. Kubo. *J. Phys. Soc. Jpn.* **1962**, 17, 975.
7. A. Einstein. *Ann. Phys.* **1905**, 322, 549.
8. R. P. Feynman; *Miniaturization*, **Reinhold**: New York, , **1961**.
9. C. N. R. Rao and A. K. Cheetham. *J. Mater. Chem.* **2001**, 11, 2887.
10. C. N. R. Rao, S. R. C. Vivekchand, K. Biswas and A. Govindaraj. *Dalton Trans.* **2007**, 3728.
11. C. N. R. Rao and K. Biswas. *Ann. Rev. Anal. Chem.* **2009**, 2, 435.
12. L. Xu, W. Ma, L. Wang, C. Xu, H. Kuang and N. A. Kotov. *Chem. Soc. Rev.* **2013**, 42, 3114.
13. J. L. Dormann and D. E. Fiorani *Magnetic properties of Fine Particles*: North-Holland, Amsterdam, **1992**.
14. M. Ghosh, E. V. Sampathkumaran and C. N. R. Rao. *Chem. Mater.* **2005**, 17, 2348.
15. M. Jagodic, Z. Jaglicic, A. Jelen, L. Jin Bae, K. Young-Min, K. Hae Jin and J. Dolinsek. *J. Phys. Cond. Matter* **2009**, 21, 215302.
16. A. Sundaresan and C. N. R. Rao. *Nano Today* **2009**, 4, 96.
17. S. Iijima. *Nature* **1991**, 354, 56.
18. C. N. R. Rao and A. Govindaraj *Nanotubes and Nanowires, Second Edition*; **Royal Society of Chemistry**: London, **2011**.
19. C. N. R. Rao and M. Nath. *Dalton Trans.* **2003**, 1.
20. C. N. R. Rao and A. Govindaraj. *Adv. Mater.* **2009**, 21, 4208.



21. M. F. L. De Volder, S. H. Tawfick, R. H. Baughman and A. J. Hart. *Science* **2013**, 339, 535.
22. M. Terrones. *Ann. Rev. Mater. Res.* **2003**, 33, 419.
23. Kenry and C. T. Lim. *Progress Mater. Sci.* **2013**, 58, 705.
24. M. K. Sunkara, C. Pendyala, D. Cummins, P. Meduri, J. Jasinski, V. Kumar, H. B. Russell, E. L. Clark and J. H. Kim. *J. Phys. D* **2011**, 44, 174032.
25. H. Pritesh, U. Husnu Emrah and A. J. A. Gehan. *Nanotechnol.* **2012**, 23, 194002.
26. X. Yang, X. Dou, A. Rouhanipour, L. Zhi, H. J. Rader and K. Mullen. *J. Am. Chem. Soc.* **2008**, 130, 4216.
27. Y. Xia, P. Yang, Y. Sun, Y. Wu, B. Mayers, B. Gates, Y. Yin, F. Kim and H. Yan. *Adv. Mater.* **2003**, 15, 353.
28. A. K. Geim and K. S. Novoselov. *Nat. Mater.* **2007**, 6, 183.
29. Y. Xia, P. Yang, Y. Sun, Y. Wu, B. Mayers, B. Gates, Y. Yin, F. Kim and H. Yan. *Adv. Mater.* **2003**, 15, 353.
30. S. K. Pati, T. Enoki and C. N. R. Rao. in *Graphene and its fascinating attributes World Scientific Publishing Co.*, Chennai, India, 2010.
31. C. N. R. Rao, A. K. Sood, K. S. Subrahmanyam and A. Govindaraj. *Angew. Chem. Int. Ed.* **2009**, 48, 7752.
32. C. N. R. Rao and K. P. Kalyanikutty. *Acc. Chem. Res.* **2008**, 41, 489.
33. X. Wang, W. Tian, M. Liao, Y. Bando and D. Golberg. *Chem. Soc. Rev.* **2014**.
34. E. Fortunato, P. Barquinha and R. Martins. *Adv. Mater.* **2012**, 24, 2945.
35. N. Kaiser. *Appl Optics* **2002**, 41, 3053.
36. S. B. Ogale *Thin Films and Heterostructures for Oxide Electronics (Multifunctional Thin Film Series)*; **Springer**: New York, **2005**.
37. S. E. Ramanathan *Thin Film Metal-Oxides*; **Springer**: New York, **2010**.
38. M. Xu, T. Liang, M. Shi and H. Chen. *Chem. Rev.* **2013**, 113, 3766.
39. X. Huang, Z. Zeng and H. Zhang. *Chem. Soc. Rev.* **2013**, 42, 1934.
40. C. N. R. Rao, H. S. S. Ramakrishna Matte and U. Maitra. *Angew. Chem. Int. Ed.* **2013**, 52, 13162.



# ***PART I***

## ***Investigations of Metal nanoparticles***

### ***Introduction***

Nanoparticles constitute a major part of nanomaterials. These zero-dimensional materials have interesting history and wide range of attributes.<sup>1</sup> Since the time of Romans, metal nanoparticles have been used as decorative pigments an example of which is the famous Lycurgus Cup. Colloidal gold nanoparticles were first prepared by Faraday<sup>2</sup> in as early as 1857. As quoted by Faraday, Au in its divided state changes colour from bright yellow of bulk to a range of colours spanning the entire range from blue to purple to wine red. Optical properties of Au nanoparticles since this pioneering work of Michel Faraday been the most studied property of noble metal nanoparticles. This refers to the so-called surface plasmon resonance (SPR) which arises when the free conduction electrons in metal oscillate in response to the alternating electric field of the incident electromagnetic radiation. Apart from the nature of the nanoparticle, its shape and size, the environment in which the metal particles are dispersed determine the optical properties. The refractive index of the surrounding medium and the average distance between neighboring metal nanoparticles are among those that influence its optical properties.<sup>3,4</sup> The change in surface plasmon absorption of Au and Ag nanoparticles has been used in detection especially of biomolecules.<sup>5-7</sup> The first chapter in this part deals with the optical properties of Au nanoparticles dispersed in a polymer matrix. A brief introduction to surface plasmon resonance, its origin and its dependence on the interparticle distance has been provided in the first chapter.

Surface plasmon resonance has been used to enhance the surface sensitivity of several spectroscopic measurements including fluorescence, Raman scattering and second

## ***Metal nanoparticles***

---

harmonic generation utilizing the highly enhanced local electric fields near the metal surface due to SPR. Surface enhanced Raman scattering is one such surface sensitive technique that enhances Raman scattering by molecules adsorbed on a rough metal surface or metal nanoparticles thereby allowing detection of very small concentrations of molecules (upto single molecule). The increase in intensity of Raman signal on a metal surface mainly occurs because of enhancement of electric field when a light of particular frequency excites the surface plasmon resonance on the metal surface. In 1970's it was shown that rough Au surface can enhance Raman signal manifold, commonly known as surface enhanced Raman scattering (SERS).<sup>8</sup> SERS is being developed as a powerful diagnostic tool. Chapter II.2 discusses the use of nanoparticulate Au and Ag films prepared at organic-aqueous interface as an efficient substrate for SERS.

Another important property of noble metal nanoparticles or clusters that has emerged in the past few years is its magnetic properties. While bulk gold is diamagnetic, clusters of Au and small nanoparticles of Au are found to be magnetic.<sup>9-11</sup> A dominant view that is present today on magnetism of Au nanoparticles is that they show permanent magnetic moments only when capped with strongly binding molecules that can cause electronic modification of the surface atoms.<sup>12-16</sup> In the third chapter of this section we have tried to experimentally show that Au nanoparticles show ferromagnetism even in absence of any capping agent. A summary of literature report on magnetism of Au nanoparticles have been provided in the third chapter.

Au nanoparticles have been studied vastly for catalysis both heterogeneous and homogenous.<sup>17</sup> While bulk Au is catalytically inactive, nanoclusters of Au or Au nanoparticles supported on substrates are catalytically very active. In this part a brief outline of basic synthetic techniques used for the synthesis of noble metal nanoparticles will be provided.

All existing methods for the synthesis of metal nanoparticles are beyond the scope of this section. The section is therefore restricted to some of the most widely used techniques for synthesis of noble metal nanoparticles. The most popular method for the synthesis of Au nanoparticles is from  $\text{HAuCl}_4$ . Wine red dispersion of Au nanoparticles of average diameter 10-100 nm are obtained in water by the reduction of  $\text{HAuCl}_4$  in a

boiling sodium citrate solution.<sup>18</sup> Reduction using citrate has been applied for the production of Au, Ag and Pt colloids with much smaller particle size of 2-4 nm.<sup>19</sup> Biphasic synthesis of Au nanoparticles is another most widely used technique for the synthesis of Au nanoparticles. HAuCl<sub>4</sub> dissolved in water is first transferred to organic layer by means of phase transfer agent tetraoctylammoniumbromide (TOAB). The toluene solution is then stirred with sodium borohydride in the presence of thioalkanes and aminoalkanes. Depending on the ratio of Au salt to the thiol and amine capping agent, particle size has been tuned between 1-10 nm.<sup>20,21</sup> Murray and co-workers<sup>22</sup> synthesized monolayer protected clusters by ligand place exchange reactions. Polymer protected Au nanoparticles have been produced, especially with the use of poly(vinyl pyrrolidone).<sup>23-25</sup>

Au nanoparticles have been produced in varied shapes and sizes. One of the first synthesis of Au nanorods involved electrochemical reduction of HAuCl<sub>4</sub> in the presence of shape inducing cationic surfactants and other additives.<sup>26</sup> Two cationic surfactants like cetyltrimethylammonium bromide (CTAB) and the much more hydrophobic tetradecylammonium bromide (TDAB) or TOAB constitute the cationic micellar system. The ratio between the surfactants controls the average aspect ratio of the Au nanorods. A simpler method for the synthesis of nanorod involves the use of preformed Ag or Au seeds on which additional metal is grown in solution by means of a mild reducing agent like ascorbic acid and a surfactant like CTAB.<sup>27,28</sup> The addition of different volumes of the seed solution produces Au nanorods with different aspect ratios. Similarly, cubes, disks,<sup>29</sup> wires, tubes,<sup>30</sup> branched,<sup>31</sup> triangular prisms,<sup>32</sup> and tetrahedral nanoparticles and nanoparticles of various other shapes have been generated in gold, silver and platinum with various reduction techniques and capping materials.<sup>29</sup> Inverse micelles have been used to generate many different sizes and shapes of nanoparticles.<sup>29,33</sup> Small pockets of water are created in an otherwise organic phase by the use of surfactants. Metal salt in water is conjugated to the surfactant prior to addition of reducing agent, thereby allowing the formation of monodisperse crystalline nanoparticles. Nanocrystalline films of Au, Ag, Pt and Pd have been obtained at low temperatures at the organic-aqueous interface. The particle size can simply be varied by variation of temperature. While metal salt (e.g. Au(PPh<sub>3</sub>)Cl) is taken in organic phase the reducing agent is taken in aqueous phase.<sup>34</sup> The

## ***Metal nanoparticles***

---

product formed by the reaction at the interface contains ultra-thin nanocrystalline films of the metal nanoparticles formed by closely packed nanocrystals.

In this part of the thesis, following studies have been presented

***Chapter I. 1*** *Scaling behaviour of plasmon coupling in Au and ReO<sub>3</sub> nanoparticles incorporated in polymer matrices*

***Chapter I. 2*** *Nanocrystalline Au and Ag films formed at the organic–aqueous interface as SERS*

***Chapter I. 3*** *Magnetism of noble metal nanoparticles*

## References

1. C. N. R. Rao, P. J. Thomas and G. U. Kulkarni *Nanocrystals:: Synthesis, Properties and Applications*; Springer Berlin Heidelberg, 2007.
2. M. Faraday. *Phil. Trans. R. Soc. Lond.* **1857** 147, 145.
3. L. M. Liz-Marzán. *Mater. Today* **2004**, 7, 26.
4. S. Eustis and M. A. El-Sayed. *Chem. Soc. Rev.* **2006**, 35, 209.
5. N. L. Rosi and C. A. Mirkin. *Chem. Rev.* **2005**, 105, 1547.
6. C. L. Haynes and R. P. Van Duyne. *J. Phys. Chem. B* **2001**, 105, 5599.
7. A. J. Haes, W. P. Hall, L. Chang, W. L. Klein and R. P. Van Duyne. *Nano Lett.* **2004**, 4, 1029.
8. A. Campion and P. Kambhampati. *Chem. Soc. Rev.* **1998**, 27, 241.
9. S. Trudel. *Gold Bull.* **2011**, 44, 3.
10. V. Tuboltsev, A. Savin, A. Pirojenko and J. Räisänen. *ACS Nano* **2013**, 7, 6691.
11. G. L. Nealon, B. Donnio, R. Greget, J.-P. Kappler, E. Terazzi and J.-L. Gallani. *Nanoscale* **2012**, 4, 5244.
12. H. Hori, T. Teranishi, Y. Nakae, Y. Seino, M. Miyake and S. Yamada. *Phys. Lett. A* **1999**, 263, 406.
13. P. Crespo, R. Litrán, T. C. Rojas, M. Multigner, J. M. de la Fuente, J. C. Sánchez-López, M. A. García, A. Hernando, S. Penadés and A. Fernández. *Phys. Rev. Lett.* **2004**, 93, 087204.
14. A. Hernando, P. Crespo and M. A. García. *Phys. Rev. Lett.* **2006**, 96, 057206.
15. E. Guerrero, M. A. Muñoz-Márquez, M. A. García, P. Crespo, E. Fernández-Pinel, A. Hernando and A. Fernández. *Nanotechnol.* **2008**, 19, 175701.
16. Y. Negishi, H. Tsunoyama, M. Suzuki, N. Kawamura, M. M. Matsushita, K. Maruyama, T. Sugawara, T. Yokoyama and T. Tsukuda. *J. Am. Chem. Soc.* **2006**, 128, 12034.
17. A. Corma and H. Gracia. *Chem. Soc. Rev.* **2008**, 37, 2096.
18. J. Turkevich, P. C. Stevenson and J. Hiller. *Discuss. Faraday Soc.* **1951**, 11, 55.
19. J. Turkevich, R. S. Miner and L. Babenkova. *J. Phys. Chem.* **1986**, 90, 4765.
20. L. M. Liz-Marzan. *Chem. Comm.* **2013**, 49, 16.

### ***Metal nanoparticles***

---

21. M. Brust, J. Fink, D. Bethell, D. J. Schiffrin and C. Kiely. *J. Chem. Soc., Chem. Comm.* **1995**, 1655.
22. M. J. Hostetler, S. J. Green, J. J. Stokes and R. W. Murray. *J. Am. Chem. Soc.* **1996**, 118, 4212.
23. H. Zhang, M. Okumura and N. Toshima. *J. Phys. Chem. C* **2011**, 115, 14883.
24. M. Zhang, L. Liu, C. Wu, G. Fu, H. Zhao and B. He. *Polym. J.* **2007**, 48, 1989.
25. S. Panigrahi, S. Basu, S. Praharaj, S. Pande, S. Jana, A. Pal, S. K. Ghosh and T. Pal. *J. Phys. Chem. C* **2007**, 111, 4596.
26. Yu, S.-S. Chang, C.-L. Lee and C. R. C. Wang. *J. Phys. Chem. B* **1997**, 101, 6661.
27. C. J. Murphy and N. R. Jana. *Adv. Mater.* **2002**, 14, 80.
28. N. R. Jana, L. Gearheart and C. J. Murphy. *J. Phys. Chem. B* **2001**, 105, 4065.
29. M.-P. Pileni. *Nature Mater.* **2003**, 2, 145
30. Y. Xia, P. Yang, Y. Sun, Y. Wu, B. Mayers, B. Gates, Y. Yin, F. Kim and H. Yan. *Adv. Mater.* **2003**, 15, 353.
31. Y. Lee and T. G. Park. *Langmuir* **2011**, 27, 2965.
32. L. Balan, V. Melinte, T. Buruiana, R. Schneider and L. Vidal. *Polym. J.* **2013**.
33. M. P. Pileni. *Langmuir* **1997**, 13, 3266.
34. C. N. R. Rao and K. P. Kalyanikutty. *Acc. Chem. Res.* **2008**, 41, 489.

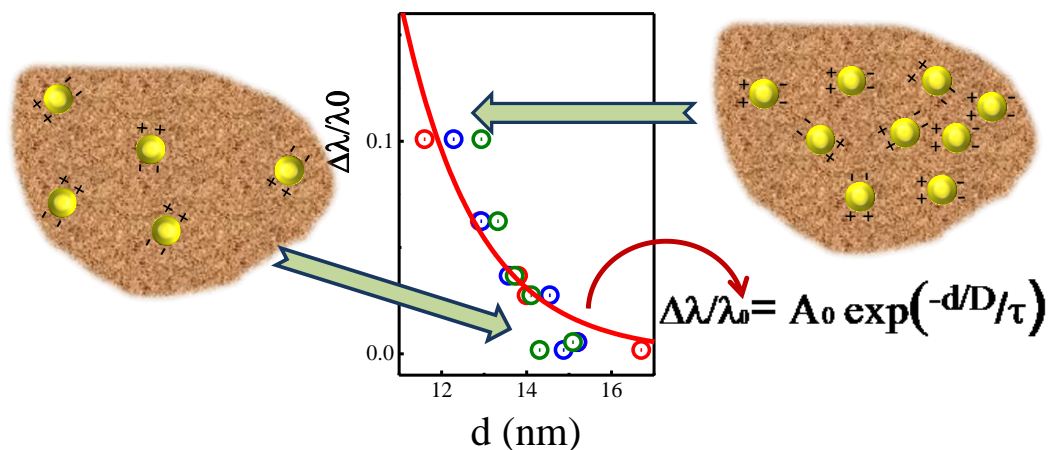


# Chapter I.1

## *Scaling behavior of Plasmon coupling in Au nanoparticles incorporated in Polymer Matrices*

### *Summary\**

*Interparticle dipolar coupling leads to a shift in plasmon absorption maxima as particles are brought from infinite distance to the proximity of each other. The distance between the particles can thus be related to the shift in the plasmon band. Polymer nanocomposites containing different concentrations of Au nanoparticles have been investigated by small angle X-ray scattering and electronic absorption spectroscopy. The plasmon coupling in the 3-dimensional assembly of Au nanoparticles happens along all three dimensions and scales with volume fraction. The plasmon coupling scaling law holds true for  $\text{ReO}_3$  nanoparticles in PVA with shift in plasmon band scaling with concentration.*



\*A paper based on this work has appeared in *Physica Status Solidi (RRL)*, 2010

## 1. Introduction:

The valence electrons in metals are assumed to be completely free from their ions (according to Drude model) and form a free flowing cloud of electrons travelling within the rigid crystal structure of the solid. In Au and Ag, the d electrons form the free valence electrons. The mean free path or the path over which an electron can travel freely throughout the material without scattering is 50 nm in gold and silver. Therefore, in Au and Ag nanoparticles smaller than 50nm electrons do not experience any scattering from the bulk of the metal. The collective oscillation of free electron gas density is called plasmon. The equation of motion of free electrons in an electric field is called the plasma equation, represented as,

$$m \frac{d^2x}{dt^2} = -eE,$$

if  $x$  and  $e$  have the same time dependence as  $e^{-i\omega t}$  then,

$$-\omega^2 mx = -eE, \quad x = eE/m\omega^2$$

the dipole moment of one electron is,  $-ex = -e^2E/m\omega^2$

and polarization i.e., dipole moment per unit volume is,  $-nex = -ne^2E/m\omega^2$ ,

where  $n$  = electron concentration,  $\varepsilon(\omega) = 1 + \frac{P(\omega)}{\varepsilon_0 E(\omega)}$

$$\varepsilon(\omega) = 1 - \frac{ne^2}{\varepsilon_0 m \omega^2} \text{ or } \varepsilon(\omega) = 1 - \frac{\omega_p^2}{\omega^2}, \text{ such that } \omega_p^2 = \frac{ne^2}{\varepsilon_0 m},$$

$\omega_p$  is defined as the plasma frequency.

A plasma is therefore a medium with equal concentration of positive and negative charges, of which generally the negative charge constituted of electrons is mobile with frequency  $\omega_p$  and the positive charges composed of ion cores (in solids) is stationary.

When a wave of frequency  $\omega > \omega_p$  is incident on the surface, the electromagnetic wave propagates while for  $\omega < \omega_p$ ,  $\varepsilon$  is negative and the wave is totally reflected. At the interface (metal-air/ metal-liquid so on) of the nanoparticles where the real part of dielectric function changes sign, the plasmon is called the surface plasmon. When wavelength of light is much larger than the nanoparticle size it sets up standing waves

causing the surface plasmon to oscillate in resonance with frequency of light. For nanoparticles smaller than the wavelength of the exciting light such that  $\lambda \gg 2R$  ( $R$ = radius of the particle, only dipole absorption of the Mie equation contributes to the exciton cross section of the nanoparticles. The Mie theory thus reduces to<sup>1,2</sup>

$$\sigma_{ext} = \frac{9V\varepsilon_m^{3/2}}{c} \frac{\omega\varepsilon_2(\omega)}{[\varepsilon_1(\omega)+2\varepsilon_m]+\varepsilon_2(\omega)^2} \quad (1)$$

where,  $\sigma$  is the extinction coefficient,  $V$  is the particle volume,  $c$  is the speed of light,  $\omega$  is the angular frequency of the exciting radiation,  $\varepsilon_m$  dielectric constant of the surrounding medium and  $\varepsilon_1$  and  $\varepsilon_2$  are the real and imaginary parts of the dielectric function of the particle material. It therefore follows that the resonance occurs when  $\varepsilon_1(\omega)$  is equal to  $-2\varepsilon_m$  such that  $\varepsilon_2(\omega)$  is negligible. Though the dipole approximation does not account for size dependence, a strong size and shape dependence of plasmon frequency and bandwidth is observed. It is to be noted that at sizes below the mean free path of conduction electrons, the dielectric function of the particle becomes size dependent. Shape of the nanoparticle determines the surface geometry of the nanoparticle and causes a shift in the electric field density on the surface. The oscillation frequency of electrons at the surface depends on the electric field in its vicinity. Nanoparticles of different shapes therefore generate different cross-sections of absorption and scattering properties. Similarly, changing the dielectric constant of the surrounding medium changes the ability of the surface to accommodate electron charge density from the nanoparticles and thereby affects surface plasmon resonance (SPR).

The near field on one nanoparticle can interact with that on the adjacent particle in close proximity resulting in coupling of plasmon oscillations. This interparticle plasmon coupling results in intense enhancement of field at the nanoparticle junctions and forms the basis of strong enhancement of the spectroscopic signals that finds applications in sensing, detection and photonic waveguides. Coupled frequency of plasmon oscillation occurs at a frequency that is shifted from the single-particle SPR. Magnitude of assembly-induced plasmon shift depends on the strength of interparticle coupling which in turn depends on the proximity of the particles.

## ***2. Scope of the present investigations***

Interparticle dipolar coupling leads to a shift in plasmon absorption maxima as particles are brought from infinite distance to the proximity of each other. The distance between the particles can thus be related to the shift in the plasmon band<sup>3-5</sup>. Sonnichsen *et al.*<sup>4</sup> and Reinhard *et al.*<sup>5</sup> designed a plasmon ruler equation based on this principle. Using an appropriate biomolecular binding scheme they achieved coupling of gold nanoparticles and measured nanoscale distances in biological systems based on the observed shift in the plasmon band. Few quantitative studies have been carried out on the distance dependence of dipolar plasmon coupling in systems in which metal particles are separated by a dielectric gap and a universal scaling behavior has been predicted.<sup>6-9</sup> Such studies include lithographically fabricated Au nanodiscs in polymers,<sup>6,7,10</sup> dielectric core-Au nanoshells,<sup>8,11</sup> head-to-tail dimers of elongated particles of different aspect ratios and curvatures and a trimer of nanospheres<sup>9</sup>. We considered it to be of interest to examine whether the same scaling law extends to a 3-dimensional assembly of metal particles e.g. those frozen in polymer matrices. The validity of the scaling model for a trimer of nanospheres was envisaged as a step towards its extension to 3-dimensions.<sup>9</sup> This encouraged us to undertake a study of the scaling behavior of plasmon coupling in a 3-dimensional assembly of gold nanoparticles which were prepared in-situ in a polymer matrix characterized by small angle X-ray scattering (SAXS). SPR shift was recorded as a function of Au nanoparticle concentration making use of the fact that concentration is inversely proportional to inter-particle separation. We have extended it to the ReO<sub>3</sub>, metallic oxides which exhibits a plasmon band around 535 nm<sup>12,13</sup> that can be tuned by encapsulating them in different media<sup>14</sup> and can be exploited in surface enhanced Raman scattering (SERS)<sup>15</sup>. SPR shift was studied as a function of concentration making use of the fact that concentration is inversely proportional to inter-particle separation.

### 3. Experimental section

#### *Synthesis of composites*

##### ***Au-PVA:***

Au-PVA nanocomposites with 1-3.5 weight percent of Au nanoparticles were prepared in situ.<sup>16,17</sup> In a typical synthesis, 1 g of PVA was dissolved in 20 mL of water by warming it slightly. Calculated amounts of 1.0 mM HAuCl<sub>4</sub> solution was added to the polymer solution. 1% sodium citrate solution (1mL per 5 mL of HAuCl<sub>4</sub> solution) was then added to it and the mixture was allowed to stir at room temperature for 30 mins. The mixture was then dried in Petri dishes at 35-40 °C for 3 days allowing the film to cure and dry sufficiently such that it leaves the surface of the petridish.

##### ***ReO<sub>3</sub>-PVA:***

ReO<sub>3</sub> nanoparticles were synthesized by the solvothermal decomposition of the rhenium(VII) oxide-dioxane (RDC) complex as reported in the literature.<sup>13</sup> The Re<sub>2</sub>O<sub>7</sub>-(C<sub>4</sub>H<sub>8</sub>O<sub>2</sub>)<sub>x</sub> was prepared following literature procedure.<sup>18</sup> In a typical synthesis, 0.05 g of Re<sub>2</sub>O<sub>7</sub> and 0.5 mL of 1,4-dioxane were warmed to 70 °C followed by cooling in an ice bath. Once the mixture froze it was allowed to melt by keeping it at room temperature. The processes was repeated several times till pearl grey deposit of Re<sub>2</sub>O<sub>7</sub>-(C<sub>4</sub>H<sub>8</sub>O<sub>2</sub>)<sub>x</sub> were obtained. The supernatant was removed by decantation and the precipitate was dissolved in 2 mL ethanol. The solution was taken in 45 mL toluene and sealed in a Teflon-lined stainless steel autoclave of 80 mL capacity (at 70% filling fraction). It was then heated to 200 °C for 4 h. The red precipitate of ReO<sub>3</sub> was washed several times with acetone.

These nanoparticles were used as fillers in different polymers like polyethylene oxide (PEO), polymethyl methacrylate (PMMA) and polyvinyl alcohol (PVA) to produce the different nanocomposites. The polymer was first dissolved in a suitable solvent (chloroform in case of PEO, toluene in case of PMMA and water in case of PVA) and calculated amounts of ReO<sub>3</sub> nanoparticles were then added to the solution to yield a fixed ReO<sub>3</sub> vs. polymer weight ratio in the solution. For example, to produce a 5 % ReO<sub>3</sub>-PEO nanocomposite solution, 1 g of PEO was first dissolved in 20 mL

chloroform and then 50 mg of  $\text{ReO}_3$  nanoparticles were added to it. This solution was sonicated for 1 h to aid mixing of the nanoparticles and the polymer in solution. The solution was poured in a Petri dish and incubated in an oven set at 42 °C till the solvent evaporated yielding a film of the  $\text{ReO}_3$ -polymer nanocomposite. Films of  $\text{ReO}_3$ -polymer nanocomposites with PEO, PMMA and PVA containing  $\text{ReO}_3$  concentrations 0.2, 0.6, 1, 5, 10 and 20 weight percent were prepared. The intensities obtained in SAXS for  $\text{ReO}_3$  polymer nanocomposites were too low to calculate interparticle distances reliably.

### ***Characterization***

The polymer nanocomposites were characterized using x-ray diffraction (XRD), electronic absorption spectroscopy, field emission scanning electron microscopy (FESEM) and transmission electron microscopy (TEM). TEM studies of Au-PVA films were conducted by re-dissolving the films in water and drying a drop of this on a holey carbon-coated copper grid and were observed under TEM. Samples for FESEM were prepared by directly drying the polymer-nanoparticles solution over silicon substrates. Electronic absorption spectra were recorded by placing the films directly in the path of light taking air as background. SAXS measurements were carried out. in the  $q$  range of 0.007 to 0.21  $\text{\AA}^{-1}$ , (i.e,  $2\theta = 0.1$  to  $3^\circ$ ).

## ***4. Results and discussion***

The synthesis of Au-PVA composites was carried out in-situ with tri-sodium citrate as the reducing and capping agent. Nanoparticles formed immediately on addition of sodium citrate which was evident from the immediate change in colour to wine red from light yellow of aurochloric acid. On stirring for 10 mins the colour slowly changed to dark burgundy and stabilizes. No visible colour difference was observed in the course of curing the films implying the particle size does not vary during curing. TEM and FESEM images were taken by dissolving the film in water and drop casting it on to TEM grid or silicon substrates, respectively. Figure 1(a) shows a TEM image of the 2 % Au-PVA film

along with the particle size distribution. The Au nanoparticles have average particle diameter of 9 nm. An FESEM image of the polymer Au nanocomposite film shown in Figure 1(b) reveals small aggregates of Au nanoparticles with an average size of 50 nm (~ 20 particles).

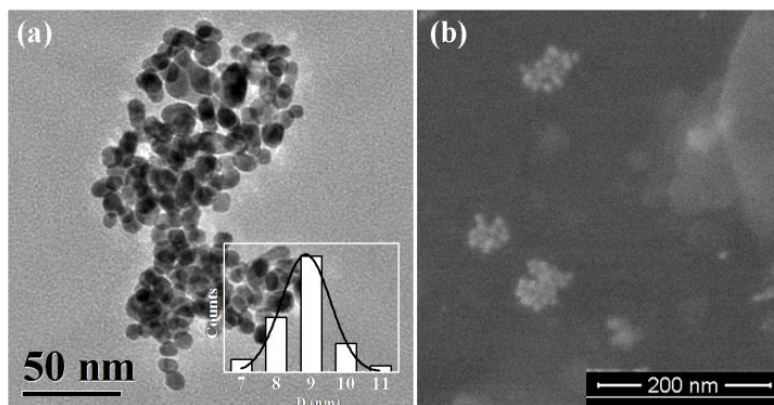


**Figure 1.** (a) TEM image of Au nanoparticles with particle size distribution in inset, (b) FESEM image of Au nanoparticles synthesized in situ in polymer matrices.

For Au-PVA systems, interparticle separation is determined from SAXS curves. We have noticed broad bands in the SAXS curves which might have occurred due to lower intensity of the x-ray source as compared to that of synchrotron radiation. Another possible reason for broad peaks could be short range ordering of Au nanoparticles in our system. SAXS curve for PVA and 2% Au-PVA composite in Figure 2(a) shows that PVA gives a strong background and therefore the peaks for the composite appear broad. The SAXS curves give the scattering intensity as function of the scattering factor ( $q$ ). SAXS measurements give 3 peaks corresponding to 3 inter-particle distances. We believe this could arise from cubic close packing for the Au nanoparticles in PVA matrix. In Figure. 2(b) we show the data for 2% Au in PVA after background correction which gives rise to three distinct peaks. The various  $d$  values ( $d_1$ ,  $d_2$  and  $d_3$ ) and then calculated from these peaks using the expression  $d = 2\pi/q$ . The scattering factor,  $q$ , and the inter-particle distance,  $d$  values for the films with different proportion of Au nanoparticles are shown in Table 1.  $q_1$ ,  $q_2$  and  $q_3$  represent  $q$  values for the 3 peaks obtained from SAXS data while  $d_1$ ,  $d_2$  and  $d_3$  represent the corresponding distances obtained. The SPR band positions of

the Au-PVA nanocomposites with varying concentration of Au nanoparticles are also listed in Table 1.

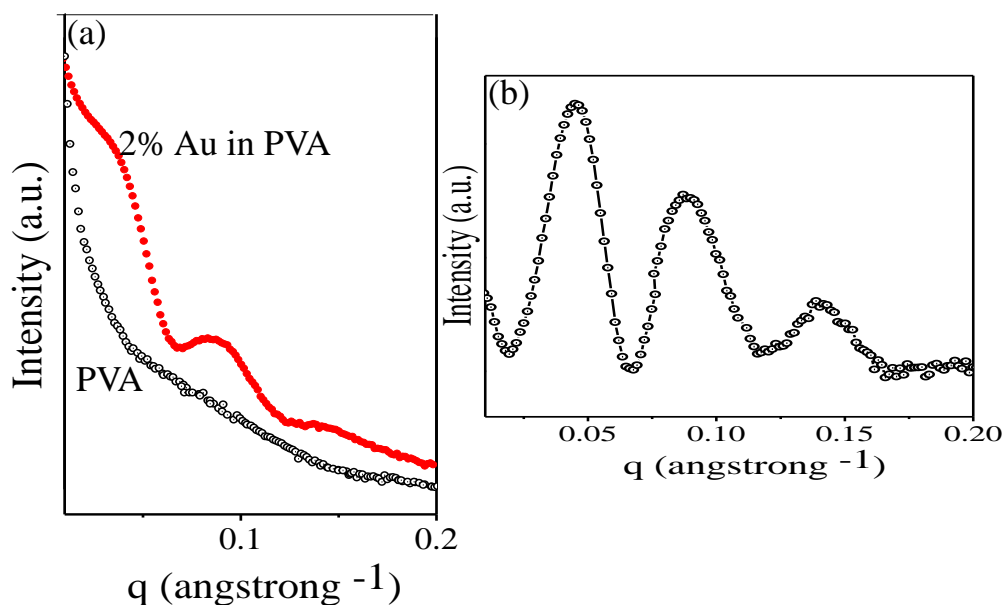


**Figure 2.** SAXS curves of (a) PVA and 2% Au-PVA composite and of (b) 2% Au-PVA composite after background subtraction.

**Table 1**  $q$  and  $d$  values obtained from SAXS measurements and corresponding absorption maxima. Ratio of different  $d$ -values obtained from SAXS is also listed.

Au % in PVA	From SAXS								UV-Vis
	$q_1$ ( $\text{\AA}^{-1}$ )	Distance (nm) $d_1$	$q_2$ ( $\text{\AA}^{-1}$ )	Distance (nm) $d_2$	$d_1/d_2$	$q_3$ ( $\text{\AA}^{-1}$ )	Distance (nm) $d_3$	$d_1/d_3$	$\lambda_{\max}$ (nm)
1	0.038	16.7	0.086	7.3	2.2	0.138	4.6	3.6	<b>546</b>
1.5	0.041	15.2	0.081	7.7	2.0	0.133	4.7	3.1	<b>548</b>
2	0.045	14	0.087	7.2	1.9	0.139	4.5	3.1	<b>560</b>
2.5	0.046	13.8	0.089	7.0	2.0	0.149	4.2	3.2	<b>565</b>
3	0.048	12.9	0.092	6.8	1.9	0.159	4	3.1	<b>579</b>
3.5	0.051	11.6	0.099	6.6	1.8	0.165	3.8	3.0	<b>600</b>



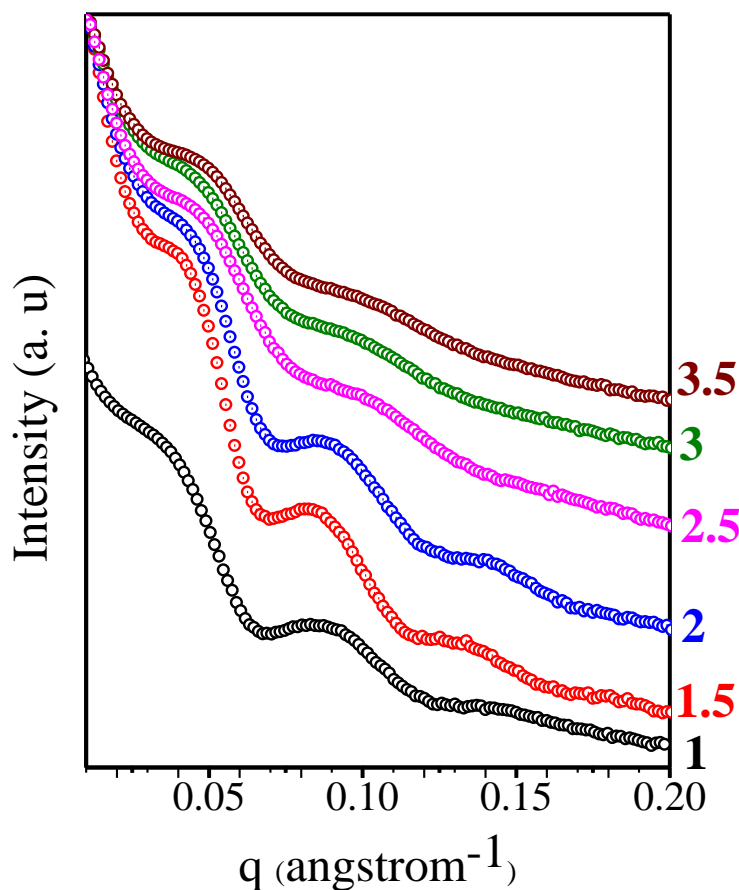


**Figure 3.**  $q$  vs. intensity plot for various concentrations of Au nanoparticles in Au-PVA nanocomposites obtained from SAXS. Weight % of Au nanoparticles is shown against each curve.

Figure 3 shows the SAXS curves of composites with different concentration of Au nanoparticles. All the samples show similar SAXS curves before and after background subtractions with three prominent peaks. The  $d$  values of all the peaks are listed in Table 1. The ratio of the distances  $d_1/d_2$  and  $d_1/d_3$  obtained from the peak position are 2 and 3 respectively (see Table 1) which can be approximated to the  $d_{111}/d_{222}$  and  $d_{111}/d_{422}$  ratio for the ccp structure. Such packing has been reported on self-assembled Au nanoparticles.<sup>19,20</sup>

Electronic absorption spectra of Au-PVA films of different compositions are shown in Figure 4(a). We observe a continuous red shift in the absorption maximum of the SPR band with the change in concentration of the Au nanoparticles. The composite containing the highest concentration of Au nanoparticles has the maximum red shift with an absorption band centered around 600 nm while 1% Au-PVA films shows absorption maxima 546 nm, i.e. a considerable difference of 54 nm.

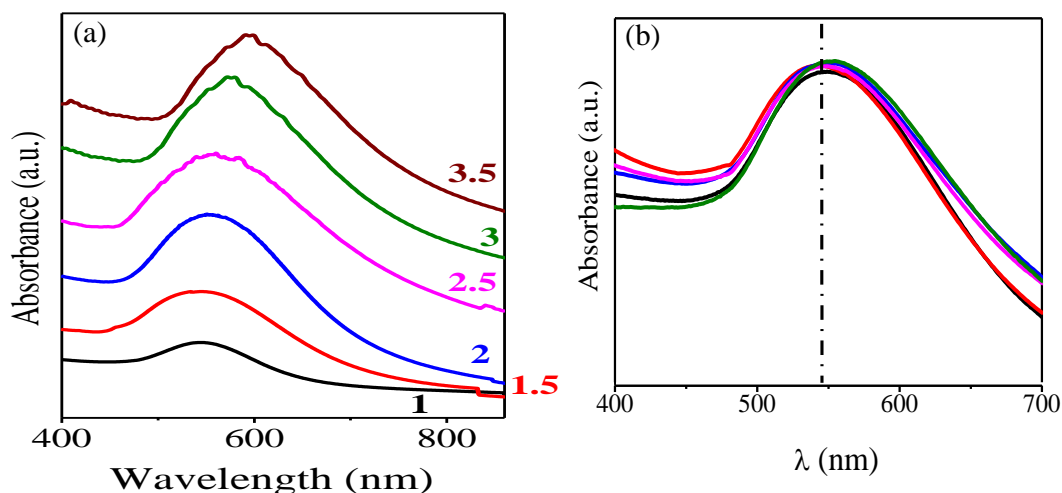


**Figure 4.** (a) Electronic absorption spectra of Au-PVA films with different weight % of Au nanoparticles. Inset shows the spectra of films dissolved in water.

Au-PVA composites were dispersed in fixed quantity of water by stirring at 30°C for ~10 hrs. Figure 4(b) shows the electronic absorption spectra of solutions of Au-PVA. While films show a large variation in absorption maxima on re-dissolving the films in water all the composites show a constant absorption maxima of 545 nm, nearly equal to the absorption maxima of 9-10 nm Au nanoparticles prepared without addition of PVA (~543 nm). Solution medium thus represents isolated Au nanoparticles of 9 nm diameter. Clearly, the large shift in the absorption maxima of composite films with concentration is a manifestation of bringing the Au nanoparticles close enough to each other thereby allowing plasmon coupling.

We have plotted the fractional plasmon shift  $\Delta\lambda/\lambda_0$  as a function of increasing distance  $d_1$  (first peak obtained in SAXS) in Figure 5(a).  $\lambda_0$  is the absorption maxima considering isolated Au nanoparticles being infinitely separated from each other, i.e. not showing any effect due to coupling. Absorption maxima of solution of Au in PVA was taken as  $\lambda_0$  (545 nm) from Figure 4(b).  $\Delta\lambda$  is the difference of absorption maxima of each composite film from  $\lambda_0$ . The curve of  $\Delta\lambda/\lambda_0$  vs interparticle distance follows universal scaling of the distance decay of plasmon coupling.

The data fitted to exponential decay equation,

$$\Delta\lambda/\lambda_0 = A_0 \exp(-d/D/\tau) \quad (1)$$

where,  $A_0$  and  $\tau$  are constants ( $\tau$  is called the decay constant),  $d$  is the interparticle separation as calculated from SAXS and  $D$  the diameter of particle (9 nm).<sup>10</sup>

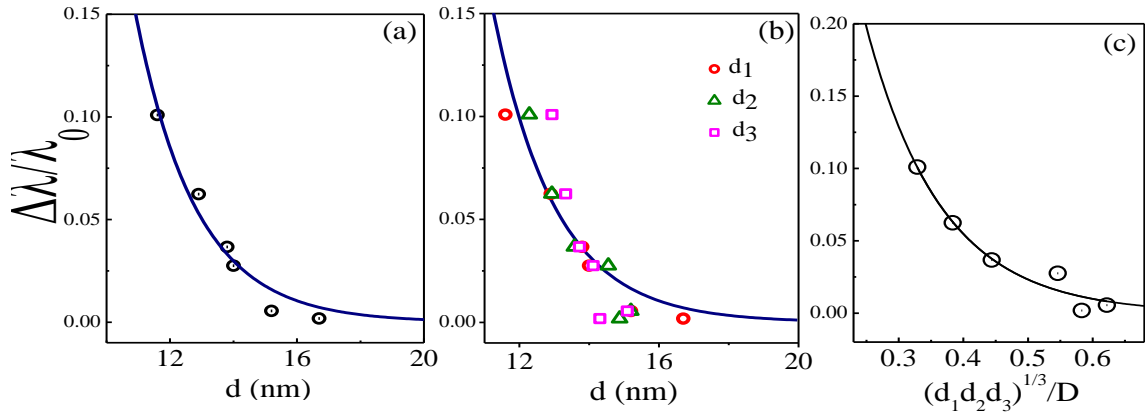


**Figure 5.** (a) Plot of variation of relative shift in plasmon maxima as a function of interparticle distance calculated from SAXS with the fitted curve. (b) Variation of shift in plasmon maxima vs. all the distances scaled as  $d_1$ ,  $d_2 \times 2$  and  $d_3 \times 3$  with the fit, (c) Variation of relative shift of surface plasmon resonance with volume fraction.

The value of  $\tau$  is found to be 0.19, which agrees well with that found for lithographically fabricated Au nanoparticles ( $\sim 0.2$ ).<sup>6</sup> Gunnarson *et al.*<sup>21</sup> estimated the decay constant of Ag nanodisc pairs to be  $\sim 0.22$ . Interestingly, the above equation holds good for the other distances obtained from SAXS data as well, shown in Figure 5(b). We find good fits for the plots with  $d_1$  and  $d_2$ . The plot for  $d_3$  also is similar, but with more deviations possibly because of the greater uncertainty in determining  $d_3$ . Interestingly, the relative shift in plasmon peak scales with the volume fraction of the cube (Figure 5(c)) with the decay constant being 0.22, a value comparable that found by Gunnarson *et al.*<sup>21</sup> The decay length  $l$  obtained from equation,

$$y = y_0 + a \cdot \exp(-d/D/l) \quad (2)$$

is 1.74 nm which is around 0.2 times the particle size (9 nm). This is in agreement with values reported by Jain *et al.*<sup>6</sup>

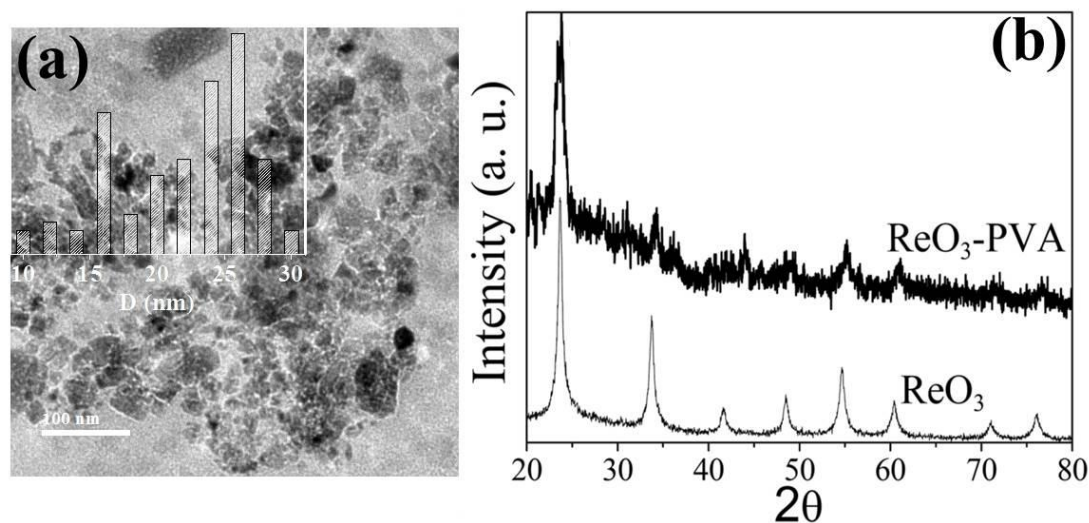


**Figure 6.** (a) TEM image of as synthesized  $\text{ReO}_3$  nanoparticles along with particle size distribution and (b) XRD of as prepared  $\text{ReO}_3$  nanoparticles and  $\text{ReO}_3$ -PVA polymer composite.

To realize the universality of plasmon coupling in plasmonic systems other than noble metals we studied the plasmon coupling of  $\text{ReO}_3$  nanoparticles embedded in polymer matrix. As prepared  $\text{ReO}_3$  nanoparticles vary in size from 15-27 nm as shown in Figure 6(a). Particles crystallize in cubic lattice and can be indexed to  $Pm-3m \{221\}$  space group (JCPDS 00-24-1009). The average particle size estimated by Scherrer formula was 22 nm (Figure 6 (b)). PVA composites films of  $\text{ReO}_3$  show similar XRD pattern with slightly higher background noise due to the amorphous nature of the polymer matrix. We show typical electronic absorption spectra obtained with  $\text{ReO}_3$ -PVA nanocomposites in Figure 7(a) along with the spectrum for pure PVA for comparison. A continuous shift in the absorption maximum of the plasmon band with change in concentration of the  $\text{ReO}_3$  nanoparticles in the nanocomposites can be clearly seen. The SPR band appears at the lowest wavelength ( $\sim 496$  nm) in the case of the composite containing smallest quantity of  $\text{ReO}_3$ . Furthermore, as the concentration of  $\text{ReO}_3$  nanoparticles is increased, the plasmon band shifts toward longer wavelengths. When the concentration of  $\text{ReO}_3$  nanoparticles is least in the polymer nanocomposites, the SPR band occurs at the lowest wavelength since the interparticle distance would be largest corresponding to least dipolar plasmon coupling. As the concentration is increased, the particles come near to

each other leading to more intensive coupling and hence shifting of the plasmon absorption to longer wavelength. We find this behavior with  $\text{ReO}_3$  nanoparticles embedded in all the three polymers.

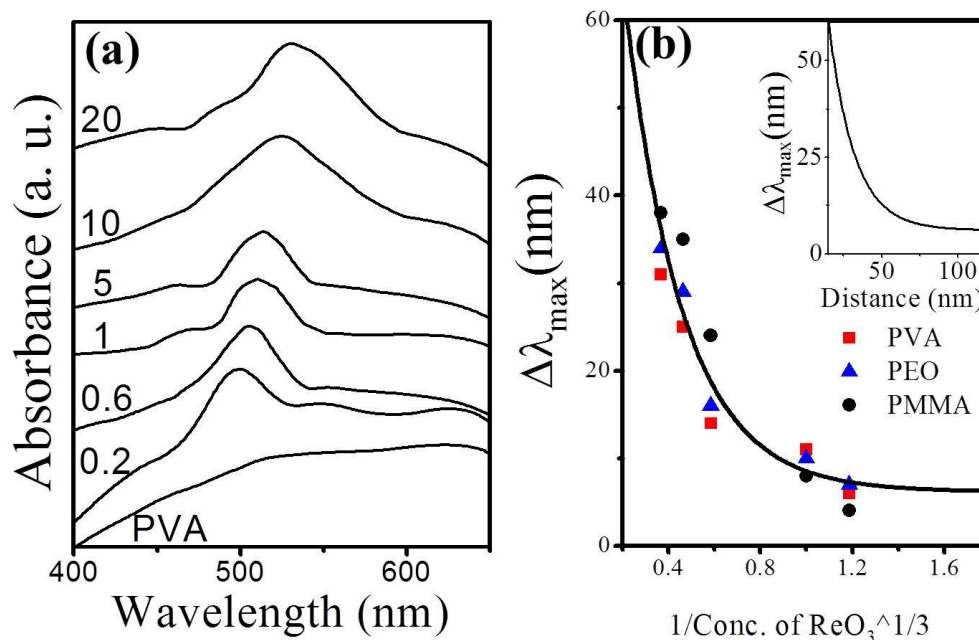


**Figure 7.** (a) Electronic absorption spectra of  $\text{ReO}_3$ -PVA nanocomposites showing the variation of the plasmon band of  $\text{ReO}_3$  nanoparticles with the increase in concentration of the nanoparticles (as weight % of  $\text{ReO}_3$ ) in the composites. (b) Shifts in the plasmon band of the  $\text{ReO}_3$  nanoparticles embedded in polymer matrices as plotted against the reciprocal of concentration of  $\text{ReO}_3$ , the fitted curve along with. Inset shows the shifts as a function of the estimated interparticle distance.

To understand the shifts in the SPR bands of  $\text{ReO}_3$  nanocomposites, we have plotted the shifts against the reciprocal of concentration of  $\text{ReO}_3$  nanoparticles in Figure 7(b). For Au nanoparticles in solution the plasmon maximum that we observe is that for the isolated particles (assumed to be at infinite dilution). In the case of  $\text{ReO}_3$  nanocomposites, we can take the band position at the lowest concentration as corresponding to the isolated particles. With the lowest concentration (0.2 %) of  $\text{ReO}_3$  nanoparticles as the reference, we have calculated the shifts of the plasmon band maxima for other concentrations of  $\text{ReO}_3$ . The shifts follow an exponential decay nature

similar to that of Au-PVA samples. At the highest concentration of the  $\text{ReO}_3$  nanoparticles in the polymer, the plasmon band is most red-shifted implying that the dipolar plasmon coupling is maximum owing to smallest interparticle separation. In order to estimate the interparticle separation, we have used the highest concentration (20 %) of  $\text{ReO}_3$  nanoparticles wherein the particles are most closely spaced as the reference. Here the interparticle distance can at best be equal to the centre-to-centre distance which would be around 25 nm, the particle size being  $\sim 23$  nm. Using this reference, we have estimated the centre-to-centre interparticle distances and re-plotted the shifts in the plasmon maxima as against the inter-particle separation (see the inset in Figure 7(b)). This curve shows the same trend as the one in Figure 7(b) and follows an exponential decay with decay constant of 0.17. The strength of the interparticle dipolar plasmon coupling becomes independent of distance beyond  $\approx 200$  nm. From the fit, the decay length found to be around 17 nm. The shifts in plasmon are much more pronounced in case of Au-PVA systems as compared to that of  $\text{ReO}_3$ -polymer systems.

## ***5. Conclusions***

It is noteworthy that Au nanoparticles dispersed in a polymer show variation in the SPR band with concentration. Concentration is inversely proportional to interparticle distance which was probed by SAXS studies. The shift in SPR with concentration can be described by a simple scaling law as a function of interparticle separation. Previous studies showing scaling of plasmon coupling was conducted in lithographically patterned systems where only two Au nanoparticles interacted with each other. Such a system can be described as two dimensional system in terms of coupling phenomenon. In our study Au nanoparticles form a 3dimensional assembly with cubic type arrangement of particles. The plasmon coupling also happens along all three dimensions. The study thus establishes the universality of scaling behavior of plasmon coupling in Au nanoparticles in a 3-dimensional assembly. What is significant is that the scaling of shift in plasmon peak with distance (or concentration) holds good in the case of metallic  $\text{ReO}_3$ -polymer nanocomposites as well. The study therefore establishes

the universality of scaling behavior of plasmon coupling in three dimensional assembly of all metallic nanoparticles.

## References

1. J. A. Creighton and D. G. Eadon. *J. Chem. Soc., Faraday Trans.* **1991**, 87, 3881.
2. S. Link and M. A. El-Sayed. *J. Phys. Chem. B* **1999**, 103, 4212.
3. J. J. Storhoff, A. A. Lazarides, R. C. Mucic, C. A. Mirkin, R. L. Letsinger and G. C. Schatz. *J. Am. Chem. Soc.* **2000**, 122, 4640.
4. C. Sönnichsen, B. M. Reinhard, J. Liphardt and P. A. Alivisatos. *Nature Biotechnol.* **2005**, 23, 741.
5. B. M. Reinhard, S. Sheikholeslami, A. Mastroianni, A. P. Alivisatos and J. Liphardt. *Proc. Natl Acad. Sc., USA* **2007**, 104, 2667.
6. P. K. Jain, W. Huang and M. A. El-Sayed. *Nano Lett.* **2007**, 7, 2080.
7. W. Huang, W. Qian, P. K. Jain and M. A. El-Sayed. *Nano Lett.* **2007**, 7, 3227.
8. P. K. Jain and M. A. El-Sayed. *J. Phys. Chem. C* **2007**, 111, 17451.
9. P. K. Jain and M. A. El-Sayed. *J. Phys. Chem. C* **2008**, 112, 4954.
10. J. Aizpurua, G. W. Bryant, L. J. Richter, F. J. García de Abajo, B. K. Kelley and T. Mallouk. *Phys. Rev. B* **2005**, 71, 235420.
11. P. K. Jain and M. A. El-Sayed. *Nano Lett.* **2007**, 7, 2854.
12. R. Edreva-Kardzhieva and A. A. Andreev. *Z. Neorg. Khim.* **1977**, 22, 1089.
13. K. Biswas and C. N. R. Rao. *J. Phys. Chem. B* **2005**, 110, 842.
14. S. Ghosh, K. Biswas and C. N. R. Rao. *J Mater. Chem.* **2007**, 17, 2412.
15. K. Biswas, S. V. Bhat and C. N. R. Rao. *J Phys. Chem. C* **2007**, 111, 5689.
16. J. Turkevich, P. C. Stevenson and J. Hillier. *Discuss. Faraday Soc.* **1951**, 11, 55.
17. J. Kimling, M. Maier, B. Okenve, V. Kotaidis, H. Ballot and A. Plech. *J. Phys. Chem. B* **2006**, 110, 15700.
18. H. Nechamkin, A. N. Kurtz and C. F. Hiskey. *J. Am. Chem. Soc.* **1951**, 73, 2828.
19. E. S. Shibu, K. Kimura and T. Pradeep. *Chem. Mater.* **2009**, 21, 3773.

***Chapter I.1 Scaling of Plasmon coupling .....***

---

20. J. Zhuang, H. Wu, Y. Yang and Y. C. Cao. *J. Am. Chem. Soc.* **2007**, 129, 14166.
21. L. Gunnarsson, T. Rindzevicius, J. Prikulis, B. Kasemo, M. Käll, S. Zou and G. C. Schatz. *J. Phys. Chem. B* **2004**, 109, 1079.



# Chapter I.2

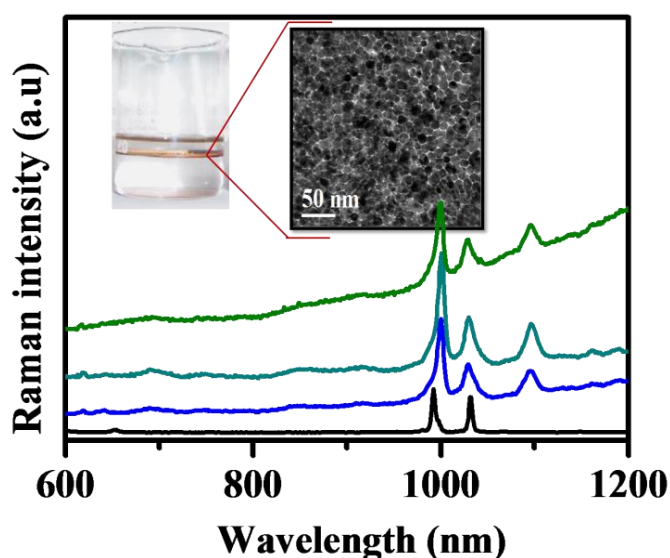
---

## *SERS on nanocrystalline Au and Ag films formed at the organic-aqueous interface*

---

### *Summary\**

*Surface-enhanced Raman scattering (SERS) of pyridine adsorbed on ultrathin nanocrystalline Au and Ag films generated at the liquid-liquid interface has been investigated. The shifts and intensification of bands formed with these films comprising metal nanoparticles are comparable to those found with other types of Au and Ag substrates. SERS of rhodamine 6G adsorbed on Ag films has also been studied. The results demonstrate that nanocrystalline metal films prepared by the simple method involving the organic-aqueous interface can be used effectively for SERS investigations.*



---

\*A paper based on this work has appeared in: *Chem. Phys. Lett.*, 2009

## **1. Introduction**

Surface-enhanced Raman scattering (SERS) was discovered, though not recognized as such, by Fleischmann *et al.*<sup>1</sup> in 1974 who observed intense Raman scattering from pyridine adsorbed onto a roughened silver electrode surface from aqueous solution. Jeanmaire and Van Duyne<sup>2</sup> and Albrecht and Creighton<sup>3</sup> recognized independently that the large intensities observed could not be accounted for simply by the increase in the number of scatterers present and proposed that an enhancement of the scattered intensity occurred in the adsorbed state. Interestingly enough, these papers presaged a debate about the SERS mechanism which ran furiously for nearly a decade and about which research is still being conducted. Jeanmaire and Van Duyne tentatively proposed an electric field enhancement mechanism whereas Albrecht and Creighton speculated that resonance Raman scattering from molecular electronic states, broadened by their interaction with the metal surface, might be responsible. They were both right in concept, though not in detail. In the following two decades, SERS was reported for a variety of molecules adsorbed on the surfaces of a few metals in a variety of morphologies and physical environments. Silver, copper and gold are by far the dominant SERS substrates. The largest enhancements occur for surfaces which are rough on the nanoscale (10–100 nm). As a result of intense research activity mechanistic understanding of the primary observation - the  $10^6$  fold intensity enhancement of Raman scattering, also grew. The 1985 review article by Martin Moskovits,<sup>4</sup> eloquently summarizes the majority view of that time that the Raman enhancement factor,  $EF = 10^6$  could be understood as the product of two major contributions: (1) an electromagnetic enhancement mechanism and (2) a chemical enhancement mechanism. Of course, there really are no other choices since the intensity of Raman scattering is directly proportional to the square of the induced dipole moment,  $\mu_{\text{ind}}$  which, in turn, is the product of the Raman polarizability,  $\alpha$ , and the magnitude of the incident electromagnetic field,  $E$ . As a consequence of exciting the localized surface plasmon resonance (LSPR) of a nanostructured or nanoparticulate metal surface, the local electromagnetic field is enhanced by say a factor of 10. Since Raman scattering approximately scales as  $E^4$ , the electromagnetic enhancement factor is of order  $10^4$ . The chemical enhancement factor of  $10^2$  was viewed as arising from the excitation of adsorbate localized electronic resonances or metal-to-adsorbate charge transfer

resonances (viz., resonance Raman scattering (RRS)). It is also worthwhile noting that surface-enhanced resonance Raman scattering (SERRS) with combined SERS and RRS gives enhancement factors in the  $10^9$ – $10^{10}$  range.

Enormous enhancement in the Raman intensity, coupled with the suppression of fluorescence, suggests the possibility that SERS could provide an invaluable tool as a reliable, high-resolution detection technique for extremely minute quantities of target molecules. Indeed, recent technical advances have shown the way to detection with enhancement factors as large as  $10^{14}$ .<sup>5–11</sup>

## ***2. Scope of the present investigations***

Surface roughness, particle size and shape, the nature of the analyte and the wave length of laser excitation are the important factors that determine the magnitude of surface enhancement.<sup>12–17</sup> In early studies on SERS, roughened Au and Ag surfaces were used as substrates. SERS studies based on Ag,<sup>1,18–25</sup> Au,<sup>18,19,26–29</sup> and other metals such as Pt, Ru, Rh, Pd, Fe, Co and Ni<sup>30–35</sup> as well as the metallic oxide  $\text{ReO}_3$ ,<sup>36</sup> have been reported. Since wider applications of SERS depend on the development of highly enhancing substrates, there have been efforts to develop improved substrates for enhancement. Thus, Yan and co-workers<sup>37</sup> used silver-coated zeolite crystals as SERS substrates while Wei et al.<sup>38</sup> found Ag films to be more Raman active than clusters or nanocrystals. Chaney et al.<sup>39</sup> found SERS activity of Ag nanorods arrays to depend on the length of the rods. Reproducibility of SERS signals from place to place on films is generally not satisfactory. Atomic layer deposition and template electrodeposition have been employed to obtain uniform and reproducible SERS signals from films.<sup>40, 41</sup> Wang and co-workers<sup>42</sup> have studied the effect of the morphology of Au films on the SERS signal. Bimetallic Au-Ag structures have also been employed as SERS substrates.<sup>43, 44</sup> Since films are desirable substrates for SERS, we considered it important to investigate SERS activity of molecules on nanocrystalline films of Au and Ag which can be readily prepared at the organic–aqueous interface.<sup>45–47</sup> This technique of preparing film substrates is simple and involves generating the metallic films at the interface by the reaction of a

metal precursor in the organic phase with a reducing agent in the aqueous phase. The films so prepared contain nanoparticles of Au or Ag whose diameter can be varied by varying the temperature. Reaction parameters such as temperature, reaction time, concentrations of the metal precursor and the reducing agent, and the viscosity of the aqueous layer affect the nature and properties of the nanocrystalline films.<sup>46, 47</sup> An additional advantage of the films generated at the interface is that they are easily transferred onto solid substrates. In this article, we present the results of our investigations of SERS of pyridine and rhodamine 6G on ultrathin nanocrystalline metallic films formed at the organic–aqueous interface.

### ***3. Experimental Section***

#### ***Preparation of nanocrystalline films of Au and Ag***

Nanocrystalline films of gold were prepared using Au(PPh<sub>3</sub>)Cl (Ph = phenyl) and Ag(PPh<sub>3</sub>)<sub>4</sub>NO<sub>3</sub> as precursors by the literature procedure.<sup>48,49</sup> Tetrakis(hydroxymethyl)phosphonium chloride (THPC) was used as the reducing agent. In a typical preparation, 10 mL of a 1.5 mM solution of Au(PPh<sub>3</sub>)Cl in toluene was allowed to stand in contact with 16 mL of 6.25 mM aqueous alkali in a 100 mL beaker at room temperature. Once the two layers stabilized, 330 μL of 50 mM THPC solution in water was injected into the aqueous layer using a syringe with minimal disturbance to the toluene layer. The onset of reduction was marked by a faint pink coloration of the toluene–water interface. The reduction was allowed to proceed without disturbance for 4 h. With the passage of time, the colour became more vivid, finally resulting in a robust elastic film at the liquid–liquid interface.<sup>35</sup> To vary the particle size, the films were formed at different temperatures. Films of Ag were prepared by a similar procedure.<sup>35</sup> Nanocrystalline films of gold were also prepared by using hydrazine hydrate (50 μL in 20 mL water) as the reducing agent, maintaining the temperature at 323 K. Au–Ag alloy films were prepared using the procedure reported in the literature.<sup>40</sup> Alloy formation was confirmed by changes in the visible spectra where the plasmon band shifts with the composition. 1:1 ratio of metal precursors (1.5 mM) in 10 mL toluene formed the organic

layer and 16 mL, 6.25 mM NaOH formed lower aqueous layer. 330  $\mu$ L 50 mM THPC was used as reducing agent and the temperature maintained at 348 K. The nanocrystalline films were characterized by transmission electron microscopy (TEM) and other techniques. The thickness of the films was generally around 60 nm. Properties of the films were entirely reproducible, provided the conditions of preparation were kept the same.

### ***Raman measurements***

For SERS measurements, we used pyridine and rhodamine 6G (Rh6G) solutions in water. For each measurement 10  $\mu$ L of the liquid analyte was dropped on nanocrystalline metallic film on a silicon wafer. Raman spectra were recorded with a LabRAM HR high-resolution Raman spectrometer (Horiba-Jobin Yvon) using a He-Ne laser ( $\lambda = 632.8$  or 514 nm). We have obtained relative enhancement ratios ( $R$ ) of the adsorbate bands relative to those of the pure liquid<sup>35, 51, 52</sup> and have estimated the values of surface enhancement factor ( $EF$ ). The relative enhancement ratio,  $R$ , is defined as the relative intensity of the Raman band of liquid analyte adsorbed on the nanocrystalline film divided by the relative intensity of corresponding band of liquid pyridine or Rh6G solution. The surface enhancement factor,  $EF$ , was calculated by the equation.<sup>3,19</sup>

$$EF = \left( I_{SERS} / I_{bulk} \right) \cdot \left( N_{bulk} / N_{ads} \right) \quad (1)$$

where,  $I_{SERS}$ ,  $I_{bulk}$ ,  $N_{bulk}$  and  $N_{ads}$  respectively represent the measured SERS intensity of adsorbed molecules on the Au/Ag nanocrystalline film, the normal Raman intensity from the liquid analyte, the number of probe molecules under laser illumination in the bulk sample and the number of probe molecules on the nanocrystalline film respectively.  $N_{ads}$  is calculated from the average radius of adsorbate nanoparticles, the surface density of the adsorbate molecule, the area of the laser spot and surface coverage of adsorbate nanoparticles.  $N_{bulk}$  was obtained from the area of the laser spot, the penetration depth,

the density of the analyte and the molecular weight of the analyte. SERS measurements were made on different places of a given sample to ensure reproducibility of the results.

## **4. Results and discussion**

### ***SERS of Pyridine on Au films***

We first carried out SERS of pyridine on nanocrystalline Au films generated at the liquid–liquid interface by using THPC as the reducing agent. In Figure 1(a–c), we show TEM images of the nanocrystalline Au films formed at different temperatures.

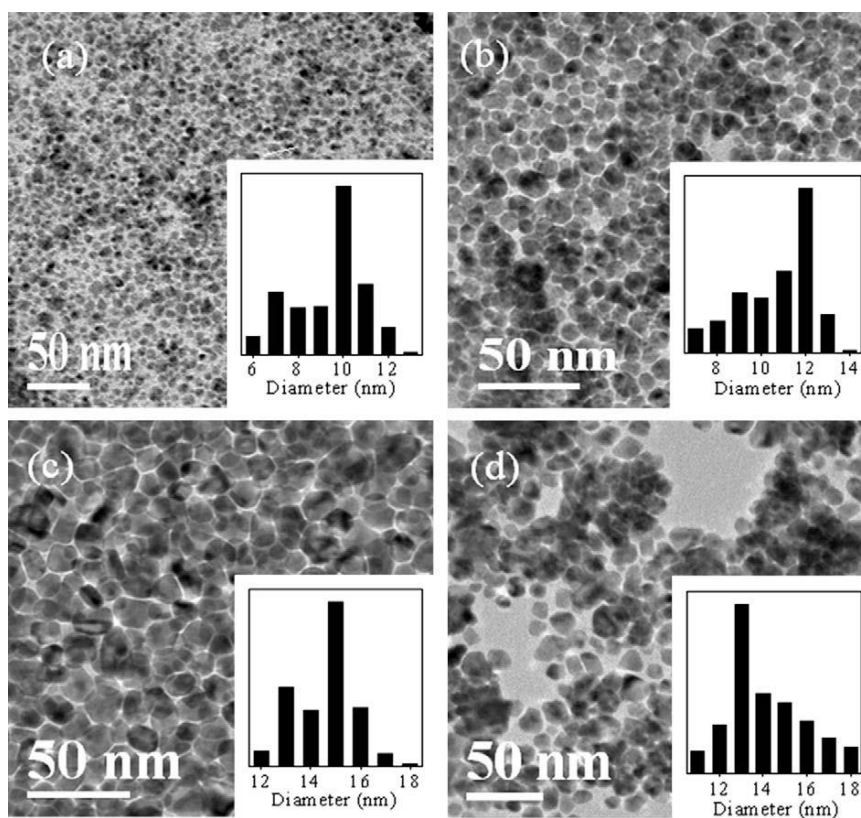


**Figure 1.** TEM images of the ultrathin nanocrystalline Au films obtained at the liquid–liquid interface using THPC as the reducing agent at (a) 298 K, (b) 313 K, (c) 348 K and of (d) with hydrazine hydrate as the reducing agent at 323 K. Histograms of particle size distribution are shown as insets.

The Au particles in the films formed at 298, 313 and 348 K had average diameters of 10, 12 and 15 nm respectively. Films of Au particles were also prepared with other reducing agents like hydrazine hydrate formed at 323 K. TEM images of these films show that the nanocrystals had an average diameter of 13 nm. In Figure 2 (a) we have plotted the Raman spectrum of pyridine on the Au nanocrystalline films containing particles of different diameters, along with the spectrum of the pure liquid. We clearly see SERS on the Au films. Thus, on adsorption of pyridine on the Au film containing particles of 15 nm diameter, we observe bands at  $619\text{ cm}^{-1}$  ( $\nu_{6a}$ , A1, asymmetric ring breathing),  $689\text{ cm}^{-1}$  ( $\nu_{6b}$ , B2, ring in plane deformation),  $1001\text{ cm}^{-1}$  ( $\nu_1$ , A1, symmetric ring breathing),  $1030\text{ cm}^{-1}$  ( $\nu_{12}$ , A1, trigonal ring breathing),  $1096\text{ cm}^{-1}$  ( $\nu_{18a}$ , A1) and  $1298\text{ cm}^{-1}$  ( $\nu_{9a}$ , A1, C-H in plane deformation) respectively.

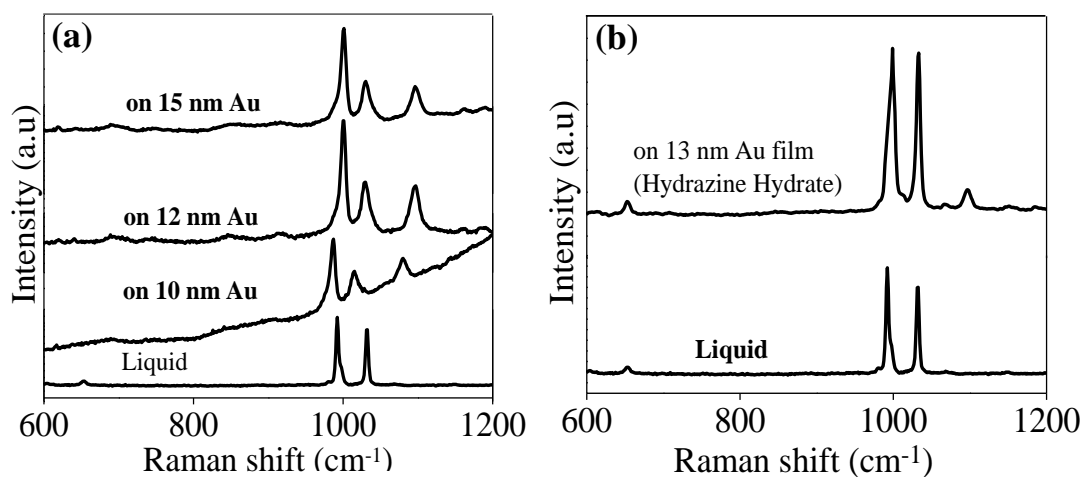


**Figure 2.** Comparison of Raman spectra of pyridine ( $\lambda_{\text{laser}} = 632\text{ nm}$ ) (a) in the liquid state with that on Au films with particles of varying diameter prepared at toluene-water interface using THPC as the reducing agent and (b) in liquid with that on nanocrystalline Au film prepared with hydrazine hydrate as reducing agent.

In Table 1, we have compared the Raman band positions of pyridine on Au nanocrystalline films with different particle diameters along with their relative intensities. Data of liquid pyridine is given for comparison. We see that almost all the bands are shifted to higher frequencies (relative to the positions of the pure liquid), except those at

**Table 1.** Raman band positions ( $\text{cm}^{-1}$ ) and relative enhancement ratios of pyridine on nanocrystalline Au films.

Liquid peak positions (relative intensity)	V	Film of 10 nm Au <sup>a</sup>			Films of 13 nm Au <sup>b</sup>			Films of 15 nm Au <sup>a</sup>			Films of 13 nm Au <sup>b</sup>		
		Peak positions (relative intensity)	R	EF ( $10^4$ )	Peak positions (relative intensity)	R	EF ( $10^4$ )	Peak positions (relative intensity)	R	EF ( $10^4$ )	Peak positions (relative intensity)	R	EF ( $10^4$ )
604, (2)	A <sub>1</sub> , 6a	617(7)	4		620(3)	2		619(4)	2		616(1.5)	0.75	
652, (5)	B <sub>2</sub> , 6b	692(5)	1		689(7)	1		689(5)	1		653(9)	2.0	
992, (100)	A <sub>1</sub> , 1	1000(100)	1	3.3	1000(100)	1	4	1001(100)	1	4	999(100)	1	0.33
1032, (82)	A <sub>1</sub> , 12	1029(39)	0.5	1.6	1029(42)	0.5	2	1030(41)	0.5	2	103(98)	1.2	0.31
1068, (2)	A <sub>1</sub> , 18a	1096(30)	15	46	1097(43)	22	60	1096(33)	17	60	1096(11.5)	6.0	2.9
1149, (2)	B <sub>2</sub> , 15				1163(4)	2		1161(5)	3		1152 (3)	1.5	
					1191(4)			1190(4)			1185 (2)		
1218, (7)	A <sub>1</sub> , 9a							1298(5)	0.7		1218(8)	1	
1441, (1)	B <sub>2</sub> , 19b				1437(5)	5		1440(3)	3		1436 (3)	3	
1482, (2)	A <sub>1</sub> , 19a				1480(3)	2		1483(1)	0.5		1485(2)	1	
1573, (2)	B <sub>2</sub> , 8b				1572(3)	2					1575(9)	4.5	
1583, (2)	A <sub>1</sub> , 8a	1585(97)	49		1585(21)	11		1585(56)	28		1584(11)	5.5	

a = by THPC route, b = by hydrazine hydrate route, v = wilson number, R = relative enhancement ratio



1032, 1441 and 1482  $\text{cm}^{-1}$ . The highest frequency shifts are exhibited by the bands at 652 ( $\nu_{6b}$ , B<sub>2</sub>) and 1068  $\text{cm}^{-1}$  ( $\nu_{18a}$ , A<sub>1</sub>). The highest intensity is found in the case of the symmetric ring breathing mode ( $\nu_1$ ) at 1001  $\text{cm}^{-1}$ . The frequency of this mode is sensitive to weak  $\sigma$  donation and the large  $\sigma/\pi$  back donation. In the case of Au and other metals, the  $\nu_1$  mode is known to be shifted to higher frequencies, with the pyridine molecule in the end-on configuration (binding by nitrogen lone pair of electrons).<sup>26, 35</sup> That we observe similar shifts of  $\nu_1$  in the present study, on adsorbing pyridine on the Au nanocrystalline films, suggests the end-on configuration for the adsorbed molecule. We also observe additional bands around 1190 and 1185  $\text{cm}^{-1}$ . We have measured the relative enhancement ratios,  $R$ , of pyridine on the Au nanocrystalline films and found it to vary between 1.0 and 22, depending on the particle size (Table 1), the maximum values of  $R$  being found with the 12 nm particles. The SERS intensity is optimal when the particle size is small with respect to the wavelength of the exciting light as long as the size is not smaller than the electronic mean free path of the conduction electrons.

TEM images of Au films formed at 323 K with hydrazine hydrate as the reducing agent show that the nanocrystals had an average diameter of 13 nm (Figure 1(d)). The Raman spectrum of pyridine on this nanocrystalline film is shown along with spectrum of pure pyridine in Figure 2(b). We find the shifts and intensification of the pyridine bands on this Au film to be similar to those found with the films prepared with THPC. The  $R$  values of the pyridine bands vary in the range 1–26. In order to calculate  $EF$ , we have used the value of monolayer surface density of pyridine<sup>26</sup> on Au as  $4 \times 10^{-10} \text{ mol.cm}^{-2}$ . We have calculated  $EF$  values for the three most intense bands in liquid pyridine spectra:  $\nu_1$  (992  $\text{cm}^{-1}$ , A<sub>1</sub>),  $\nu_{12}$  (1332 $\text{cm}^{-1}$ , A<sub>1</sub>) and  $\nu_{18a}$  (1068  $\text{cm}^{-1}$ , A<sub>1</sub>). The  $EF$  values listed in Table 1 show that they are generally of the order of  $\sim 10^5$  and comparable to those reported in other SERS studies.<sup>13</sup>

### ***SERS of Pyridine of Ag films***

We have measured SERS activity of pyridine on Ag nanocrystalline films formed at the liquid-liquid interface at 348 K and containing particles with an average diameter of around 35 nm (see Figure 3(a)) All the Raman bands of pyridine show shifts to higher frequencies on the Ag film (Figure 3(b)), but the shifts are less than those on Au films.

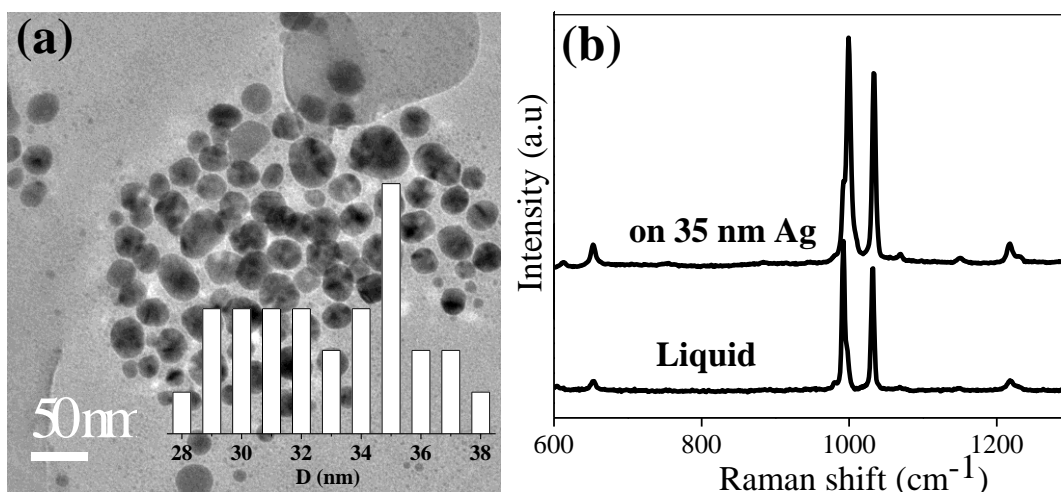


**Figure 3** (a) TEM image of nanocrystalline film of Ag obtained at the liquid–liquid interface along with particle size distribution in inset and (b) Raman spectra of pyridine ( $\lambda_{\text{laser}}=632$  nm) in the liquid state, and on a ultrathin nanocrystalline Ag film with 35 nm particles.

**Table 2.** Raman band positions ( $\text{cm}^{-1}$ ) and relative enhancement ratios and enhancement factors (EF) of pyridine on nanocrystalline Ag films

Liquid peak positions (relative intensity)	$\nu$	Film of 12 nm Au <sup>a</sup>		
		Peak positions (relative intensity)	R	EF ( $10^4$ )
604, (2)	A <sub>1</sub> ,6a	612(3)	2	
652, (5)	B <sub>2</sub> ,6b	653(9)	2	
992,(100)	A <sub>1</sub> ,1	1000(100)	1	6.5
1032, (82)	A <sub>1</sub> ,12	1033(84)	1	6.7
1068, (2)	A <sub>1</sub> ,18a	1069(2)	1	7.0
1149, (2)	B <sub>2</sub> ,15	1152(2)	1	
1218, (7)	A <sub>1</sub> 9a	1218(9)	1	
1441, (1)	B <sub>2</sub> ,19b			
1482, (2)	A <sub>1</sub> ,19a	1487(3)	2	
1573, (2)	B <sub>2</sub> ,8b	1576(5)	3	
1583(2)	A <sub>1</sub> ,8a	1592(5)	3	

$\nu$  = Wilson number. R = relative enhancement ratio

The value of  $R$  varies between 1 to 3 while  $EF$  is  $6.5 \times 10^4$ ,  $6.7 \times 10^4$  and  $7.0 \times 10^4$  for the  $\nu_1$  ( $992 \text{ cm}^{-1}, A_1$ ),  $\nu_{12}$  ( $1032 \text{ cm}^{-1}$ ) and  $\nu_{18a}$  ( $1068 \text{ cm}^{-1}, A_1$ ) modes respectively. The intensity of the  $\nu_{12}$  band gets enhanced much more on the Ag film than on the Au films. It is known that the potential energy distribution of the  $\nu_{12}$  mode varies substantially for metals with different Fermi levels.<sup>13</sup> Unlike on the Au films where few of the pyridine bands show intensification, all the bands of pyridine show intensification in the case Ag (see Table 2), suggesting that EM enhancement plays a more important role and that chemical interaction between pyridine and Ag is relatively weak.<sup>13, 53</sup> In the case of Au films, however, both EM and chemical enhancements occur. Measurements of SERS of pyridine with films comprising nanoparticles of the 1:1 alloy of Au-Ag show  $R$  values comparable to those on Au and Ag films.

### SERS of Rhodamine 6G on Ag films

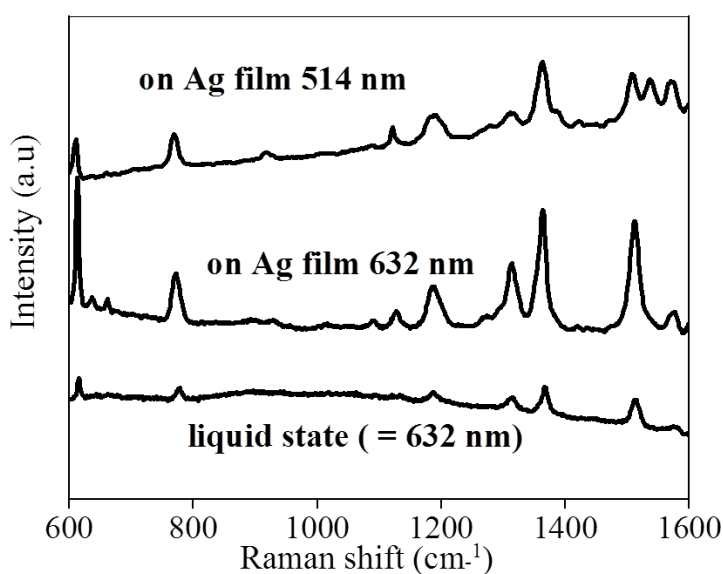


**Figure 4.** Raman spectra of rhodamine 6G (in water) in the liquid state and on the nanocrystalline Ag films under 632 nm and 514 nm lasers.

The spectrum of the pure liquid is shown for comparison. On adsorption of rhodamine 6G on the Ag film, we observe a large number of bands, all shifted to lower frequencies.<sup>53</sup> We also observe additional bands at  $636$ ,  $1270$ ,  $1293$  and  $1476 \text{ cm}^{-1}$ .

SERS activity of rhodamine-6G was investigated on the 35 nm Ag film, by recording the spectra with both 632 nm and 514 nm laser excitations, since the dye shows strong fluorescence with an absorbance maximum at 520 nm. Figure 4 shows the Raman spectra of  $10^{-2}$  M rhodamine 6G (in water) adsorbed on the Ag film using both 632 nm and 514 nm laser

**Chapter I.2 SERS on Au and Ag nanoparticles.....**

The two most intense bands of rhodamine 6G  $1367\text{ cm}^{-1}$  [ $\nu(\text{CC}) + \nu(\text{CN})$ ] and  $1515\text{ cm}^{-1}$  [ $\nu(\text{CC})$ ] are shifted to  $1363\text{ cm}^{-1}$  and  $1512\text{ cm}^{-1}$  respectively on adsorption on the Ag film. The band positions relative intensities and values of R for adsorbed R6G on Ag film is noted down in Table 3.

**Table 3.** Raman band positions ( $\text{cm}^{-1}$ ), relative enhancement ratios and enhancement factors (EF) of Rhodamine 6G on nanocrystalline Ag films

Liquid peak positions (relative intensity)	$\nu$	$\lambda_{\text{laser}} = 632\text{ nm}$			$\lambda_{\text{laser}} = 514\text{ nm}$		
		Peak positions (relative intensity)	R	EF ( $10^4$ )	Peak positions (relative intensity)	R	EF ( $10^4$ )
615 (81)	53	612(109)	1.4	1.4	610(59)	0.72	4.4
	54	636 (8)			635(3)		
662 (14)	55	661(13)	1.0		659(4)	0.28	
					705(2)		
778(43)	65	771(41)	1		768(46)	1.1	
					917(10)		
1091(10)	94	1091(8)	0.8		1085(4)	0.4	
1133(12)	97	1127 (15)	1.3		1121(28)	2.4	
1187(36)	103	1184 (35.5)	1		1184(37)	1	
					1191(39)		
	110	1270(1)			1277(6)		
	111	1273(2)					
	112	1293(2)			1310(20)		
1314(43)	115	1313(56)	1.3	1.3	1315(19)	0.4	
	117	1363(100)	1	1	1363(100)	1	1.4
					1385(25)		
	127	1419(4)			1421(9)		
	128	1435(3)			1449(4)		
	139	1476(1)					
1515(100)	146	1512(96)	1	1	1508(48)	0.5	2.9
	147	1532(0.5)			1536(35)		
11575(23)	151	1574(26)	1.1		1570(42)	1.8	
1600(12)	152	1600(17)	1.4		1598(12)		
	153	1612(2)			1612(2)		
1654(42)	154	1651(52)	1.2		1650(126)	3	1.5

$\nu$  = Wilson number. R = relative enhancement ratio

The R values of rhodamine 6G on Ag vary between 1.0 to 1.4. The EF values for the four most intense bands of rhodamine 6G  $\nu_{53}$  at  $615\text{ cm}^{-1}$ ,  $\nu_{115}$  at  $1314\text{ cm}^{-1}$ ,  $\nu_{117}$  at  $1367\text{ cm}^{-1}$  and  $\nu_{146}$  at  $1515\text{ cm}^{-1}$  was found to be of the order of  $10^4$  (see Table 3).

## 5. Conclusions

The results of the present study show that nanocrystalline films of Au and Ag generated at the organic-aqueous interface can be used as substrates for SERS studies of

molecules. The intensity enhancement and band shifts of pyridine found on these thin films are comparable to those reported for other Au and Ag substrates. The ease with which nanocrystalline metal films are prepared at the interface favour their use for SERS studies.

## Reference

1. M. Fleischmann, P. J. Hendra, A. J. McQuillan, *Chem. Phys. Lett.* **1974**, 26, 163.
2. D. L. Jeanmaire, R. P. Van Duyne, *J. Electroanal. Chem.* **1977**, 84, 1.
3. M. G. Albrecht, J. A. Creighton, *J. Am. Chem. Soc.* **1977**, 99, 5215.
4. M. Moskovits, *Rev. Mod. Phys.* **1985**, 57, 783.
5. S. Nie, X S. R. Emory, *Science* **1997**, 275, 1102.
6. K. Kneipp, Y. Wang, H. Kneipp, L. Perelman, I. Itzkan, R. R. Dasari, M. S. Feld, *Phys. Rev. Lett.* **1997**, 78, 166755.
7. H. Xu, E. Bjerneld, M. Kall, L. Borjesson, *Phys. Rev. Lett.* **1999**, 83, 4357.
8. G. C. Schatz, M. A. Young, R. P. Van Duyne, *Topics in Applied Physics*, In *Surface Enhanced Raman Scattering: Physics and Applications* K. Kneipp, M. Moskovits, H. Kneipp, Eds. **Springer**: Berlin **2006**.
9. A. M. Michaels, J. Jiang, L. E. Brus, *J. Phys. Chem. B* **2000**, 104, 11965.
10. K. A. Bosnick, J. Jiang, L. E. Brus, *J. Phys. Chem. B* **2002**, 106, 8096.
11. J. Jiang, K. Bosnick, M. Maillard, L. Brus, *J. Phys. Chem. B* **2003**, 107, 9964.
12. R.K. Chang, T.E. Furtak, *Surface Enhanced Raman Scattering*, New York, Plenum Press, **1982**.
13. Z.Q. Tian, B. Ren, D.Y. Wu, *J. Phys. Chem. B* **2002** 106, 9463.
14. M.J. Moskovits, *Raman Spectrosc.* **2005**, 36, 485.
15. K. Kneipp, H. Kneipp, I. Itzkan, R.R. Dasari, M.S. Feld, *Chem. Rev.* **1999**, 99, 1957.
16. C.J. Orendorff, A. Gole, T.K. Sau, C.J. Murphy, *Anal. Chem.* **2005**, 77, 3261.

17. A. Campion, P. Kambhampati, *Chem. Soc. Rev.* **1998**, 27, 241.
18. C. Lee, S.J. Bae, M. Gong, K. Kim, S.W. Joo, *J. Raman Spectrosc.* **2002**, 33, 429.
19. C.J. Orendorff, L. Gearheart, N.R. Jana, C.J. Murphy, *Phys. Chem. Chem. Phys.* **2006**, 8, 165.
20. M. Kerker, *Pure Appl. Chem.* **1984**, 56, 1429.
21. R. Dornhaus, M.B. Long, R.E. Benner, R.K. Chang, *Surf. Sci.* **1980**, 93, 240.
22. M.M. Miranda, N. Neto, G. Sbrana, *J. Phys. Chem.* **1988**, 92, 954.
23. H.H. Wang et al., *Adv. Mater.* **2006**, 18, 491.
24. A.M. Michaels, M. Nirmal, L.E. Brus, *J. Am. Chem. Soc.* **1999**, 121, 9932.
25. K.A.B. Snick, J. Jiang, L.E. Brus, *J. Phys. Chem. B* **2002**, 106, 8096.
26. A.G. Brolo, D.E. Irish, J. Lipkowsky, *J. Phys. Chem. B* **1997**, 101, 3906.
27. N. Félidj, S. Lau Truong, J. Aubard, G. Lévi, J. R. Krenn, A. Hohenau, A. Leitner, F. R. Aussenegg, *J. Chem. Phys.* **2004**, 120, 7141.
28. X.C. Yang, Y. Fang, *J. Phys. Chem. B* **2003**, 107, 10100.
29. Z. Zhu, T. Zhu, Z. Liu, *Nanotechnol.* **2004**, 15, 357.
30. B. Ren, Q.J. Huang, W.B. Chai, B.W. Mao, F.M. Liu, Z.Q. Tian, *J. Electroanal. Chem.* **1996**, 415, 175.
31. J.S. Gao, Z.Q. Tian, *Spectrochim. Acta A* **1997**, 53, 1595.
32. Q.J. Huang, J.L. Yao, R.A. Gu, Z.Q. Tian, *Chem. Phys. Lett.* **1997**, 271, 101.
33. P. G. Cao, J. L. Yao, B. Ren, B. W. Mao, R. A. Gu, Z. Q. Tian, *Chem. Phys. Lett.* **2000**, 316, 1.

34. D.Y. Wu, Y. Xie, B. Ren, J.W. Yan, B.W. Mao, Z.Q. Tian, *Phys. Chem. Commun.* **2001**, 18, 1.
35. C. Zou, P.W. Jagodzinski, *J. Phys. Chem. B* **2005**, 109, 1788.
36. K. Biswas, S.V. Bhat, C.N.R. Rao, *J. Phys. Chem. C* **2007**, 111, 5689.
37. W. Yan, L. Bao, S.M. Mahurin, S. Dai, *Appl. Spectrosc.* **2006**, 58, 18.
38. G. Wei, H. Zhou, Z. Liu, Z. Li, *Appl. Surf. Sci.* **2005**, 240, 260.
39. S.B. Chaney, S. Shanmukh, R.A. Dluhy, Y.P. Zhao, *Appl. Phys. Lett.* **2005**, 87, 031908.
40. J.A. Dieringer et al., *Faraday Discuss.* **2006**, 132, 9.
41. M. E. Abdelsalam, P. N. Bartlett, J. J. Baumberg, S. Cintra, T. A. Kelf, A. E. Russell, *Electrochem. Commun.* **2005**, 7, 740.
42. C. H. Wang, D. C. Sun, X. H. Xia, *Nanotechnol.* **2006**, 17, 651.
43. S.E. Hunyadi, C.J. Murphy, *J. Mater. Chem.* **2006**, 16, 3929.
44. Y. Wang, H. Chen, H. Dong, E. Wang, *J. Chem. Phys.* **2006**, 125, 044710.
45. C.N.R. Rao, G.U. Kulkarni, P.J. Thomas, V.V. Agrawal, P. Saravanan, *J. Phys. Chem. B* **2003**, 107, 7391.
46. C.N.R. Rao, G.U. Kulkarni, V.V. Agrawal, U.K. Gautam, M. Ghosh, U. Tumkurkar, *J. Colloid Interface Sci.* **2005**, 289, 305.
47. C.N.R. Rao, K.P. Kalyanikutty, *Acc. Chem. Res.* **2008**, 41, 489.
48. P. Braunstein, H. Lehner, D. Matt, *Inorg. Synth.* **1990**, 7, 218.
49. M. Khan, C. Oldham, D.G. Tuck, *Can. J. Chem.* **1981**, 59, 2714.
50. V.V. Agrawal, P. Mahalakshmi, G.U. Kulkarni, C.N.R. Rao, *Langmuir* **2006**, 22, 1846.



51. S. Astilean, M. Bolboaca, D. Mainu, T. Iliescu, *Romanian Rep. Phys.* **2004**, 56, 346.
52. P. Hildebrandt, M. Stockburger, *J. Phys. Chem.* **1984**, 88, 5935.
53. H. Watanabe, N. Hayazawa, Y. Inouye, S. Kawata, *J. Phys. Chem. B* **2005**, 109, 5012.

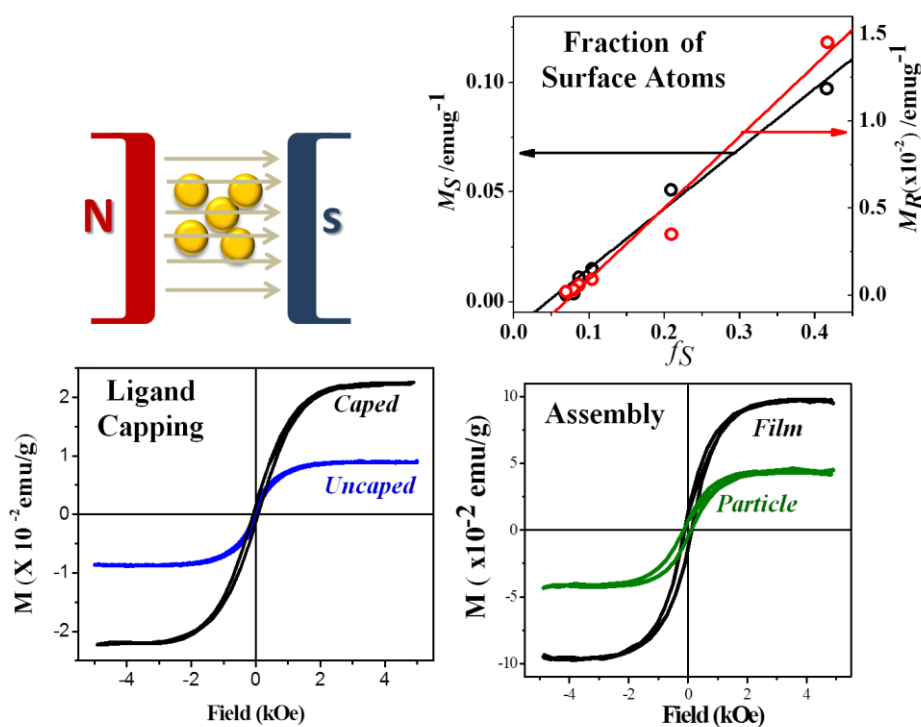


# Chapter I.3

## *Ferromagnetism of noble metal nanoparticles*

### *Summary\**

*Au nanoparticles and films of Au nanoparticles exhibit ferromagnetism wherein the saturation magnetization ( $M_S$ ) increases with decrease in diameter and varies linearly with the fraction of surface atoms. The value of  $M_S$  is higher when the particles are present as a film instead of a sol. Capping with strongly interacting ligands such as alkane thiols results in a higher  $M_S$ . Even bare nanoparticles of Au possess ferromagnetism though weak, which gets accentuated in the presence of capping agents, specially alkane thiols which form strong metal-sulfur bonds. Pt and Ag nanoparticles are also ferromagnetic with  $M_S$  depending on the strength of metal-sulfur bond.*



\* A paper based on this work has appeared in *Chem. Phys. Chem*, 2011

## **1. Introduction**

It is commonly accepted that ferromagnetism occurs in systems with partially filled d or f electrons. However, all the d and f block elements are not magnetic, with only Fe, Co, Ni being ferromagnetic. Cr is an antiferromagnet and a vast majority of metals are paramagnetic or diamagnetic. Magnetic properties of nanoparticles are however different from those of bulk.<sup>1</sup> Reduced coordination number and higher symmetry in nanoparticles leads to enhanced ferromagnetism in nanoparticles of ferromagnetic materials and appearance of magnetization in nonmagnetic materials.<sup>2-5</sup> Several diamagnetic oxides and other inorganic materials have been reported to be ferromagnetic when reduced to nano dimensions.<sup>6-8</sup> Au and Ag nanoparticles with a broad range of applications from optics to sensing, drug delivery, imaging and catalysis hold immense possibilities for multi-functional systems. Magnetism is an additional attribute of Au nanoparticles and was first observed in 1999, by Hori *et al.*<sup>9</sup>, in ~ 3 nm Au and Pd nanoparticles protected by polyvinylpyrrolidone (PVP) with unexpectedly large magnetic moments of ~ 20 spins per particle. In 2003, it was observed that self-assembled mono-layers of organic molecules on Au substrates were magnetic. Since then, a few other authors have reported magnetism in Au nanoparticles,<sup>10-15</sup> although the origin of ferromagnetism in Au nanoparticles has remained somewhat unclear. In most of the studies reported, the Au nanoparticles were covered with capping agents such as thiols and amines. Crespo *et al.*<sup>11</sup> have reported that gold nanoparticles capped with weakly interacting reagents like tetraalkylammonium bromide are diamagnetic, but those protected by strongly interacting thiols are ferromagnetic because of the 5d localized holes generated through Au-S charge-transfer. The origin of orbital magnetism arising out of spin-orbit coupling as a result of this charge-transfer has been discussed.<sup>12,13</sup> Hori and co-workers<sup>10</sup> have, however, observed greater ferromagnetic spin coupling in gold nanoparticles weakly protected with polyacrylonitrile, polyallylamine hydrochloride and PVP. They attribute the particle size dependence of ferromagnetism to the ferromagnetic nature of the surface Au atoms due to the so-called Fermi hole effect. Based on a x-ray circular dichroism study Negishi *et al.*<sup>16</sup> concluded that localized holes created by Au-S bonding was responsible for the spin polarization of gold clusters. While it would seem that the presence of thiol or amine capping agents is necessary for the magnetism of Au

nanoparticles on the basis of some of the reports, it should be noted that Reich *et al.*<sup>17</sup> observed magnetism in 27 nm thin films of Au deposited on Pyrex glass. More recently, Wu *et al.*<sup>18</sup> have reported that icosahedral gold nanoparticles prepared by the gas condensation method are ferromagnetic, where the moments of the core and surface atoms point in opposite directions.

## **2. Scope of the present investigations**

A magnetic property of Au nanoparticles is indeed puzzling and a unifying theory explaining the origin of Au nanoparticles is lacking. Theoretical explanations do not explain all experimental observations. As observed by Nealon *et al.*<sup>19</sup> there is a lack of reproducibility in the nature and magnitudes of magnetic moments of different experimental observations making it even harder to provide a unique theory of magnetism in Au nanoparticles.

In view of the uncertain origin of magnetism of metal nanoparticles, we have carried out a careful and systematic study of the magnetic properties of nanoparticles of Au and other noble metals of various sizes prepared at the organic-aqueous interface<sup>20</sup> by varying diameter between 2.5–15 nm. We have employed THPC as the reducing agent in our experiments at the organic-aqueous interface, without the use of any other capping agent.<sup>20,21</sup> THPC acts as the reducing agent as well as a capping agent simultaneously. Since, washing the THPC-covered Au nanoparticles with HCl is known to clean the metal surface effectively,<sup>22</sup> we have measured the magnetic properties with different extents of washing. We have examined the effect of the capping agent on the magnetic properties by comparing the properties of nanoparticles capped with different reagents and to different extents. We have studied the effect of temperature and particle size on magnetic properties of Au nanoparticles, besides comparing the properties of the Au nanoparticles with those of platinum and silver. In order to look for unique signatures of magnetic interactions in Au nanoparticles, we have carefully studied the temperature variation of magnetization.

### **3. Experimental section**

#### *Synthesis*

##### *Au nanoparticulate films:*

Nanocrystalline films of gold were prepared at the organic-aqueous interface using Au(PPh<sub>3</sub>)Cl (Ph = phenyl) as the precursor following the procedure described in the literature with THPC as the reducing agent.<sup>23</sup> Typically, 100 mL of a 1.5 mM solution of Au(PPh<sub>3</sub>)Cl in toluene was allowed to stand in contact with 160 mL of 6.25 mM aqueous alkali in a 1 L beaker at room temperature. Once the two layers stabilized, 3.3 mL of 50 mM THPC solution in water was injected into the aqueous layer using a syringe with minimal disturbance to the toluene layer. The onset of reduction was marked by a faint pink coloration of the toluene–water interface. The reduction was allowed to proceed without disturbance for 12 hours. With the passage of time, the colour became more vivid, finally resulting in a robust elastic film at the liquid–liquid interface. This gave nanocrystalline films containing 10 nm Au nanoparticles. To vary the particle size, the films were formed at different temperatures and reactant concentrations. Films with larger particle size were formed by varying the temperatures in the range 40-80 °C. Films with very small particles (~2 nm) could be prepared using 80 mM concentration of THPC as reducing agent. The conditions of preparation of different nanoparticles of Au studied by us are listed in Table 1.

##### *Au nanoparticles as sol:*

Hydrosols containing Au and Ag nanoparticles were prepared with THPC as the reducing agent by the method of Duff and Baiker.<sup>21</sup> Aqueous solution of Au nanoparticles was thus obtained using THPC as reducing agent. Typically, 10 mL of 1.5 mM solution of HAuCl<sub>4</sub>.3H<sub>2</sub>O in water was added to a mixture of 16 mL, 6.25 mM NaOH and 330 µL, 50 mM THPC under constant stirring. Solid Au nanoparticles were precipitated from the hydrosol using excess of ethanol.

##### *Thiol capped Au nanoparticles:*

Thiol-capped Au nanoparticles were obtained from the nanocrystalline films formed at the organic-aqueous interface by adding dodecane-thiol to the organic layer.<sup>23</sup> Few

$\mu$ moles of dodecanethiol was added to the toluene layer. The film disappeared with colouration of the toluene layer. Au nanoparticles were then precipitated using excess of ethanol.

Sols of thiol capped Au nanoparticles were also prepared by Brust method.<sup>24</sup>[19] For this, 15 mL of (0.03M)  $\text{HAuCl}_4 \cdot 3\text{H}_2\text{O}$  in water and 10 mL of 0.1M tetraoctylammonium bromide in toluene were vigorously stirred till the aqueous phase becomes completely colourless. Tetraoctylammonium bromide acts as the phase transfer agent. To the organic phase 3.13 mL of 0.04 M dodecane thiol in toluene was added followed by addition of aqueous solution of 12.5 mL of 0.04M  $\text{NaBH}_4$  to the aqueous phase. The reaction mixture was allowed to stir rapidly for 12 h. The organic phase was separated and reduced to 5 mL in rotavapour and precipitated with ethanol. Dodecanethiol capped Pt and Ag nanoparticles were similarly prepared starting from  $\text{H}_2\text{PtCl}_6 \cdot 6\text{H}_2\text{O}$  and  $\text{AgNO}_3$  solutions.<sup>25,26</sup>

***Bare Au nanoparticles:***

To de-cap or remove THPC functional groups from the surface of Au nanoparticles a the Au nanoparticle films were washed several times with acid. Films of Au nanoparticles obtained at the organic-aqueous interface were dried so as to obtain a powder. This was then sonicated with 3N HCl solution for 10 mins and washed with water by centrifugation. This process of washing was repeated several times before magnetic measurement. Bare Au nanoparticles were also prepared by photochemical reaction in absence of any capping agent.<sup>27</sup> For this purpose 10 ml,  $10^{-4}$  M  $\text{HAuCl}_4 \cdot 3\text{H}_2\text{O}$  solution containing 5  $\mu\text{L}$  of acetone and isopropanol was exposed to UV irradiation for 30 min and particles were allowed to settle.

Care was taken during sample preparation and measurements to avoid contact with materials containing magnetic elements thereby ruling out possibility of magnetic impurities.

For magnetic measurements all samples were obtained as powder. Magnetic measurements were carried out with vibrating sample magnetometer in Physical Properties Measurement System (PPMS, Quantum Design, USA). Particle size was

determined from transmission electron microscopy images obtained with a JEOL JEM 3010 operating at an accelerating voltage of 300 kV.

## **4. Results and discussion**

We first investigated the dependence of magnetic properties on surface area and particle size of the nanoparticles. In order to see the effect of particle size alone it was necessary to fix the concentration of capping agent and obtain the variation of particle size by variation of physical parameters like temperature or time. For this purpose we prepared ultrathin films of Au nanoparticles at the organic-aqueous interface by using THPC as the reducing agent. TEM images of some of the nanoparticulate films formed at the interface are shown in Figure 1 with the corresponding particle size distribution shown as inset.

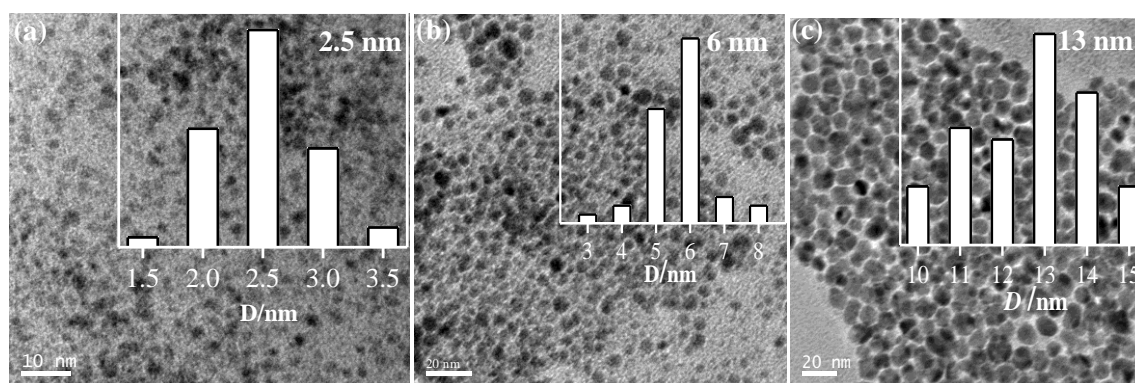


**Figure 1.** TEM image of Au nanoparticulate films formed at organic-aqueous interface with their particle size distribution shown in inset.

In Figure 2 (a), we show the magnetic hysteresis data Au nanoparticles with a mean diameter 2.5 nm using THPC as the reducing agent. The particles are ferromagnetic over the temperature range 5-300 K, with the magnetization increasing with lowering of temperature. Saturation magnetization ( $M_S$ ) at 5 K is double that at 300 K. The coercive field ( $H_C$ ) is 50 Oe at 300 K and increases to 140 Oe at 5 K (inset in Figure 2 (a)). The temperature dependence of magnetization of the 2.5 nm Au nanoparticles shown in Figure 2 (b) reveals divergence below 300 K between the field-cooled (FC) and the zero-field-cooled (ZFC) data measured at 1 T field. We also observe a low temperature



upturn showing a Curie-like tail. This has been observed in several graphitic materials [15] and Pd nanoparticles. [16]

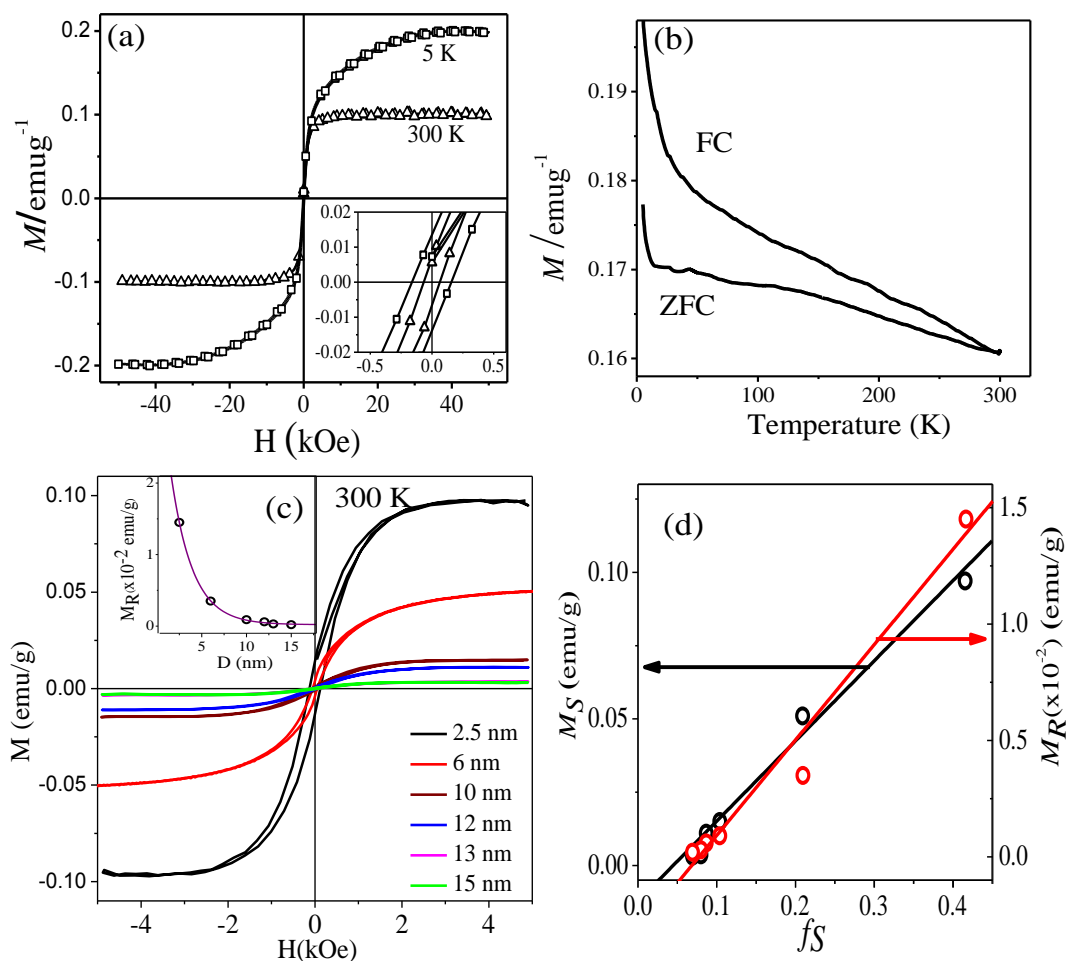


**Figure 2.** (a) Magnetic hysteresis of 2.5 nm Au nanoparticles prepared at the organic aqueous interface using THPC as reducing agent 5 K ( $\square$ ) and 300 K ( $\Delta$ ). Inset shows the magnified view of the hysteresis loop at low field showing that the particles possess  $H_C$  at 5 K ( $\square$ ) and 300 K ( $\Delta$ ) and (b) the ZFC and FC Magnetization data at 1T for the same, (c) Magnetic hysteresis of Au nanoparticles of varying sizes prepared at the organic-aqueous interface using THPC as the reducing agent. Inset shows a variation of  $M_R$  with diameter and (d) the dependence of saturation magnetization ( $M_S$ ) and remnant magnetization ( $M_R$ ) on  $M_S$  and  $M_R$  with fraction of surface atoms ( $f_S$ ).

**Table 1.** Preparation conditions and Magnetic properties (at 300K) of Au nanoparticles

Au diameter (nm)	State <sup>(a)</sup>	Preparation Conditions	M <sub>S</sub> (emu/g)	M <sub>R</sub> (emu/g)	H <sub>C</sub> (Oe)
2.5	NC Film	RT, 80mM THPC	$9.7 \times 10^{-2}$	$1.5 \times 10^{-2}$	136
6.0	NC Film	RT, 65mM THPC	$5.1 \times 10^{-2}$	$3.5 \times 10^{-3}$	95
10	NC Film	RT, 50mM THPC	$1.5 \times 10^{-2}$	$9 \times 10^{-4}$	85
12	NC Film	40°C, 50mM THPC	$1.1 \times 10^{-2}$	$6 \times 10^{-4}$	60
13	NC Film	60°C, 50mM THPC	$3.6 \times 10^{-3}$	$3 \times 10^{-4}$	60
15	NC Film	80°C, 50mM THPC	$3.2 \times 10^{-3}$	$2 \times 10^{-4}$	89
2	Hydrosol	RT, 50mM THPC	$4.4 \times 10^{-2}$	$6.5 \times 10^{-3}$	120
2.5	NC Film	RT, 80mM THPC, DT as capping agent <sup>(b)</sup>	$1.6 \times 10^{-1}$	$6.9 \times 10^{-3}$	61
2	Organosol	Brust method, DT as capping agent <sup>(b)</sup>	$1.1 \times 10^{-1}$	$9 \times 10^{-3}$	54
10 nm	Film	RT, 50mM THPC, DT as capping agent <sup>(b)</sup>	$2.2 \times 10^{-2}$	$1.3 \times 10^{-3}$	40

<sup>(a)</sup> NC Film stands for film formed nanocrystals.

<sup>(b)</sup> DT stands for dodecane thiol.

To see the effect of particle size on the magnetic properties, we have recorded room-temperature magnetic hysteresis of the Au nanoparticles in the diameter range 2.5-15 nm prepared with THPC and we show these results in Figure 2(c). We see that the 2.5 nm particles show the maximum value of M<sub>S</sub> and remnant magnetization (M<sub>R</sub>) as well as H<sub>C</sub> (Table 1). M<sub>S</sub> values reported by us are one order of magnitude less than those reported by Hori *et al.*<sup>9</sup> and Crespo *et al.*<sup>11</sup> However, it is higher than those found for icosahedral Au nanoparticles reported by Wu *et al.*<sup>18</sup> All the particles upto 15 nm diameter are ferromagnetic with considerable coercive field. Both M<sub>S</sub> and M<sub>R</sub> decrease with the increase in particle diameter (Figure 2(c)), the values of M<sub>S</sub> and M<sub>R</sub> having been calculated after subtracting the diamagnetic signal from the core Au and sample holder. The coercive field (H<sub>C</sub>) too decreases with increasing particle diameter (Table 1). The Fermi hole in case of Au is equal to the surface spin correlation depth. The Au particles prepared by us with diameters 2.5 nm or larger prepared using THPC as the reducing agent follow an exponential decay (see inset of Figure 2(c)) instead of showing maxima in the curve as reported elsewhere.<sup>10</sup> In Figure 2(d) we have plotted the M<sub>S</sub> and M<sub>R</sub> values against the fraction of surface atoms in the nanoparticles. The variation of M<sub>S</sub> and

$M_R$  is linear with respect to the fraction of surface atoms with a positive slope suggesting that a magnetic contribution mainly originates from the surface atoms. Since the concentration of reducing cum capping agent (THPC) was maintained same for all samples the above observed effect is solely an outcome of reduction of particle size.

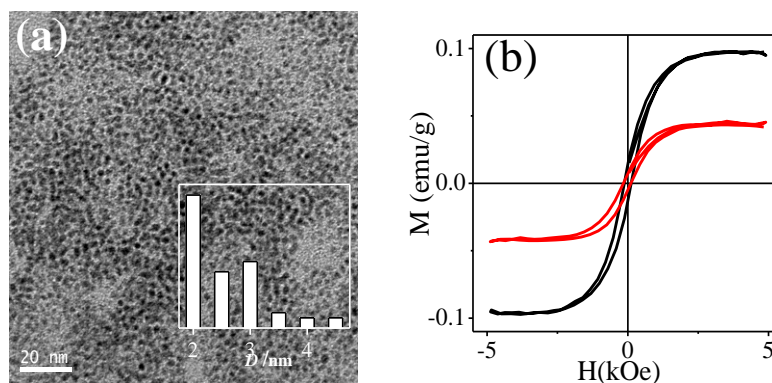


**Figure 3.** TEM images of (a) Au nanoparticles prepared as a hydrosol using THPC as the reducing agent and (b) magnetic hysteresis curves of Au nanoparticles prepared at the organic-aqueous interface (black) with those of in hydrosol (red).

It is interesting that Au nanoparticles of comparable diameters prepared using same reducing agent shows a difference in magnetization when in the form of films and as a sol. Figure 3(a) shows the TEM image of Au nanoparticles obtained in hydrosol using THPC as reducing agent. Inset in the figure shows the particle size distribution of the same, revealing most of the nanoparticles are about 2 nm in diameter. Magnetization of 2.5 nm Au nanoparticles generated at the organic-aqueous interface with THPC as the reducing agent is more than twice that of 2 nm Au nanoparticles prepared as a hydrosol as can be seen in the inset of Figure 3 (b). Thus, particles present in the form of thin nanocrystalline films show enhanced magnetization when confined to films where the particles are closely spaced forming an assembly as compared to those in sol.  $M_R$  for films is about 2.3 times that of sols and  $H_C$  for films are slightly higher than that for sols (Table 1.). An increased  $H_C$  indicates increase in magnetic anisotropy. Greater anisotropy in films could be due to interparticle magnetic interactions. It is worth remembering at this stage that formation of self-assembled monolayers on Au has been reported to increase anisotropy.<sup>18</sup> Considering the Fermi hole theory of magnetism in Au nanoparticles, it is probable that confining the growth to only organic-aqueous interface

during film formation creates greater number of surface defects or “5d holes”<sup>11</sup> resulting in greater saturation magnetization.

It has been argued that interaction of Au nanoparticles with strongly ligating groups like thiols creates greater 5d holes on the surface.<sup>11</sup> If then we consider that particles prepared at the interface as films tend to have greater number of surface defects or “5d holes”, it implies that films and sols bearing a strongly ligating group would have lesser difference between  $M_S$  values. Also considering that interparticle magnetic interactions exist, it is then possible that these interactions can be tuned by tuning the nature of capping agent that covers the particle surface. In order to see the effect of surface groups on the magnetic properties dodecanethiol capped Au nanoparticles were prepared both as films and in sol. Figure 4(a) shows the TEM image of dodecanethiol capped Au nanoparticles prepared by two different methods. Au nanoparticles prepared by Brust method had a negligible size distribution with maximum particles being in the range 2-2.5 nm (see lower inset in Figure 4(a)).

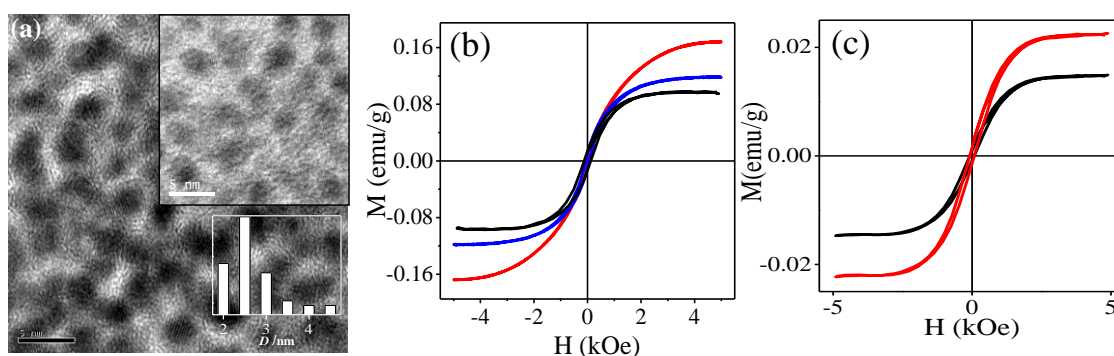


**Figure 4** (a) TEM image of dodecanethiol-capped Au nanoparticles prepared by the Brust method. Inset in (a) shows the TEM image of Au nanoparticles obtained as a film at the organic-aqueous interface and then capped with dodecanethiol, (b) Magnetic hysteresis of 2.5 nm Au nanoparticles prepared at the organic-aqueous interface with THPC (black) and the same when capped with dodecanethiol (red) and 2 nm particles in toluene prepared by Brust method (blue), (c) magnetic hysteresis of Au nanoparticles of size 10 nm prepared at the organic-aqueous interface using THPC (black) and same particles when treated with dodecanethiol (red).

Dodecanethiol capping of nanoparticulate films generated at the organic aqueous interface does not bring about any change in particle size as shown for thiol capped 2.5 nm Au particle films in top inset in Figure 4(a). Figure 4 (b) shows the magnetic hysteresis data of thiol-capped 2.5 nm Au nanoparticles obtained from the films at the organic-aqueous interface using THPC (red) and the thiol capped nanoparticles obtained as sol by Brust method (blue). As in the case of THPC capped nanoparticles, the thiol capped nanoparticles from the films too show a magnetization value higher than that of the particles obtained by Brust method in toluene (Figure 4 (b)). Thus, particles present in the form of thin nanocrystalline films show enhanced magnetization irrespective of the type of capping agent. However, as discussed earlier the difference between the  $M_S$  values for films and sols are indeed less for thiol capped particles as compared to THPC capped ones. The enhancement of saturation magnetization, i.e.  $M_S$  films/  $M_S$  Sol, was 2.2 for THPC capped particles and 1.5 for thiol capped ones. Again inter-particle interaction would be greater when the particles are capped with weakly interacting agents (such as THPC) rather than a strongly interacting capping agent like an alkane thiol. THPC capped nanoparticulate films show greater anisotropy than thiol capped ones and the difference in  $H_C$  of respective films and sols follows suit. Capping agent and its interaction strength clearly affect magnetic interactions.

It is well known that thiol capping of Au nanoparticles increases the  $M_S$ . We have generally found that when particles whether in form of films or as sols show greater  $M_S$  when capped with thiols than when capped with THPC. Figure 4(b) shows the magnetic hysteresis of 2.5 nm Au nanoparticles prepared at the organic-aqueous interface with THPC (black) and the same when capped with dodecanethiol (red). A similar behaviour was observed with 10 nm Au nanoparticles as shown in the Figure 4 (c). Thus, the  $M_S$  varies with nature of surface capping and depends on the strength of interaction of the capping agent with the metal particle. Thus, thiol-capped particles show higher  $M_S$  than THPC capped particles. Thiol capping results in formation of Au-S bonds which is much stronger than Au-P bonds found in THPC capped nanoparticles. At this stage it is worth mentioning that our results are consistent with some of the earlier reports on capped Au nanoparticles<sup>11,13</sup>, but differs from the work of Hori *et al.*<sup>9</sup>, who report a reduction in magnetization on capping with dodecanethiol. Interestingly, while  $M_S$

increases on thiol capping  $M_R$  and  $H_C$  decreases. For 2.5 nm particles prepared as films at the organic-aqueous interface the  $M_R$  reduces to half and  $H_C$  to one third of its value on thiol capping as compared to THPC capped particles. This was true for particles prepared as sols too. A probable reason for this as discussed above could be that capping surface with strongly interacting ligands reduces the anisotropy caused by interparticle magnetic interactions.

Since capping agents and the strength of its interaction with Au affect magnetic properties of Au nanoparticles, it is consequential that keeping the same capping agent if the metal nanoparticle is varied so as to change the strength of the metal-ligand we would end up with similar effects. To verify the fact that magnetic properties of noble metal nanoparticles indeed depends on binding strength of metal-ligand bond we prepared dodecanethiol and THPC-capped Ag nanoparticles and compared its magnetic properties with that of Au nanoparticles. Thiol capped Pt nanoparticles were also prepared by Brust method. Duff method was used to prepare THPC-capped Ag nanoparticles. However, Pt nanoparticles of uniform size could not be prepared using THPC as reducing agent. Citrate coated Pt nanoparticles were thus prepared using citric acid as reducing and capping agent.

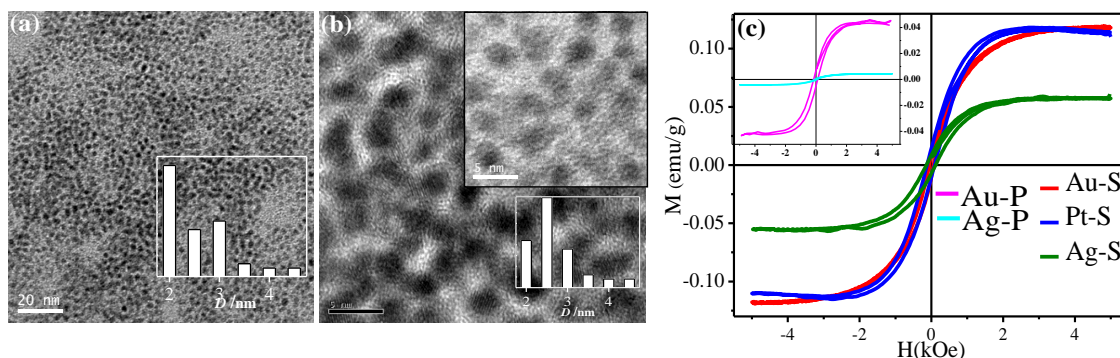


**Figure 5.** TEM images of thiol-capped nanoparticles (a) Ag and (b) Pt prepared by the modified Brust method. (c) Magnetic hysteresis of dodecanethiol-capped 2 nm Au (red), 4 nm Pt (blue) and 2 nm Ag (green) and of THPC-capped 2 nm Au (pink) and 3.5 nm Ag nanoparticles (cyan) shown in inset in (c).

Figures 5(a) and (b) show TEM images of thiol capped Ag and Pt nanoparticles prepared by Brust method. The dodecanethiol capped particles of Ag and Pt prepared by

modified Brust method had average diameter of 2 and 4 nm respectively (Figure 5(a)). THPC-capped nanoparticles of Ag prepared by a modified Duff method was approximately 3.5 nm. In Figure 5 (c) we show the magnetization data of Au, Pt and Ag nanoparticles capped with dodecanethiol. Saturation magnetization of dodecanethiol-capped 2 nm Au nanoparticles ( $1.1 \times 10^{-1}$  emu/g) is around the same as that of thiol-capped Pt nanoparticles of diameter 4 nm. Thiol-capped 2 nm Ag nanoparticles, however, show a smaller value of saturation magnetization ( $5.1 \times 10^{-2}$  emu/g). This can be understood in terms of strength of binding of thiols to the metal. The binding energy for metal-S bond follows the order Pt > Au > Ag.<sup>28</sup> The strength of binding directly affects the value of saturation magnetization, since any mechanism that involves charge-transfer between metal and the capping agent determines the strength of magnetization. In the same line 2 nm Au nanoparticles capped with THPC show stronger magnetization than 3.5 nm Ag nanoparticles (see Figure 5(c)), the determining factor being the strength of metal-P bond with Au-P > Ag-P. Pt nanoparticle (5 nm) prepared by the citrate route show considerably smaller  $M_s$ , in agreement with the above postulate, the strength of Pt-C bond being less than Ag/Au-P.

The preceding results clearly indicate that capping agents the strength of charge transfer from metal to ligand to metal affects magnetic properties of noble metal nanoparticles. The question that still remains to be probed is the presence of surface ligating group necessary for Au nanoparticles to show magnetism. Sarathy et al.<sup>22</sup> have reported that washing THPC reduced Au nanoparticles with dilute HCl solution removes the reagents from the surface, based on x-ray photoelectron spectroscopic study. We have carried out several washing cycles of THPC reduced Au nanoparticles with 3N HCl solution and studied their magnetic hysteresis. Figure 6 (a) shows that on washing the Au nanoparticles with HCl once, the magnetization decreases slightly. After 4 cycles of washing the magnetization value decreases to half of its original value but ferromagnetism is retained even after repeated cycles of washing with HCl when the Au nanoparticles may no longer have a capping agent layer. The absence of capping agent on the surface of Au nanoparticles was probed by IR spectroscopy (Figure 6(b)). What one cannot be certain is whether there was absolutely no capping agent on the surface after such acid washing below the limit of detection of surface spectroscopies. Interestingly,

we observed magnetic hysteresis in Au nanoparticles of assorted sizes (5-30 nm) prepared photochemically in absence of any capping agent, only organic compound present being acetone and isopropanol (Figure 6 (a)).

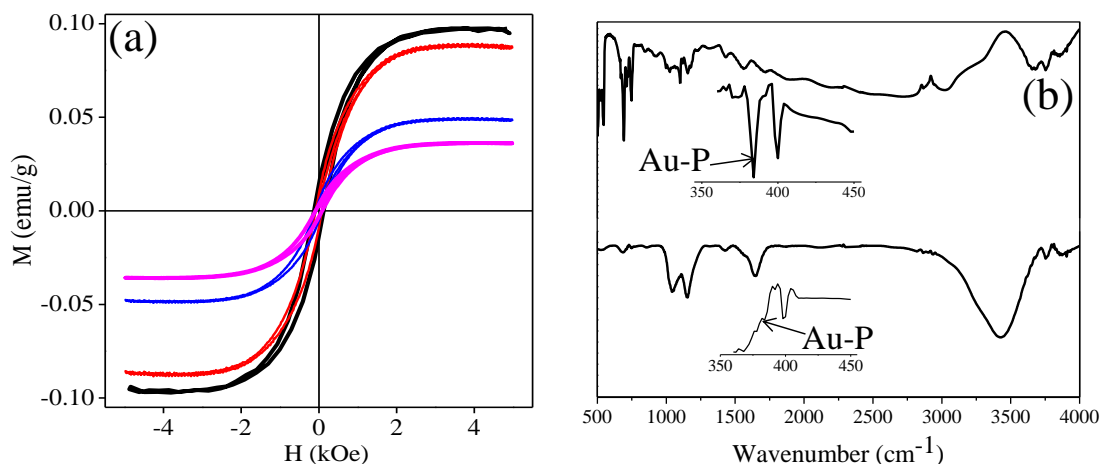


**Figure 6.** (a) Magnetic hysteresis of 2.5 nm Au nanoparticles prepared at the organic-aqueous (black) interface as prepared (not washed with HCl), (red) washed once with HCl, (blue) washed 4 times with HCl and (pink) magnetic hysteresis of Au nanoparticles (5-30 nm) prepared photochemically. (b) IR spectra of 2.5 nm Au nanoparticles prepared using THPC (top) and the same washed with HCl 4 times (bottom).

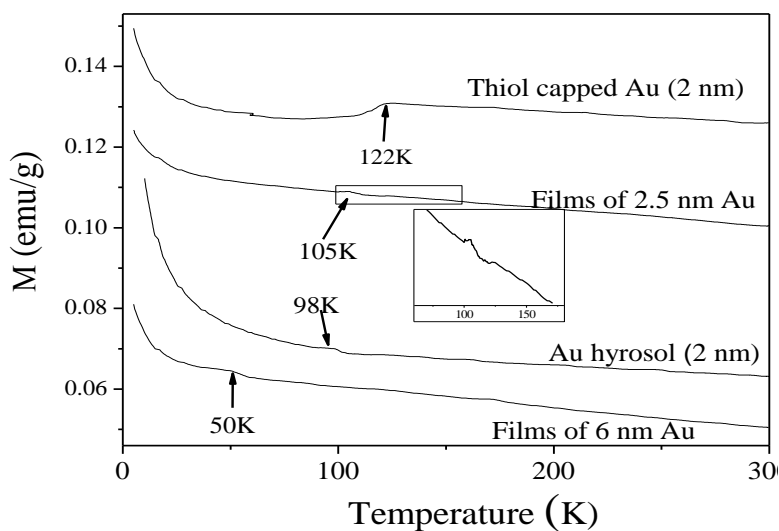


**Figure 7.** Temperature dependence of magnetization of Au nanoparticles of two different sizes. Notice the jumps marked by arrows. Inset shows a magnified view of small portion of the curve for films of 2.5 nm Au particles.

We have examined temperature dependence of magnetization of the Au nanoparticles of two different sizes prepared at the organic-aqueous interface or in the



form of hydrosols. We observe a jump in the magnetism in the FC data (Figure 7). A comparison between M-T curve of Au nanoparticles prepared at the organic-aqueous interface shows that the jump shifts to lower temperature with increase in particle size. Au nanoparticles of comparable size prepared at the interface or in hydrosol show jumps at a similar temperature, while thiol-capped nanoparticles show a much stronger jump and at a higher temperature. Since our particles are all ferromagnetic at room temperature, the jump in the FC curve does not represent a blocking temperature. Such breaks in the M-T curves have been considered to arise from interactions between core and surface spins in Au nanoparticle, with the spins pointing in opposite directions.<sup>18</sup> Smaller the particle size, greater will be the interactions between the core and the surface spins and therefore higher temperature is required to remove these interactions. In the case of thiol-capped nanoparticles the interaction is greater, resulting in a shift of the jump to higher temperatures along with increase in sharpness of the jump. Above this temperature interactions persist, giving rise to magnetism at room temperature. These results suggest that small Au nanoparticles could indeed possess weak ferromagnetism as an inherent feature.

## **5. Conclusions**

The present study underscores the role of capping agents in imparting ferromagnetism on nanoparticles of noble metals such as Pt, Au and Ag, the magnitude of saturation magnetization depending on the strength of the metal-ligand bonding. Small, bare metal nanoparticles in the absence of any capping agent could indeed be weakly ferromagnetic as indicated by the temperature-variation of magnetization of nanoparticles along with linear variation of magnetization with fraction of surface atoms. The fact that ferromagnetism of Au nanoparticles prepared at the organic-aqueous interface could not be completely removed after repeated washing with HCl supports such a conjecture. Furthermore, observation of ferromagnetism in the presence of weakly interacting ligands such as citrate as well as in particles prepared photochemically in the presence of acetone and isopropyl alcohol also lend support to this conjecture. It is noteworthy that the

***Chapter I.3 Ferromagnetism of Au nanoparticles.....***

---

magnetization of thiol capped noble metal particles varies as Pt > Au > Ag, reflecting the order of variation of the strength of the metal-sulfur bond.

## Reference:

1. L. Néel. *Comptes Rendus*, **1949**, 228, 664.
2. J. P. Bucher, D. C. Douglass and L. A. Bloomfield. *Phys. Rev. Lett.* **1991**, 66, 3052.
3. D. C. Douglass, A. J. Cox, J. P. Bucher and L. A. Bloomfield. *Phys. Rev. B* **1993**, 47, 12874.
4. I. M. L. Billas, J. A. Becker, A. Châtelain and W. A. de Heer. *Phys. Rev. Lett.* **1993**, 71, 4067.
5. T. Shinohara, T. Sato and T. Taniyama. *Phys. Rev. Lett.* **2003**, 91, 197201.
6. J. M. D. Coey and S. A. Chambers. *MRS Bulletin* **2008**, 33, 1053.
7. A. Sundaresan and C. N. R. Rao. *Solid State Comm.* **2009**, 149, 1197.
8. A. Sundaresan and C. N. R. Rao. *Nano Today* **2009**, 4, 96.
9. H. Hori, T. Teranishi, Y. Nakae, Y. Seino, M. Miyake and S. Yamada. *Phys. Lett. A* **1999**, 263, 406.
10. H. Hori, Y. Yamamoto, T. Iwamoto, T. Miura, T. Teranishi and M. Miyake. *Phys. Rev. B* **2004**, 69, 174411.
11. P. Crespo, R. Litrán, T. C. Rojas, M. Multigner, J. M. de la Fuente, J. C. Sánchez-López, M. A. García, A. Hernando, S. Penadés and A. Fernández. *Phys. Rev. Lett.* **2004**, 93, 087204.
12. A. Hernando, P. Crespo and M. A. García. *Phys. Rev. Lett.* **2006**, 96, 057206.
13. E. Guerrero, M. A. Muñoz-Márquez, M. A. García, P. Crespo, E. Fernández-Pinel, A. Hernando and A. Fernández. *Nanotechnol.* **2008**, 19, 175701.
14. C. Gonzalez, Y. Simón-Manso, M. Marquez and V. Mujica. *J. Phys. Chem. B* **2005**, 110, 687.
15. Y. Yamamoto, T. Miura, M. Suzuki, N. Kawamura, H. Miyagawa, T. Nakamura, K. Kobayashi, T. Teranishi and H. Hori. *Phys. Rev. Lett.* **2004**, 93, 116801.
16. Y. Negishi, H. Tsunoyama, M. Suzuki, N. Kawamura, M. M. Matsushita, K. Maruyama, T. Sugawara, T. Yokoyama and T. Tsukuda. *J. Am. Chem. Soc.* **2006**, 128, 12034.
17. S. Reich, G. Leitius and Y. Feldman. *Appl. Phys. Lett.* **2006**, 88, 222502.

18. C.-M. Wu, C.-Y. Li, Y.-T. Kuo, C.-W. Wang, S.-Y. Wu and W.-H. Li. *J. Nanoparticle Res.* **2010**, 12, 177.
19. G. L. Nealon, B. Donnio, R. Greget, J.-P. Kappler, E. Terazzi and J.-L. Gallani. *Nanoscale* **2012**, 4, 5244.
20. C. N. R. Rao and K. P. Kalyanikutty. *Acc. Chem. Res.* **2008**, 41, 489.
21. D. G. Duff, A. Baiker and P. P. Edwards. *Langmuir* **1993**, 9, 2301.
22. K. V. Sarathy, G. Raina, R. T. Yadav, G. U. Kulkarni and C. N. R. Rao. *J. Phys. Chem. B* **1997**, 101, 9876.
23. C. N. R. Rao, G. U. Kulkarni, P. J. Thomas, V. V. Agrawal and P. Saravanan. *J. Phys. Chem. B* **2003**, 107, 7391.
24. M. Brust, M. Walker, D. Bethell, D. J. Schiffrin and R. Whyman. *J. Chem. Soc., Chem. Comm.* **1994**, 801.
25. D. V. Leff, P. C. Ohara, J. R. Heath and W. M. Gelbart. *J. Phys. Chem.* **1995**, 99, 7036.
26. E. G. Castro, R. V. Salvatierra, W. H. Schreiner, M. M. Oliveira and A. J. G. Zarbin. *Chem. Mater.* **2009**, 22, 360.
27. J. S. Garitaonandia, M. Insausti, E. Goikolea, M. Suzuki, J. D. Cashion, N. Kawamura, H. Ohsawa, I. Gil de Muro, K. Suzuki, F. Plazaola and T. Rojo. *Nano Lett.* **2008**, 8, 661.
28. D. R. Lide. *CRC Handbook of Chemistry and Physics*, **CRC Press, UK, 2010**, 9.

# ***PART II***

## ***Investigations of Nanodiamond, graphene and related 2D materials***

### ***Introduction***

In Nature, carbon exists in two forms, graphite and diamond, composed of  $sp^2$  and  $sp^3$  hybridized carbons respectively. Diamond is the metastable form of carbon that possesses a three dimensional cubic lattice with lattice constant of 3.57 Å and C–C bond length of 1.54 Å. The nano analogue of diamond, known as nanodiamond, is formed of aggregates of 5 nm particles of  $sp^3$  hybridized carbon. Nanodiamond is popularly known as detonation diamond or ultra-disperse diamond and is obtained during detonation of carbon based explosives in oxygen free atmosphere. Nanodiamond finds large scale use as abrasive, dry lubricant, reinforcement in plastics and polymers etc. Being spontaneously saturated with surface functional groups, nanodiamond is highly biocompatible and finds use in bio-imaging.

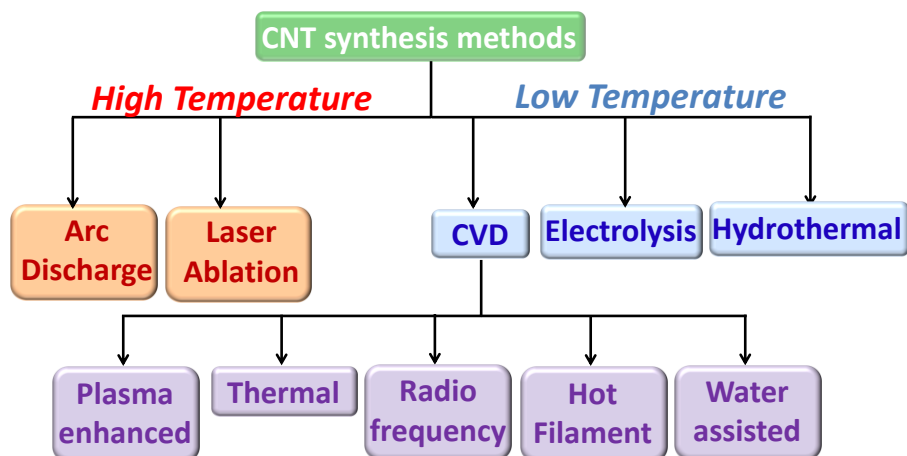
Graphite is the thermodynamically more stable form of carbon with a layered structure composed of hexagonal honeycomb of  $sp^2$  bonded carbon atoms having C-C bond length of 1.42 Å and an interlayer spacing of 3.35 Å corresponding to the van der Waals distance of  $sp^2$  bonded carbon. Last three decades has witnessed colossal activity in the field of nano forms of carbon with 0D fullerenes, 1D carbon nanotube and 2D graphene being the frontrunners. Graphene is the single layer of  $sp^2$  bonded carbon derived from graphite. Of all the recent developments in the chemistry of materials, the discovery of graphene has created the greatest sensation because of its fascinating properties.<sup>1-5</sup> This two-dimensional network of  $sp^2$  carbon atoms exhibit high electron

mobility and ballistic conduction because of its unusual electronic structure. In the last 6-7 years, synthesis, properties and applications of graphene have been pursued widely. Besides single-layer graphene, two-, three- and few-layer graphenes are being investigated. Graphene is often viewed as the building block of other  $sp^2$  hybridized nanocarbons. Fullerenes are spherical, seamless caged molecules with carbon atoms located at the corners of a polyhedral cage composed of pentagons and hexagons, the most stable of them being  $C_{60}$ . Another fairly common fullerene is  $C_{70}$ , while fullerenes with 72, 76, 84 and even up to 100 carbon atoms are also obtained. Fullerenes are made by arc evaporation of graphite. The discovery of fullerenes won the first Nobel Prize in chemistry of nanocarbons in 1996. Like fullerenes, carbon nanotubes are made of seamless cylinders of  $sp^2$  hybridized carbons. Two major categories of carbon nanotubes are single walled nanotubes (SWNTs) and multi walled nanotubes (MWNTs). While SWNTs are like cylindrical fullerenes or rolled graphene sheets with length varying from less than a micrometer to almost millimeter, MWNTs consist of multiple concentric tubes of graphene. Depending on the way the hexagonal carbon sheet wraps, SWNTs are either metallic or semiconducting. Carbon nanotubes are one of the strongest and the stiffest materials known to man and possess unique electronic optical and thermal properties.<sup>6-8</sup> Owing to high surface area they find use in storage and catalytic applications too. Other forms of nanocarbons include nanoribbons formed by unzipping of carbon nanotubes or cutting graphene sheets, carbon nanoscrolls, carbon nano-onions, carbon nanohorns etc.

This part of the thesis mainly deals with magnetic, optical, storage and mechanical studies of nanodiamonds, carbon nanotubes and graphene. A brief introduction to nanodiamond has been provided in the first chapter. Since a detailed discussion on synthesis properties and applications of carbon nanotubes is beyond the scope of this thesis, a small introduction to synthetic techniques used by us for the preparation of nanotubes and graphene is being provided below. The discovery of graphene has drawn attention to the study of other two-dimensional materials as well. Just as the inorganic analogues of zero-dimensional fullerenes and one-dimensional carbon nanotubes were prepared some time ago, in the last 2-3 years serious efforts have been made to generate graphene-like layered inorganic structures.<sup>9-17</sup> The third chapter deals with synthesis of nanoribbons and nanoscrolls of graphene and graphene analogues of BN and  $MoS_2$  and

their magnetic properties. A brief introduction to methods of synthesis of graphene analogues of inorganic layered materials has been provided below.

**Synthesis of Carbon nanotubes:** Sizable quantities of carbon nanotubes can be produced by different methods as demonstrated in scheme 1. Among them, laser ablation and arc discharge techniques are among the first ones to develop.<sup>18</sup> Figure 1 shows TEM and FESEM images of SWNT, DWNT and MWNTs grown by some of the most common methods.



**Scheme 1.** Most common methods for the synthesis of carbon nanotubes (adapted from reference<sup>19</sup>)

**Arc discharge:** This technique requires temperature above 1700°C and is carried out by DC arc discharge between two graphite that are generally water-cooled in a chamber low pressure of helium. Often hydrogen, methane or other higher hydrocarbons are also used instead of He.<sup>20 21</sup> The pressure in the chamber is generally varied between 50 to 150 Torr and greatly effects the growth of nanotubes. MWNTs of an average thickness 10 nm and few microns in length composed of 5-15 walls is generally formed by this method. While arc discharge in absence of any catalyst yields MWNTs, that in presence of metal catalyst nanoparticles yield SWNTs. The graphite anode in synthesis of MWNTs is replaced by

composite anodes made of a mixture of graphite and metal, such as Ni, Fe, Co, Pd, Ag, Pt or a mixture of these metals like Co–Ni, Fe–Ni, Fe–No, Co–Cu, Ni–Cu, Ni–Ti, Ni–Y etc.<sup>22-24</sup>

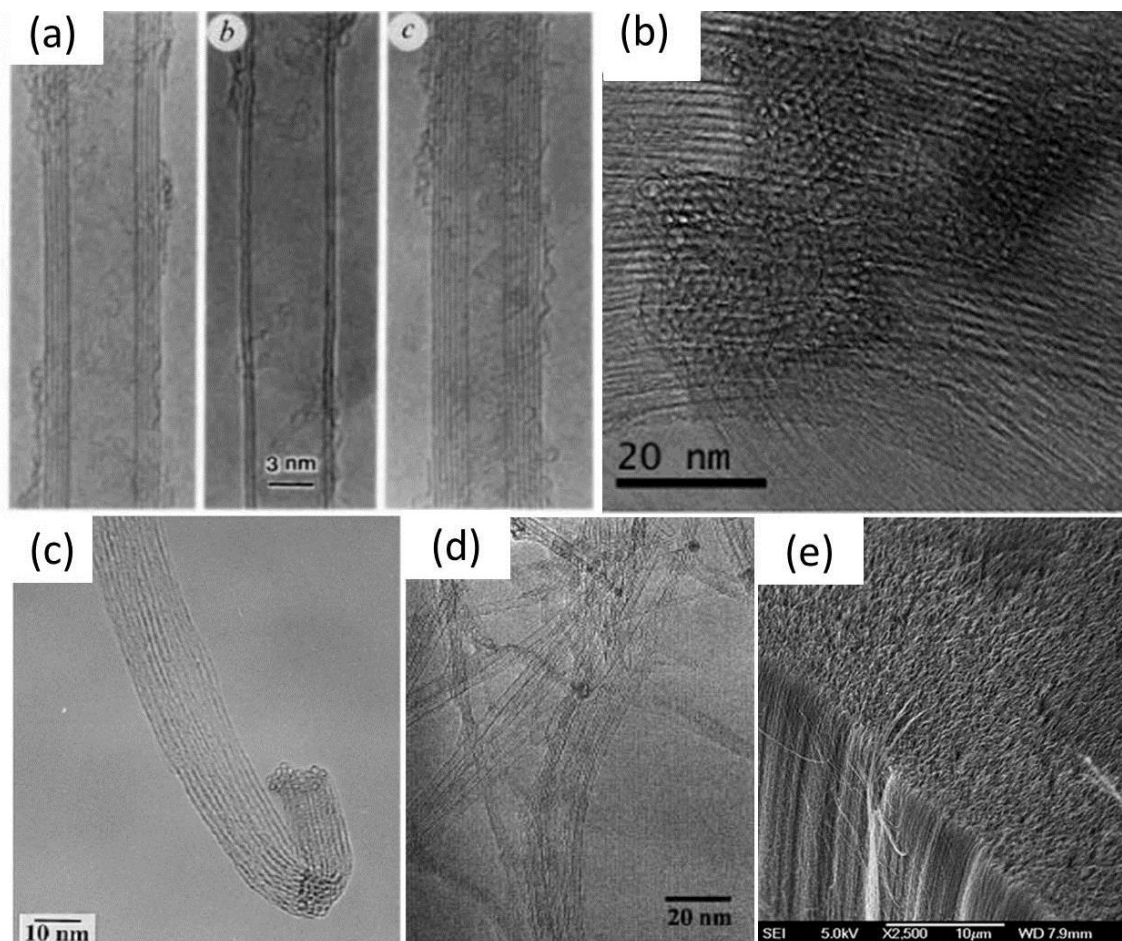


**Figure 1.** TEM images of (a) Arc discharge MWNT, DWNT<sup>6</sup> and (b) Arc discharge SWNT<sup>25</sup>, (c) SWNT by laser ablation<sup>26</sup> and (d) SWNT by thermal CVD<sup>27</sup> and (e) MWNT forest grown by plasma enhanced CVD<sup>28</sup>

**Laser ablation:** Pulsed laser deposition which uses laser ablation technique yields superior quality SWNTs and was first demonstrated by Smalley and co-workers.<sup>29</sup> The properties of SWNTs prepared by this method largely depends on the deposition processes like energy fluence peak power repetition rate and oscillation wavelength. The principles and mechanisms of synthesis of SWNTs by laser ablation are similar to arc



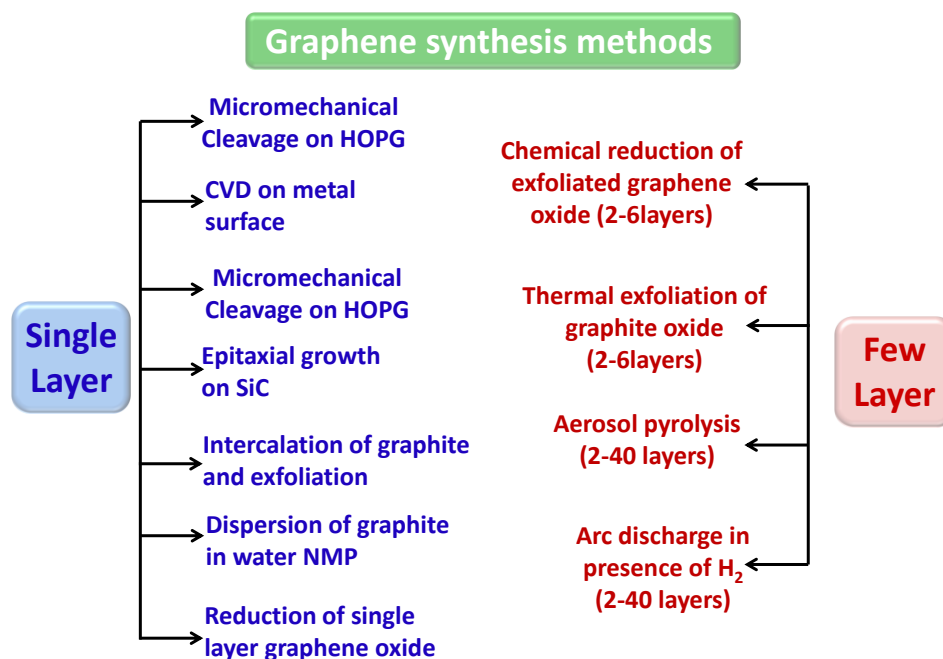
discharge with the difference that the energy is provided by a laser hitting a graphite pellet containing catalyst materials (usually nickel or cobalt).<sup>30</sup>

***Chemical vapour deposition (CVD):*** It is the most standard method for producing CNTs, and can be subdivided into catalytic chemical vapour deposition (CCVD) - either thermal<sup>31</sup> or plasma enhanced (PE), water assisted CVD,<sup>32-34</sup> oxygen assisted CVD,<sup>35</sup> hot-filament (HFCVD),<sup>36</sup> microwave plasma (MPECVD)<sup>28,37,38</sup> or radiofrequency CVD (RF-CVD).<sup>38</sup> CVD happens at lower temperature as compared to arc discharge technique or laser ablation. Metal nanoparticles act as catalysts and growth happens either by tip growth or base growth models, depending on the position of metal nanoparticle during and after the synthesis. Depending on the growth temperature, catalyst particle gaseous mixture used SWNTs, DWNTs and MWNTs are obtained by CVD. Liquid pyrolysis i.e. pyrolysis of carbon containing aerosols such as aerosol of ferrocene and hydrocarbon is yet another simple technique to CNTs.<sup>39,40</sup> Growth of CNTs by CVD being a low cost and easily controllable technique has been most widely used technique for the synthesis of CNTs.

***Synthesis of Single and Few-layered graphene:*** Single and few layered graphenes can be synthesized by several methods. In scheme 2. we have listed some of these methods. The synthesis procedure can be broadly classified into exfoliation, chemical vapour deposition, arc discharge and from reduction of graphene oxide. Stacking of sheets in graphite is the result of overlap of partially filled  $p_z$  or  $\pi$  orbitals perpendicular to the plane of the sheet (involving van der Waals forces). Exfoliation is the reverse of stacking. Due to the weak bonding and large lattice spacing in the perpendicular direction compared to the small lattice spacing and stronger bonding in the hexagonal lattice plane, it has been tempting to generate graphene sheets through exfoliation of graphite. Optical and electron microscopic images of graphene samples prepared by different methods are shown in Figure 2.

***Mechanical Exfoliation:*** Graphene sheets of different thickness can be obtained through mechanical exfoliation, or peeling off layers from graphitic materials such as highly

ordered pyrolytic graphite (HOPG), single crystal graphite or natural graphite. Peeling and manipulation of graphene sheets have been achieved through AFM and STM tips.<sup>41-</sup>  
<sup>46</sup> Greater control over folding and unfolding could be achieved by modulating the distance or bias voltage between the tip and the sample.<sup>46</sup> Noveslov *et al.*<sup>1</sup> first demonstrated the use of mechanical exfoliation to prepare single layer thick graphene sheets. Though mechanical exfoliation produces graphene of the highest quality (with least defects), the method is limited by low productivity.



**Scheme 2.** Most common methods for the synthesis of carbon nanotubes (adapted from reference<sup>4</sup>)

**Chemical Exfoliation:** Chemical exfoliation, on the other hand, possesses advantages of bulk scale production. Chemical exfoliation is a two-step process. The first step is to increase the interlayer spacing, thereby reducing the interlayer van der Waals forces. This is achieved by intercalating graphite to prepare graphene intercalated compounds (GIC).<sup>47</sup> The GICs are then exfoliated into graphene with single to few layers by rapid heating or sonication. A classic example of chemical exfoliation is the generation of single layer graphene oxide (SGO) prepared from graphite oxide by ultrasonication.<sup>48-53</sup> Graphite

oxide (GO) is readily prepared by Hummers method involving the oxidation of graphite with strong oxidizing agents like  $\text{KMnO}_4$  and  $\text{NaNO}_3$  in  $\text{H}_2\text{SO}_4/\text{H}_3\text{PO}_4$ .<sup>48,50</sup> On oxidation, the interlayer spacing increases from 3.7 Å to 9.5 Å and exfoliation giving single-layer graphene is achieved by simple ultrasonication in a DMF:water (9:1) mixture. The SGO so prepared has a high density of functional groups and reduction needs to be carried out to obtain graphene-like properties. Chemical reduction has been achieved with hydrazine monohydrate to give well dispersed single layer graphene sheets.<sup>49,52</sup> Thermal exfoliation and reduction of graphite oxide also produces good quality graphene, generally referred to as reduced graphene oxide (RGO). Rapid heating ( $>200$  °C/min) to 1050 °C also breaks up functionalized GO into individual sheets through evolution of  $\text{CO}_2$ .<sup>54,55</sup> <sup>56</sup> On rapid heating decomposition rate of the epoxy and hydroxyl groups of GO exceeds the diffusion rate of the evolved gases resulting in pressures that exceed the van der Waals forces holding the graphene sheets together and exfoliation occurs. Exfoliated graphene sheets are highly wrinkled and possess defects. As a result, these sheets do not collapse back to graphite but remain as highly agglomerated graphene sheets. Guoqing *et al.*<sup>57</sup> used microwaves to give thermal shock to acid intercalated graphite oxide in order to carry out exfoliation.

GICs are prepared by the intercalation of alkali metal ions. GICs on treatment with ethanol undergo a vigorous reaction to yield exfoliated few-layered graphene.<sup>58</sup> Potassium-intercalated GICs are also prepared using the ternary potassium salt  $\text{K}(\text{THF})_x\text{C}_{24}$  and they get readily exfoliated in NMP yielding a dispersion of negatively charged single layered graphene which can then be deposited onto any substrate.<sup>59</sup> Solution-phase exfoliation of graphite in an organic solvent such as N-methylpyrrolidone (NMP) yields single-layer graphene in high yields.<sup>60</sup> In this case, the energy required to exfoliate graphene is balanced by the solvent-graphene interaction. Such solvent-graphene interactions are also used to disperse graphene in perfluorinated aromatic solvents,<sup>61</sup> orthodichloro benzene<sup>62</sup> and even in low-boiling solvents such as like chloroform and isopropanol.<sup>63</sup> Hernandez *et al.*<sup>64</sup> carried out detailed study on dispersibility of graphene in 40 different solvents and proposed that good solvents for graphene are characterized by a Hildebrand and Hansen solubility parameters.

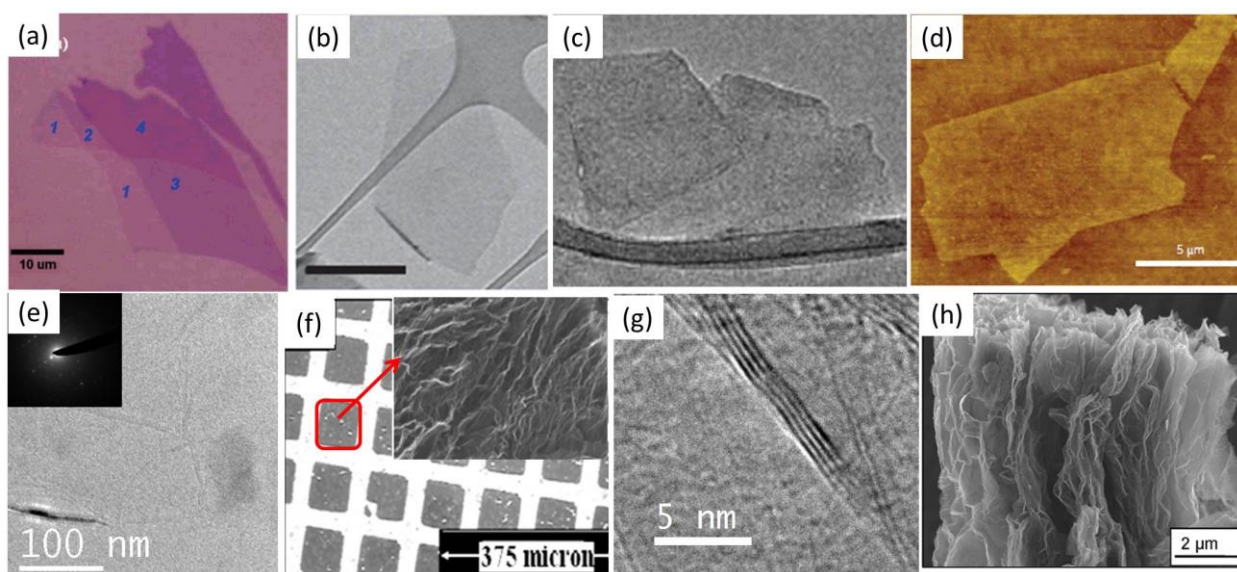


**Figure 2.** Different graphene samples prepared by (a) micromechanical cleavage (optical microscopic image)<sup>65</sup>, (b) solvent exfoliation in NMP (TEM image)<sup>60</sup>, (c) Laser exfoliation in DMF (TEM image)<sup>66</sup>, (d) reduced graphene oxide (AFM image)<sup>52</sup>, (e) chemical vapour deposition of methane over Ni surface (TEM image),<sup>67</sup> (f) laser induced reduction of graphene oxide (FESEM image)<sup>68</sup>, (g) arc discharge in presence of H<sub>2</sub> (TEM image)<sup>69</sup> and (h) thermal exfoliation of graphite oxide (FESEM image)<sup>70</sup>

**Chemical Vapor Deposition:** The most promising, inexpensive and readily accessible approach for the deposition of reasonably high quality graphene is chemical vapor deposition (CVD) onto transition metal substrates such as Ni,<sup>71</sup> Pd,<sup>72</sup> Ru,<sup>73</sup> Ir<sup>74</sup> or Cu.<sup>71</sup> The process is based on the carbon-saturation of a transition metal upon exposure to a hydrocarbon gas at high temperature. While cooling the substrate, the solubility of carbon in the transition metal decreases and a thin film of carbon is thought to precipitate from the surface.<sup>75</sup> Different hydrocarbons such as methane, ethylene, acetylene and benzene were decomposed on various transition metal substrates like Ni, Cu, Co, Au and Ru.<sup>75</sup> Radio frequency plasma enhanced chemical vapor deposition (PECVD) system has been used to synthesize graphene on a variety of substrates such as Si, W, Mo, Zr, Ti, Hf, Nb, Ta, Cr, 304 stainless steel, SiO<sub>2</sub> and Al<sub>2</sub>O<sub>3</sub>. This method reduces energy consumption and

prevents the formation of amorphous carbon or other types of unwanted products.<sup>67,76-79</sup> Graphene obtained using CVD process can be transferred to other substrates by etching of the underlying transition metal and can be transformed in to any arbitrary substrate.

***Arc Discharge:*** Synthesis of graphene by the arc evaporation of graphite in the presence of hydrogen has been reported.<sup>67,69</sup> This procedure yields graphene (HG) sheets with 2-3 layers having flake size of 100-200 nm. This makes use of the knowledge that the presence of H<sub>2</sub> during arc-discharge process terminates the dangling carbon bonds with hydrogen and prevents the formation of closed structures. The conditions that are favorable for obtaining graphene in the inner walls are the high current (above 100 A), the high voltage (>50 V), and the high pressure of hydrogen (above 200 torr). This method has been conveniently employed to dope graphene with boron and nitrogen.<sup>80</sup> To prepare boron and nitrogen doped graphene (B-HG and N-HG) the discharge is carried out in the presence of H<sub>2</sub> + diborane and H<sub>2</sub> + (pyridine or ammonia) respectively.

***Reduction of Graphite oxide:*** Chemical reduction of graphite oxide is one of the established procedures to prepare graphene in large quantities.<sup>50</sup> Graphite oxide when ultra sonicated in water forms a homogenous colloidal dispersion of predominantly single layer graphene oxide in water. Reduced graphene oxide with properties similar to that of graphene is prepared through chemical, thermal, or electrochemical reduction pathways.<sup>81</sup> While most strong reductants have slight to strong reactivity with water, hydrazine monohydrate does not, making it an attractive option for reducing aqueous dispersions of graphene oxide. Other reducing agents used include NaBH<sub>4</sub><sup>82</sup>, phenyl hydrazine<sup>83</sup>, hydroxylamine,<sup>84</sup> glucose,<sup>85</sup> ascorbic acid,<sup>86</sup> hydroquinone,<sup>87</sup> alkaline solutions<sup>88</sup>, pyrrole<sup>89</sup> etc. Electrochemical reduction is another means to synthesize graphene in large scale.<sup>90-92</sup> The reduction initiates at -0.8 V and is completed by -1.5 V with formation of black precipitate onto the bare graphite electrode. Photothermal and photochemical reduction of GO is a rapid, clean, and versatile way to RGO. Ding *et al.*<sup>93</sup> reduced GO using UV irradiation to obtain single to few layered graphene sheets without the use of any photocatalyst. Cote *et al.*<sup>94</sup> prepared RGO by photothermal reduction of GO using

Xenon flash at ambient conditions and patterned GO or GO/polymer films using photomask. Nanosecond laser pulses of KrF excimer laser or 335 nm and 532 nm were shown to effectively reduce dispersions of GO to thermally and chemically stable graphene.<sup>95</sup> High quality RGO has been prepared by irradiating GO with sunlight, ultraviolet light and KrF excimer laser.<sup>67</sup> Photochemical reduction of GO and single layer graphene oxide (SGO) to graphene has also been exploited for patterning. For this purpose GO films deposited on Si substrates were subjected to excimer laser radiation (Lambda Physik KrF excimer laser, 248 nm wavelength, 30 ns life time, 300 mJ laser energy, 5 Hz repetition rate, 200 shots), after inserting a TEM grid as the mask and covering them with a quartz plate.<sup>96</sup> Graphene oxide can be reversibly reduced and oxidized using electrical stimulus. Controlled reduction and oxidation in two-terminal devices containing multilayer graphene oxide films was demonstrated by Ekiz *et al.*<sup>97</sup> and by Yao *et al.*<sup>98</sup> Microwave irradiation (MWI) induced heating has been used as a rapid way to synthesize graphene sheets. Due to the difference in the solvent and reactant dielectric constants, selective dielectric heating can provide significant enhancement in the transfer of energy directly to the reactants which causes an instantaneous internal temperature rise and thereby reduction of GO.<sup>99</sup> Dry GO absorbs MWI strongly with a sudden increase in surface temperature of the GO up to ~400°C within just two seconds leading to an ultrafast reduction of GO to RGO.<sup>100</sup>

### ***Synthesis of graphene analogues:***

#### ***Metal dichalcogenides:***

The various methods which are employed for the synthesis of graphene are equally effective for 2D layered metal chalcogenides. These methods can mostly be categorized as top-down methods involving exfoliation of layered bulk crystals like mechanical cleavage,<sup>101-103</sup> Li-intercalation and exfoliation,<sup>104</sup> exfoliation in liquid phase by ultrasonication<sup>105</sup> and laser thinning.<sup>106</sup> Bottom up approaches involve CVD growth,<sup>107,108</sup> wet chemical synthesis like hydrothermal synthesis,<sup>109,110</sup> and high temperature synthesis from precursors.<sup>110</sup> Figure 3 (a-d) shows HRTEM, AFM and optical microscopic image of metal di-chalcogenides prepared by different methods. In 1960's Frindt for the first

time prepared ultra-thin sheets of MoS<sub>2</sub> with thickness of about 5-6 molecular layers (3.5 to 4.0 nm) by micromechanical cleavage.<sup>111</sup> Using the same technique Novoselov *et. al.*<sup>9</sup> were able to prepare single layer flakes of MoS<sub>2</sub> and characterize them using optical contrast microscopy, AFM, SEM and TEM. Liquid phase exfoliation or ultrasonication is another simple route to defect-free graphene dispersions from bulk graphite. Single- and few-layered transition metal dichalcogenides such as MoS<sub>2</sub>, WS<sub>2</sub>, MoSe<sub>2</sub>, MoTe<sub>2</sub>, TaSe<sub>2</sub>, NbSe<sub>2</sub> and NiTe<sub>2</sub> have been successfully prepared by liquid phase exfoliation.<sup>105,112</sup> Zhou *et. al.*<sup>113</sup> studied dispersibility of layered materials like MoS<sub>2</sub>, WS<sub>2</sub> and BN in mixed solvent, specifically water-ethanol mixture. Laser-irradiation of dispersions of bulk metal dichalcogenides (MoS<sub>2</sub>/WS<sub>2</sub>/MoSe<sub>2</sub> and WSe<sub>2</sub>) in dimethylformamide by a KrF excimer laser, with a laser fluence of 1.5 J/cm<sup>2</sup> and a repetition rate of 5 Hz for 1 hour, has been used to produce single- and few-layer materials. After laser exfoliation, the resultant solutions are kept for 24 hours and then centrifuged at 2500 rpm for 5 minutes.<sup>114</sup>

In the 1980's, Frindt *et. al.*<sup>115</sup> carried out lithium intercalation of MoS<sub>2</sub> followed by exfoliation using water. Li-intercalation was achieved reaction of MoS<sub>2</sub> with n-butyl lithium in hexane under inert conditions. The Li-intercalated sample reacts vigorously when exposed to water during which profuse gas evolution occurs, giving rise to an opaque suspension of single and few-layer MoS<sub>2</sub>.<sup>115,116</sup> A detailed structural investigation of the X-ray diffraction of single-layer MoS<sub>2</sub> has revealed that it existed as the 1T polymorph in contrast to 2H-type bulk MoS<sub>2</sub>.<sup>117</sup> Nanosheets have also been synthesized by electrochemical Li intercalation and subsequent exfoliation in water.<sup>118</sup> Large scale synthesis of few-layered MoS<sub>2</sub>, WS<sub>2</sub>, MoSe<sub>2</sub> and WSe<sub>2</sub> has been achieved by reaction of molybdic acid with thiourea/selenourea. Excess of thiourea/selenourea (48 times by weight) is ground with molybdic acid and heated to 773 K in horizontal tube furnace for 3 hours in a N<sub>2</sub> atmosphere.<sup>110,119</sup> This method essentially produces single- to few-layer graphene analogues. MoS<sub>2</sub> has been grown on graphene oxide and perylene-3,4,9,10-tetracarboxylate of potassium coated SiO<sub>2</sub>/Si substrates by CVD using MoO<sub>3</sub> and S powders as reactants.<sup>108</sup> Recently, few-layer MoS<sub>2</sub> has been synthesized on a graphitic surface by heating amorphous MoS<sub>3</sub> and reduced graphite oxide at 1000 °C under high-vacuum conditions.<sup>120</sup> Mo films deposited on SiO<sub>2</sub> substrates have been used to grow large area MoS<sub>2</sub> sheets by treatment with sulphur vapours at 500-750 °C.<sup>121</sup> Few-layer

MoS<sub>2</sub> can be easily obtained at low temperatures under hydrothermal conditions. Reaction of MoO<sub>3</sub> with KSCN (as the sulfur source) in water as the solvent at 453 K for 24h yielded few-layer MoS<sub>2</sub>.<sup>110</sup> Microwave treatment of MoO<sub>3</sub> and KSCN under mild reducing conditions (using ethylene glycol) yielded few-layer MoS<sub>2</sub> when heated at 450W for 15 min in a domestic microwave oven operating at 2.45 GHz.<sup>114</sup> Free-standing nanosheets of MoS<sub>2</sub> and WS<sub>2</sub> can also be synthesized by low-temperature (360°C) decomposition of single-source precursors (ammonium tetrathiotungstate, ammonium tetrathiomolybdate) in oleylamine.<sup>122</sup>

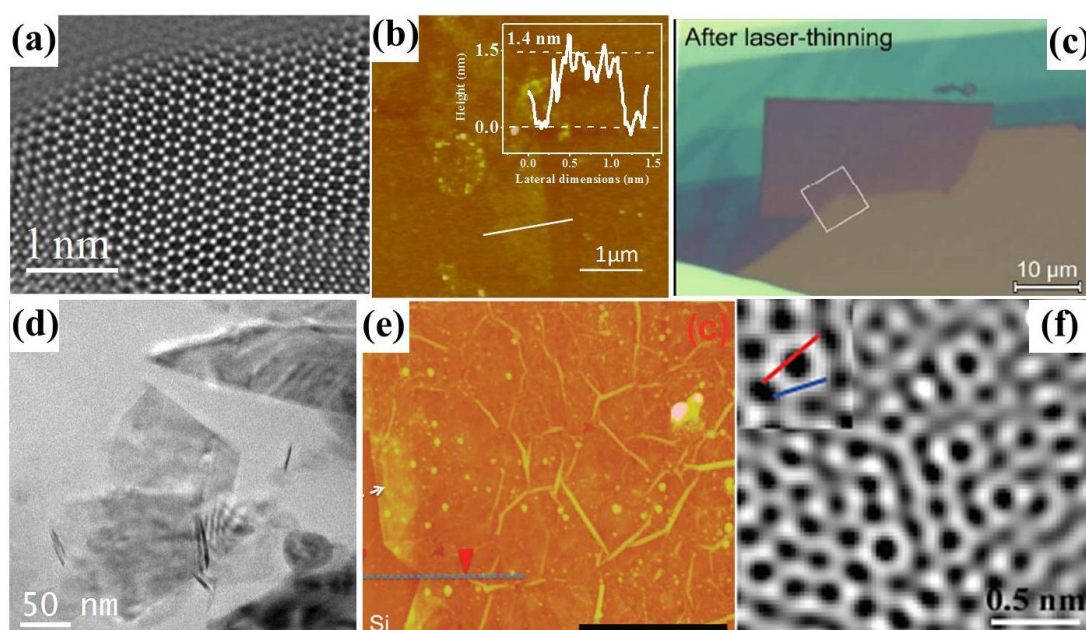


**Figure 3.** (a) HRTEM image of few-layer MoSe<sub>2</sub> prepared by high temperature reaction of molybdic acid with selenourea,<sup>123</sup> (b) AFM image for single layer WSe<sub>2</sub> prepared by Li intercalation and exfoliation,<sup>123</sup> (c) Optical microscope image of single and few-layer MoS<sub>2</sub> prepared by laser thinning<sup>123</sup> (d) TEM image of few-layer MoS<sub>2</sub> by laser exfoliation in solvent,<sup>123</sup> (e) AFM image of few-layer layer BN obtained by CVD of ammonia-borane (NH<sub>3</sub>-BH<sub>3</sub>) on preannealed Cu foils<sup>123</sup> and (f) HRTEM few-layer BN prepared by high temperature reaction of boric acid and urea.<sup>123</sup>

### **Boron nitride**

Boron nitride is the structural analogue of graphene with a hexagonal unit consisting of 3 B and 3 N atoms. BN is, however an insulator and its layers could find uses such as dielectric gate and so on. <sup>124</sup> A monolayer BN film was first prepared by the pyrolysis of



borazine on single crystalline Ni and Cu substrates.<sup>125,126</sup> Corso et al.<sup>127</sup> observed that on Rh(111) substrate with a high lattice mismatch, nanomesh-like morphology is obtained. On using a different chemical precursor such as trichloroborazine instead of borazine, islands and superstructures of BN are formed.<sup>128,129</sup> Free-standing few-layer BN flakes can be obtained by micromechanical cleavage.<sup>130</sup> Few-layer BN flakes obtained by mechanical cleavage can be thinned down to monolayers by reactive ion etching<sup>131</sup> or by irradiation with a high energy electron beam.<sup>132</sup> Ball milling has also been used to prepare BN nanosheets.<sup>133-135</sup> The method, however, yields BN sheets with high density of defects. BN nanosheets can be exfoliated by applying a shear force on the surface of bulk BN. Chen et al.<sup>136</sup> rotated a dispersion of BN in NMP at 8000rpm at an angle 45° in a vortex fluidic device to exfoliate BN into nanosheets. Similar effects were obtained by application of high pressure to a dispersion of BN in a DMF-chloroform mixture flowing through a microfluidic channel.<sup>137</sup>

Like all layered materials, interlayer van der Waals forces in BN can be overcome by ultrasonication in solution.<sup>138-140</sup> Vigorous sonication of BN particles in a highly polar solvent such as DMF results in exfoliation.<sup>139</sup> The resulting dispersion when centrifuged yields few-layer BN in the supernatant. A majority of the sheets obtained are around 10 layers thick with the thinnest sheet having 3 layers. Polar solvents like NMP, N,N-dimethylacetamide and ethylene glycol can be used for solvent-based exfoliation of BN.<sup>124</sup> Lin et al.<sup>140</sup> carried out chemical functionalization-induced exfoliation to obtain stable and optically transparent dispersions of few-layer BN. The amine groups of lipophilic and hydrophilic amine molecules are used to functionalize BN nanosheets using Lewis acid-base interactions between the amine group of the functional molecules and the electron-deficient boron atoms in BN. Interestingly, nanosheets and nanoribbons of BN could be prepared by sonication of BN in water. Water acts as a hydrolyzing agent cutting BN nanosheets with the release of NH<sub>3</sub>.<sup>141</sup> Exfoliation and dispersion via noncovalent interaction was demonstrated by Han et al.<sup>142</sup> using a dichloroethane solution of a conjugated polymer, poly(m-phenylenevinylene-co-2,5-dioxy-p-phenylenevinylene).

High yields are obtained by combustion of boric acid with sodamide, ammonium bromide and ammonium carbonate, followed by heating to temperatures above

1000 °C.<sup>143</sup> Surface segregation method, i.e. vacuum thermal treatment of B and N doped transition metal alloys, has long been used to prepare thin films of BN.<sup>144-146</sup> Presence of a low percentage of sulfur impurity in Fe-Cr-Ni alloy allows formation of predominantly mono and bi-layer BN films by surface segregation.<sup>147</sup> Large-area BN films are made possible by chemical vapor deposition (CVD) of ammonia and borane or borazine on polycrystalline Ni and Cu.<sup>107,148,149</sup> Films as thin as 3-5 layers and flake size of upto few nm were obtained on preannealed Cu foils with ammonia-borane (NH<sub>3</sub>-BH<sub>3</sub>) at 1000 °C.<sup>148</sup> Figure 3(e) shows AFM image of such large area few-layered BN films. A decaborane-ammonia mixture can also be used to prepare nanosheets of BN on polycrystalline substrates.<sup>150</sup> The films thus obtained need to be transferred to other substrates for characterization. The process thus involves multiple steps before the product can be actually put into application. Mono and few-layer BN films can be directly deposited on Si substrates by microwave plasma chemical vapour deposition of BF<sub>3</sub>-H<sub>2</sub>-N<sub>2</sub>, without the use of any catalyst.<sup>151</sup> The growth of BN sheets in the absence of a catalyst is ascribed to etching by the fluorine containing gases. BN films have been grown over graphene by CVD based on ammonia-borane.<sup>152,153</sup> The method has been used to prepare BN films on pyrolytic graphite or mechanically exfoliated graphene as well as stacks of graphene/BN. Graphene can be used as a sacrificial template to obtain BN and BN-C films from B<sub>2</sub>O<sub>3</sub> and graphene mixture treated to 1650 °C.<sup>154</sup> Han et al.<sup>154</sup> used graphene as a sacrificial template with B<sub>2</sub>O<sub>3</sub> as B source and N<sub>2</sub> gas as N source to prepare BN nanosheets by heating to 1650 °C. Pakdel et al.<sup>155</sup> mixed boron powder with MgO and FeO catalysts to obtain vertically aligned BN nanosheets on Si/SiO<sub>2</sub> substrates.

Bulk scale synthesis of BN nanosheets has been achieved by the reaction of boric acid with urea.<sup>156</sup> The method not only gives a high yield of BN sheets but also a good control over the number of layers. Boric acid and urea with different molar ratio (1:6, 1:12, 1:24 and 1:48) are used to prepare BN with different number of layers. Figure 3(f) shows HRTEM image of single layer BN obtained with 1:48 molar ratio of Boric acid and urea. The BN nanosheets prepared by the urea route are readily solubilized in Lewis bases.<sup>156</sup> High quality two atomic layer thick BN films were grown by magnetron sputtering of boron in a mixture of N<sub>2</sub>-Ar. The films showed pin hole free insulating behaviour upto  $\mu\text{m}^2$  scale demonstrating that they could be used as high quality thin film dielectrics.<sup>157</sup>

*In this part of the thesis following studies are presented:*

**Chapter II. 1** *Covalently and non-covalently functionalized nanodiamonds and its covalently linked composites.*

**Chapter II. 2** *Mechanical properties of polymer nanocomposites of nanodiamond and other nanocarbons.*

**Chapter II. 3** *Birch reduction of carbon nanotubes and graphene nanoribbons for chemical H<sub>2</sub> storage*

**Chapter II. 4** *Temperature effects on the Raman spectra of graphene and graphene nanoribbons.*

**Chapter II. 5** *Nanoribbons and nanoscrolls of graphene and graphene analogues of BN and MoS<sub>2</sub>*

## **References**

1. K. S. Novoselov, A. K. Geim, S. V. Morozov, D. Jiang, Y. Zhang, S. V. Dubonos, I. V. Grigorieva and A. A. Firsov. *Science* **2004**, 306, 666.
2. K. S. Novoselov, A. K. Geim, S. V. Morozov, D. Jiang, M. I. Katsnelson, I. V. Grigorieva, S. V. Dubonos and A. A. Firsov. *Nature* **2005**, 438, 197.
3. A. K. Geim and K. S. Novoselov. *Nat. Mater.* **2007**, 6, 183.
4. C. N. R. Rao, A. K. Sood, K. S. Subrahmanyam and A. Govindaraj. *Angew. Chem. Int. Ed.* **2009**, 48, 7752.
5. C. N. R. Rao, H. S. S. R. Matte and K. S. Subrahmanyam. *Acc. Chem. Res.* **2013**, 46, 149.
6. S. Iijima. *Nature* **1991**, 354, 56.
7. M. Terrones. *Ann. Rev. Mater. Res.* **2003**, 33, 419.
8. S. Iijima and T. Ichihashi. *Nature* **1993**, 363, 603.
9. K. S. Novoselov, D. Jiang, F. Schedin, T. J. Booth, V. V. Khotkevich, S. V. Morozov and A. K. Geim. *Proc. Natl. Acad. Sci. USA* **2005**, 102, 10451.
10. C. N. R. Rao and A. Nag. *Eur-J. Inorg. Chem.* **2010**, 201, 4244.
11. K. Raidongia, A. Gomathi and C. N. R. Rao. *Israel J. Chem.* **2010**, 50, 399.
12. R. Mas-Balleste, C. Gomez-Navarro, J. Gomez-Herrero and F. Zamora. *Nanoscale* **2011**, 3, 20.
13. X. Huang, Z. Zeng and H. Zhang. *Chem. Soc. Rev.* **2013**, 42, 1934.
14. M. Xu, T. Liang, M. Shi and H. Chen. *Chem. Rev.* **2013**.
15. Q. H. Wang, K. Kalantar-Zadeh, A. Kis, J. N. Coleman and M. S. Strano. *Nature Nanotechnol.* **2012**, 7, 699.
16. M. Chhowalla, H. S. Shin, G. Eda, L.-J. Li, K. P. Loh and H. Zhang. *Nature chem.* **2013**, 5, 263.
17. X. Song, J. Hu and H. Zeng. *J. Mater. Chem. C* **2013**, 1, 2952.
18. C. N. R. Rao and A. Govindaraj *Nanotubes and Nanowires, Second ed.; Royal Society of Chemistry: London, 2011.*
19. J. Prasek, J. Drbohlavova, J. Chomoucka, J. Hubalek, O. Jasek, V. Adam and R. Kizek. *J. Mater. Chem.* **2011**, 21, 15872.

20. T. W. Ebbesen and P. M. Ajayan. *Nature* **1992**, 358, 220.
21. X. Zhao, M. Ohkohchi, M. Wang, S. Iijima, T. Ichihashi and Y. Ando. *Carbon* **1997**, 35, 775.
22. D. S. Bethune, C. H. Kiang, d. V. M. S., G. Gorman, R. Savoy, V. J. and R. Beyers. *Nature* **1993**, 363, 605
23. Y. Saito, K. Nishikubo, K. Kawabata and T. Matsumoto. *J. Appl. Phys.* **1996**, 80, 3062.
24. Y. Saito, M. Okuda, M. Tomita and T. Hayashi. *Chem. Phys. Lett.* **1995**, 236, 419.
25. S. R. C. Vivekchand, A. Govindaraj, M. M. Seikh and C. N. R. Rao. *J. Phys. Chem. B* **2004**, 108, 6935.
26. W. K. Maser, E. Munoz, A. M. Benito, M. T. Martinez, G. F. de la Fuente, Y. Maniette, E. Anglaret and J. L. Sauvajol. *Chem. Phys. Lett.* **1998**, 292, 456.
27. J. Kong, A. M. Cassell and H. Dai. *Chem. Phys. Lett.* **1998**, 292, 567.
28. Z. Luo, Z. X. Shen and J. Lin. *Nanoscale research letters* **2010**, 5, 1377.
29. T. Guo, P. Nikolaev, A. Thess, D. T. Colbert and R. E. Smalley. *Chem. Phys. Lett.* **1995**, 243, 49.
30. T. Ikegami, F. Nakanishi, M. Uchiyama and K. Ebihara. *Thin Solid Films* **2004**, 457, 7.
31. S. A. Steiner, T. F. Baumann, B. C. Bayer, R. Blume, M. A. Worsley, W. J. MoberlyChan, E. L. Shaw, R. Schlögl, A. J. Hart, S. Hofmann and B. L. Wardle. *J. Am. Chem. Soc.* **2009**, 131, 12144.
32. H. Tempel, R. Joshi and J. J. Schneider. *Mater. Chem. Phys.* **2010**, 121, 178.
33. R. Smajda, J. C. Andresen, M. Duchamp, R. Meunier, S. Casimirius, K. Hernádi, L. Forró and A. Magrez. *Physica Status Solidi B* **2009**, 246, 2457.
34. S. P. Patole, P. S. Alegaonkar, H.-C. Lee and J.-B. Yoo. *Carbon* **2008**, 46, 1987.
35. H. R. Byon, H. Lim, H. J. Song and C. H. Choi. *Bull. Korean Chem. Soc* **2007**, 28 2056.
36. Y. M. Chen and H. Y. Zhang *Advances in Composites; Trans Tech Publications Ltd: Stafa-Zurich*, **2011**.
37. B. Brown, C. B. Parker, B. R. Stoner and J. T. Glass. *Carbon* **2011**, 49, 266.

38. Y. Zhang, S. F. Ali, E. Dervishi, Y. Xu, Z. Li, D. Casciano and A. S. Biris. *ACS Nano* **2010**, 4, 3181.
39. J. Liu, Y. Zhang, M. I. Ionescu, R. Li and X. Sun. *Appl. Surf. Sc.* **2011**, 257, 7837.
40. I. Khatri, T. Soga, T. Jimbo, S. Adhikari, H. R. Aryal and M. Umeno. *Diamond Rel. Mater.* **2009**, 18, 319.
41. H. Hiura, T. W. Ebbesen, J. Fujita, K. Tanigaki and T. Takada. *Nature* **1994**, 367, 148.
42. T. W. Ebbesen and H. Hiura. *Adv. Mater.* **1995**, 7, 582.
43. T. M. Bernhardt, B. Kaiser and K. Rademann. *Surf. Sci.* **1998**, 408, 86.
44. H. Roy. *J. Appl. Phys.* **1998**, 83, 4695.
45. X. Lu, M. Yu, H. Huang and R. S. Ruoff. *Nanotechnol.* **1999**, 10, 269.
46. H. V. Roy, C. Kallinger and K. Sattler. *Surf. Sci.* **1998**, 407, 1.
47. Y. H. Wu, T. Yu and Z. X. Shen. *J. Appl. Phys.* **2010**, 108, 071301.
48. D. C. Marcano, D. V. Kosynkin, J. M. Berlin, A. Sinitskii, Z. Sun, A. Slesarev, L. B. Alemany, W. Lu and J. M. Tour. *ACS Nano* **2010**, 4, 4806.
49. S. Park, J. An, I. Jung, R. D. Piner, S. J. An, X. Li, A. Velamakanni and R. S. Ruoff. *Nano Lett.* **2009**, 9, 1593.
50. W. S. Hummers and R. E. Offeman. *J. Am. Chem. Soc.* **1958**, 80, 1339.
51. M. J. Allen, V. C. Tung and R. B. Kaner. *Chem. Rev.* **2009**, 110, 132.
52. V. C. Tung, M. J. Allen, Y. Yang and R. B. Kaner. *Nat. Nanotechnol.* **2009**, 4, 25.
53. J. I. Paredes, S. Villar-Rodil, A. Marti'nez-Alonso and J. M. D. Tasco'n. *Langmuir* **2008**, 24, 10560.
54. H. C. Schniepp, J.-L. Li, M. J. McAllister, H. Sai, M. Herrera-Alonso, D. H. Adamson, R. K. Prud'homme, R. Car, D. A. Saville and I. A. Aksay. *J. Phys. Chem. B* **2006**, 110, 8535.
55. M. J. McAllister, J.-L. Li, D. H. Adamson, H. C. Schniepp, A. A. Abdala, J. Liu, M. Herrera-Alonso, D. L. Milius, R. Car, R. K. Prud'homme and I. A. Aksay. *Chem. Mater.* **2007**, 19, 4396.

56. X. Li, G. Zhang, X. Bai, X. Sun, X. Wang, E. Wang and H. Dai. *Nat. Nanotechnol.* **2008**, 3, 538.
57. X. Guoqing, H. Wontae, K. Namhun, M. C. Sung and C. Heeyeop. *Nanotechnol.* **2010**, 21, 405201.
58. L. M. Viculis, J. J. Mack, O. M. Mayer, H. T. Hahn and R. B. Kaner. *J. Mater. Chem.* **2005**, 15, 974.
59. C. ValleÌs, C. Drummond, H. Saadaoui, C. A. Furtado, M. He, O. Roubeau, L. Ortolani, M. Monthieux and A. Peinicaud. *J. Am. Chem. Soc.* **2008**, 130, 15802.
60. Y. Hernandez, V. Nicolosi, M. Lotya, F. M. Blighe, Z. Sun, S. De, I. T. McGovern, B. Holland, M. Byrne, Y. K. Gun'Ko, J. J. Boland, P. Niraj, G. Duesberg, S. Krishnamurthy, R. Goodhue, J. Hutchison, V. Scardaci, A. C. Ferrari and J. N. Coleman. *Nat. Nanotechnol.* **2008**, 3, 563.
61. A. B. Bourlinos, V. Georgakilas, R. Zboril, T. A. Steriotis and A. K. Stubos. *Small* **2009**, 5, 1841.
62. C. E. Hamilton, J. R. Lomeda, Z. Sun, J. M. Tour and A. R. Barron. *Nano. Lett.* **2009**, 9, 3460.
63. A. O'Neill, U. Khan, P. N. Nirmalraj, J. Boland and J. N. Coleman. *J. Phys. Chem. C* **2011**, 115, 5422.
64. Y. Hernandez, M. Lotya, D. Rickard, S. D. Bergin and J. N. Coleman. *Langmuir* **2009**, 26, 3208.
65. Z. H. Ni, H. M. Wang, J. Kasim, H. M. Fan, T. Yu, Y. H. Wu, Y. P. Feng and Z. X. Shen. *Nano Lett.* **2007**, 7, 2758.
66. P. Kumar. *RSC Adv* **2013**, 3, 11987.
67. C. N. R. Rao, K. S. Subrahmanyam, H. S. S. Ramakrishna Matte, B. Abdulhakeem, A. Govindaraj, B. Das, P. Kumar, A. Ghosh and D. J. Late. *Sci. Tech. Adv. Mater.* **2010**, 11, 054502.
68. P. Kumar, B. Das, B. Chitara, K. S. Subrahmanyam, K. Gopalakrishnan, S. B. Krupanidhi and C. N. R. Rao. *Macromol. Chem. Phys.* **2012**, 213, 1146.
69. K. S. Subrahmanyam, L. S. Panchakarla, A. Govindaraj and C. N. R. Rao. *J. Phys. Chem. C* **2009**, 113, 4257.

70. B. Das, K. E. Prasad, U. Ramamurty and C. N. R. Rao. *Nanotechnol.* **2009**, 20, 125705.
71. K. S. Kim, Y. Zhao, H. Jang, S. Y. Lee, J. M. Kim, K. S. Kim, J.-H. Ahn, P. Kim, J.-Y. Choi and B. H. Hong. *Nature* **2009**, 457, 706.
72. S.-Y. Kwon, C. V. Ciobanu, V. Petrova, V. B. Shenoy, J. Barenó, V. Gambin, I. Petrov and S. Kodambaka. *Nano Lett.* **2009**, 9, 3985.
73. P. W. Sutter, J.-I. Flege and E. A. Sutter. *Nat. Mater.* **2008**, 7, 406.
74. J. Coraux, A. T. N`Diaye, C. Busse and T. Michely. *Nano Lett.* **2008**, 8, 565.
75. A. Reina, X. Jia, J. Ho, D. Nezich, H. Son, V. Bulovic, M. S. Dresselhaus and J. Kong. *Nano. Lett.* **2008**, 9, 30.
76. J. J. Wang, M. Y. Zhu, R. A. Outlaw, X. Zhao, D. M. Manos, B. C. Holloway and V. P. Mammana. *Appl. Phys. Lett.* **2004**, 85, 1265.
77. J. Wang, M. Zhu, R. A. Outlaw, X. Zhao, D. M. Manos and B. C. Holloway. *Carbon* **2004**, 42, 2867.
78. M. Zhu, J. Wang, B. C. Holloway, R. A. Outlaw, X. Zhao, K. Hou, V. Shutthanandan and D. M. Manos. *Carbon* **2007**, 45, 2229.
79. S. K. Pati, T. Enoki and C. N. R. Rao *Graphene: Synthesis, Functionalization and Properties World Scientific Publishing Co.:* Chennai, India, **2010**.
80. L. S. Panchakarla, A. Govindaraj and C. N. R. Rao. *Inorg. Chim. Acta* **2009**, 363, 4163.
81. D. R. Dreyer, S. Park, C. W. Bielawski and R. S. Ruoff. *Chem. Soc. Rev.* **2010**, 39, 228.
82. H.-J. Shin, K. K. Kim, A. Benayad, S.-M. Yoon, H. K. Park, I.-S. Jung, M. H. Jin, H.-K. Jeong, J. M. Kim, J.-Y. Choi and Y. H. Lee. *Adv. Funct. Mater.* **2009**, 19, 1987.
83. V. H. Pham, T. V. Cuong, T.-D. Nguyen-Phan, H. D. Pham, E. J. Kim, S. H. Hur, E. W. Shin, S. Kim and J. S. Chung. *Chem. Comm.* **2010**, 46, 4375.
84. X. Zhou, J. Zhang, H. Wu, H. Yang, J. Zhang and S. Guo. *J. Phys. Chem. C* **2011**, 115, 11957.
85. C. Zhu, S. Guo, Y. Fang and S. Dong. *ACS Nano* **2010**, 4, 2429.



86. J. Zhang, H. Yang, G. Shen, P. Cheng, J. Zhang and S. Guo. *Chem. Commun.* **2010**, 46, 1112.
87. G. Wang, J. Yang, J. Park, X. Gou, B. Wang, H. Liu and J. Yao. *J. Phys. Chem.* **2008**, 112, 8192.
88. X. Fan, W. Peng, Y. Li, X. Li, S. Wang, G. Zhang and F. Zhang. *Adv. Mater.* **2008**, 20, 4490.
89. C. A. Amarnath, C. E. Hong, N. H. Kim, B.-C. Ku, T. Kuila and J. H. Lee. *Carbon* **2011**, 49, 3497.
90. H.-L. Guo, X.-F. Wang, Q.-Y. Qian, F.-B. Wang and X.-H. Xia. *ACS Nano* **2009**, 3, 2653.
91. R. S. Sundaram, C. Gómez-Navarro, K. Balasubramanian, M. Burghard and K. Kern. *Adv. Mater.* **2008**, 20, 3050.
92. O. C. Compton, B. Jain, D. A. Dikin, A. Abouimrane, K. Amine and S. T. Nguyen. *ACS Nano* **2011**, 5, 4380.
93. Y. H. Ding and et al. *Nanotechnol.* **2011**, 22, 215601.
94. L. J. Cote, R. Cruz-Silva and J. Huang. *J. Am. Chem. Soc.* **2009**, 131, 11027.
95. V. Abdelsayed, S. Moussa, H. M. Hassan, H. S. Aluri, M. M. Collinson and M. S. El-Shall. *J. Phys. Chem. Lett.* **2010**, 1, 2804.
96. P. Kumar, K. S. Subrahmanyam and C. N. R. Rao. *Mater. Exp.* **2011**, 1, 252.
97. O. O. Ekiz, M. Urel, H. Guner, A. K. Mizrak and A. Dana. *ACS Nano* **2011**, 5, 2475.
98. P. Yao, P. Chen, L. Jiang, H. Zhao, H. Zhu, D. Zhou, W. Hu, B.-H. Han and M. Liu. *Adv. Mater.* **2010**, 22, 5008.
99. H. M. A. Hassan, V. Abdelsayed, A. E. R. S. Khder, K. M. AbouZeid, J. Turner, M. S. El-Shall, S. I. Al-Resayes and A. A. El-Azhary. *J. Mater. Chem.* **2009**, 19, 3832.
100. Z. Li, Y. Yao, Z. Lin, K.-S. Moon, W. Lin and C. Wong. *J. Mater. Chem.* **2010**, 20, 4781.
101. K. S. Novoselov, D. Jiang, F. Schedin, T. J. Booth, V. V. Khotkevich, S. V. Morozov and A. K. Geim. *Proc. Natl. Acad. Sci. USA* **2005** 102, , 10451.

102. Z. Yin, H. Li, H. Li, L. Jiang, Y. Shi, Y. Sun, G. Lu, Q. Zhang, X. Chen and H. Zhang. *ACS Nano* **2011**, 6, 74.
103. B. Radisavljevic., A. Radenovic., J. Brivio., V. Giacometti. and A. Kis. *Nat. Nanotechnol.* **2011**, 6, 147.
104. G. Eda, H. Yamaguchi, D. Voiry, T. Fujita, M. Chen and M. Chhowalla. *Nano Lett.* **2011**, 11, 5111.
105. J. N. Coleman, M. Lotya, A. O'Neill, S. D. Bergin, P. J. King, U. Khan, K. Young, A. Gaucher, S. De, R. J. Smith, I. V. Shvets, S. K. Arora, G. Stanton, H.-Y. Kim, K. Lee, G. T. Kim, G. S. Duesberg, T. Hallam, J. J. Boland, J. J. Wang, J. F. Donegan, J. C. Grunlan, G. Moriarty, A. Shmeliov, R. J. Nicholls, J. M. Perkins, E. M. Grievson, K. Theuwissen, D. W. McComb, P. D. Nellist and V. Nicolosi. *Science* **2011**, 331, 568.
106. A. Castellanos-Gomez, M. Barkelid, A. M. Goossens, V. E. Calado, H. S. J. van der Zant and G. A. Steele. *Nano Lett.* **2012**, 12, 3187.
107. K.-K. Liu, W. Zhang, Y.-H. Lee, Y.-C. Lin, M.-T. Chang, C.-Y. Su, C.-S. Chang, H. Li, Y. Shi, H. Zhang, C.-S. Lai and L.-J. Li. *Nano Lett.* **2012**, 12, 1538.
108. Y.-H. Lee, X.-Q. Zhang, W. Zhang, M.-T. Chang, C.-T. Lin, K.-D. Chang, Y.-C. Yu, J. T.-W. Wang, C.-S. Chang, L.-J. Li and T.-W. Lin. *Adv. Mater.* **2012**, 24, 2320.
109. K. Chang and W. Chen. *ACS Nano* **2011**, 5, 4720.
110. H. S. S. R. Matte, A. Gomathi, A. K. Manna, D. J. Late, R. Datta, S. K. Pati and C. N. R. Rao. *Angew. Chem. Int. Ed.* **2010**, 49, 4059.
111. R. F. Frindt. *J. Appl. Phys.* **1966**, 37, 1928.
112. G. Cunningham, M. Lotya, C. S. Cucinotta, S. Sanvito, S. D. Bergin, R. Menzel, M. S. P. Shaffer and J. N. Coleman. *ACS Nano* **2012**, 6, 3468.
113. K.-G. Zhou, N.-N. Mao, H.-X. Wang, Y. Peng and H.-L. Zhang. *Angew. Chemie Int. Ed.* **2011**, 50, 10839.
114. H. S. S. R. Matte, U. Maitra, P. Kumar, B. Govinda Rao, K. Pramoda and C. N. R. Rao. *Z. Anorg. Allg. Chem.* **2012**, 638, 2617.
115. P. Joensen, R. F. Frindt and S. R. Morrison. *Mat. Res. Bull.* **1986**, 21, 457.

116. D. Yang and R. F. Frindt. *J. Phys. Chem. Solids* **1996**, 57, 1113.
117. D. Yang, S. J. Sandoval, W. M. R. Divigalpitiya, J. C. Irwin and R. F. Frindt. *Phys. Rev. B* **1991**, 43, 12053.
118. Z. Zeng, Z. Yin, X. Huang, H. Li, Q. He, G. Lu, F. Boey and H. Zhang. *Angew. Chem. Int. Ed.* **2011**, 50, 11093.
119. H. S. S. R. Matte, B. Plowman, R. Datta and C. N. R. Rao. *Dalton Trans.* **2011**, 40, 10322.
120. V. O. Koroteev, L. G. Bulusheva, A. V. Okotrub, N. F. Yudanov and D. V. Vyalikh. *Phys. Status Solidi B* **2011**, 248, 2740.
121. Y. Zhan, Z. Liu, S. Najmaei, P. M. Ajayan and J. Lou. *Small* **2012**, 8, 966.
122. C. Altavilla, M. Sarno and P. Ciambelli. *Chem. Mater.* **2011**, 23, 3879.
123. C. N. R. Rao, H. S. S. Ramakrishna Matte and U. Maitra. *Angew. Chem. Int. Ed.* **2013**, 52, 13162.
124. Y. Lin and J. W. Connell. *Nanoscale* **2012**, 4, 6908.
125. A. Nagashima, N. Tejima, Y. Gamou, T. Kawai and C. Oshima. *Phys. Rev. B* **1995**, 51, 4606.
126. A. B. Preobrajenski, A. S. Vinogradov and N. Mårtensson. *Surf. Sci.* **2005**, 582, 21.
127. M. Corso, W. Auwärter, M. Muntwiler, A. Tamai, T. Greber and J. Osterwalder. *Science* **2004**, 303, 217.
128. W. Auwärter, H. U. Suter, H. Sachdev and T. Greber. *Chem. Mater.* **2003**, 16, 343.
129. F. Müller, K. Stöwe and H. Sachdev. *Chem. Mater.* **2005**, 17, 3464.
130. D. Pacile, J. C. Meyer, C. O. Girit and A. Zettl. *Appl. Phys. Lett.* **2008**, 92, 133107.
131. N. Alem, R. Erni, C. Kisielowski, M. D. Rossell, W. Gannett and A. Zettl. *Phys. Rev. B* **2009**, 80, 155425.
132. J. C. Meyer, A. Chuvilin, G. Algara-Siller, J. Biskupek and U. Kaiser. *Nano Lett.* **2009**, 9, 2683.
133. Y. Lin, T. V. Williams and J. W. Connell. *J. Phys. Lett.* **2009**, 1, 277.
134. J. Y. Huang, H. Yasuda and H. Mori. *J. Am. Cer. Soc.* **2000**, 83, 403.

135. L. H. Li, Y. Chen, G. Behan, H. Zhang, M. Petracic and A. M. Glushenkov. *J. Mater. Chem.* **2011**, 21, 11862.
136. X. Chen, J. F. Dobson and C. L. Raston. *Chem. Comm.* **2012**, 48, 3703.
137. H. Yurdakul, Y. Göncü, O. Durukan, A. Akay, A. T. Seyhan, N. Ay and S. Turan. *Cer. Int.* **2012**, 38, 2187.
138. W.-Q. Han, L. Wu, Y. Zhu, K. Watanabe and T. Taniguchi. *Appl. Phys. Lett.* **2008**, 93, 223103.
139. C. Zhi, Y. Bando, C. Tang, H. Kuwahara and D. Golberg. *Adv. Mater.* **2009**, 21, 2889.
140. M. Jagodic, Z. Jaglicic, A. Jelen, L. Jin Bae, K. Young-Min, K. Hae Jin and J. Dolinsek. *J. Phys. Cond. Matter* **2009**, 21, 215302.
141. Y. Lin, T. V. Williams, T.-B. Xu, W. Cao, H. E. Elsayed-Ali and J. W. Connell. *J. Phys. Chem. C* **2011**, 115, 2679.
142. X. Liang, A. S. P. Chang, Y. Zhang, B. D. Harteneck, H. Choo, D. L. Olynick and S. Cabrini. *Nano Lett.* **2008**, 9, 467.
143. Z. Zhao, Z. Yang, Y. Wen and Y. Wang. *J. Am. Cer. Soc.* **2011**, 94, 4496.
144. D. Fujita and T. Homma. *J. Vacuum Sc. Tech. A* **1988**, 6, 230.
145. K. Yoshihara, M. Tosa and K. Nii. *J. Vacuum Sc. Techn. A* **1985**, 3, 1804.
146. Y. Minami, A. Tohyama and T. Yamada. *J. Vacuum Sc. Techn. A* **1989**, 7, 1585.
147. M. Xu, D. Fujita, H. Chen and N. Hanagata. *Nanoscale* **2011**, 3, 2854.
148. L. Song, L. Ci, H. Lu, P. B. Sorokin, C. Jin, J. Ni, A. G. Kvashnin, D. G. Kvashnin, J. Lou, B. I. Yakobson and P. M. Ajayan. *Nano Lett.* **2010**, 10, 3209.
149. H. Hiura, H. Miyazaki and K. Tsukagoshi. *Appl. Phys. Exp.* **2010**, 3, 095101
150. S. Chatterjee, Z. Luo, M. Acerce, D. M. Yates, A. T. C. Johnson and L. G. Sneddon. *Chem. Mater.* **2011**, 23, 4414.
151. Q. Li, Y. Jie, L. Mingyu, L. Fei and B. Xuedong. *Nanotech.* **2011**, 22, 215602.
152. Z. Liu, L. Song, S. Zhao, J. Huang, L. Ma, J. Zhang, J. Lou and P. M. Ajayan. *Nano Lett.* **2011**, 11, 2032.

153. K. K. Kim, A. Hsu, X. Jia, S. M. Kim, Y. Shi, M. Hofmann, D. Nezich, J. F. Rodriguez-Nieva, M. Dresselhaus, T. Palacios and J. Kong. *Nano Lett.* **2012**, 12, 161.
154. W.-Q. Han, H.-G. Yu and Z. Liu. *Appl. Phys. Lett.* **2011**, 98, 203112.
155. A. Pakdel, C. Zhi, Y. Bando, T. Nakayama and D. Golberg. *ACS Nano* **2011**, 5, 6507.
156. A. Nag, K. Raidongia, K. P. S. S. Hembram, R. Datta, U. V. Waghmare and C. N. R. Rao. *ACS Nano* **2010**, 4, 1539.
157. P. Sutter, J. Lahiri, P. Zahl, B. Wang and E. Sutter. *Nano Lett.* **2012**, 13, 276.

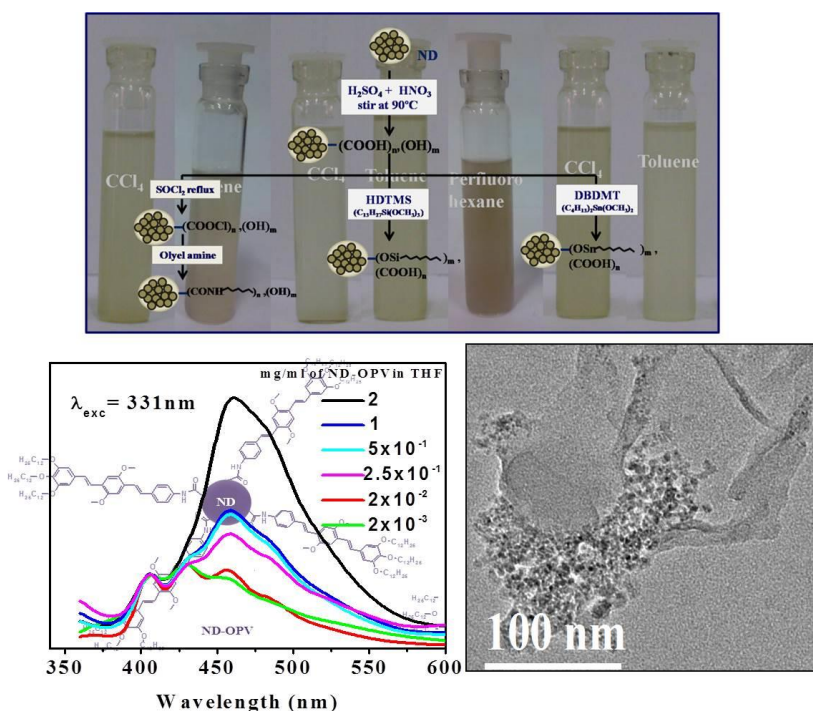


# Chapter II.1

## *Covalently and non-covalently functionalized nanodiamond and its covalently linked composites*

### *Summary\**

*Covalent and Non-covalent functionalization of nanodiamond have been carried out for solubilization of nanodiamond (ND) in various polar and non-polar solvents. While covalent functionalization of ND involves forming functional groups on nanodiamond that can covalently bind to required moieties, non-covalent functionalization utilizes surface functional groups on ND to non-covalently bind to surfactants. Covalent functionalization was used to prepare luminescent chromophore-functionalized nanodiamond. Covalent linkage was also used to bind ND to other nanocarbons like graphene and carbon nanotubes to obtain binary conjugates of nanocarbons of different dimensionality and thereby different functionality.*



\*Papers based on this work have appeared in *J. Exp. Nanosci.*, 2008, *Nanoscale*, 2011 and *J. Chem. Sci.*, 2012

## **1. Introduction**

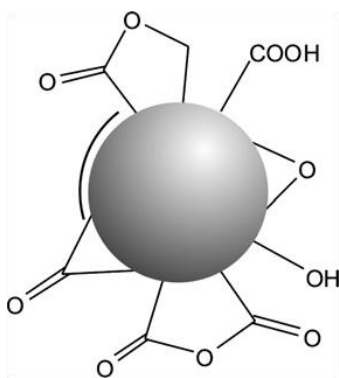
Diamond is a widely investigated material for its remarkable properties, for example, hardness, thermal conductivity, dopability or optical transparency over a wide spectral range, to name only a few.<sup>1</sup> Diamond films, in particular, have become a focus of interest. Their production by chemical vapour deposition (CVD)<sup>2</sup> and detonation.<sup>3,4</sup> has evolved into a commercially available technique that is able to produce industrial amount of surface coatings and freestanding films for a broad range of applications, such as electronic and electrochemical devices, sensors, protective coatings and optical windows.<sup>5-7</sup> Diamond structures at the nanoscale (length  $\sim 1$  to 100nm) include pure-phase diamond films, nanocrystalline diamond particles (called '*nanodiamond*' or '*ultra-nanocrystalline diamond*'), recently fabricated 1-D diamond nanorods and 2-D diamond nanoplatelets. Of all these materials nanodiamond (nanoscopic versions of  $sp^3$  carbon) has come into focus in the last decade due to its unique properties originating from the lattice structure, large surface area and sometimes functionalised surface. This material is not only interesting for the basic understanding of the universe of carbon modifications, but it has a multitude of potential applications in the macroscopic world. While retaining the merits inherent in the diamond, nanodiamond (ND) exhibits a number of remarkable features both in their structure and in their physicochemical properties. These features give us the ground to consider ND as a specific nanocarbon material belonging to the popular family of nanocarbons.

Historically speaking, nanodiamond is not really a new carbon modification. Back in 60's Russian and American scientists had detonated graphite to produce diamonds.<sup>8-10</sup> First accessible reports on detonation synthesis of diamond however appeared in the Soviet magazine *Doklady Akademii Nauk*<sup>3</sup> and in *Nature*.<sup>4</sup> There are several methods to prepare nanodiamond particles. The simplest one would be milling of micron sized natural or synthetic diamonds. Diamond being the hardest material known, this process is difficult. Other methods of synthesis are based on phase diagram of carbon. Pressure and temperature reached during such synthesis ( $P \approx 20-30$  GPa and  $T \approx 3000-4000$  K) lie in the region of thermal stability of diamond and this is what accounts for the formation of diamond crystals directly from the carbon of explosives in the course of explosion.<sup>11</sup> The kinetics of the process determines the purity of the product. Once crystals of diamond



form, the P-T parameters must drop rapidly to the region of thermodynamic instability of diamond. If the temperature is still high enough to sustain a high mobility of the carbon atoms (above the Debye temperature of diamond,  $T_D \approx 1800$  K), the diamond-graphite reverse transition will occur. The higher the cooling rate, the shorter is the time the product of detonation synthesis spends in the region of kinetic instability of the diamond and, accordingly, the lower is the probability of formation of the  $sp^2$  hybridized carbon which coats the surface of a diamond grain.

Detonation synthesis is the most common method of synthesis of nanodiamond with the process being scaled upto industrial level. Usually a mixture of 2,4,6-trinitrotoluene (TNT) and hexanol is used, with the latter contributing the major part of the energy and the TNT producing most of the soot.<sup>12-8</sup> Within the detonation wave that is passing through this reactor the pressure and temperature are high enough to form diamond. ND synthesized by detonation method consists of clusters of 3-5 nm primary particles covered by graphitic shells forming micron sized aggregates. Commercially available detonation ND powder undergoes several purification cycles which includes heating with oxidizing mineral acids to selectively oxidize existing graphitic material, amorphous soot and metal impurities. Additionally functional groups are installed on the surface of primary particles and also on the outer side of larger agglomerates. Scheme 1 shows a schematic view of commercial ND with several functional groups on the surface.<sup>13</sup>



**Scheme 1.** Schematic representation of as prepared detonation nanodiamond with different surface functional groups.

Non-covalent or covalent modification of these surface functional groups can change the properties of these materials.<sup>14,15</sup> Several chemical approaches have been developed to modify the surfaces of the ND powder by the covalent attachment of various functional groups.<sup>16-19</sup> Because of having several functional groups on the surface it has strong non-

covalent interaction via hydrogen bonding or other electronic interaction. Further functionalization, for example, free amino groups, gives the possibility to graft DNA pieces onto the coated diamond particles. Owing to its biocompatibility ND is an attractive candidate for a variety of biological applications like targeted drug delivery. Lattice defects in ND like N-V centers have non-blinking, non-bleaching fluorescence in the red and infrared, which is very valuable for bio-labeling purposes. Other properties like mechanical properties of polymer nanocomposites have been found to enhance significantly with diamond as nanofillers.<sup>20</sup> This chapter deals with the functionalization and composites of nanodiamond.

## ***2. Scope of the present investigations***

Commercially available ND has a variety of functional groups on its surface as shown in scheme 1. Inhomogeneity of surface functional groups stands as a major obstacle in using ND for covalent grafting of molecules, noncovalent interactions or solubilisation. It is therefore necessary to achieve a homogenized surface structure by chemical modification. Solubilisation is necessary for majority of the applications discussed above. For example, for use in biological systems stable dispersion of ND in water is necessary. Surface functionalization and dispersion is necessary for interaction of ND with polymer in case of polymer nanocomposites so as to achieve superior mechanical properties.

Even though there have been many reports on reactions of ND surfaces with several chemicals or compounds, covalent functionalization of ND is not fully accomplished. Furthermore clear evidence for functionalization has not been provided by spectroscopic, microscopic, and other physical measurements. Solubilization in different solvents has also not been reported. In the view of the importance of functionalizing ND, with the objective of solubilizing it in polar and non-polar solvents as well as water, we wanted to carry out careful investigations making use of the literature on solubilization of inorganic nanotubes, carbon nanotubes and graphene and also by employing organosilane and organotin reagents.<sup>21-24</sup>

Nanodiamonds have emerged as an important class of fluorescent nanocarbons because of the stable luminescence and relative ease of surface functionalization.

Moreover, ND particles have a low cytotoxicity compared to the other carbon-based nanomaterials being studied thereby enabling their use in biocompatible and non-blinking fluorescent labelling.<sup>20</sup> Fluorescent ND has been prepared either by ion implantation or by organic functionalization. Red (N-V, type 1b) and green fluorescent (N-V, type 1a) ND arise from nitrogen defect centers produced by high energy ion beam irradiation.<sup>25-27</sup> Recently blue fluorescence has been reported in nanodiamonds by simple chemical functionalization with octadecylamine.<sup>28</sup> Though the origin of blue fluorescence is not clearly understood it is likely to originate from the graphitic part of the nanodiamond.<sup>29</sup> The blue fluorescence in the high energy region gives ND hybrid materials a new platform for optical modification through energy transfer to green- or red-emitting chromophores.<sup>30</sup> Chromophore-functionalized ND constructs which exhibit the combined properties of both ND and  $\pi$ -conjugated systems have not yet been explored adequately for photoluminescence and other photo-physical properties.<sup>31</sup> Chromophore-functionalized ND allows easy tuning of luminescence through an appropriate choice of the fluorophore. Furthermore energy or electron transfer processes allow the use of optical and electronic properties of ND and the chromophore in synchronization, rendering these hybrid materials as potent candidates for light harvesting and other optoelectronic applications.<sup>32</sup> Recently energy transfer from ND to an IR dye, taking advantage of the red emission of ND has been demonstrated.<sup>33</sup> Studies exploiting the blue regime of ND fluorescence have not yet been explored. Oligo(phenylenevinylene) (OPV) is a member of the family poly phenylene vinylene, a yellow fluorescent conducting polymer. OPV based  $\pi$ -conjugated systems have high fluorescence quantum yields and have been extensively used for the design of liquid-crystalline and self-assembled functional materials.<sup>34,35</sup> OPV amine a derivative of OPV absorbs blue light and gives a strong green emission. Since the blue fluorescence of nanodiamond coincides with the absorption of OPV amine we expected an energy transfer from ND to OPV in ND-OPV hybrid such that a tuneability of the fluorescence of ND from blue to green can be achieved. The three dodecyl chains at the gallic wedge of the OPV-amine molecule were expected to render the resulting hybrid material soluble enabling easy processibility for any device fabrication or casting.

One of the important factors that determines the nature and properties of nanomaterials is their dimensionality. Among the various nanomaterials synthesized and characterized in recent years, nanocarbons of different dimensionalities are of special interest. While ND is zero dimensional, carbon nanotubes and graphene are one and two-dimensional, respectively. As already discussed ND exhibits useful mechanical, electrical and optical properties.<sup>2,8,26,36</sup> Beneficial properties of single walled carbon nanotube (SWNTs) are well-documented,<sup>37-39</sup> while those of graphene (G) have been discovered more recently.<sup>40</sup> Binary combinations of nanocarbons with different dimensionalities may lead to integration of properties of the constituent units as well as result in new properties. It could be of some advantage if binary combinations of nanostructures are prepared by covalent modification over non-covalent methods. Covalently linked carbon nanostructures will have better interactions between the two nanostructures which might lead to better properties. Diamond is the hardest material known and ND has since long been used as an abrasive and for wear resistant parts. Graphene and SWNT are one of the hardest materials discovered of late and have been used in composites to increase hardness and strength. One of the effects of covalently linking the two might be benefits in mechanical properties from better mixing and greater interactions of the individual components. Again ND-SWNT composites have been used to prepare cold cathodes.<sup>41</sup> Covalently linked ND with SWNT might be studied for enhanced activities in such applications too. There are few reports on the covalent crosslinking of carbon nanotubes. Chiu *et al.*<sup>42</sup> have reported crosslinking of two chloride terminated carbon nanotubes via diamines while Frehill *et al.*<sup>43</sup> have used inorganic metal complexes to crosslink carbon nanotubes. Bundles of carbon nanotubes can be linked by means of [2+1] cycloaddition using nitrenes.<sup>44</sup> To our knowledge, there are no reports on the covalent conjugation of nanocarbons of different dimensionalities. We have therefore carried out covalent crosslinking of ND with itself and with nanocarbons of different dimensionalities. Such homo- and hetero-nanocarbon adducts may find use in special applications related to high performance materials.

### 3. Experimental Section

#### *Surface Homogenization of Nanodiamond*

Nanodiamond (ND) with phase purity higher than 98% and an average particle size of around 5 nm (Tokyo Diamond Tools, Tokyo, Japan) was used for the studies. The sample was first characterized to check particle size, crystallinity and surface functional groups. To get homogenous functional groups on the surface it was treated with strong oxidizing acids. For this purpose, 100 mg of the ND was refluxed with 5 mL conc.  $\text{HNO}_3$  and 45 mL conc.  $\text{H}_2\text{SO}_4$  for 12 h.<sup>45</sup> The acid-treated ND was washed with distilled water and dried under vacuum. This should generate carboxyl and hydroxyl groups homogeneously on the surface of ND. Further functionalization of these acid treated species with thionyl chloride generates  $-\text{COCl}$  groups on the surface. For this the acid-treated ND was reacted with excess of thionyl chloride for 12 h in a nitrogen atmosphere. Care is to be taken to prevent exposure to moisture (exposure to moisture converts  $-\text{COCl}$  back to  $-\text{COOH}$ ). This was then reacted with an excess of oleyl amine refluxed for 12 h, washed with toluene, and dried under vacuum overnight.

#### *Functionalization with organotin and organosilane reagent*

Hexadecyltrimethoxysilane (HDTMS), dibutyldimethoxytin (DBDMT) and perfluoro-octyltriethoxysilane (PFOTES) were purchased from Sigma Aldrich and used without any further purification. The solvents used were distilled and stored over sodium. All air and moisture sensitive compounds were handled under a nitrogen atmosphere. In a typical experiment to coat the ND with the organosilicon or an organotin reagent, about 30 mg of the acid treated ND were ground using an agate mortar and pestle and placed in a clean and dry round-bottomed flask. To this 20 mL of dry toluene was added and the mixture was placed in a sonic bath for 30 minutes. Organosilane or organotin reagent was then added to the nanoparticles at a 1:1 (organosilane or organotin : ND) molar ratio by micropipette in a nitrogen atmosphere. The mixture was refluxed at 373 K for 12 h after which the mixture was cooled down and the residue washed with dry hexane and then with water–acetone mixture (20% of  $\text{H}_2\text{O}$ ). The functionalized ND was dried in vacuum for one day under ambient temperature. Dispersion studies were carried by sonication of

the functionalized ND in an organic solvent for 5 minutes. Excess ND was removed by centrifugation and the dispersion kept undisturbed to check stability.

### ***Functionalization with Surfactants***

Surfactant-induced noncovalent dispersions of ND were obtained as follows. Surfactant solutions of 20 mM strength were prepared in different solvents. A known quantity of the ND (5 mg) was dispersed in 20 mL of the solution and sonicated in a water bath for 1 h. The dispersion was allowed to stand for 24 h and then characterized. In the case of IGEPAL, 1 mM solution was prepared in water to which this 5 mg of acid-treated ND was added and sonicated for 30 min. The dispersion thus obtained was left undisturbed for 24 hours to study the stability of the dispersion. Thus functionalized samples were characterized by XRD, FESEM, TEM and IR spectroscopy.

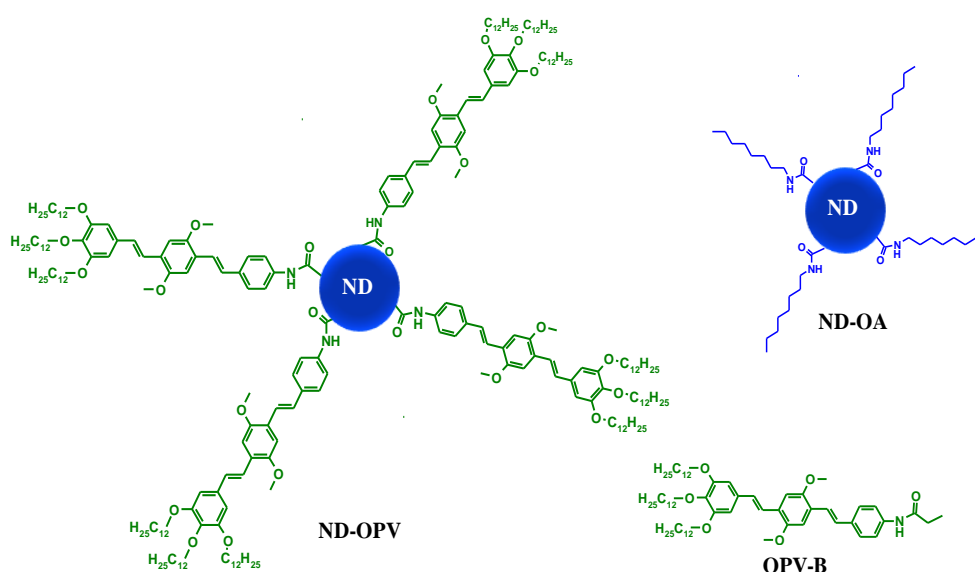
### ***Functionalization with octyl amine (ND-OA) and OPV (ND-OPV)***

Covalently linked conjugates of ND with OA and OPV were prepared via amide linkage. First, 50 mg of ND powder was refluxed with 20 mL of H<sub>2</sub>SO<sub>4</sub>: HNO<sub>3</sub> (9:1) for 12 h. This was then filtered, washed with distilled water several times and dried under vacuum. Dried acid derivative of ND was then refluxed with 50 ml of SOCl<sub>2</sub> and 1 mL DMF for 12 h under inert atmosphere. The brown liquid was decanted and then dried under N<sub>2</sub> flow to form acyl chloride derivative of ND. The acyl chloride derivative being moisture sensitive was used immediately for the subsequent step without any further purification. 5 mg of **ND-COCl** was dispersed in 10 mL of dry toluene and 1 mL of octyl amine was added to it. The mixture was stirred at 80 °C for 12 hrs. After cooling excess octylamine was removed by washing with ethanol and dried under vacuum. For **ND-OPV** same procedure was followed using 20 mg of OPV amine instead of octylamine.

*Synthesis of OPV-acetyl amide (OPV-B):* A mixture of OPV-NH<sub>2</sub> (20 mg, 0.022 mmoles), propionic acid (~ 2 μL, 0.024 mmoles), DCC (5 mg, 0.024 mmoles) and DMAP (2.5 mg) were taken in 10 ml THF and allowed to stir 18 hrs under Argon atmosphere, at room temperature. TLC was used to monitor the complete consumption of the reactant. After the reaction THF was evaporated *in vacuo* and the mixture was extracted with CHCl<sub>3</sub> and water thrice. CHCl<sub>3</sub> layer was dried over anhydrous Na<sub>2</sub>SO<sub>4</sub>

and evaporated *in vacuo*. The mixture was purified by a silica gel column using  $\text{CHCl}_3$  as eluent, followed by a preparative size exclusion chromatography (Bio Beads, SX-3) to afford 70.6 % yield of OPV-B.  $^1\text{H}$  NMR (400 MHz,  $\text{CDCl}_3$ )  $\delta$ /ppm: 7.51 (m, 4H), 7.41 (d, 2H,  $J = 16$  Hz), 7.31 (d, 2H,  $J = 16$  Hz), 7.18 (s, 1H), 7.10 (d, 2H,  $J = 8.4$  Hz), 7.07 (d, 2H,  $J = 16.8$  Hz), 7.01 (d, 2H,  $J = 16.4$  Hz), 6.74 (s, 2H), 4.05 - 3.96 (m, 6H), 3.92 (s, 3H), 3.91 (s, 3H), 2.40 (q, 2H), 1.80-1.27 (m, 72H), 0.89 (t, 9H). MALDI-TOF MS  $m/z$ , calculated for  $\text{C}_{63}\text{H}_{99}\text{N}_1\text{O}_6$ : 966.49 [ $\text{M}^+$ ], found: 966.43.

A schematic representation of the products ND-OPV, ND-OA and OPV-B are given in Scheme 2.



**Scheme 2.** Molecular structures of ND-OPV, ND-OA and OPV-B.

For dynamic light scattering (DLS) experiments 2 mg/mL stock solution of **ND-OPV** was prepared in THF, calculated volume of which was injected into solvent to obtain the required solution. For Confocal Microscopy imaging sample was prepared by sealing the solution between two glass plates. UV-Vis and photoluminescence measurements were carried out in solution state with different dilution. UV-Vis spectra were recorded in 1 cm and 1 mm path length quartz cuvettes.

***Preparation of covalent binary conjugates of nanocarbons***

We aim to prepare binary conjugates of ND, G and SWNT. First we functionalized the carbon nanostructures to get acid groups (-COOH) on their surface. A diamine linker was used to covalently conjugate acid functionalized nanocarbons. We used N, N'-Dicyclohexylcarbodiimide (DCC) as a coupling reagent to enhance the reaction of acid functionalized nanocarbons with a diamine. For acid functionalization, ND (100 mg) was refluxed with 5 mL conc. HNO<sub>3</sub> and 45 mL conc. H<sub>2</sub>SO<sub>4</sub> for 12 h. The acid-functionalized ND was washed with distilled water and dried under vacuum. SWNT and G were functionalized with acid groups by the following procedure. A mixture of conc. HNO<sub>3</sub>, conc. H<sub>2</sub>SO<sub>4</sub>, water, and the corresponding nanocarbon was heated in a microwave oven for about 5–8 min under hydrothermal conditions. The mixture was further heated at 100 °C for 6–8 h in an oven. The product thus obtained was washed with distilled water and filtered through a sintered glass funnel to yield nanocarbons functionalized with -COOH and -OH groups. Acid treated nanocarbons were washed thoroughly with water, dried and used for further reactions.

To prepare binary nanocarbon conjugates of same type, nanocarbon (5 mg) of interest was taken in DMF (20 mL), sonicated for 10 min for thorough mixing. To this mixture coupling reagent DCC (1 mg) and 1,2-ethylene diamine (ED) linker (1 mL) were added. Reaction mixture was stirred for 4 h under inert atmosphere and the products were collected by centrifugation. The product was washed with copious amounts of water, acetonitrile and ethanol. The sample was dried under vacuo and used for further characterization. For the preparation of hetero-conjugates of nanocarbons with different dimensionality, a two-step covalent crosslinking procedure was followed. Mono-protected Boc-1,2-ethylenediamine was first coupled to a acid functionalized nanocarbon through a amide linkage which was then subjected to Boc-deprotection using trifluoroacetic acid. The nanocarbon with free amine generated was further coupled to another acid functionalized nanocarbon through an amide linkage to obtain ED linked hetero-conjugate of nanocarbons. This procedure eliminates the possibility of obtaining undesired products resulting from inter- and intramolecular cross-coupling reactions. For this an acid functionalized nanocarbon (5 mg) was taken in DMF (20 mL), sonicated for 10 min to get a homogenous mixture. To this mixture DCC (1 mg) and mono-protected



Boc-1,2-ethelynediamine (1 mL) were added. The reaction mixture was stirred for 4 h under inert atmosphere and the products were collected by centrifugation. The product was washed with copious amounts of water, acetonitrile and ethanol, dried under vacuo. Next mono Boc-1,2-ethelynediamine modified nanocarbon was subjected to Boc-deprtection using 50% trifluoroacetic acid in dichloromethane for 1 h. The free-amine of the ED-nanocarbon generated was dried under vacuo and used for further reaction. The ED functionalized nanocarbon (5 mg) and an acid functionalized nanocarbon (5 mg) were dispersed in DMF (20 mL) and sonicated for 10 min for thorough mixing. To this mixture DCC (1 mg) was added and reaction was stirred for 4 h under inert atmosphere and the conjugate was collected by centrifugation. The product was washed with copious amounts of water, acetonitrile and ethanol, dried under vacuo and used for characterization. Raman and IR spectroscopy were carried out to confirm functionalization. TEM images were obtained to observe conjugate formation.

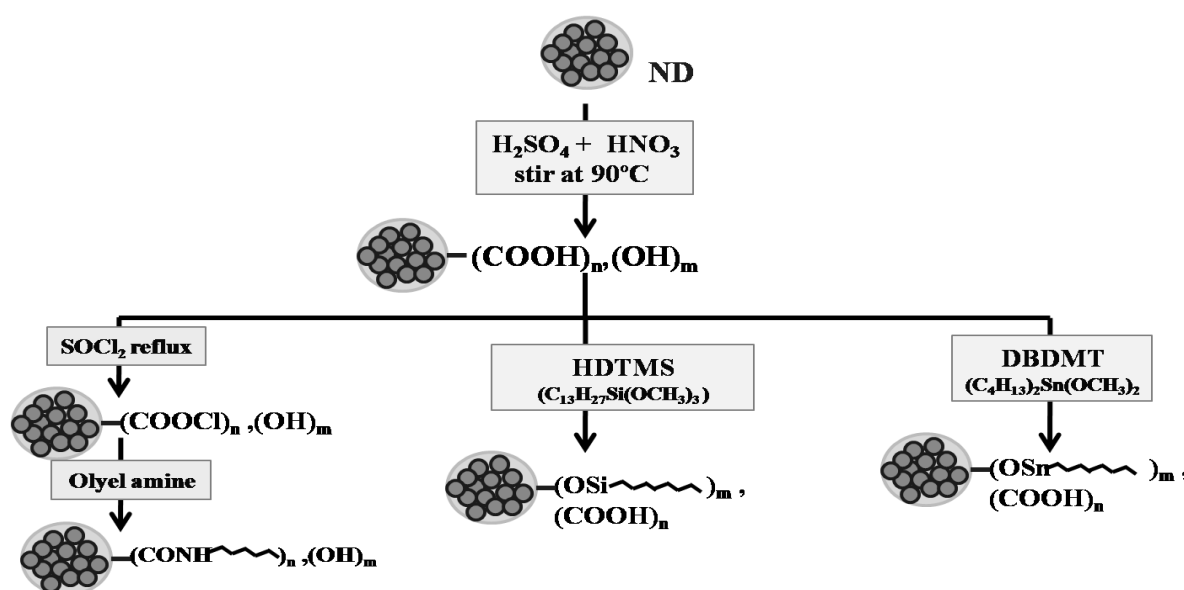
*Synthesis of NI-(t-Boc)-1,2-Ethylenediamine:* The solution of di-tert-butyl dicarbonate (5 g, 22.9 mmol) in dichloromethane (10 mL) was added dropwise to a stirred solution of 1,2-ethylenediamine (9.1 mL, 137.5 mmol) in dichloromethane (40 mL) under nitrogen atmosphere and the reaction was allowed to continue for 20 h. Solvent was evaporated under vacuo and the residue was re-dissolved into water and the mixture was filtered. The filtrate was extracted using ethyl acetate (3 x 30 mL) and the combined organic layer was dried over sodium sulphate, evaporated under vacuo and the residue was purified by column chromatography using petroleum ether-ethylacetate (1:9) as eluent. The mono-protected Boc-1,2-ethylenedimaine was obtained as colorless oil. Yield: 2.95 g (80.6%).  $^1\text{H}$  NMR (400 MHz,  $\text{CDCl}_3$ ):  $\delta_{\text{ppm}}$  5.58 (br, NH, 1H), 3.35-3.32 (t, 2H), 3.00-2.97 (t, 2H), 1.93 (NH, 2H), 1.41(s, 9H);  $^{13}\text{C}$  NMR (400 MHz,  $\text{CDCl}_3$ ):  $\delta_{\text{ppm}}$  156.6, 79.7, 40.6, 40.0, 28.5. GCMS: 161.0 [ $\text{M} + \text{H}^+$ ], calcd. 160.2 for  $\text{C}_7\text{H}_{16}\text{N}_2\text{O}_2$ .

Details of charecterization techniques is provided in Appendix.

## 4. Results and Discussion

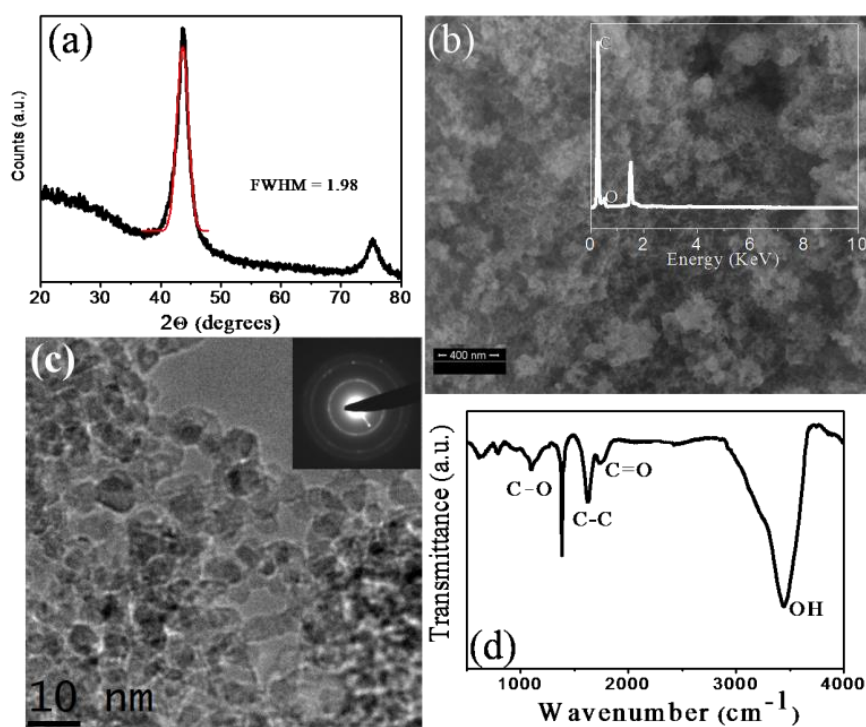
### A. Solubilization by Covalent and Non-covalent Functionalization

Stepwise functionalization of ND has been carried out. One important thing to remember is that ND remains as aggregates of 20-100 nm. Even when functionalization is carried out it is the aggregate as a whole that gets functionalized. Scheme 3. shows a schematic representation of stepwise functionalization adopted.



**Scheme 3.** Schematics of functionalization of ND.

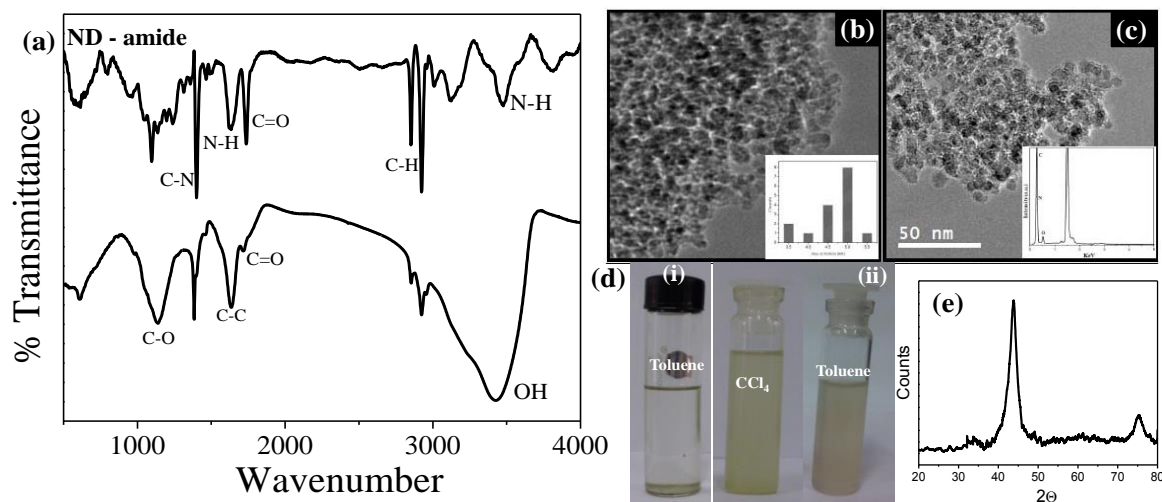
As obtained ND samples were first characterized using XRD, TEM, FESEM and IR spectroscopy. XRD pattern of ND in Figure 1(a) shows that as obtained ND is crystalline. Broadness of the peak is because of smaller crystallite size. FESEM image (Figure 1(b)) show agglomerates of ND. EDAX spectra of ND (inset of Figure 1(b)) show presence of only C and O. In TEM image (Figure 1(c)) it is seen that the pristine ND has an average diameter of 5 nm. Sharp lines in the electron diffraction pattern shown in the inset of Figure 1(c) adds to the proof of crystallinity of ND. IR spectra in Figure 1(d) shows the presence of C=O, C-O O-H and C-C stretches thus proving the presence of acid, ester, alcohol and aldehydic groups on the surface of as obtained ND.



**Figure 1.** (a) XRD pattern along with Gaussian fit to determine the FWHM, (b) FESEM image with EDAX as inset, (c) TEM image with ED pattern as inset, (d) IR spectra of as obtained ND.

Acid-treated ND would be expected to have carboxyl and hydroxyl groups on the surface. Accordingly the IR spectrum of the ND after acid treatment, shown in Figure 2(a), shows strong carbonyl band at  $1720\text{ cm}^{-1}$  and hydroxyl band at  $3400\text{ cm}^{-1}$ . It is clear that on acid functionalization the strength of C-O and O-H stretching frequencies increases manifold. The IR spectrum of amide derivative of ND shows amide I band at  $1710\text{ cm}^{-1}$  and amide II band at  $1540\text{ cm}^{-1}$  and bands due to alkyl groups at  $2850$  and  $2950\text{ cm}^{-1}$ . In Figure 2(b, c), we compare the TEM image of the acid functionalized ND with that of amide derivative. From the figure it is clear that diameter is not affected by amidation. The EDAX spectrum at the inset of Figure 2(c) shows presence of nitrogen. The amide-derivatized NDs were soluble in non-polar solvents like toluene and  $\text{CCl}_4$ . In Figure 2 (d-ii)), we show the photograph of the dispersions of amide-derivatized ND in non-polar solvents taken after 4h. For comparison an image of as obtained ND dispersed in organic

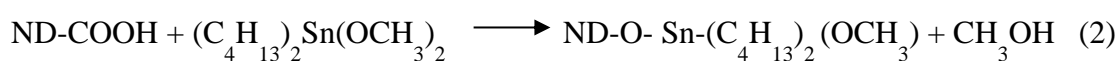
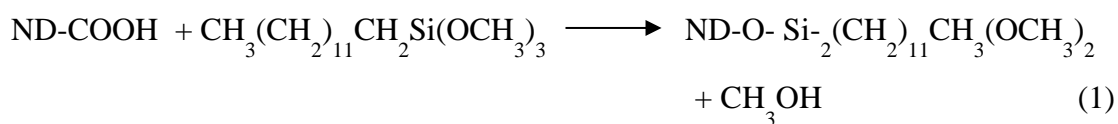
solvents is put in Figure 2(d-(i)) The XRD pattern of the amide-derivatized residue after evaporating the solvent gave characteristic (111) and (220) peaks of diamond (Figure 2(e)).



**Figure 2.** (a) IR spectra of acid treated (bottom) and oleyl amine treated (top) ND. (b) TEM image of the acid functionalized ND (c) amide derivative (d) images of dispersions of (i) as obtained and (ii) amide derivetized ND in organic solvents taken after 4 hrs, (d) XRD pattern of amide derivatized ND.

Functionalization of ND with organosilane and organotin reagents was established through IR spectroscopy. In Figure 3(a) we show the IR spectra of organosilane and organotin coated NDs. HDTMS-coated ND shows a band at  $1100\text{ cm}^{-1}$  due to the Si-O stretching along with bands due to the alkyl groups around  $2850\text{ cm}^{-1}$  and  $2950\text{ cm}^{-1}$ .<sup>27</sup> DBDMT-coated ND shows characteristic Sn-O stretching band at  $500\text{-}600\text{ cm}^{-1}$  along with C-H stretching bands for the alkyl groups.<sup>28</sup> The product of the reaction between acid-treated ND with PFOTES shows strong C-F stretching bands in the region  $1130\text{ - }1230\text{ cm}^{-1}$  in the IR spectrum.

The likely reaction between acid-treated ND and organosilane and organotin reagents is as follows:



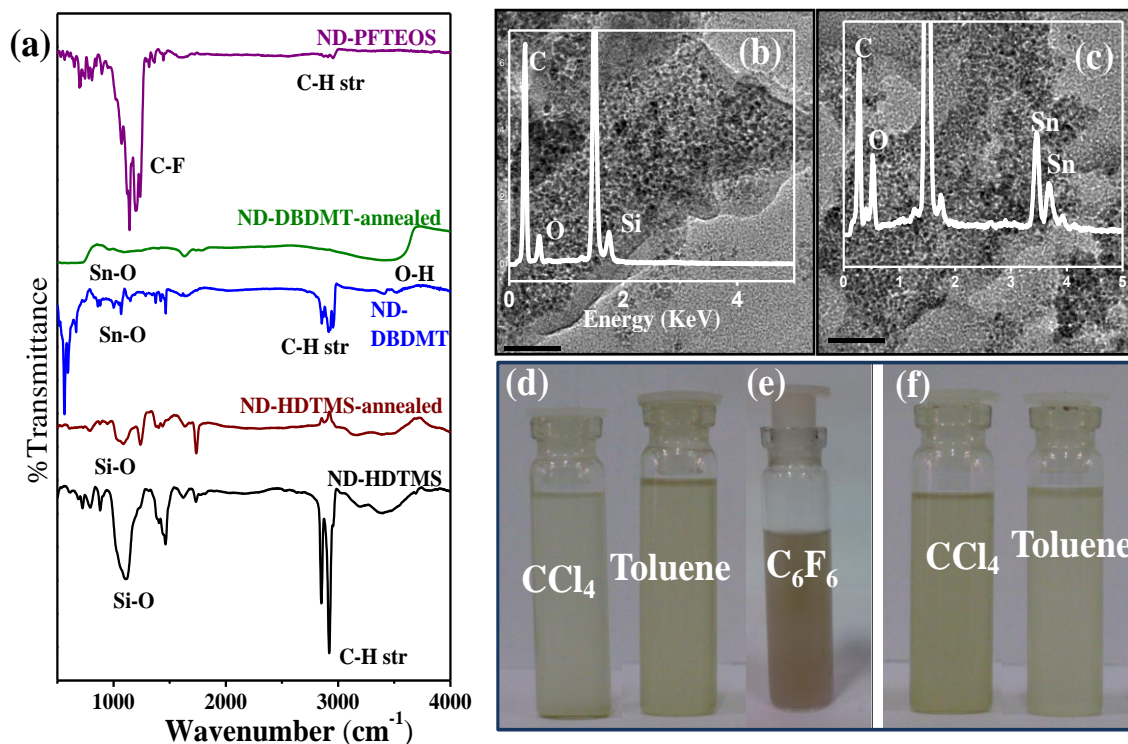


**Figure 3.** (a) IR spectra of organosilane, organotin and perfluorosilane treated ND and the annealed samples, TEM image of (b) HDTMS coated and (c) DBDMT coated ND with EDAX spectra in the inset. Photographs of the dispersions of the (d) HDTMS, (e) PFOTES and (f) DBDMT-coated ND in different solvents (marked along with the photograph).

TEM images of HDTMS-coated and DBDMT-coated ND are shown along with the EDAX spectra in Figure 3(b) and (c) respectively. From the TEM images it can be seen that the ND is coated with the organosilane or organotin reagent. The presence of the organosilane and organotin coating is confirmed by EDAX analysis. Thus the EDAX spectrum of HDTMS-coated ND (inset in Figure 3(b)) shows the presence of silicon and that of the DBDMT-coated ND (inset Figure 3(c)) shows the presence of tin. In Figure 3(d-f) we show the photographs of the dispersions of the HDTMS, PFOTES and DBDMT-coated ND respectively. The photographs were taken 4h after preparation of dispersions. Interestingly, we could obtain stable dispersions of ND in the highly polar solvent perfluorohexane by using PFOTES. It appears that functionalization of ND with

the long-chain oleyl amine or treatment with HDTMS and DBDMT and PFOTES renders the surface hydrophobic which in turn induces the dispersion in non-polar solvents. The XRD patterns of HDTMS and DBDMT-coated ND obtained after solvent evaporation were similar to that of diamond with characteristic peaks of (111) and (220) planes.

Functionalized ND	Solvent	Dispersibility
ND-CONH <sub>2</sub>	CCl <sub>4</sub>	1 mg / 6 ml
	Toluene	1mg / 8 ml
ND-HDTMS	CCl <sub>4</sub>	1 mg / 4 ml
	Toluene	1 mg / 5 ml
ND-PFOTES	Perflurohexane	1 mg / 6 ml
ND-DBDMT	CCl <sub>4</sub>	1 mg / 5ml
	Toluene	1mg / 6 ml

**Table 1.** Dispersibility of functionalized ND in various organic solvents.

In Table 1 listed the dispersibility (in g/mL) of ND functionalized with various reagents in toluene and CCl<sub>4</sub>. The dispersions were checked for minimum of 6 hrs. It is clear that in general CCl<sub>4</sub> is a better solvent for dispersions. Dispersibility of perflurosilane treated sample in perfluro solvents is also quite good. It appears that silane treated ND with CCl<sub>4</sub> is the best combination.

On heating the silane-coated ND in nitrogen atmosphere at 400 °C for 1h, silica-coated ND was obtained. The presence of silica coating was confirmed by EDAX (Figure 4(a)) spectrum which showed the presence of silicon. The IR spectrum (Figure 3(a)) also shows that the Si-O stretching band at 1100 cm<sup>-1</sup> is retained while the bands due to the alkyl groups have disappeared. The silica coating is, however, X-ray amorphous. Heating the organotin-coated ND produces SnO<sub>2</sub> - coated ND. This is confirmed by the EDAX spectrum (Figure 4(b)) which showed the presence of tin and the IR spectrum shown in Figure 3(a) which shows that the band due to Sn-O stretching around 500-600cm<sup>-1</sup> is retained. The XRD pattern (Figure 4(c)) of SnO<sub>2</sub>-coated ND showed peaks characteristic of tetragonal SnO<sub>2</sub> which crystallizes in the space group *P4<sub>2</sub>/mnm* with lattice parameters (a = 4.71 Å, c = 3.17 Å, JCPDS card no: 01-0657).

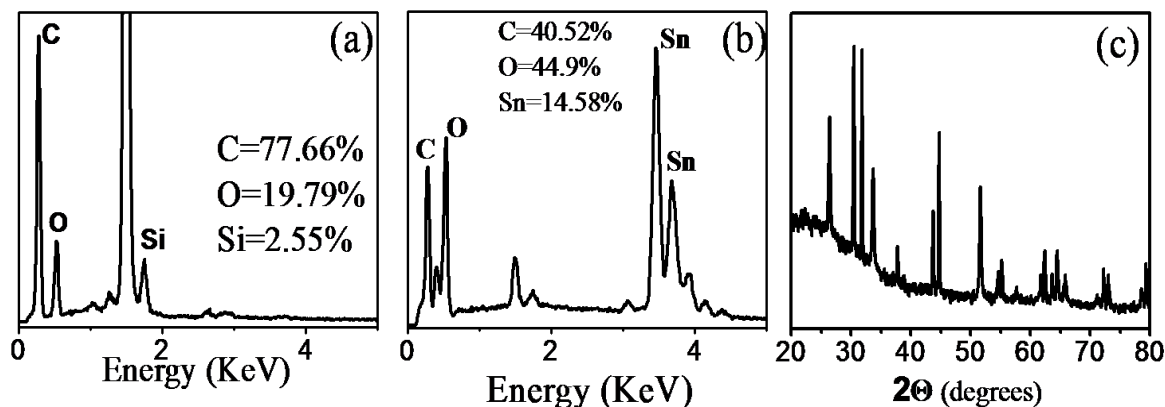


**Figure 4** EDAX spectrum of (a) ND\_HDTMS and (b) ND-DBDMT after annealing in  $N_2$ , (c) XRD pattern ND-DBDMT after annealing in  $N_2$ .

ND treated with acids readily disperse in water. However the dispersions are not very stable for long periods. In order to obtain stable dispersion of ND in water, noncovalent functionalization using various surfactants have been carried out. We have used several surfactants. Figure 5(a–e) show photographs of surfactant-induced dispersions of acid treated ND in water taken 24 h after preparation.

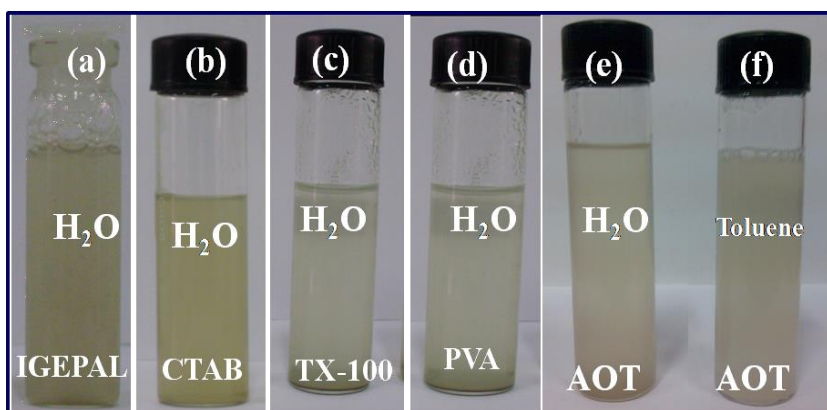


**Figure 5.** Photographs of dispersions of ND induced by (a) IGEPAL, (b) CTAB, (c) TX-100, (d) PVA and (e) AOT in water and (f) AOT in toluene.

The surfactants which hold the NDs in water for long periods are sodium bis(2-ethylhexyl) sulphosuccinate (AOT), Triton X-100 (TX-100), polyvinyl alcohol (PVA), cetyltrimethylammonium bromide (CTAB) and tert-octylphenoxy poly (oxyethylene)

ethanol (IGEPAL). Interestingly AOT can produce stable dispersions in water as well as toluene which is shown in Figure 5 (e, f). All these dispersions were stable for a week. All the surfactants invariably required a concentration of 20 mM of the surfactants to produce stable dispersion. In case of IGEPAL stable dispersions in water were obtained at a much less concentration of about 1 mM. The dispersion was stable for longer durations compared to other surfactants (Table 2).

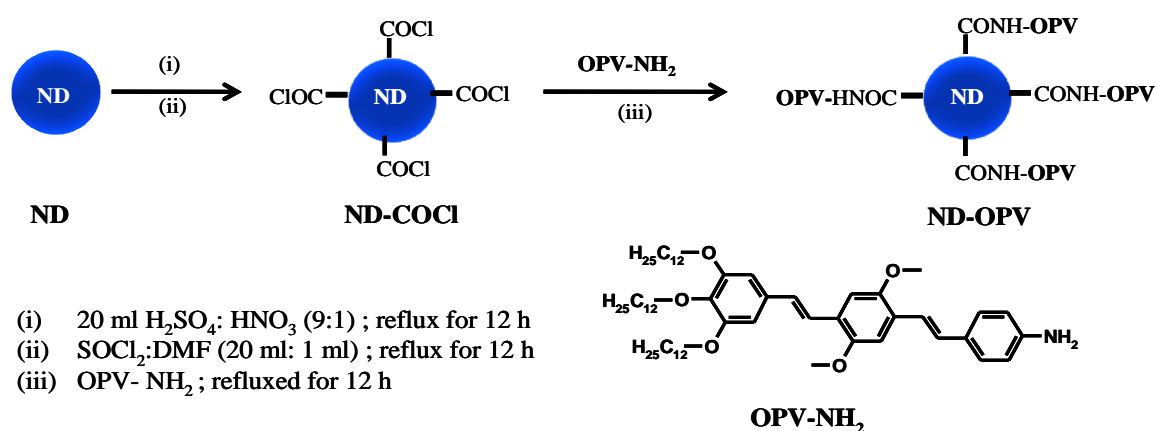
**Table 2.** Dispersibility of 5 mg ND non-covalently functionalized with various surfactants and polymers in water as well as toluene. Concentration of surfactant required for stable dispersion is also noted down.

Surfactant	Solvent	Concentration of surfactant
IGEPAL	Water	1 mM
CTAB	Water	20 mM
TX-100	Water	20 mM
PVA	Water	20 mM
AOT	Water	20 mM
	Toluene	20 mM



**B. Covalent conjugate of ND with OPV**

In our effort to design chromophore-appended nanodiamond we have carried out the synthesis of luminescent chromophore-functionalized nanodiamond by covalent attachment with  $\pi$ -conjugated oligomers and investigated the optical properties of the resulting hybrid material. OPV amine with absorption in the blue region of the spectrum was chosen as the  $\pi$ -conjugated oligomers. The amine group of OPV amine can be used to form covalent bond with acyl chloride functionalized ND. ND-OPV conjugate was thus synthesized via amide linkage as shown in Scheme 4.



**Scheme 4.** Synthetic route for the preparation of ND-OPV conjugate

ND powder was first acid functionalized and was then refluxed with  $\text{SOCl}_2$  for 12 h in a nitrogen atmosphere. The infrared spectrum of the acid treated ND shows  $\nu_{\text{C=O}}$  at  $\sim 1710 \text{ cm}^{-1}$  which shifts to higher frequency ( $\sim 1725 \text{ cm}^{-1}$ ) in the acyl chloride (ND-COCl). The acyl chloride was reacted with the amine-functionalized OPV (OPV- $\text{NH}_2$ )<sup>46</sup> under inert conditions to obtain the corresponding amide ND-OPV hybrid. In the amide derivative,  $\nu_{\text{C=O}}$  appears at a lower frequency ( $\sim 1640 \text{ cm}^{-1}$ , amide I) along with the appearance of amide II band at  $\sim 1560 \text{ cm}^{-1}$  (Figure 6(a)). Strong C-H stretching band in the range  $2850\text{--}2980 \text{ cm}^{-1}$  also appears in the amide derivative. ND-OPV so obtained was purified by washing with ethanol several times followed by centrifugation so as to ensure complete removal of any physically absorbed OPV- $\text{NH}_2$ . We have also synthesized the octyl amine functionalized nano diamond (ND-OA)<sup>29</sup> and the OPV-acetyl amide (OPV-B)<sup>46</sup>

following literature procedures in order to compare the optical characteristics. ND-OA has been chosen as a blank for later measurements since attachment of octyl group makes ND soluble in THF without conferring any optical properties.

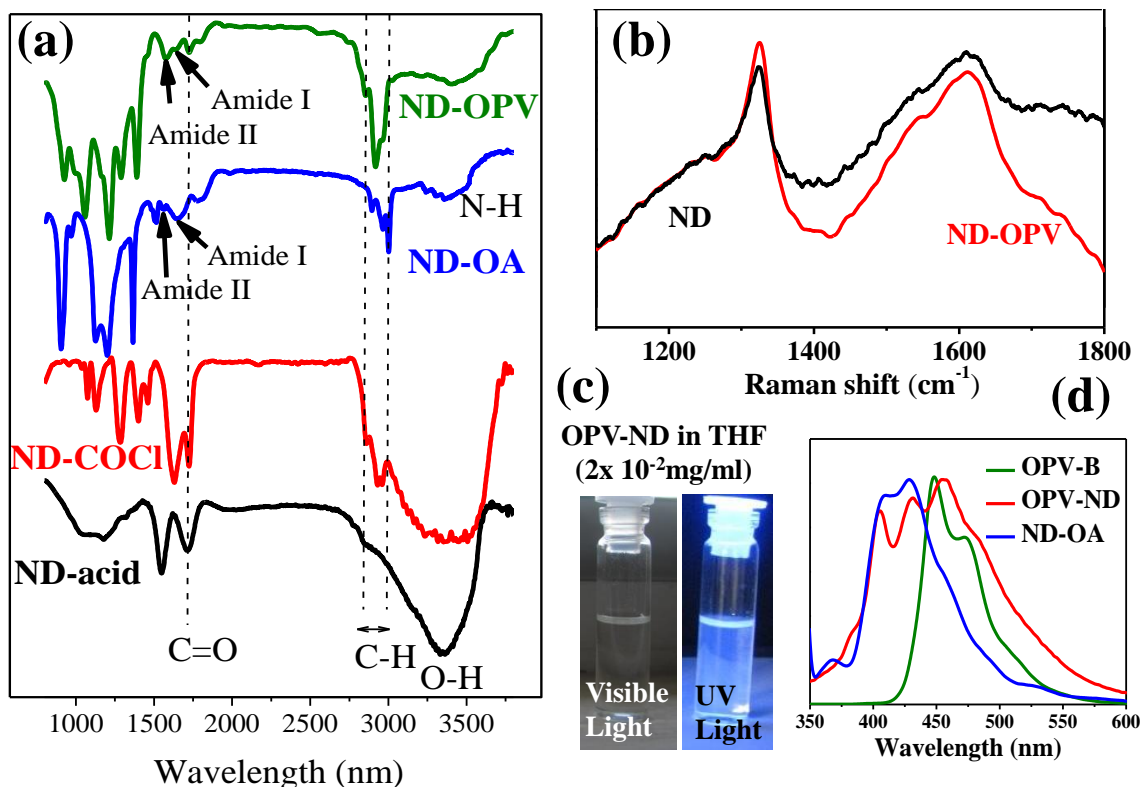


**Figure 6.** (a) IR spectra of various ND derivatives, (b) Raman spectra of ND and ND-OPV, (c) Photographs of the dispersion of ND-OPV in THF ( $c = 2 \times 10^{-2}$  mg/ml) and upon exposure to UV illumination. (d) Normalized emission spectra of ND-OPV ( $2 \times 10^{-3}$  mg/ml), ND-OA and OPV-B in THF,  $\lambda_{exc} = 331$  nm.

Raman spectrum of as obtained ND and OPV functionalized ND obtained using 514 nm laser are given in Figure 6 (b). The Raman spectrum of nanodiamond shows broad band and an asymmetric G band. D band  $\sim 1326$  cm<sup>-1</sup> is characteristic of sp<sup>3</sup> hybridized C originates from diamond core as well as the graphitic shell. The D band in ND is expected to be broad and slightly red shifted as compared to D band of bulk diamond due to quantum confinement effects.<sup>47</sup> Other than the prominent D band, broad Raman band composed of bands around 1400 cm<sup>-1</sup> (disordered and amorphous sp<sup>2</sup> carbon), 1600 cm<sup>-1</sup> (G band), 1640 cm<sup>-1</sup> (O-H bending) and 1740 cm<sup>-1</sup> (C=O stretching), respectively.<sup>47</sup> The

intensity ratio of D band to G band increases on OPV functionalization indicating functionalization of the  $sp^3$  C on the surface graphitic layer. Interestingly, the disorder induced band ( $sp^2$  C) at  $1400\text{ cm}^{-1}$  and the band at  $1640\text{ cm}^{-1}$  due to O-H bending vibrations decreases in intensity indicating loss of some O-H functional groups. The hydrophobic  $\pi$ -conjugated system and the long alkyl chains in ND-OPV hybrid favour its solubility in organic solvents. Thus, up to  $2\text{ mg/mL}$  of ND-OPV could be dispersed in THF by sonicating the samples to form a stable suspension. The photographs in Figure 6(c) shows the stability of suspensions of ND-OPV in THF, the photographs being taken after the dispersion was left undisturbed for 6 h. THF was used as solvent in all the optical studies henceforth as stable dispersions of both ND-OA and ND-OPV could be obtained in THF. ND-OA and OPV-B show fluorescence bands in the blue ( $350\text{ nm}$ - $450\text{ nm}$ ) and green regions ( $450\text{ nm}$  -  $550\text{ nm}$ ) on illuminating with  $\lambda_{\text{exc}} = 331\text{ nm}$ , respectively. On the other hand, ND-OPV in THF ( $2 \times 10^{-3}\text{ mg/mL}$ ,) shows a broad emission with three maxima at  $405\text{ nm}$ ,  $430\text{ nm}$ ,  $455\text{ nm}$  and a shoulder at  $480\text{ nm}$  (Figure 6(d)), a combination of the characteristic bands of OPV and ND confirming the functionalization of ND.

Figure 7 (a) shows TEM image of acid treated ND with particle size of  $\sim 5\text{ nm}$ . ND is known to exist as small clusters containing 10-50 ND particles each  $5\text{ nm}$  in diameter. This clustering happens during the detonation synthesis and the process of purification thereof whereby the core ND or the cluster bears a thin sheet of high functionalized graphitic carbon. It is known that on functionalization it is this entire cluster that gets functionalized and not the individual nanoparticles. TEM image of ND-OPV in Figure 7 (b) shows such an agglomerate of ND particles with a thin film on the surface. When ND-OPV hybrids are visualized under confocal fluorescence microscope, highly green fluorescent agglomerates of particles could be observed, while the rest of the solution does not fluoresce. Figure 7(c) shows the green fluorescence of the agglomerate. In Figure 7(d) we have shown the corresponding bright-field image of the agglomerate. The observation of fluorescent nanoparticles further confirms the chromophore-functionalization of ND surfaces and shows that the origin of fluorescence is the ND-OPV conjugate. With increasing ND-OPV concentration we observe appearance of predominant green fluorescence, corresponding to the OPV emission. Whereas, in dilute

solutions only blue fluorescence of ND is observed (Figure 6(c)), suggesting the presence of additional photo-physical processes at higher concentrations (vide infra).

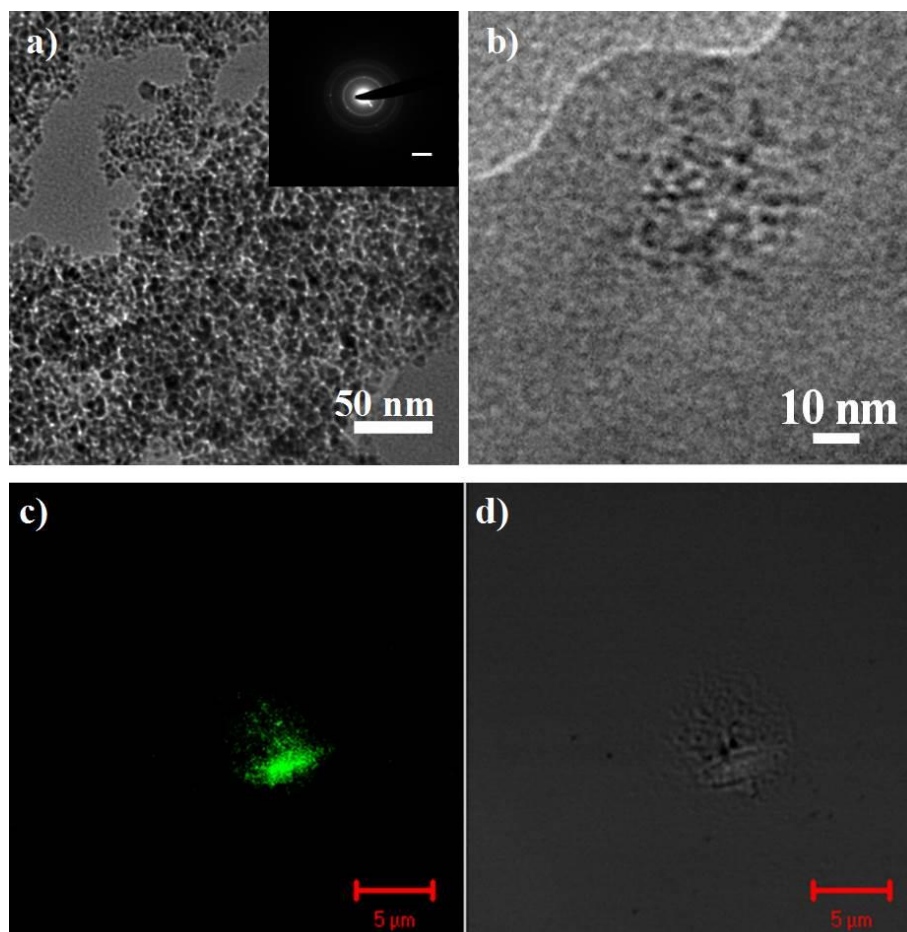


**Figure 7.** TEM images of (a) ND-acid (inset diffraction scale = 10 μm) and (b) ND-OPV agglomerates. (c) Fluorescence and (d) bright-field images of ND-OPV agglomerates.

In order to get an insight into enhancement of green fluorescence of the ND-OPV hybrid particles at higher concentrations, we have carried out concentration dependent fluorescence measurements ( $\lambda_{\text{exc}} = 331 \text{ nm}$ ). Figure 8(a) shows the emission spectra of ND-OPV at different concentrations in THF, normalized at the nanodiamond emission ( $\lambda_{\text{norm}} = 410 \text{ nm}$ ).

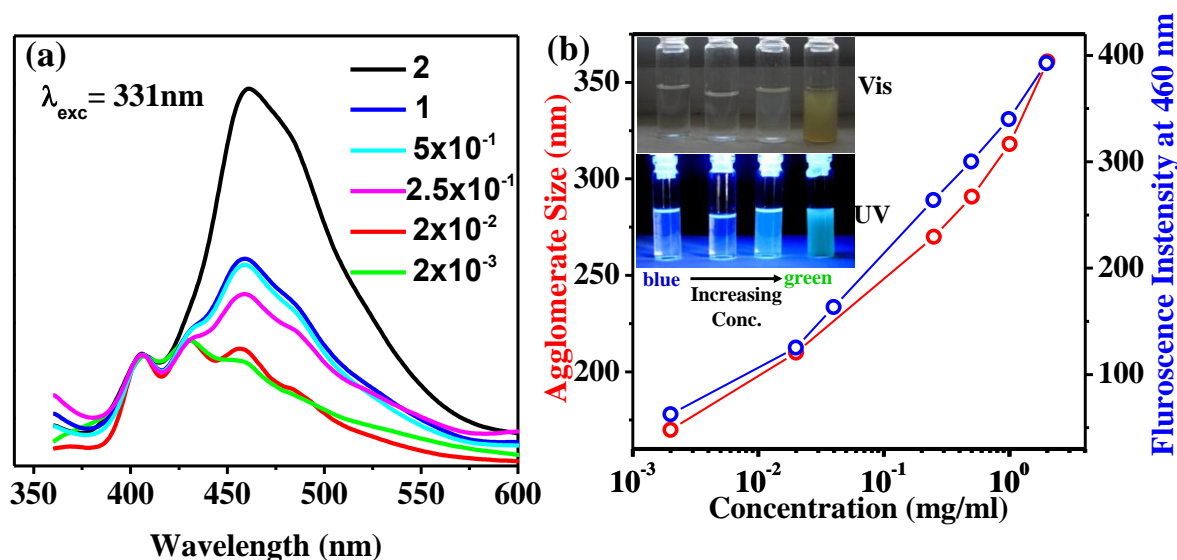
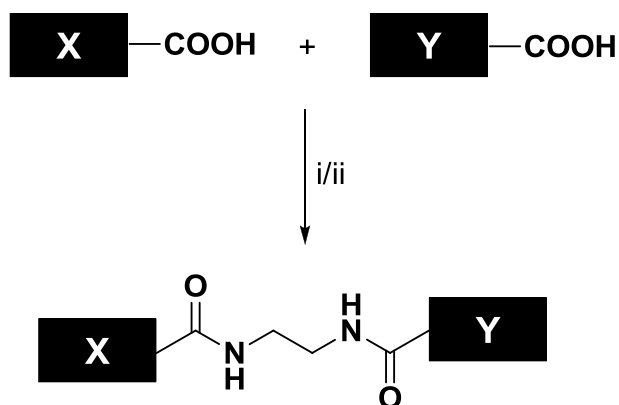


**Figure 8.** (a) Fluorescence spectra ( $\lambda_{\text{exc}} = 331 \text{ nm}$ ) of ND-OPV hybrids in THF at different concentrations. (b) Dependence of agglomerate size on concentration of ND-OPV in THF. (Inset) Photograph of the solutions of ND-OPV (top) at increasing concentrations ( $2 \times 10^{-3} \text{ mg/mL}$  to  $2 \text{ mg/mL}$ ) and the corresponding images upon exposure to UV light (bottom).

As the concentration increases, the emission spectrum of the ND-OPV conjugate showed an enhancement in green fluorescence (480 nm, OPV origin) with concomitant quenching of the blue fluorescence (400-450 nm, ND origin). The photograph in the inset of Figure 8 (b) shows the fluorescence changes of the hybrids from blue to green. This observation suggested the occurrence of a concentration dependent photo-physical phenomenon with the OPV emission intensity showing proportionality to the concentration. This observation is consistent with the aggregation phenomenon. From dynamic light scattering studies of different concentrations of the conjugate we obtained the agglomerate size versus concentration plot with agglomerate size showing an approximately logarithmic dependence on concentration. Figure 8 (b) also shows that the intensity of fluorescence at 460 nm varies approximately logarithmically with concentration, a trend similar to that of agglomerate size. We were thus able to obtain a tune ability of fluorescence from blue to green by simply varying the concentration of the ND-OPV conjugate in the solution.

### C. Covalently linked binary conjugates of ND with graphene and carbon nanotubes

The various nanocarbon conjugates of ND, SWNT and G were prepared are shown in Scheme 5.



**Scheme 5.:** *Preparation of binary conjugates.* Nanocarbons (X, Y): ND, SWNT, and G containing COOH groups. (i) For homoconjugates: nanocarbon (X = Y), DCC, ED, DMF, 4 h. (ii) For heteroconjugates: nanocarbon (X), mono-Boc-ethylenediamine, DCC, DMF, 4 h followed by TFA-DCM (1:1), 1 h. and nanocarbon (Y, Y ≠ X), DCC, DMF, 4 h.

A simple diamine linker 1,2-ethylenediamine was used to selectively conjugate two same or different forms of nanocarbons. Nanocarbons of same type were covalently linked through amide-linkages to obtain symmetrical homo-conjugates in an one step process. A two-step amide-linkage process was followed to obtain hetero-conjugates of nanocarbons with different dimensionality. First one of the carboxylic acid functionalized nanocarbons was modified with mono-protected Boc-1,2-ethylenediamine through an amide linkage using DCC coupling protocol. The free amine generated from the Boc-1,2-ethylenediamine modified nanocarbon upon acid treatment was coupled to another carboxylic acid functionalized nanocarbons.

Figure 9(a) shows the TEM micrographs of ND-ND with G-G conjugates as inset. ND exists in the form of small clusters and these clusters as a result of covalent conjugation crosslink to each other forming larger clusters. Similarly graphene sheets

crosslink to each other mostly through the edges. In case of ND-G, clusters of ND covalently crosslinked to G sheets as shown in Figure 9(b). Inset shows a magnified view of the encircled region. There exist a close crosslinking between graphene sheets and clusters of ND particles. Figure 9(c) and (d) shows the TEM micrographs of G-SWNT and ND-SWNT conjugates respectively.

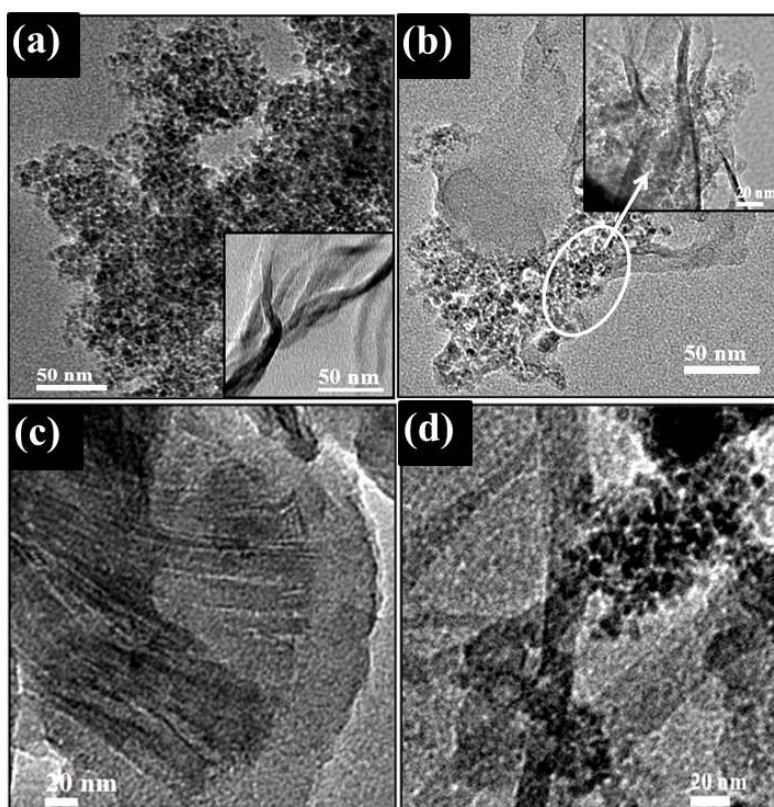


**Figure 9.** TEM images of (a) ND-ND conjugate and a G-G conjugate (in the inset), (b) of a ND-G conjugate (with magnified version in the inset), (c) G-SWNT conjugate and (d) ND-SWNT conjugate.

Close crosslinking of SWNT bundles with G sheets and ND clusters respectively is observed. Such association of two nanocarbons could be observed everywhere and which can only be explained by assuming covalent crosslinking between nanocarbons. IR spectra of the covalently conjugated samples were recorded. All covalently linked samples (Figure 10(a)) show distinct amide I and amide II peaks along with C-N stretching mode. In case of covalent conjugates the C=O peak is known to be shifted to lower frequencies than that of corresponding acids.<sup>48</sup> For acid (-COOH) functionalized

ND  $\nu_{C=O}$  was observed at  $1730\text{ cm}^{-1}$  shifts to  $1715\text{ cm}^{-1}$  in ND-ND which is clear indication of the formation of amide bond. The bond stretching frequencies of  $\nu_{O-H}$  and  $\nu_{N-H}$  can also be seen in the IR spectra. Some  $\nu_{O-H}$  can come from original acid treated samples getting partially functionalized with  $-OH$  functional groups on the surface. Acid treated samples do not show presence of  $\nu_{C-N}$  and amide II ( $\nu_{N-H}$  bending) bands. Other than these, C-H stretching frequencies can be observed in all the samples.

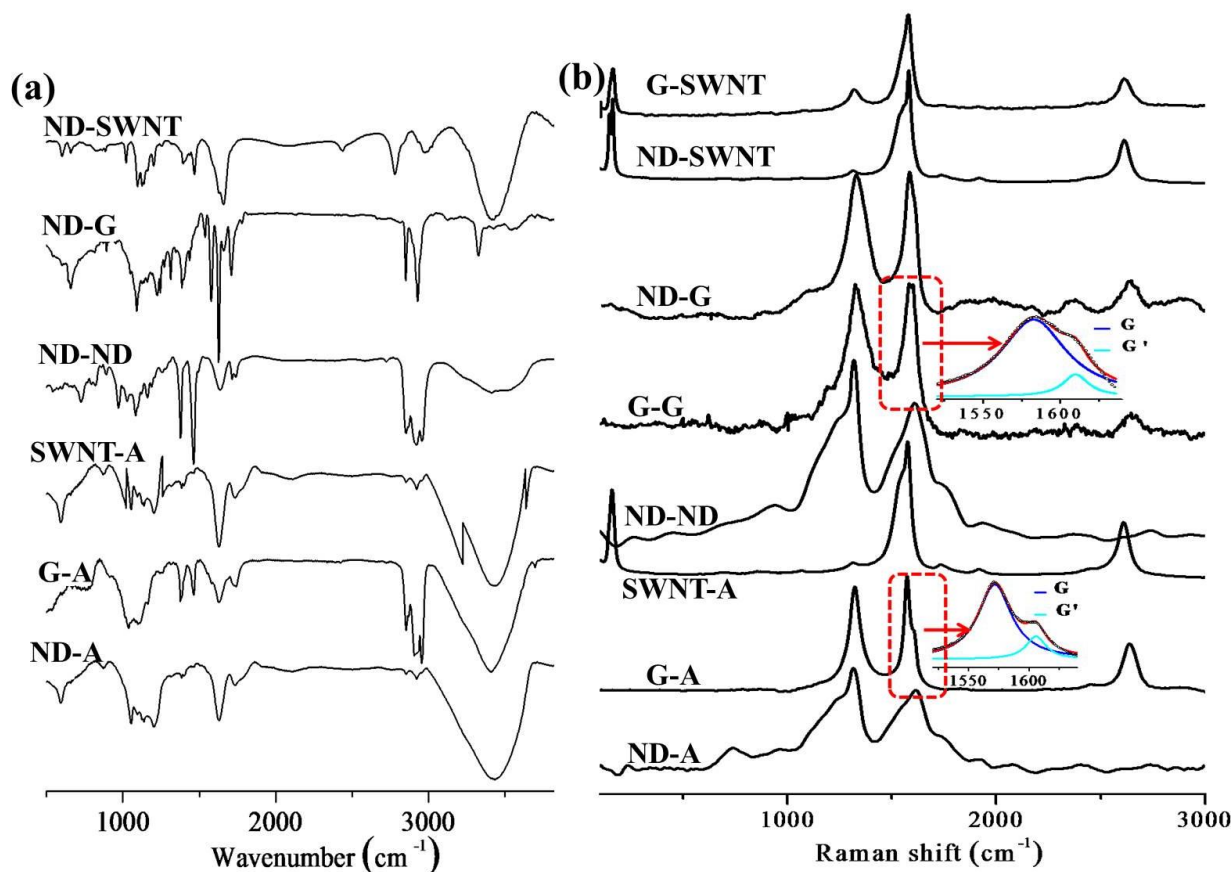


**Figure 10.** (a) IR-spectra and (b) Raman spectra of different covalent nanocarbon conjugates.

Formation of amide linkage between the diamine linker molecule and nanocarbons was further supported by Raman spectroscopic data (Figure 10(b)). Raman spectra show all characteristic G, D and 2D bands observed in case of graphene and SWNT. In case of ND, 2D band was not observed and the D band was slightly higher in intensity than G band, though both were broad. It is well known that the D band, also known as the defect induced band increases in intensity with introduction of defects in the graphene lattice.



Keeping this in mind we compared the  $I_D/I_G$  ratios of all the samples. It is seen that on conjugation the  $I_D/I_G$  ratio increases (Figure 11(a)).

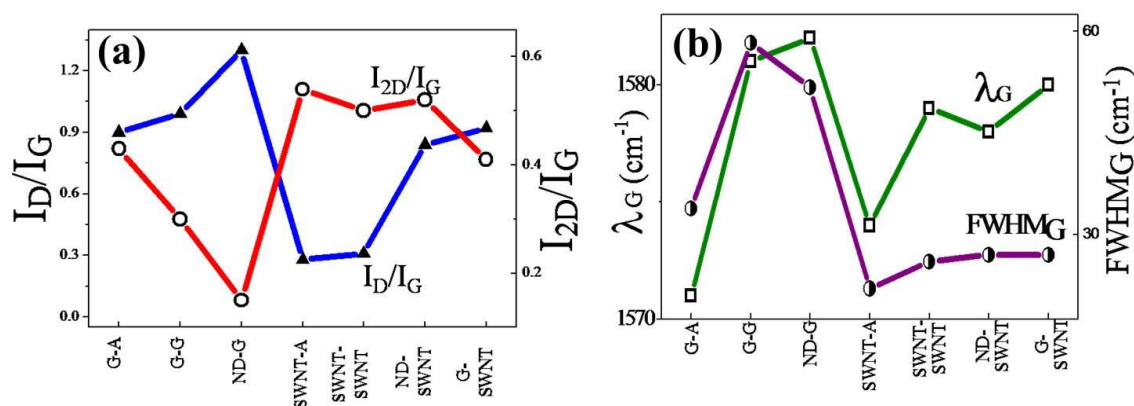


**Figure 11.** Variation of (a) intensity ratios of D and 2D band with respect to G band and (b) the peak position and width of G band for different binary conjugates.

In case of G-G the  $I_D/I_G$  increases to 0.99 from 0.9 observed for acid treated graphene, while for SWNT-SWNT the ratio increases to 0.31 from 0.28 observed for acid treated SWNTs. Similarly all the covalently linked samples show higher  $I_D/I_G$  ratios than that of corresponding acid treated samples. This indicates an increase in the defects in the graphene lattice. Introduction of defects can be because of introduction of functional groups on the surface. Again we see that  $I_{2D}/I_G$  ratio decreases on coupling. It is documented in the literature that with charge transfer or by doping  $I_{2D}/I_G$  decreases.<sup>49,50</sup> Similar charge transfer can occur due to amide linkage and thereby decreasing  $I_{2D}/I_G$  ratio. This is a clear proof for the covalent crosslinking of nanocarbons through amide linkages. The G band in Raman spectrum of graphene can further be resolved into two bands G and G'. On fitting the spectra with two Lorentzians as shown in Figure 10(b) (insets) it is clear that both G and G' bands shift considerably on coupling via amide linkage. While G band shifts by almost 3 nm, G' band shifts by 2 nm. 2D band also shifts considerably ( $2 \text{ cm}^{-1}$ ) on conjugation. Similar shift is noticed in all the samples after covalent conjugation (Figure 11(b)). There is also a considerable increase in the peak width of G band after covalent conjugation, however for G' band the increase in width is

minimal. Taken together data discussed above supports the covalent conjugation of nanocarbons via amide linkages.

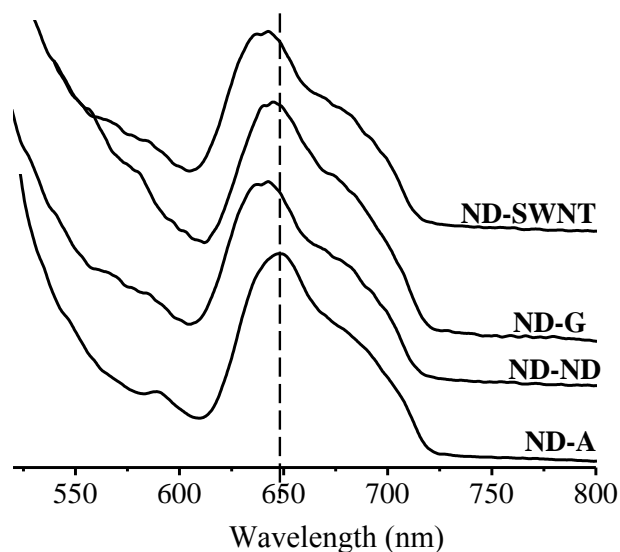


**Figure 12.** Photoluminescence spectra of ND conjugates

ND is known to show photoluminescence with broad band at ~ 650 nm. All ND containing samples were characterized using photoluminescence spectroscopy. The samples for the photoluminescence spectroscopic measurements were prepared by dispersing the conjugates in dimethyl formamide (DMF). The dispersions were sonicated for 15 min. UV excitation of 488 nm was used for recording photoluminescence spectra. All samples containing ND as one of the constituent unit show characteristic photoluminescence spectra of ND (Figure 12). Photoluminescence bands red-shift on conjugation through amide linkage. Proximity effect could be a probable reason for this red-shift of the PL band.

Interestingly all the covalently crosslinked binary conjugates of nanocarbons form stable homogenous dispersions in dimethyl formamide. In Figure. 13. we show the photographs of dispersion of acid treated nanocarbons and their conjugates in DMF. Acid treated nanocarbons do not disperse well in DMF while all the dispersions of the conjugates are stable upto 6 h at a concentration of 1mg/3mL. This better dispersibility of the conjugates can be due to presence of unused amine groups left on the surface of nanocarbons. The dispersions of nanocarbon conjugates can be used for the preparation

of polymer-nanofiller composites by using polymers that dissolve in DMF. Thus, we were able to prepare homogenous films of polyethylene oxide (PEO, molecular weight 20,000 g) containing binary nanocarbon composite fillers. Mechanical properties of homo- and hetero-binary conjugates of carbon nanostructures and their polymer composites can be studied to explore the applications related to high performance materials.

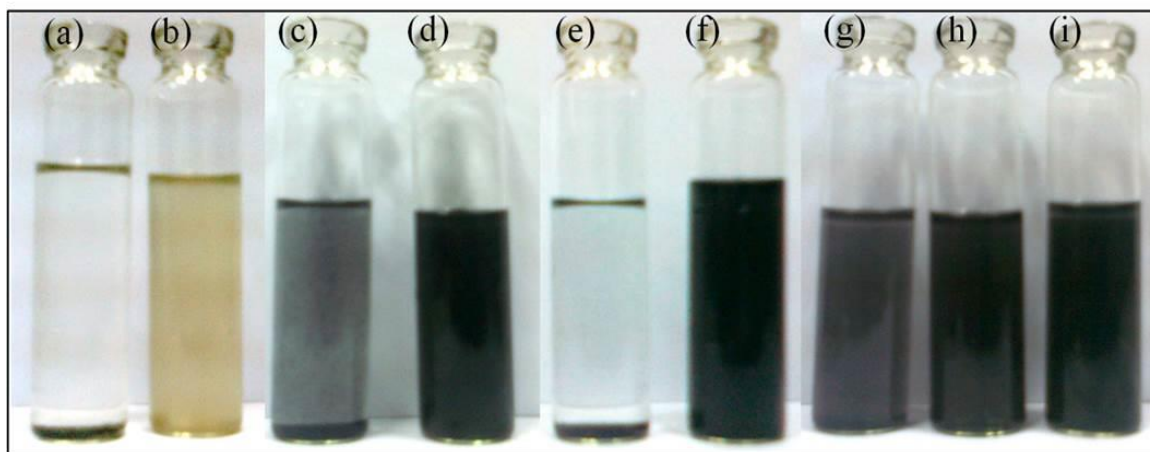


**Figure 13.** Photographs of dispersions of (a) ND-COOH, (b) ND-ND, (c) G-COOH, (d) G-G, (e) SWNT-COOH, (f) SWNT-SWNT, (g) ND-SWNT, (h) ND-G and (i) G-SWNT in DMF.

## **5. Conclusions**

Nanodiamond can be functionalized both by covalent and noncovalent means just as in the case of single walled carbon nanotubes or grapheme. The covalently functionalized ND bearing long chain alkane groups can easily be solubilized in nonpolar solvents like  $\text{CCl}_4$  and toluene. Surfactant wrapped ND forms good dispersions in water. Dispersions of ND would be of great use in the preparation of ND polymer composite films. Functionalized ND can be linked to other inorganic materials with different structures to prepare nanocomposites.

We have also carried out a simple covalent attachment of nanodiamonds with fluorescent  $\pi$ -conjugated systems to construct chromophore functionalized nanodiamond hybrids. Chromophore functionalization not only enhanced the solubility of the ND in

organic solvents but also resulted in tunable fluorescence. Fluorescence and light scattering studies of **ND-OPV** conjugates suggest a concentration dependent aggregation phenomenon. The fluorescence intensity of green emission varies similar to that of agglomerate size. This strategy can be extended to design various chromophore-functionalized fluorescent nanodiamond hybrids by an appropriate choice of the chromophore of possible use in optoelectronics and imaging.

Covalent linking strategy has also been used to prepare covalent homo- and hetero-binary conjugates of nanodiamond, SWNT and graphene, by using a diamine as the crosslinking agent. This procedure is convenient and effective for conjugation of two nanocarbon moieties through amide linkages. The binary conjugates of nanocarbons form stable dispersions in dimethyl formamide. These dispersions of nanocarbon binary conjugates can be used to prepare composites with polymers. The homo- and hetero-binary conjugates of carbon nanostructures and their polymer composites may find applications related to high performance materials.

## References

1. G. E. Harlow and R. M. Davies. *Elements*, 1, 67.
2. M. Dekker and M. P. D. M. Evelyn *Handbook of Industrial Diamonds and Diamond Films Marcel Dekker*: New York, **1998**.
3. A. I. Lymkin, E. A. Petrov, A. P. Ershov, G. V. Sakovitch, A. M. Staver and V. M. Titov. *Dokl. Akad. Nauk USSR* **1988**, 302, 611.
4. R. Greinern, D. S. Phillips, J. D. Johnson and F. Volk. *Nature* **1988**, 333, 440.
5. T. Soga, Y. Hayashi, T. Sharda, A. A. Balandin and K. L. Wang *Handbook of Semiconductor Nanostructures and Nanodevices, Vol. 2*, ; *American Scientific*,: Stevenson Ranch, USA, **2006**.
6. N. Ali, E. Titus, J. Gracio, W. Ahmed and E. Ahmed. *Recent Res. Dev. Mater. Sci.* **2004**, 5, 55.
7. O. A. Williams and M. Nesládek. *Phys. Status Solidi A* **2006**, 203, 3375.
8. D. M. G. E. O. A. Shenderova *Ultrananocrystalline Diamond*, ; *William Andrew Publishing*,: Norwich, N. Y., , **2006**.
9. K. B. Holt. *Philos. Trans. R. Soc. London, Ser. A*, **2007**,, 365, 2845.
10. V. V. Volkov and V. I. E. Danilenko. *Fiz. Goreniya Vzryva* **1990**, 26, 123.
11. B. Marina and V. Alexander. *J. Phys. D Appl. Phys.* **2007**, 40, 6300.
12. O. A. Shenderova, V. V. Zhirnov and D. W. Brenner. *Crit. Rev. Solid State Mater. Sc.* **2002**, 27, 227.
13. W. Yang, O. Auciello, J. E. Butler, W. Cai, J. A. Carlisle, J. E. Gerbi, D. M. Gruen, T. Knickerbocker, T. L. Lasseter, J. N. J. Russel, L. M. Smith and R. Hamers. *J. Nat. Mater.* **2002**, 1, 253.
14. J. B. Miller and D. W. Brown. *Langmuir* **1996**, 12, 5809.
15. J. E. Dahl, S. G. Liu and R. M. K. Carlson. *Science* **2003**, 299, 96.
16. V. S. Smentkowski and J. T. Yates. *Science* **1996**, 271, 193.
17. C. S. Kim, R. C. Mowrey, J. E. Butler and J. N. Russell. *J. Phys. Chem. B* **1998**, 102, 9290.
18. Y. Liu, Z. Gu, J. L. Margrave and V. N. Khabashesku. *Chem. Mater.* **2004**, 16, 3924.
19. T. Nakamura, M. Ishihara, T. Ohana and Y. Koga. *Chem. Comm.* **2003**, 900.

20. A. M. Schrand, H. Huang, C. Carlson, J. J. Schlager, E. Ōsawa, S. M. Hussain and L. Dai. *J. Phys. Chem. B* **2006**, 111, 2.
21. C. N. R. Rao and A. Govindaraj *Nanotubes and Nanowires*; *RSC Series on Nanoscience, Royal Society of Chemistry*, : London, **2006**. .
22. K. S. Subrahmanyam, S. R. C. Vivekchand, A. Govindaraj and C. N. R. Rao. *J. Mater. Chem.* **2008**, 18, 1517.
23. A. Gomathi, S. J. Hoseini and C. N. R. Rao. *J. Mater. Chem.* **2009**, 19, 988.
24. S. Ghosh, A. Gomathi and C. N. R. Rao. *J. Nanosci. Nanotech.* **2009**, 9, 5214.
25. C.-C. Fu, H.-Y. Lee, K. Chen, T.-S. Lim, H.-Y. Wu, P.-K. Lin, P.-K. Wei, P.-H. Tsao, H.-C. Chang and W. Fann. *Proc. Natl Acad. Sc.* **2007**, 104, 727.
26. S.-J. Yu, M.-W. Kang, H.-C. Chang, K.-M. Chen and Y.-C. Yu. *J. Am. Chem. Soc.* **2005**, 127, 17604.
27. A. Gruber, A. Dräbenstedt, C. Tietz, L. Fleury, J. Wrachtrup and C. v. Borczyskowski. *Science* **1997**, 276, 2012.
28. V. N. Mochalin and Y. Gogotsi. *J. Am. Chem. Soc.* **2009**, 131, 4594.
29. K. S. Subrahmanyam, P. Kumar, A. Nag and C. N. R. Rao. *Solid State Commun.* **2010**, 150, 1774.
30. E. Fron, L. Puhl, I. Oesterling, C. Li, K. Müllen, F. C. De Schryver, J. Hofkens and T. Vosch. *ChemPhysChem* **2011**, 12, 595.
31. T. Takimoto, T. Chano, S. Shimizu, H. Okabe, M. Ito, M. Morita, T. Kimura, T. Inubushi and N. Komatsu. *Chem. Mater.* **2010**, 22, 3462.
32. K. G. Thomas and P. V. Kamat. *Acc. Chem. Res.* **2003**, 36, 888.
33. N. Mohan, Y.-K. Tzeng, L. Yang, Y.-Y. Chen, Y. Y. Hui, C.-Y. Fang and H.-C. Chang. *Adv. Mater.* **2010**, 22, 843.
34. R. Voggu, K. V. Rao, S. J. George and C. N. R. Rao. *J. Am. Chem. Soc.* **2010**, 132, 5560.
35. A. Ghosh, K. V. Rao, S. J. George and C. N. R. Rao. *Chem. Eur. J.* **2010**, 16, 2700.
36. W. Zhu, G. P. Kochanski and S. Jin. *Science* **1998**, 282, 1471.
37. C. N. R. Rao and A. Govindaraj *Nanotubes and Nanowires*; *Royal Society of Chemistry*: Cambridge, U.K., **2005**.

38. R. Saito, G. Dresselhaus and M. S. Dresselhaus *Physical Properties of Carbon Nanotubes; Imperial College Press: London, U.K., 1998.*
39. H. Dai. *Acc. Chem. Res.* **2002**, 35, 1035.
40. C. N. R. Rao, A. K. Sood, K. S. Subrahmanyam and A. Govindaraj. *Angew. Chemie Int. Ed.* **2009**, 48, 7752.
41. V. Guglielmotti, S. Chieppa, S. Orlanducci, E. Tamburri, F. Toschi, M. L. Terranova and M. Rossi. *Appl. Phys. Lett.* **2009**, 95.
42. P. W. Chiu, G. S. Duesberg, U. Dettlaff-Weglikowska and S. Roth. *Appl. Phys. Lett.* **2002**, 80, 3811.
43. F. Frehill, J. G. Vos, S. Benrezzak, A. A. Koós, Z. Kónya, M. G. Rüther, W. J. Blau, A. Fonseca, J. B. Nagy, L. P. Biró, A. I. Minett and M. in het Panhuis. *J. Am. Chem. Soc.* **2002**, 124, 13694.
44. M. Holzinger, J. Steinmetz, D. Samaille, M. Glerup, M. Paillet, P. Bernier, L. Ley and R. Graupner. *Carbon* **2004**, 42, 941.
45. A. Krueger, J. Stegk, Y. Liang, L. Lu and G. Jarre. *Langmuir* **2008**, 24, 4200.
46. A. Ajayaghosh and V. K. Praveen. *Acc. Chem. Res.* **2007**, 40, 644.
47. V. Mochalin, S. Osswald and Y. Gogotsi. *Chem. Mater.* **2008**, 21, 273.
48. U. D. Weglikowska, J. M. Benoit, P. W. Chiu, R. Graupner, S. Lebedkin and S. Roth. *Curr. Appl. Phys.*, **2002**, 2, 497.
49. C. N. R. Rao, K. Biswas, K. S. Subrahmanyam and A. Govindaraj. *J. Mater. Chem.* **2009**, 19, 2457.
50. D. Jaramillo, N. J. Wheate, S. F. Ralph, W. A. Howard, Y. Tor and J. R. Aldrich-Wright. *Inorg. Chem.* **2006**, 45, 6004.



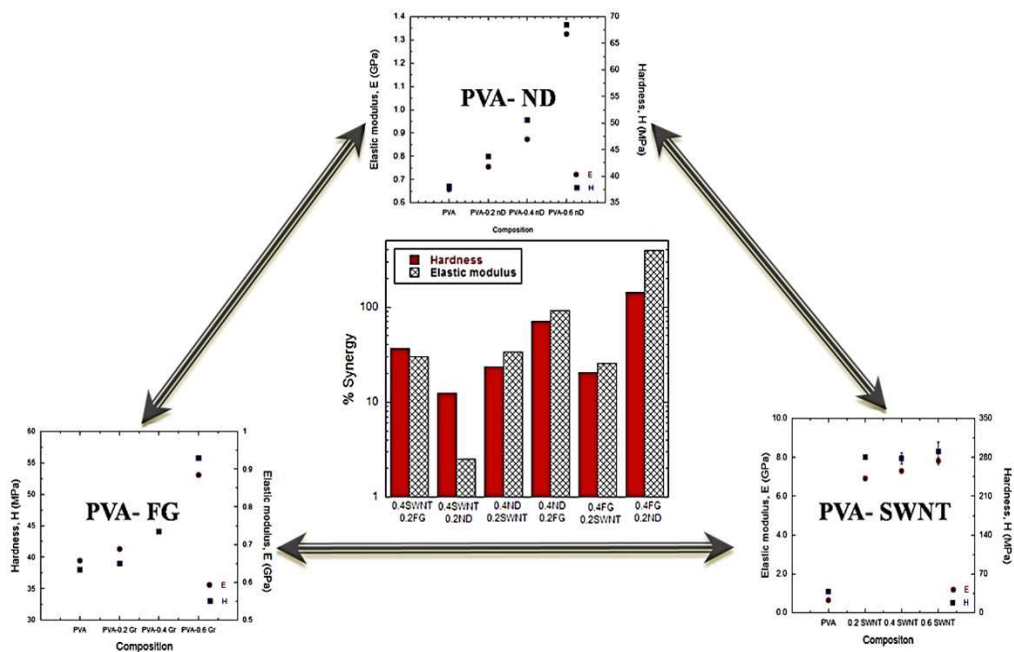


# Chapter II.2

## *Mechanical Properties of Polymer Nanocomposites of Nanodiamond and other Nanocarbons*

### *Summary\**

*Mechanical properties of poly(vinyl alcohol)-matrix (PVA) reinforced with upto 0.6 wt% of ND particles was studied by nano-indentation technique. Even small additions of ND lead to significant enhancement in the hardness and elastic modulus of PVA. Interaction of ND with PVA matrix is probable reason for such enhancements. When binary combinations of ND with few layer graphene, and single-walled nanotubes were reinforced in PVA, the mechanical properties of the resulting composites showed extraordinary synergy, improving the stiffness and hardness by as much as 400% compared to those obtained with single nanocarbon reinforcements. The results suggest a way of designing advanced materials with extraordinary mechanical properties by incorporating small amounts of nanomaterials.*



- \*Papers based on this work have appeared in *Proc. Natal. Acad. Sci., USA, 2011* and *Solid State Commun., 2009*

## **1. Introduction**

On December 15, 2009 world's most fuel efficient aircraft, 'Boeing 787 Dreamliner', went for its first flight. Most of its parts were made up of carbon fibre reinforced polymer matrix composites. Slowly all traditional materials specially metals are giving way to polymer matrix composites as engineer materials. This is because of its high strength to weight ratio and ease of processibility. Use of nanoscale fillers push this strategy to the next level by exploiting the advantages that nanometre-size particulates offer as compared to macro- or microscopic fillers, such as huge surface area per unit mass, ultra-low filler levels required for connectivity through the sample (low percolation threshold), extremely small interparticle separations in a polymer matrix, and often very high length-to-width, or aspect, ratios. Polymer nanocomposites have been known since decades. For example, the clay reinforced resin known as Bakelite was introduced in the early 1900's as one of the first mass-produced polymer-nanoparticle composites.<sup>1</sup> Even before Bakelite, nanocomposites were finding applications in the form of nanoparticle-toughened automobile tires prepared by blending carbon black, zinc oxide, and/or magnesium sulfate particles with vulcanized rubber.<sup>2</sup> However this field remained largely ignored until Toyota researchers revealed that adding mica to nylon produced a five-fold increase in the yield and tensile strength of the material.<sup>3, 4</sup> Last decade has seen an upsurge in this field. In particular, the growing availability of nanoparticles of precise size, varieties of dimensionalities and the development of instrumentation to probe small length scales, such as scanning force, laser scanning fluorescence, and electron microscopes, have spurred research aimed at probing the influence of particle size and shape on the properties of nanoparticle-polymer composites. Research has focused around designing composites that combine the desirable properties of nanoparticles and polymers. The ensuing research revealed a number of key challenges in producing nanocomposites that exhibit a desired behaviour. The greatest stumbling block to the large-scale production and commercialization of nanocomposites is the dearth of cost effective methods for controlling the dispersion of the nanoparticles in polymeric hosts. It is a general tendency of nanoparticles to form aggregates thus negating any benefits associated with the nanoscopic dimension. There is a critical need for establishing processing techniques that are effective on the nanoscale and yet are applicable to macroscopic processing. In this

chapter, we examine mechanical properties of polymer nanocomposites incorporating nanodiamond and other nanocarbons.

## ***2. Scope of the present investigations***

One way of classifying nano-filler materials is on the basis of their dimensionality (zero, one or two). Some examples are nanoclay or nanodiamond (zero-dimensional), single- or multi-walled carbon nanotubes and inorganic nanowires (one-dimensional) and single- or few-layer graphenes (two-dimensional). The mechanical properties of PMCs that are reinforced with one- or two dimensional nanofillers have received considerable attention recently.<sup>5-10</sup> There have been very few studies on zero dimensional nanofiller reinforced composites, except those of nano-clay reinforced ones.<sup>1, 11</sup> Keeping this in view, we have examined the effectiveness of nanodiamond (ND), in enhancing the mechanical properties of PVA. Choice of ND is based on the fact that it can be obtained in large quantities by detonation synthesis and is relatively inexpensive with broad applicability. Dolmatov<sup>12</sup> have studied the effect of ND (~2 wt%) addition on the mechanical properties of rubber. The particle size they used is about 44 nm. Kurin *et al.*<sup>13</sup> have made PVA-7 wt% ND fiber coatings and observed ~200 % increment in stiffness and large enhancement in breaking strength. But these composites suffer from poor ductility, which could be due to the large ND content. Behler *et al.*<sup>14</sup> have recently reported a ~400 % increase of Young's modulus and a ~200 % increase of hardness by dispersing ND (~20 wt%) into electro spun polyamide-11 fibers. However, higher concentrations of ND lead to agglomeration of the powders. One way to avoid this problem is using lower filler additions, so that the properties of the polymers are preserved with moderate enhancement in mechanical properties. Furthermore, the rate of enhancement in the mechanical properties is highest when the nanofiller concentration is at the dilute limit. There are very few recent studies on the effectiveness of ND in enhancing the mechanical properties, when ND concentration is around 1 wt%.<sup>15, 16</sup> The objective was to investigate the mechanical properties of PVA-ND composites with small additions of ND (0.2, 0.4 and 0.6 wt%).

One of the hurdles to the use of nanocomposites is the absence of understanding of structure-property relationships. While there have been some studies to correlate the

morphology of the nanocomposites with the macroscopic performance of the materials<sup>5-10</sup> none have discussed in detail variation of nature of interaction of nanofillers based on its dimensionality. Of the variety of nanomaterials synthesized and characterized in recent years, nanocarbons of different dimensionalities are of particular interest, as exemplified by nanodiamond, nanotubes and graphene with dimensionalities of 0, 1, and 2, respectively<sup>17-20</sup>. We would expect the nature of interaction of the nanocarbon constituent with the matrix to vary with the dimensionality. For example, carbon nanotubes added to a polymer can interact over the length of the polymer chain whereas a nanodiamond particle can interact only at a point, possibly at the ends of a polymer chain. While each of the nanocarbons improves the mechanical properties of the polymer matrix, we felt intuitively that incorporation of 2 nanocarbons could lead to synergistic effects in the mechanical properties, as each of them interacts with the matrix differently. We have, therefore, carried out an investigation of the effect of incorporation of different binary combinations of the nanocarbons, nanodiamond (ND), single-walled nanotube (SWNT), and few-layer graphene (FG), on the mechanical properties of polymer matrix composites (PMCs) formed with polyvinyl alcohol (PVA). We have examined all of the three possible combinations of reinforcements, ND plus FG, FG plus SWNT, and ND plus SWNT. The results have been truly exciting and not entirely expected.

### ***3. Experimental Section***

FG was prepared by the exfoliation of graphite oxide following the procedure described recently.<sup>19</sup> SWNTs were prepared by DC arc-discharge process. After preparation, the SWNTs were treated with HCl and heated in H<sub>2</sub> several times to remove the metal nanoparticles and amorphous carbon.<sup>19</sup> ND with phase purity higher than 98% and an average particle size of around 5 nm was purchased from Tokyo Diamond Tools.

#### ***Functionalization of nanofillers***

As the mechanical properties of the polymer-matrix composites depend on the efficient interaction between the polymer matrix and the filler material, the nanofillers

were functionalized to create surface carboxyl and hydroxyl groups,<sup>7, 8</sup> which interact with the PVA at molecular level. For this purpose, 100 mg of the ND was refluxed with 5 mL conc. HNO<sub>3</sub> and 45 mL conc. H<sub>2</sub>SO<sub>4</sub> for 12 h. The acid-functionalized ND was washed with distilled water and dried under vacuum. ND so prepared was dispersed in aqueous media. FG and SWNT were functionalized by acid treatment by the following procedure. A mixture of concentrated HNO<sub>3</sub>, concentrated H<sub>2</sub>SO<sub>4</sub>, water, and corresponding nanocarbon was heated in a microwave oven for about 5–8 min under hydrothermal conditions. The mixture was heated at 100 °C for 6–8 h in an oven. The product thus obtained was washed with distilled water and filtered through a sintered glass funnel. The product so obtained was functionalized with -COOH and -OH groups.<sup>18,</sup>

21

### ***Preparation of composites***

The composites of PVA with the functionalized nanocarbon were prepared in aqueous media. First we prepared composites containing only one nanofillers with 0.2, 0.4, and 0.6 wt% of each nanofillers in PVA matrix. Next step was to make all permutations of these nanofillers of wt% 0.2, 0.4 and 0.6 and add them to PVA. To prepare PVA-nanocomposites, 2 g of PVA was first dissolved in water. It was heated to 70-80 °C for complete dissolution. Required amount of nanofiller was dispersed in distilled water by sonication for 15-20 min. It was then added to the PVA solution followed by sonication for 20-30 min. The mixture was then dried in Petri dishes at 35-40 °C over a period of 3 days. Since the mechanical properties of the PVA are sensitive to the moisture content, the composites were desiccated over CaCl<sub>2</sub> for 7 days or more before performing nanoindentation experiments.

### ***Characterization***

Functionalized nanofillers were characterized by IR spectroscopy and powder XRD. For transmission electron microscopy the samples were dispersed in ethanol and dropped on to the holey carbon-coated copper grids. The grids were allowed to dry in the air. For polymer-nanocomposite films, the films were re-dissolved in water and a drop of this was dried over holey carbon copper grid. Differential scanning calorimetry (DSC) was

performed (8 mg) at a scan rate of 0.16 K/s from 50-250 °C. For PVA-ND composites SAXS measurements were carried out, to see the interparticle distances in polymer films of different concentrations.

### ***Mechanical properties\****

*(\*Nanoindentation measurements and analysis were carried out by Mr. K. Eswar Prasad and Prof. U. Ramamurthy in Dept. of Materials Engineering, Indian Institute of Science)*

Mechanical properties of the PVA-nanocomposites were determined using nano-indentation technique. Thin films of 0.5 mm in thickness (10mm×10mm area) were used for indentation. These films are stuck to a steel plate with a thin layer of glue which dried thoroughly. Quasi-static nano-indentation was carried out using Hystiron Triboindener with a Berkovich tip (a three sided pyramidal diamond tip). Since the hardness,  $H$ , and the Young's modulus,  $E$ , obtained from the instrumented indentation experiments are sensitive to the area function of the indenter, it was first calibrated by employing a quartz standard sample. Since the loads that are used are small, the area function is calibrated at the low depth range. With the new area function, the  $H$  and  $E$  values measured on the standard Al and quartz samples were found to be within the 5% standard deviation given by the manufacturer, validating the calibration. The mechanical properties of polymers are sensitive to the loading rate and the pause time at the peak load. Therefore, these indentation parameters were optimized until  $H$  and  $E$ , obtained from the nano-indentation are comparable with the available literature data.<sup>23</sup> A peak load of 1mN was chosen, such that the substrate does not influence the measured properties. The loading and the unloading rates used were 0.1 mN/s with a hold time of 10 s at the peak load. Ten indentations are made on each sample and the average values of the  $E$  and  $H$  from these measurements are reported. In all of the cases, care was taken that the penetration depth was 1000 nm. Hardness and elastic modulus were determined by the Oliver-Pharr method.<sup>24</sup>

## ***4. Results and Discussion***

Stiffness ( $E$ ) is determined by the atomic bonding characteristics as well as the structure of the material. Polymers suffer from poor stiffness because  $E$  of a polymer is

determined by the van der Waals bonding that exists between different polymer chains, which allows for relative sliding of the polymer chains rather easily. Functionalized nanocarbons form chemical bonds with the polymer chains, and affect the inter-chain bonding characteristics, making it difficult for the relative sliding to take place. Hardness ( $H$ ) reflects the resistance of the composite to plastic deformation. The controlling characteristic is the efficiency with which the applied load is transferred from the softer matrix phase to the stronger reinforcement phase. Strong adhesion between nanocarbons and polymer and also their crystallinity favor effective load transfer.

### ***PVA-Nanodiamond composites***

TEM images of as received (AR\_ND) and after functionalization (AF-ND) and PVA-0.6 wt% ND are shown in Figure. 1 (a), (b) and (c) respectively. Both AR-ND and AF-ND have an average diameter of 5 nm.

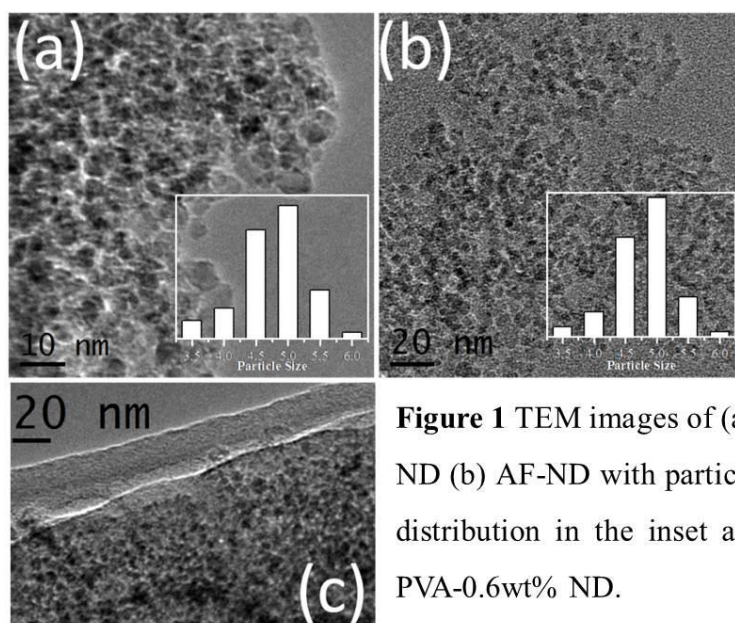


**Figure 1** TEM images of (a) AR-ND (b) AF-ND with particle size distribution in the inset and (c) PVA-0.6wt% ND.

The inset shows the particle size range and their distribution. Neither a change in the average diameter of the particles nor further agglomeration on acid functionalization was noted. The TEM image of PVA-0.6 wt% ND in Figure.1 (c) shows that the dispersion is uniform. Thin film of polymer can be seen in the image.

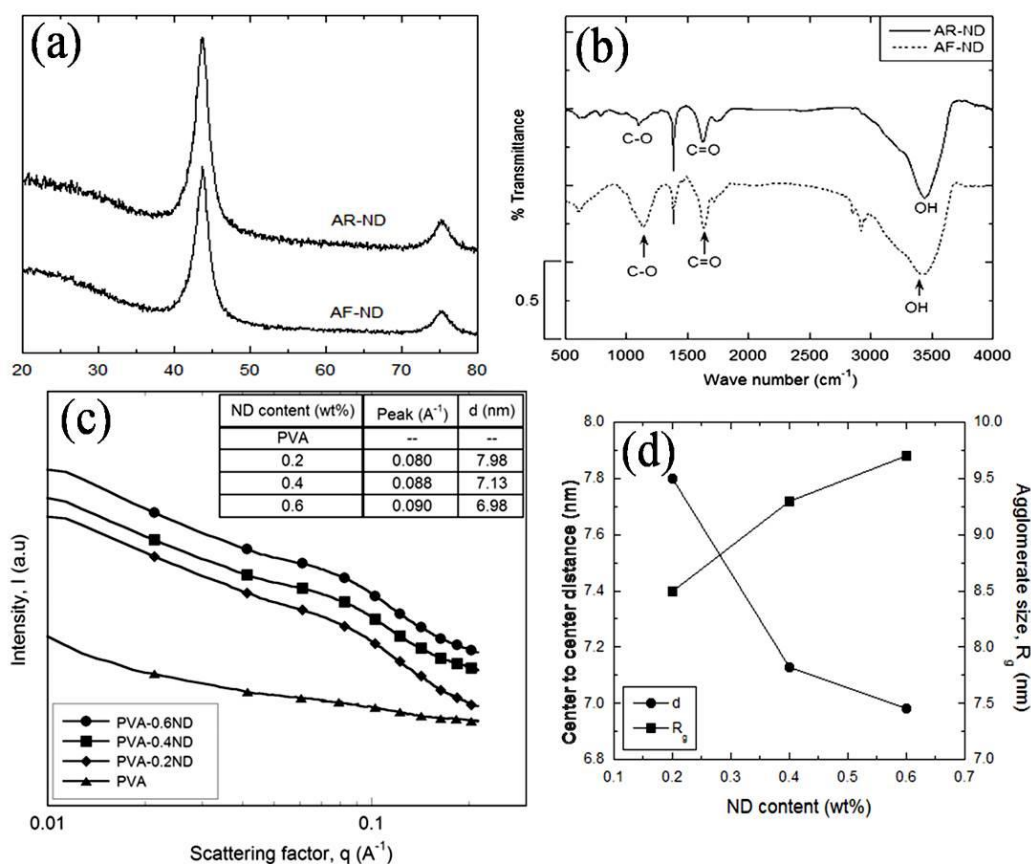


**Figure 2.** (a) XRD pattern, (b) IR-spectra of AR-ND and AF-ND, (c) SAXS curves of PVA and PVA-ND composites with table of the  $q$  and  $d$  values in the inset, (d) Variation of centre-to-centre distance and agglomerate size with wt% of ND.

The XRD patterns (Figure. 2(a)) of the AR-ND and AF-ND yield similar results. Acid functionalization does not affect crystallinity of ND. The IR spectrum of the AR-ND shows characteristic -OH and C=O, C-O band peaks (Figure 2 (b)). This is because ND during purification processes is treated with mineral acids. The intensity of these peaks increases upon acid-functionalization. Figure 2 (c) shows the SAXS data of the prepared films where the intensity is plotted as function of the scattering factor. The scattering factor,  $q$ , and the inter-particle distance,  $d$ , values are shown in the inset table (Figure 2 (c)). The inter-particle distance is calculated using the formulae  $d = 2\pi/q$  and the radius of gyration is calculated using,



$$I = G \exp\left(\frac{-R_g^2 q^2}{3}\right) \quad (1)^{25}$$

The variation of interparticle separation and agglomerate size was plotted against wt% of ND in the polymer composite. The particle separation decreases by 11% and the agglomerate size increases by 14% with increasing ND concentration from 0.2 to 0.6 wt% (Figure 2 (d)).

DSC traces of the PVA-ND composites show (Figure 3 (a)) that there is no change in the melting temperature,  $T_m$ , of the composites with the addition of ND. Degree of crystallinity was determined from enthalpy of crystallization using the equation,

$$\chi = \frac{\Delta H_{exp}}{\Delta H_{fus}} \quad (2)$$

where,  $\chi$  is the degree of crystallinity,  $\Delta H_{exp}$  is the experimentally determined value of change in enthalpy from the DSC curve and  $\Delta H_{fus}$  is the enthalpy of fusion of the PVA ( $138.6 \text{ Jg}^{-1}$ ). It is seen from Figure 3 (b) that  $\chi$  increases markedly first (by ~10 % upon the addition of 0.2 wt% ND to PVA) and then increases gradually (from ~52.5 to 62% when ND concentration is increased from 0.2 to 0.6 wt%).

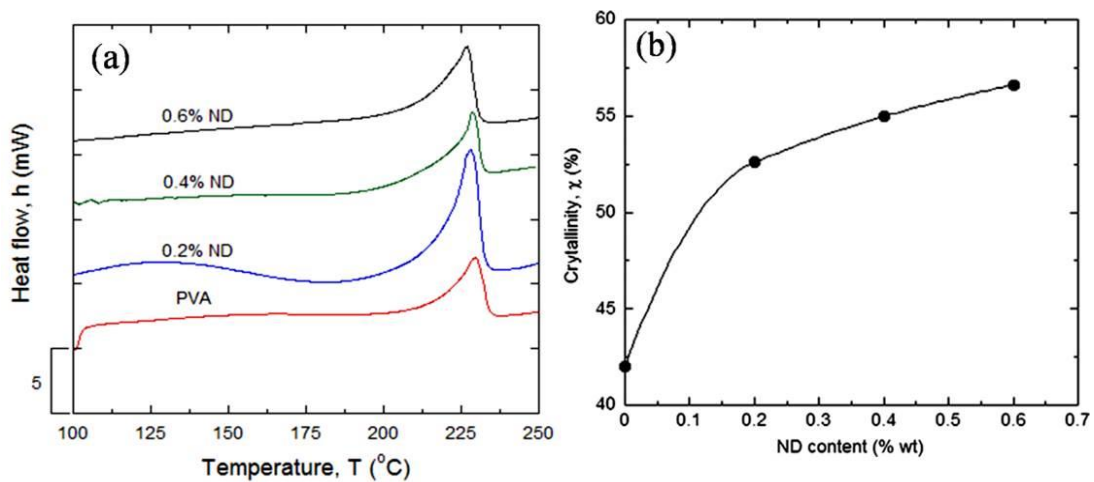


**Figure 3.** (a) DSC scans of PVA-ND composites showing the crystallization peak in the range of 220 - 235°C, (b) Variation of degree of crystallinity ( $\chi$ ) with ND content in the polymer nanocomposites.

The hardness and elastic modulus calculated from stress strain curves are listed in Table 1. These values, normalized with the respective values of blank PVA (in order to

highlight the relative changes in mechanical properties with the addition of ND), are plotted as against wt% ND in Figure 4. It is evident that both  $H$  and  $E$  of the PVA increase significantly upon the addition of ND. In Figure 4, it can be seen that the scatter in  $E$  is relatively large for 0.6 wt% ND composite. This is possibly due to the agglomeration of the ND particles at higher concentrations. While the average value of  $H$  increases by ~80%,  $E$  almost doubles with the addition of 0.6 wt% ND.

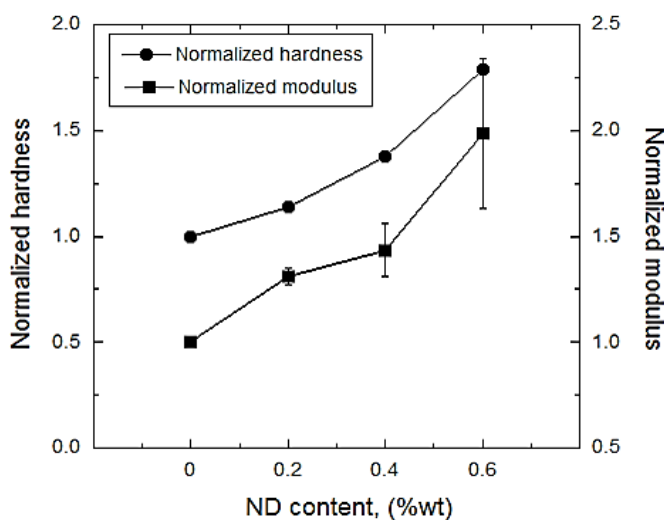


**Figure 4.**  
Variation of normalized hardness and modulus plotted as a function of ND content.

The mechanical response of a composite depends on many factors. These include,

- (a) the size and distribution of the reinforcement phase in the matrix
- (b) the characteristics of the interface between the reinforcement phase and the matrix.

Uniform distribution of the reinforcement phase is essential for obtaining high quality composites. Detailed characterization of the PVA-ND composites shows that the ND is distributed uniformly with no agglomeration. Since the size of the particle is of nm-scale, their number density (per unit volume) will be high, amplifying the strong interaction with molecular mechanisms of elastic as well as plastic deformation features of the polymer. The DSC results obtained in this study, which show increased crystallinity of the polymer with the ND addition, suggest that the adhesion between the polymer and the ND particles is strong, promoting crystallization of the matrix, which in turn enhances the mechanical response of the composite. In light of this, possible mechanisms responsible for the enhancement in elastic and plastic properties of the PVA with the addition of ND are discussed below. Since the functionalized ND particles may form chemical bonds

with the polymer chains, they affect the inter-chain bonding characteristics, making it difficult for the relative sliding to take place. In this context, it is worth noting that similar enhancements in  $E$  were reported PVA reinforced with few-layer graphene <sup>7</sup>, or MWNT <sup>5</sup> or SiC nanowires <sup>6</sup>. Post fracture microscopy of the PVA-SiC nanowire composites by Vivekchand *et al.* <sup>6</sup> showed a thin layer of matrix on the filler material, indicating a strong interaction between the two. Similar interaction can be inferred in the present case as well, as a significant increase in the degree of crystallinity (by 14% with the additions of 0.6 wt% ND) was noted.

Similar arguments can be used to rationalize the enhancement in  $H$ , which reflects the resistance of the composite to plastic deformation. Again, the strong adhesion between ND and PVA due to functionalization of the former and ND crystallinity favour effective load transfer. Another possible factor is that the hard ND resists the formation and/or propagation of shear bands, the primary mode of deformation in amorphous and semi-crystalline polymers, resulting in enhancement of hardness.

### ***Binary composites***

In case of binary composites we have examined all possible combinations of the three reinforcements, ND + FG, FG + SWNT and ND + SWNT. The maximum content of the nanocarbon reinforcement was kept 0.6 wt% since higher levels of reinforcement only likely to cause agglomeration of the nanomaterials in the matrix, with different proportions of the major (0.4) and minor (0.2) nanocarbon additives. As discussed earlier better interaction of nanofillers with polymer enhances mechanical properties. To enhance interactions of the nanofillers with the matrix, surface functionalization of the the fillers was carried out. The IR-spectra of acid treated samples (Figure 5(a)) shows presence of –OH and –COOH groups. In Figure 5(b) DSC traces of all the composites have been plotted. Though all the samples have same melting point, degree of crystallinity varies. Variation of degree of crystallinity for composites containing single nanofillers has been is shown in Figure 6 (c). Nanocomposites containing FG show least value of  $\chi$ , those with ND and SWNT have comparable values of  $\chi$ . Highest degree of crystallinity is obtained in the sample with 0.6% of SWNT.

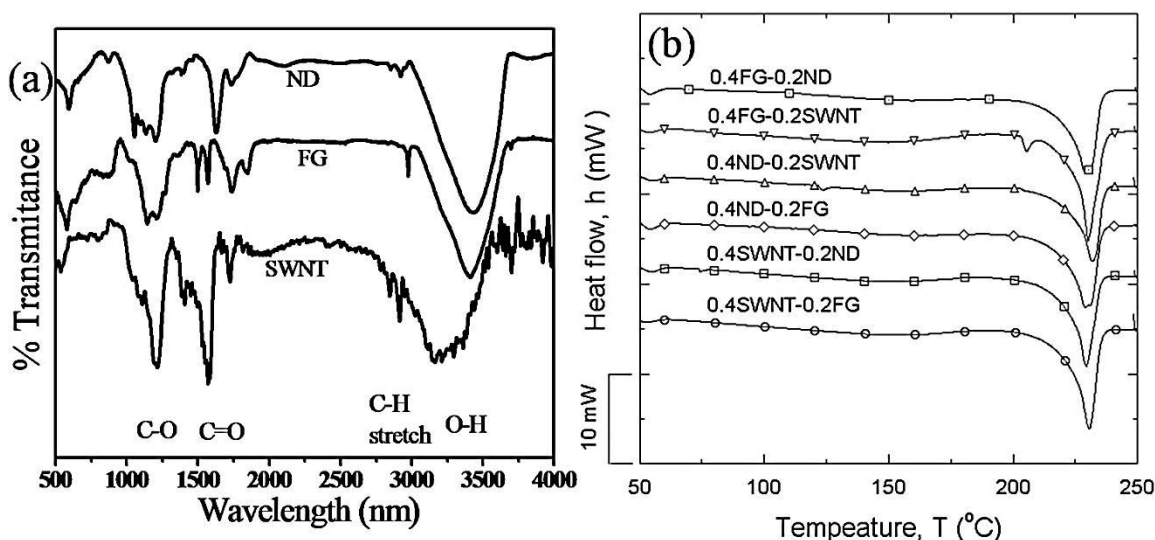


**Figure.5** (a) IR-spectra of acid treated ND, FG, SWNT peak positions characteristic of various functional groups marked below, (b) DSC traces of the nanocomposites.

In Figure 6 (a, b), we show the variation of the hardness,  $H$ , and the elastic modulus,  $E$ , of PMCs containing a single nanocarbon reinforcement as a function of the nanocarbon content. These data provide the reference for comparing the multiply reinforced composites investigated by us. All the three nanocarbons improve the mechanical properties of PVA markedly, addition of SWNT enhancing  $H$  by  $\sim 7$  times and  $E$  by an order of magnitude. These enhancements are observed even with the addition of 0.2 wt% SWNT, the properties reaching a plateau on further increase in the SWNT content, probably due to the bundling of SWNTs at higher reinforcement content. Such bundling could reduce the effective interaction volume. Unlike the SWNT-PVA composites, the ND-PVA and FG-PVA composites show a gradual increase in  $E$  and  $H$  with the increasing nanocarbon content, the rate of increase being higher in the former.

The enhancement in the mechanical properties of PVA is due to the inducement of crystallization of the polymer with the addition of the nanomaterials<sup>5, 6, 7</sup>. The values of mechanical properties are summarized in Table 1. The data reveal that the addition of a nanocarbon to PVA increases  $\chi$ . To examine whether  $\chi$  determines the enhancement in mechanical properties, we have plotted  $E$  and  $H$  against the relative change in  $\chi$  in Figure 7. The values of pure PVA (Table 1), processed and evaluated under identical conditions

as those of the PMCs were used for reference. Figure 7 suggests that crystallinity and mechanical properties are related in ND- and FG containing PMCs. The mechanical properties of SWNT-containing PMCs seem to be independent of crystallinity.

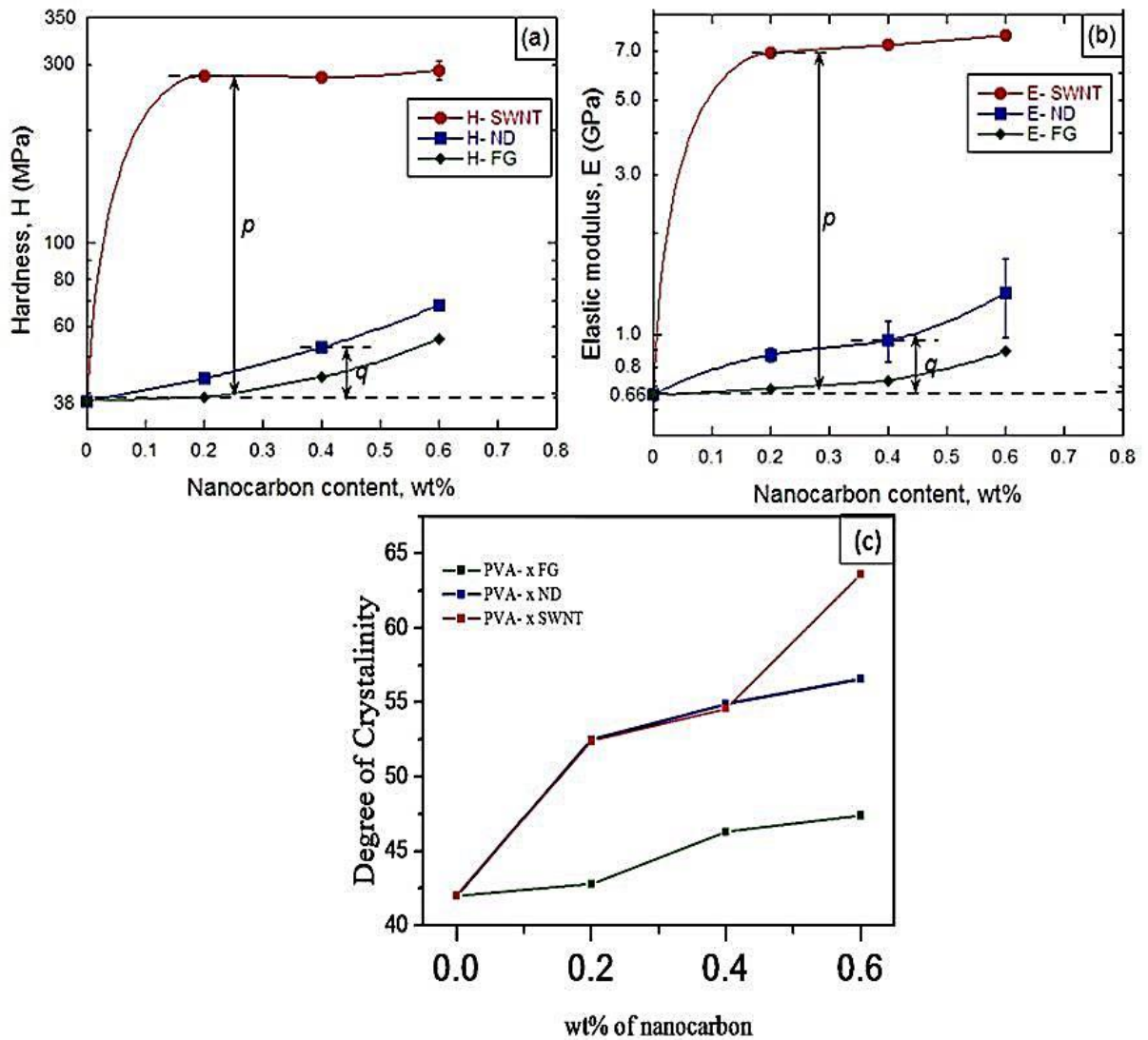


**Figure 6.** Mechanical properties of (a) hardness and (b) elastic modulus with the variation of nanocarbon content. (SWNT reinforced nanocomposites gives the superior mechanical properties compared to the FG and ND), (c) Variation of degree of crystallinity with addition of each nanocarbons to polymer matrices.

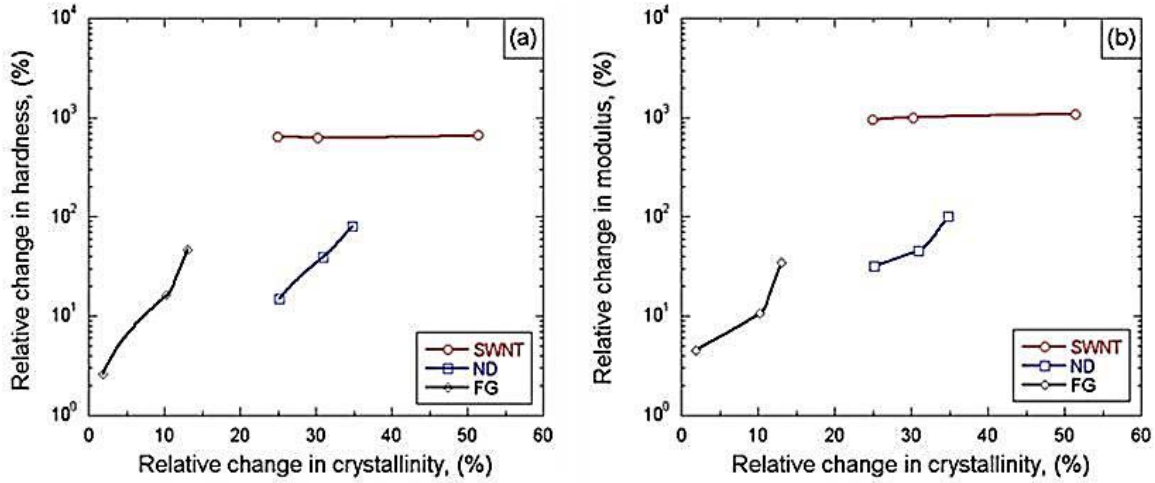


**Figure 7.** Variation of percentage relative change in the (a) hardness and (b) elastic modulus with the relative change in crystallinity.

**Table 1.** Values of Hardness (H), Elastic modulus (E) and Degree of crystallinity for nanocomposites with single nanocarbon filler.

Filler material	Hardness (MPa)	Elastic modulus (GPa)	Degree of crystallinity (%)
PVA	38.0 ± 0.01	0.66 ± 0.03	42.0
PVA-0.2 FG	39.0 ± 0.03	0.69 ± 0.03	42.8
PVA-0.4 FG	44.1 ± 0.03	0.73 ± 0.05	46.3
PVA-0.6 FG	55.7 ± 0.05	0.89 ± 0.08	47.4
PVA-0.2 ND	43.7 ± 0.01	0.87 ± 0.04	52.5
PVA-0.4 ND	52.8 ± 0.03	0.96 ± 0.13	54.9
PVA-0.6 ND	68.4 ± 0.02	1.33 ± 0.35	56.6
PVA-0.2 SWNT	277.8 ± 2.02	6.93 ± 0.05	52.4
PVA-0.4 SWNT	280.1 ± 9.82	7.30 ± 0.61	54.6
PVA-0.6 SWNT	290.2 ± 19.42	7.80 ± 0.34	63.6

Such large changes in the mechanical properties observed in SWNT-PVA composites have not been reported hitherto in the literature. There are a limited number of studies of nanotube-polymer composites, and they generally involve high reinforcement content<sup>17, 18, 26-30</sup>. Furthermore, many of the studies pertain to composites reinforced by multi-walled carbon nanotubes. Liu *et al.*<sup>27</sup>, who examined the PVA-0.8 SWNT composite, report an increase of 78% in *E* and of 48% in tensile strength, values much smaller than these observed by us in the present study. These workers did not observe any increase in crystallinity and attributed the enhancement in mechanical properties to the homogeneous distribution of fillers in the matrix. Zhang *et al.*<sup>28</sup> examined composites of PVA with

KOH treated SWNTs and report that  $H$  and  $E$  increase by 78 and 110% respectively, whereas Li *et al.*<sup>26</sup> report 30% and 75% increases for the 5 wt% SWNT–epoxy composite. These workers observe that intercalation of the nanotubes is the cause for relatively poor enhancement in mechanical properties. Cadek *et al.*<sup>5</sup> have attributed the increase in mechanical properties of composites to the interfacial bonding between the matrix and the nanotubes as reflected by the increase in crystallinity. They also argue that the mechanical properties of the composites depend critically on the aspect ratio of the nanotubes, which in their case was  $\sim 100$ . In the present study, the SWNTs had aspect ratios of 700 to 1400. Furthermore acid functionalization of SWNTs could contribute to better bonding with the polymer, because of the presence of the surface carboxyl and hydroxyl groups. In Figure 8 (a, b) the variations of hardness ( $H$ ) and elastic modulus ( $E$ ) has been plotted for two composite made of PVA-0.4% ND with various additions of FG and PVA-0.4FG-xND. For comparison  $H$  and  $E$  values for composites with single nanofillers has also been added. The composite PVA-0.4ND-xFG showed much improvement in properties compared to the composites made of either ND or FG. Similar trend is found in the modulus values. But  $E$  values reach steady state at large additions of FG. The synergistic effect is more pronounced at low concentrations of FG. To demonstrate it clearly independent effects (sum of individual effects for particular wt% of nanocarbons) and combined effect (experimental values) on  $H$  and  $E$  have been plotted in Figure 8. (c - f). However PVA-0.4FG-xND shows anomalous behaviour (Figure 8. (b)). Both  $H$  and  $E$  values increases up to 0.2% of ND and decreases with increasing ND (see highlighted parts in Figure 8. (b), (d) and (f)).

On the basis of molecular dynamics simulations, Starr *et al.*<sup>31</sup> and Smith *et al.*<sup>32</sup> have shown that the high surface area of nanoparticles provides better interaction between the polymer chains and nanoparticles. This is due to the interaction of  $-\text{OH}$  and  $-\text{COOH}$  groups that are present on the acid-functionalized graphene with the  $-\text{OH}$  group present in the long chain polymers. Schniepp *et al.*<sup>33</sup> have found that the graphene sheets possess wrinkled structures and in between the wrinkles there are regions that have a surface roughness of  $\sim 0.4\text{--}0.5$  nm. This surface roughness increases surface area of interaction with the phases when FG is dispersed in a polymer matrix. In the unreinforced polymer matrix, shear bands propagate unhindered as there are no barriers for their movement. In

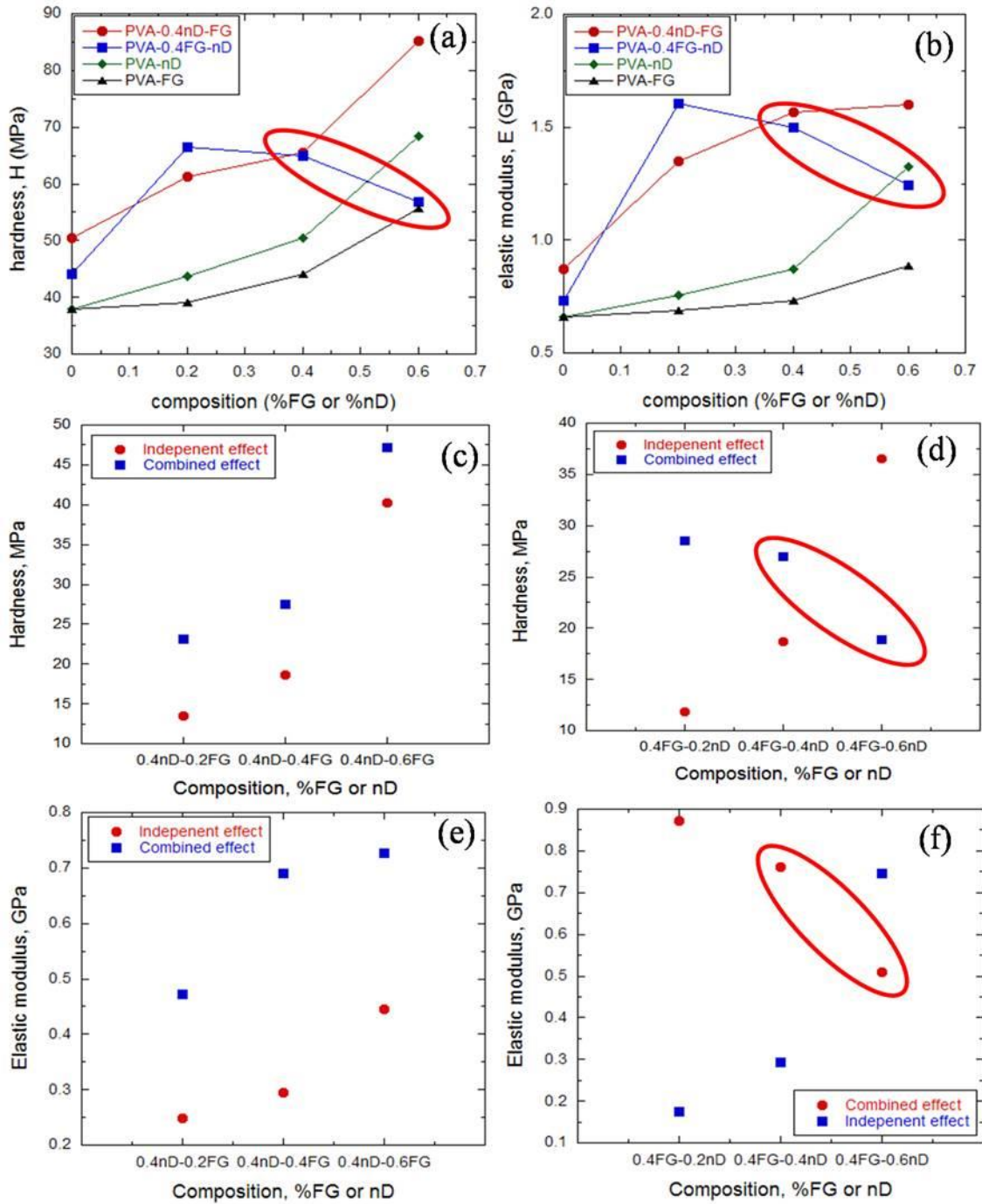


**Figure 8.** (a)Variation of hardness ( $H$ ) and (b) Elastic modulus ( $E$ ) for two binary composites PVA-0.4ND-xFG and PVA-0.4ND-xFG  $H$  and  $E$  values for composites with single nanofillers has been added for comparison. Comparison of (c-d)  $H$  and (e-f)  $E$  values of independent and combined effect for the two composites respectively.



contrast, the presence of FG in the composites could offer resistance for the propagation of shear bands because of the high surface area it provides and there by greater interaction with the polymer. Inclusion of ND into the matrix reduces the effective surface area of FG interacting with the polymer. This is because some of the functional groups of FG might interact with functional groups on ND by covalent or non-covalent interaction. Since interaction of the polymer matrix with graphene effectively reduces, the  $H$  and  $E$  values also reduce.

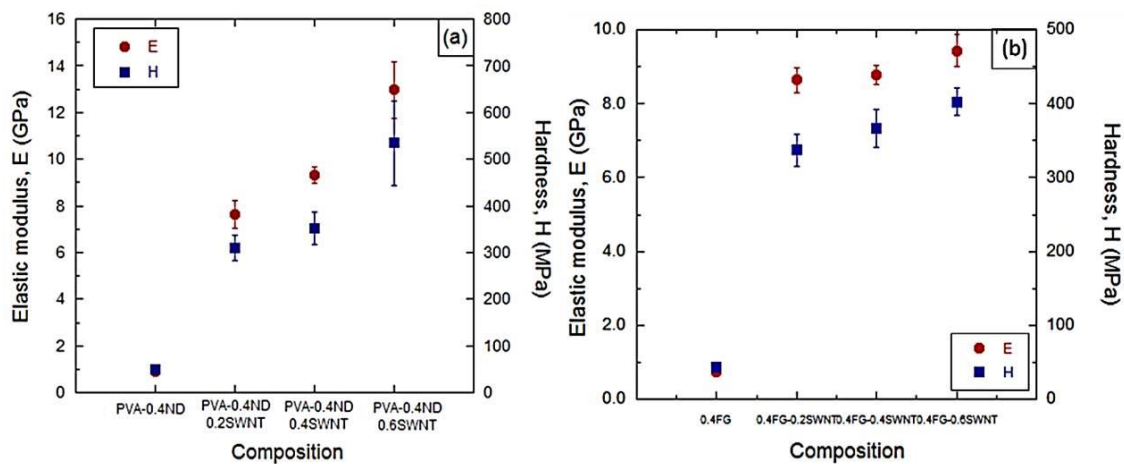


**Figure 9.** Variation of  $H$  and  $E$  for composites (a) PVA-0.4 ND-x SWNT and (b) PVA-0.4 FG-x SWNT.

In Figure 9, we show the variation of  $H$  and  $E$  values for composites PVA-0.4ND-xSWNT and PVA-0.4FG-xSWNT. For both the cases there is significant increase in both  $E$  and  $H$  values from that of individual ones. Interestingly the  $H$  and  $E$  values of this composite PVA-0.4ND-0.6SWNT were found to be  $534.3 \pm 90.6$  MPa and  $12.96 \pm 1.22$  GPa, highlighted in Figure 9.(a). These properties are superior to those of any nanocarbon-polymer composites reported in the literature. A possible reason for the high  $E$  and  $H$  values in the PVA-0.4ND-0.6SWNT composite could be because that the ND particles prevent clustering of SWNTs due to van der Waals interactions. Surfactants are generally used to generate isolated SWNTs. ND particles can similarly prevent SWNT's to slide past each other by either binding two SWNTs to each other or intercalating between the two SWNTs.

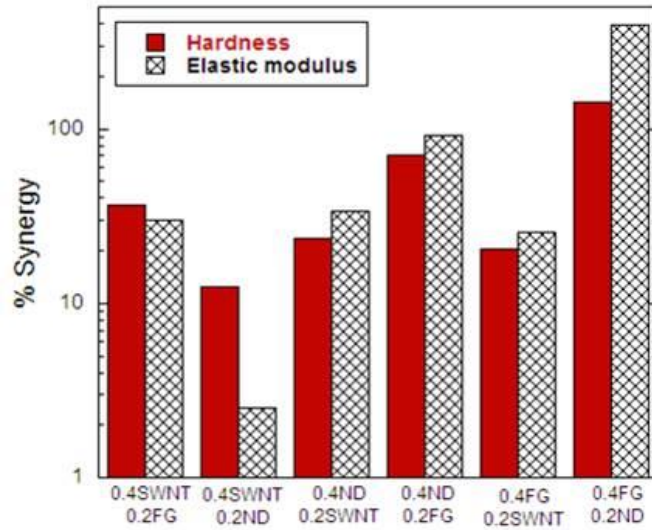


Figure 10. Percentage synergy in  $H$  and  $E$  for different binary composites

What was notable was the fact that we gained synergistic benefits by adding two nanofillers of different dimensionalities to the polymer matrix. The synergistic benefit was estimated as follows, as exemplified in the case of the PVA-0.2SWNT-0.4ND composite. The addition of 0.2% SWNT alone to PVA leads to an enhancement in  $H$  or  $E$  of PVA by  $p$  as shown in Figure 6. Likewise,  $q$  represents the enhancement in  $H$  or  $E$  of PVA due to the addition of 0.4 ND alone. The synergistic effect or % synergy attained by adding both 0.2% SWNT and 0.4% ND to PVA was computed by the relation,

$$\% \text{ synergy} = [M_H - (p + q)] \times \frac{100}{(p+q)}$$

where,  $M_H$  is the measured value for the composite.

In Figure 10. we have plotted % synergy in hardness as well as elastic modulus for the different composites. The synergistic effect is dramatic in the ND plus FG composites, with 4 and 1.5 fold increases in  $E$  and  $H$ , respectively, in PVA-0.4FG-0.2ND composite. In the case of the PVA-0.4ND-0.2FG composite, synergistic effect is somewhat less, amounting to 92 % and 71 %, respectively, in  $E$  and  $H$ . The synergy is not as apparent in the SWNT plus ND composites since the addition of SWNT alone gives rise to fairly large values of  $E$  and  $H$ .

**Table 2.** Mechanical properties of the reinforced composites incorporating two nanocarbon fillers

Composite wt%	Hardness (MPa)	Elastic modulus (GPa)	Synergy (%)		Degree of crystallinity (%)
			Hardness (MPa)	Elastic modulus (GPa)	
0.4 SWNT + 0.2 FG	366.5 ± 23.9	9.3 ± 0.43	36.4	56.5	56.5
0.4SWNT + 0.2 ND	314.2 ± 10.15	7.5 ± 0.05	12.5	55.1	55.1
0.4FG + 0.2ND	66.4 ± 5.43	1.6 ± 0.1	141.4	55.1	55.1
0.4FG + 0.2SWNT	336.9 ± 22.21	8.6 ± 0.34	20.4	57.5	57.5
0.4ND + 0.2FG	61.18 ± 0.002	1.3 ± 0.07	71.1	54.8	54.8
0.4ND + 0.2SWNT	352.9 ± 34.78	9.3 ± 0.36	23.6	33.6	57.2

Values of  $H$  and  $E$ , % synergy and degree of crystallinity have been tabulated in Table 2. Variation in the percent crystallinity (%) of the PMCs with 2 nanocarbons is around ~2%, suggesting that increase in crystallinity is not the cause of the observed synergy. From Figure 10, it is interesting to note that, in general, the synergistic benefits for both modulus and hardness accrue together. A possible reason for this strong correlation could be the fact that the nanocarbon reinforcements interact with the polymer chains at the molecular level. Such interaction not only enhances the polymer chain's stiffness (thereby increasing the composite's global modulus) but also its plastic flow resistance, which in turn leads to increased hardness. These results suggest possible new and exciting ways of obtaining high performance polymer matrix composites.

## **5. Conclusions**

We first prepared PVA polymer-matrix composites reinforced with small concentrations of functionalized ND. Detailed structural characterization, employing a variety of analytical techniques, shows that the nanoparticles are distributed uniformly and do not agglomerate. Further, they appear to interact with the polymer matrix strongly, increasing the crystallinity substantially. With only 0.6 wt% addition of ND, which is relatively small, significant enhancements to the hardness and Young's modulus of the PVA were observed. It was suggested that excellent adhesion between the matrix and the functionalized ND particles is the main reason for this marked improvement in

mechanical performance. These results indicate that ND can be successfully used as a filler material for making polymer composites.

It was also possible to prepare composites of PVA with 2 nanocarbon additives. While nanodiamond, single-walled nanotubes, and graphene individually give rise to significant improvement in the mechanical properties of PVA, incorporation of binary combinations of these nanocarbons results in extraordinary synergy in mechanical properties. It was illuminating to understand that addition small amount of nanodiamond into nanocomposites of SWNT increases strength and stiffness further, simply because of the fact that ND can act like surfactant preventing bundelling of SWNT. We should point out, however, that our study has been limited to the measurements of hardness and elastic modulus and do not include ductility and toughness. In any case, our results suggest that it would indeed be profitable to explore polymer composites with such binary reinforcements.

## Reference

1. L. H. Baekeland, *Sci. Am.* 1909, 68, 322.
2. C. Goodyear, *Dinglers Polytechnisches J.* 1856, 139, 376 .
3. A. Usuki, M. Kojima, A. Okada, Y. Fukushima, O. Kamigaito, *J. Mater. Res.* 1993, 8, 1179.
4. Y. Kojima et al., *J. Mater. Res.* 1993, 8, 1185.
5. M. Cadek, J. N. Coleman, V. Barron, K. Hedicke, W. J. Blau, *Appl. Phys. Lett.* 2002, 81, 1523.
6. S.R.C. Vivekchand, U. Ramamurty, C.N.R. Rao, *Nanotechnol.* 2006, 17, 344.
7. B. Das, K.E. Prasad, U. Ramamurty, C.N.R. Rao, *Nanotechnol.* 2009, 20, 125705.
8. T. Ramanathan, A. A. Abdala, S. Stankovich, D. A. Dikin, M. Herrera-Alonso, R. D. Piner, D. H. Adamson, H. C. Schniepp, X. Chen, R. S. Ruoff, S. T. Nguyen, I. A. Aksay, R. K. Prud'Homme, L. C. Brinson, *Nature Nanotechnol.* 2008, 3, 327.
9. K.P. Ryan, M. Cadek, V. Nicolosi, S. Walker, M. Ruether, A. Fonseca, J.B. Nagy, W.J. Blau, J.N. Coleman, *Synthetic Metals* 2006, 156, 332.
10. T. Ramanathan, et al., *J. Polym. Sci. B* 2007, 45, 2097.
11. S.C. Tjong, *Mater. Sci. Eng. R* 2006, 53, 73.
12. V.Y. Dolmatov, *J. Superhard Mater.* 2007, 29, 65.
13. T.S. Kurkin, A. N. Ozerin, A. S. Kechekyan, L. A. Ozerina, E. S. Obolonkova, M. A. Beshenko, V. Yu. Dolmatov, *Polym. Sci. Ser. A* 2008, 50, 43.
14. K.D. Behler, A. Stravato, V. Mochalin, G. Korneva, G. Yushin, Y. Gogotsi, *ACS Nano* 2009, 3, 363.
15. A.P. Korobko, N.P. Bessonova, S.V. Krasheninnikov, E.V. Konyukhova, S.N. Drozd, S.N. Chvalun, *Diam. Relat. Mater.* 2007, 16, 2141.
16. Z. Spitalský, A. Kromka, L. Matejka, P. Cernoch, J. Kovárová, J. Kotek, M. Slouf, *Adv. Compos. Lett.* 2008, 17, 29.
17. C. N. R. Rao, A. Muller, A. K. Cheetham , *Nanomaterials Chemistry: Recent Development and New Directions* ,Wiley-VCH, Weinheim , 2007.
18. C. N.R. Rao, A. Govindaraj, *Nanotubes and Nanowires*, Royal Society of Chemistry, London 2005.

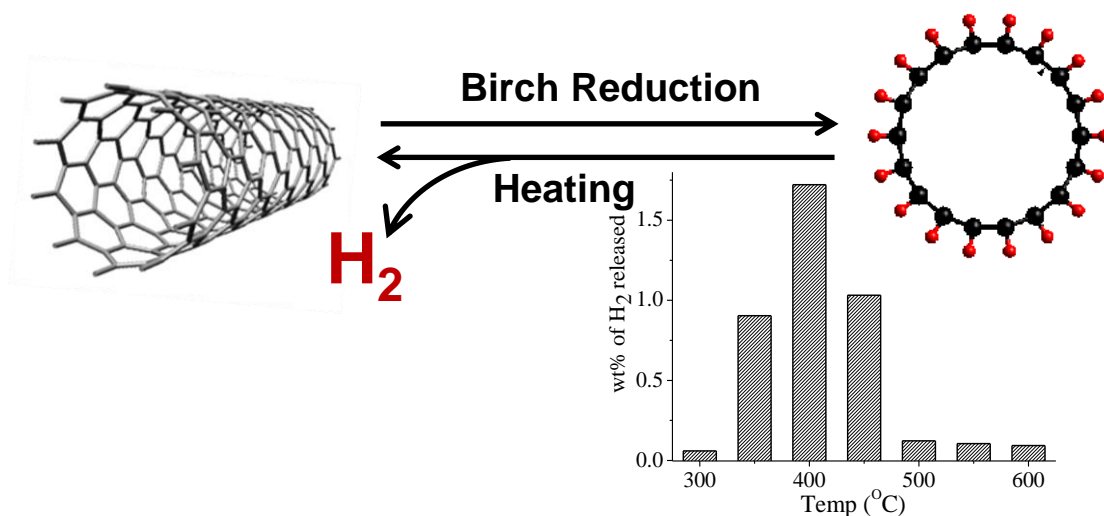
19. C. N. R. Rao, K. Biswas, K. S. Subrahmanyam, A. Govindaraj, *J. Mater Chem* 2009, 19, 2457.
20. S. R. C. Vivekchand, R. Jayakanth, A. Govindaraj A, C. N.R. Rao, *Small* 2005, 1, 920.
21. K. S. Subrahmanyam, A. Ghosh, A. Gomathi, A. Govindaraj, C. N. R. Rao, *Nanosci Nanotech Letts* 2009, 1, 28.
22. J.S. Pedersen, *J. Appl. Crystallogr.* 2004, 37, 369.
23. J. Kuljanin, M. I. C. Omor, V. Djokovic, J. M. Nedeljkovic, *Mater. Chem. Phys.* 2006, 95, 67.
24. W.C. Oliver, G.M. Pharr, *J. Mater. Res.* 1992, 7, 1564.
25. A. Guinier, *Ann. Phys.* 1939, 12, 161.
26. X. Li, H. Gao, W. A. Scrivens, D. Fei, X. Xu, M.A. Sutton, A.P. Reynolds, M.L. Myrick, *Nanotechnol.* 2004, 15, 1416.
27. L. Liu, A.H. Barber, S. Nuriel, H.D. Wagner, *Adv. Funct. Mater.* 2005, 15, 975.
28. X. Zhang, T. Liu, T.V. Sreekumar, S. Kumar, V.C. Moore, R.H. Hauge, R.E. Smalley, *Nano Lett.* 2003, 3, 1285.
29. D. Qian, E.C. Dickey, R. Andrews, T. Rantell, *App. Phys. Lett.* 2000, 76, 2868.
30. X. Xu, M.M. Thwe, C. Shearwood, K. Liao, *App. Phys. Lett.* 2002, 81, 2833.
31. F.W. Starr, T.B. Schrode, S.C. Glotzer, *Macromolecules* 2002, 35, 4481.
32. G.D. Smith, D. Bedrov, L.W. Li, O.A. Byutner, *J. Chem. Phys.* 2002, 117, 9478.
33. H. C. Schniepp, J. L. Li, M. J. McAllister, *J. Phys. Chem. B* 2006, 110, 8535.

# Chapter II.3

## *Birch reduction of carbon nanotubes and graphene nanoribbons for chemical H<sub>2</sub> storage*

### *Summary\**

*Hydrogen storage through formation of reversible chemical bonds provides advantage of having just the right interaction strength needed for a material to be used in vehicular transport. Birch reduction of the carbon nanotubes has been studied to achieve chemical storage of H<sub>2</sub>. Single, double and multi walled carbon nanotubes can reversibly store upto 4, 3 and 2 wt% of H<sub>2</sub>, respectively, the department of energy goal being 6.5 wt%. Birch reduced carbon nanotubes are stable at room temperature and the hydrogen can be progressively removed by heating to 400 °C. Slow release allows greater control over release which is desirable for most practical applications. Few-layer graphene nanoribbons can reversibly store upto 2.5 wt% of H<sub>2</sub>.*



\* Papers based on this work have appeared in *Proc. Natal. Acad. Sci. USA*, 2011, *Ind. J. Chem. Sec. A*, 2012

## **1. Introduction**

The issue of energy can be divided into two different paradigms: production of energy and storage of energy. Though both are interrelated to each other and needs to be studied hand in hand, the major focus of research in the past few decades has been generation of energy. Energy can be stored in different forms: as mechanical energy of turbines or potential energy, in an electric or magnetic field, as chemical energy of reactants and fuels or as nuclear fuel. Energy needs not only to be stored but also to be transported to the point of use. Chemical and electrical energy are the only two forms of energy that can be transported easily. Generation of electrical energy from renewable sources like sunlight, wind and water are being perused worldwide. Main sources of chemical energy over the past centuries have been fossil fuels. While the availability of fossil fuels is decreasing, the alarming emission of greenhouse gases, especially CO<sub>2</sub>, is leading to undesirable change in global climate. An attractive solution to the energy problem lies in the replacement of the fossil fuels.

Chemical energy stored per mass of hydrogen (142 MJkg<sup>-1</sup>) is three times larger than that in conventional fuels (eg. 47 MJkg<sup>-1</sup> for liquid hydrocarbons). Furthermore, hydrogen constitutes the cleanest form of energy giving off only water after burning. Hydrogen can be produced from water using a combination of photovoltaics and water electrolysis,<sup>1</sup> although many of the routes to hydrogen are expensive. An equally serious problem is to find an affordable means of storing hydrogen. Hydrogen can be stored in the form of compressed liquid or gas, adsorbed molecules, metal hydrides and covalently bonded molecules. Transportation is one of the major areas where safe, economic and clean fuel is needed. On board energy storage needs not only efficient fuel but also safe, affordable, compact and light energy containment. A modern car running for about 400 km would require about 4-8 Kg of H<sub>2</sub> depending on whether it is run on fuel cells or combustion engines. To contain this much of H<sub>2</sub> in cylinders at room temperature and 300 bar pressure would require ~220 L of tank space. This is not only impractical from the view point of space but also highly risky. Compressing H<sub>2</sub> into liquid is neither cost effective nor safe from the view point of evaporation losses under ambient conditions. Metal hydrides are safer alternatives but store upto 2 wt% of H<sub>2</sub> while the U.S.



Department of Energy (DOE) has set the energy density goal for H<sub>2</sub> to be used for automobiles to 6.5 wt% and 62 kg of H<sub>2</sub> per m<sup>3</sup>. Since efficiency, size, weight, cost and safety issues determine the efficacy of materials for hydrogen storage, adsorption on solids seems to be one of the safe ways to store hydrogen. Activated carbon with a surface area of 500-800 m<sup>2</sup>/g, has an H<sub>2</sub> uptake of 1wt% at room temperature and 10 MPa pressure.<sup>2</sup> Single-layer graphene is theoretically predicted to have a large surface area of 2600 m<sup>2</sup>/g while that for few layer graphene is 270-1550 m<sup>2</sup>/g.<sup>3,4</sup> Bhatia and Myers<sup>5</sup> calculated the optimum heat of adsorption of hydrogen on activated carbons to be 5.8 kJ/mol while the heat of adsorption needed for reversible storage of H<sub>2</sub> under ambient temperature and pressure is 15.1 kJ/mol.<sup>5</sup> A means to achieve a high uptake of hydrogen is to vary the pore diameter leading to trapping and condensation of molecules inside the pores. Single-walled carbon nanotubes (SWNTs) with diameters generally varying in the range 0.8 to 1.2 nm are candidates for such an adsorptive storage. The curved surfaces of nanotubes provide a better binding environment compared to flat surfaces.

Another advantage of SWNTs is that they are all-surface materials, generally found in bundles with a large density of inter-nanotube pores and grooves. In SWNT bundles, four types of active sites for adsorption have been identified:<sup>6</sup> inner core of the nanotubes or the axial site, the inner and outer shell of each SWNT, interstitial channels between two nanotubes and the external groove sites. Cole *et al.*<sup>7</sup> used the anisotropic Ising model to study the nature of adsorbed gases in the interstitial channels of SWNTs. It showed that adsorbed gases undergo a phase transition to the condensed state at low temperatures inside these channels. Gases adsorbed inside the core of SWNTs undergo capillary condensation.<sup>6</sup> In the case of multi-walled carbon nanotubes (MWNTs), adsorption occurs by simple physisorption, the adsorption sites being the inner and outer walls.

## **2. Scope of the present investigations**

Hydrogen adsorption at solid surfaces is carried out under applied pressure and temperature. Adsorption occurs either by physisorption or chemisorption. The distance of the molecule adsorbed from the surface determines the nature of adsorption.<sup>8</sup> In carbon nanotubes (CNT) and graphene adsorption occurs under cryogenic conditions. This is

because of the low interaction energy for adsorption of H<sub>2</sub> on graphene or CNT surface, about 2 kcal/mol. For any practical application the optimal interaction energies should be between those of physisorption and strong chemical bonds. Thermodynamics calculations show that the optimum interaction energy for significant but reversible storage under ambient conditions is around 7 kcal/mol, so that sufficient H<sub>2</sub> can be stored at room temperature. The desorption process also should have very low activation barrier such that H<sub>2</sub> can be released slowly under small perturbations like temperature or pressure. Generally, two main methods have been sought to increase the activation energy of adsorption: doping with heteroatoms or incorporating light metal atoms in order to increase the binding to H<sub>2</sub> due to charge induced dipole interactions. H<sub>2</sub> storage capacity of up to 14 wt% at ambient temperature and pressure has been reported in Li and K intercalated MWNTs.<sup>9</sup> The alkali metal centers seem to act as catalytically active centers for dissociative H<sub>2</sub> adsorption followed by spill-over of dissociated H atoms to the carbon and finally getting bonded to carbon atoms. The adsorbed H<sub>2</sub> desorbed completely on heating to 873 K. Later experiments however indicated that the high hydrogen uptake reported were from water impurities present in the system.<sup>10,11</sup> More recently, H<sub>2</sub> adsorption via Kubas interaction followed by dissociation of H<sub>2</sub> on metal particles have been reported by Reyhaniet *al.*<sup>12</sup> in metal nanoparticle decorated with MWNTs. Pd nanoparticles turn out to be the most effective with H<sub>2</sub> storage capacity of 7 wt% and highest desorption onset temperature of 62°C. Dissociative adsorption of a H<sub>2</sub> on Pt and Pd decorated SWNTs has been studied by Dag *et al.*<sup>13</sup> suggesting a similar mechanism. However in all the above cases all the H<sub>2</sub> adsorbed desorbs completely on heating to a particular temperature resulting in release of huge quantities of H<sub>2</sub> at a time. This is impractical and unsafe from the view point of use in vehicular transport. For a material to work as H<sub>2</sub> source for vehicular transport very slow release of H<sub>2</sub> under conditions like temperature or pressure with slightly but within safe limits away from ambient conditions is needed.

The strength of chemisorption of hydrogen on SWNTs is ~ 2.5 eV per H atom while that of physisorption is 0.11 eV per H<sub>2</sub> molecule.<sup>14</sup> Density functional theory (DFT) calculations suggest 7.5 wt% H<sub>2</sub> storage in graphene through the formation of C-H bonds<sup>14</sup> which is close to the theoretical uptake of hydrogen by hydrogenation. It has been

shown that reaction of single-layer graphene with hydrogen atoms generates sp<sup>3</sup> C-H bonds on the basal plane and the reduced material can be dehydrogenated on photothermal heating.<sup>15</sup> Reaction of atomic hydrogen with graphene to produce hydrogenated graphene has been reported in literature,<sup>16,17</sup> though the nature of hydrogen in the hydrogenated samples or the amount of hydrogen uptake by graphene has not been delineated. Chemical hydrogenation of CNTs was first carried out by Pekker *et al.*<sup>18</sup> in liquid ammonia in the presence of Li metal. They obtained 0.72 wt% H<sub>2</sub> desorption corresponding to C: H ratio of 10.8:1. Hydrogenation was attained using atomic hydrogen beam by Nikitin *et al.*<sup>19</sup> XPS measurements revealed 65 atomic % hydrogenation of carbon atoms which corresponds to 5.1 wt% of H<sub>2</sub>. The C-H bonds thus formed were stable at ambient temperature and pressure and broke completely above 600 °C. Molecular H<sub>2</sub> also led to hydrogenation in CNTs at elevated temperature and pressure.<sup>20</sup> At 400-450 °C and 50 bar H<sub>2</sub> pressure, one third of carbon atoms on SWNTs formed covalent C-H bonds. On annealing at 550 °C, some of these nanotubes unzipped to form nanoribbons. However in these cases the release profile that is the time and the temperature range over which release takes place has not been characterized properly. Moreover, most of these processes required high temperature or pressure or energy intensive processes like atomization of H<sub>2</sub>.

Birch reduction,<sup>21</sup> which is widely used to hydrogenate sp<sup>2</sup> carbon-based materials has since long been used to reduce C<sub>60</sub> and C<sub>70</sub> yielding C<sub>60</sub>H<sub>36</sub> and C<sub>70</sub>H<sub>30</sub>, respectively.<sup>22,23</sup> Birch reduction involves reduction of aromatic benzenoid rings to 1,4-cyclohexadienes with two H atoms attached on opposite ends. The reaction takes place in liquid ammonia in presence of alkaimetal (Li, Na or K) followed by addition of an alcohol like ethanol or tert-butanol. The Li in Liquid NH<sub>3</sub> gives the electride salt [Li(NH<sub>3</sub>)<sub>x</sub>]<sup>+</sup>e<sup>-</sup>, associated with the intense blue color. The solvated electrons can add to the aromatic ring and form radical anion which then takes an electron from the alcohol to get protonated. Depending on electron withdrawing or electron donating substituents attached to the ring the protonation takes place at the ipso-para or ortho-meta positions, respectively. Recently, Birch reduction of few-layer graphene has been achieved with up to 5 wt% of hydrogen being incorporated. The sp<sup>3</sup> bonds formed by reduction could be broken by UV or laser irradiation or by heating to 500°C. Both wt% of H<sub>2</sub> stored and the

release characteristics make it an interesting H<sub>2</sub> storage material for vehicular transport. The inherently curved surfaces of carbon nanotubes have different reactivity than planer graphene layers. The conformational deformation of CNTs has been shown to enhance the hydrogenation energy at the location of deformation.<sup>24</sup> In this context we felt it would be interesting to carry out Birch reduction of single and multi-walled CNTs for reversible H<sub>2</sub> storage.

### ***3. Experimental Section***

#### ***Synthesis of single, double and multi-walled nanotubes***

MWNTs were prepared by pyrolysis of ferrocene and acetylene as follows. A pyrolysis reactor consisting of long quartz tube was heated in a dual tube furnace fitted with independent temperature controller. 100 mg of ferrocene was taken in a quartz boat and placed in the quartz tube such that it lies at the center of the first furnace. The tube was purged with Ar. The first furnace was heated to 250°C to vaporize ferrocene which was carried with Ar (500 sscm) to the second heating stage of the quartz tube. Pyrolysis was done at 1100°C. Acetylene was passed at 10 sscm for 5 min at the end of which the reactor was allowed to cool naturally to room temperature under Ar flow. Large quantities of carbonaceous deposits accumulated in the heating zone of the second furnace. The deposits were collected and purified by heating in dilute HCl to 60°C for 12 hrs followed by centrifugation to collect the precipitate. Thus collected precipitate was dried and observed under FESEM to characterize the purity of CNTs.<sup>25 26</sup> To remove amorphous carbon impurities the precipitate was heated at 300°C in air for 10 mins.

DWNTs were prepared by chemical vapour deposition of methane over Fe-Mo catalyst. The Fe-Mo catalyst was first prepared by combustion route.<sup>27</sup> Aqueous solution of ammonium molybdate ((NH<sub>4</sub>)<sub>6</sub>Mo<sub>7</sub>O<sub>24</sub>·4H<sub>2</sub>O) ferric nitrate ((Fe(NO<sub>3</sub>)<sub>3</sub>·9H<sub>2</sub>O)) and magnesium nitrate (Mg(NO<sub>3</sub>)<sub>2</sub>·6H<sub>2</sub>O) were mixed in the proportion such that molar ratios of Mo:Fe:MgO are 0.1:0.9:13. To this mixture was added an appropriate amount of urea (three times the stoichiometric ratio). Urea acts as fuel for the combustion process. All the water was evaporated by keeping in oven at 70 °C. The slurry was then placed in a furnace preheated at 550 °C. The thick orange-red solution immediately started boiling and underwent dehydration along with frothing and white flame. The resulting light

material swelled to the capacity of the Pyrex dish. The total combustion process was over in ~10 min after which the combustion product was baked at 550°C, for 3h followed by grinding to a fine powder. The combustion route employed here gives homogeneous catalyst particles. DWNTs were synthesized from ~200 mg of this catalyst being taken in a quartz boat placed inside a quartz tube reactor. The boat was placed at the heating zone of the furnace and heated to 950 °C in an argon atmosphere at a heating rate of 3 °C/min. A mixture of methane and Ar maintained at flow rates of 50 and 150 sscm were passed through the reactor for ~20 min, once the temperature stabilizes at 950 °C. The reactor was then allowed to cool to room temperature naturally. A dense mass of black products formed in the boat which was purified with dil. HCl treatment to obtain pure DWNTs.

SWNTs were produced by arc-discharge of composite graphite rods containing Y<sub>2</sub>O<sub>3</sub> (1 atom%), Ni (4.2 atom%).<sup>28</sup> The catalyst composite rod was prepared by drilling out graphite rods and collecting the graphite powder from the rod. The powder was then mixed with required amounts of Y<sub>2</sub>O<sub>3</sub> and Ni metal powder, grinded thoroughly and refilled into the hollowed graphite rod. Two ends of the rod were sealed with a sealant glue and reduced at 1000 °C. Reduced rod was used as the cathode and arced under He pressure of 660 Torr with a current of 100 A and 30 V. A web of carbonaceous materials was produced inside the chamber. The web was collected and purified by several cycles of acid treatment and heat treatment to remove catalyst nanoparticles and amorphous carbon respectively. First purification treatment involved heating at 300 °C for 24 h in air to remove the amorphous carbonaceous materials. This was followed by acid treatment by stirring in with conc. nitric acid 50 °C for about 12 h and washed with distilled water to remove the dissolved metal particles. Following acid treatment the purified product was heat treated at 750 °C in Ar atmosphere to remove further amorphous carbon impurities. The cycle of acid treatment followed by heat treatment in inert atmosphere was repeated 4 to 5 times until pure SWNTs were obtained. SWNTs were characterized by FESEM and HRTEM imaging.

### *Synthesis of graphene nanoribbons*

Graphene nanoribbons were prepared by oxidative unzipping of MWNTs resulting in the formation of multi walled and double walled graphene nanoribbons (MWGNR).For

### ***Chapter II.3. Chemical storage of H<sub>2</sub>.....***

---

this purpose 50 mg of MWNT was suspended in 20 ml of conc. H<sub>2</sub>SO<sub>4</sub> for over 1h by stirring at room temperature. H<sub>3</sub>PO<sub>4</sub> (85%, 2.5 ml) was then added to this dispersion and allowed to stir for ~15 min. 250 mg of KMnO<sub>4</sub> was then added to the mixture ensuring the temperature does not rise above room temperature. The reaction mixture was then heated to 65°C and allowed to stir for 2hrs and allowed to cool to room temperature. After the reaction mixture has cooled to room temperature the entire solution was poured into 100 ml ice containing 5ml H<sub>2</sub>O<sub>2</sub> (30%) and the product was allowed to stir for 1 h and then allowed to coagulate overnight. The product was filtered through PTFE membrane (200 nm pore size). It was then washed by suspending it in 30% HCl solution for 2h with stirring and then allowed to coagulate. This was filtered through PTFE membrane and suspended again in ethanol for 5h followed by coagulation and filtration. Final filtered product was filtered with ether (2ml) and allowed to dry. FESEM and TEM characterization of the product was carried out before use.

#### ***Birch reduction***

Birch reduction of CNTs and GNRs was carried out as follows: 70 mg of CNT/GNR was suspended in a round bottom flask containing 40 ml dry liquid NH<sub>3</sub> and 700 mg of Li metal. The resulting solution turned intense blue colour on complete dissolution of Li metal in ammonia. The solution was refluxed at -33°C for 1 h by connecting the round bottom flask to a reflux condenser containing slurry of liquid N<sub>2</sub>- water and methanol. At the end of the reaction 10 ml of 2-methyl 1-propanol was added slowly. The reaction was slowly heated to room temperature and allowed to stand till all ammonia evaporates. The black product contains large amounts of LiOH and was washed several times with water, dil HCl and methanol to remove all impurities. The sample was dried at 50 °C

#### ***Characterization***

The obtained products were characterized via IR spectroscopy to identify reduction and formation of C-H bonds. For IR spectra small amounts of the sample was mixed with completely dried KBr and pelletized. Raman and XPS analysis were used to characterize the ration of sp<sup>2</sup> to sp<sup>3</sup> carbon in the sample. Weight percent of hydrogen was accurately

determined using elemental analysis-CHNS analysis and gas chromatography. Details of characterization are provided in Appendix.

### ***H<sub>2</sub> release studies***

H<sub>2</sub> release was studied by combination of different techniques. Gas chromatography (GC) was carried out in the temperature range room temperature to 700°C to determine the release profile of H<sub>2</sub>. For this 50 mg of sample was heated in a closed steel tube with the evolved gases being carried to gas chromatograph by a flow of 10 sscm of N<sub>2</sub>. Sampling was done after every five minutes with the sample being maintained at a particular temperature till all the H<sub>2</sub> evolution at that temperature becomes negligible. The GC was earlier calibrated with 1000 ppm H<sub>2</sub> in N<sub>2</sub> mixture with the flow being maintained at 10 sscm. Temperature programmed thermo gravimetric analysis was carried out (27°C-120°C @ 2°C/ min holding at 120°C for 30 min to remove all water followed by heating from 120°C to 800°C @ 1 °C/min) to determine the amount of H<sub>2</sub> given out. Elemental analysis-CHNS analysis of initial and products heated to different temperature provide the percentage of H<sub>2</sub> recovered on heating.

## ***4. Results and Discussion***

As discussed already CNTs were chosen as matrix to achieve chemical storage of H<sub>2</sub> based on the fact that curved surfaces in CNTs intrinsically provide enhanced hydrogenation energies than flat surface of graphene. Graphene nanoribbons unlike graphene are composed mainly of edges and are inherently more reactive than graphene. First step to achieve efficient chemical storage of H<sub>2</sub> in these materials was to obtain pure form of these nanomaterials. Characterization of synthesized CNTs and GNRs is necessary since most of these materials are obtained as mixture of amorphous carbon and crystalline product in the initial step of production. Further purification yields pure nanomaterials. FESEM and TEM imaging are most commonly used and effective characterization techniques for these nanomaterials.

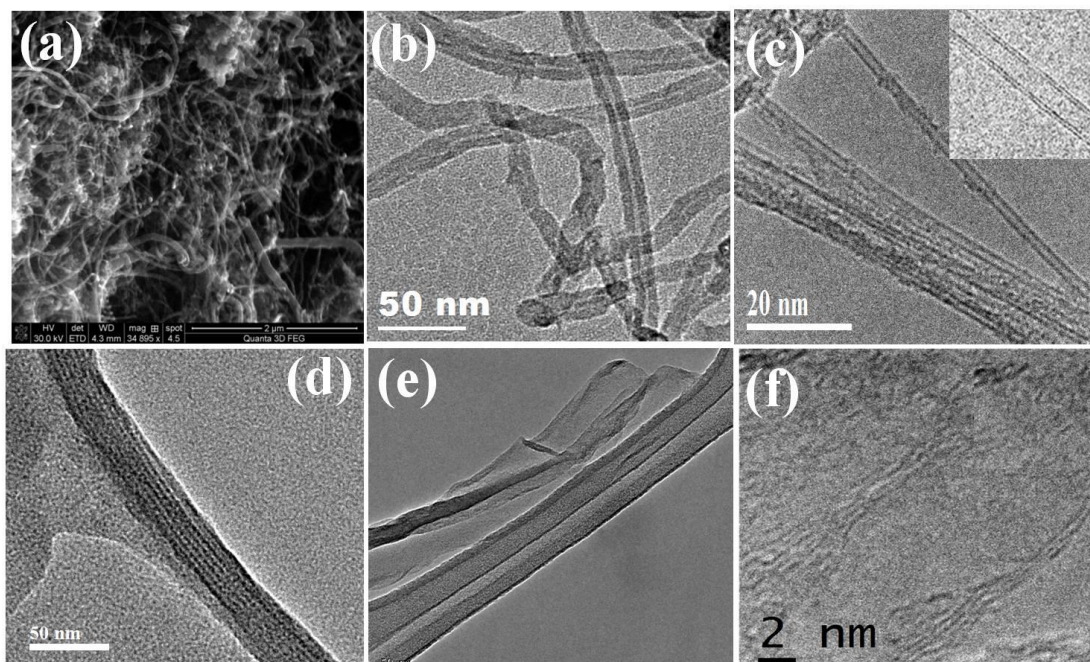


**Figure 1.** (a) FESEM image of as prepared MWNT, TEM images of purified (b) MWNT, (c) DWNT, (d) SWNT and (e) MWGNR, (f) HRTEM of MWGNR. Inset in (c) shows the HRTEM of DWNT.

Figure 1 (a) shows the FESEM image of as obtained MWNTs containing majority of nanotubes along with some metal nanoparticles and small quantities of amorphous carbon. Treatment with dil. HCl followed by washing removes the metal nanoparticle impurities while heat treatment in air subsequent to acid treatment removes most of the amorphous carbon impurity. TEM images of purified MWNTs are shown in Figure 1 (b). Figure 1(c) shows TEM image of a purified DWNT sample showing a group of three DWNTs with the HRTEM image of one of them is shown as inset. The HRTEM image clearly shows double walled edges of the nanotubes. DWNTs prepared by this method are generally straight unlike MWNTs which are more curled. However both MWNTs and DWNTs exist as individual nanotubes, while SWNTs are formed in bundles. Figure 1 (d) shows the TEM image of one such bundle composed of about 5-6 straight SWNTs. GNRs were produced by oxidative unzipping of MWNTs and DWNTs. Figure 1 (e) show the TEM image of GNRs prepared from MNWTs (MWGNR) by oxidation induced cutting of the wall of MWNTs along one line. The GNRs are about 30-60 nm wide and over a micron in length. Unlike, MWNTs from which they are made, GNRs are much more flexible and



are composed of rough edges on both sides of the ribbon. Figure 1 (f) shows the HRTEM image of a GNR made from DWNTs, showing clearly double layers with uneven edges and flexible ribbon like nature.

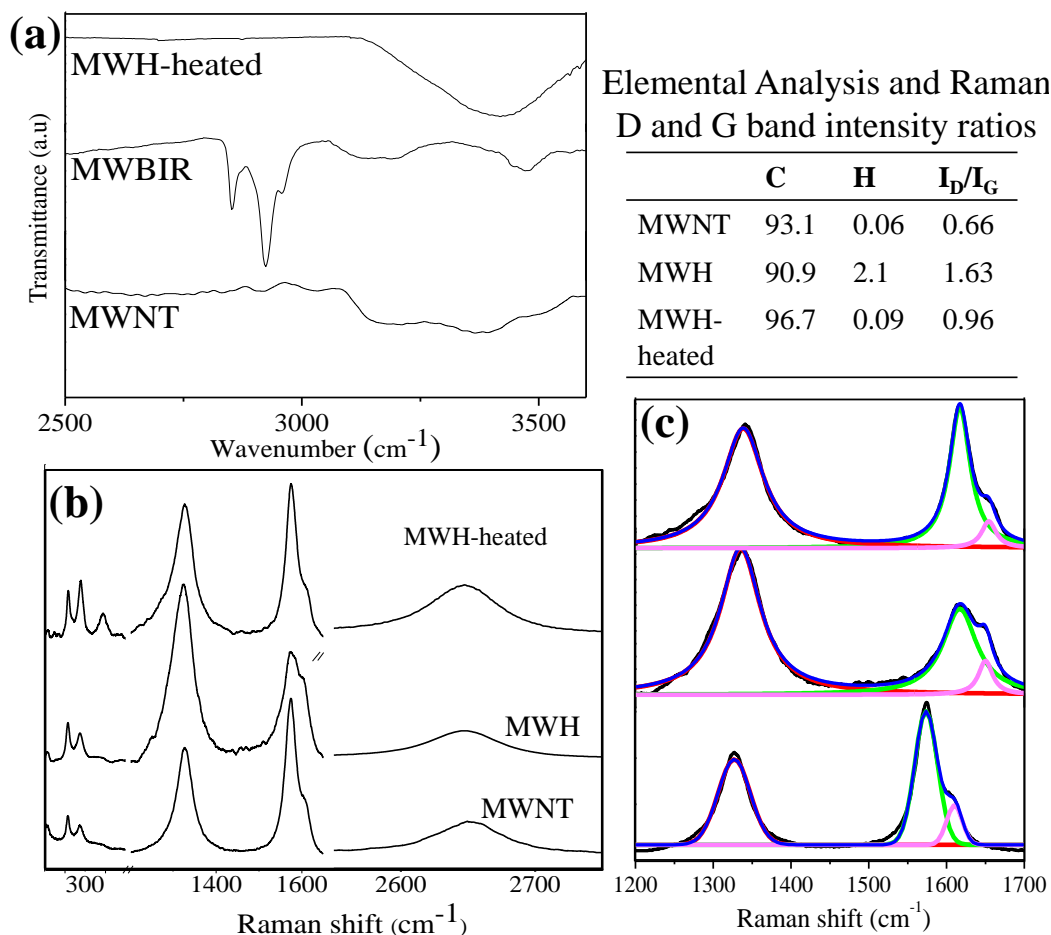


**Figure 2.** (a) IR spectra, (b) Raman spectra of MWNTs, MWH and MWH heated to 700°C. (c) Raman spectra fitted to show the D, G and G' band. The table gives the wt% of C and H in each sample and the intensity ratios of Raman D and G bands.

Birch reduction of MWNTs were carried out as described in the experimental section. IR spectroscopy was used as an initial characterization tool for hydrogenation of MWNTs. IR spectra of purified MWNTs do not show any characteristic bands except the broad band due O-H stretching in the range 3300-3600 cm<sup>-1</sup>. The IR spectra of hydrogenated MWNTs on the other hand show strong C-H stretching bands at 2850–2950 cm<sup>-1</sup> region while the initial nanotubes did not show a band in this region. The

Elemental analysis of the samples indicates wt% of H in hydrogenated MWNT to be ~2.1% while pristine MWNTs did not have any H. Raman spectra of the pristine MWNTs show D and G bands characteristic of Carbon samples. The G band at around 1570-1590 cm<sup>-1</sup> arises from sp<sup>2</sup> hybridized carbon of graphitic origin while the D band at ~1325-1330 cm<sup>-1</sup> is known to originate from sp<sup>3</sup> hybridized carbon in graphene matrix. The G' band a double resonant band also has its origin in defects in sp<sup>2</sup> layers. On hydrogenation the intensity of both the D and the G' bands in MWNT increased, while the position of the bands remained roughly the same. The intensity ratio of D band to G band is an indicator of the sp<sup>3</sup> to sp<sup>2</sup> C ratio. The I<sub>D</sub>/I<sub>G</sub> increases from 0.83 to 1.63 on hydrogenation indicating a marked increase in sp<sup>3</sup> C content. Relative increase in sp<sup>3</sup> carbon content can also be monitored by XPS analysis.

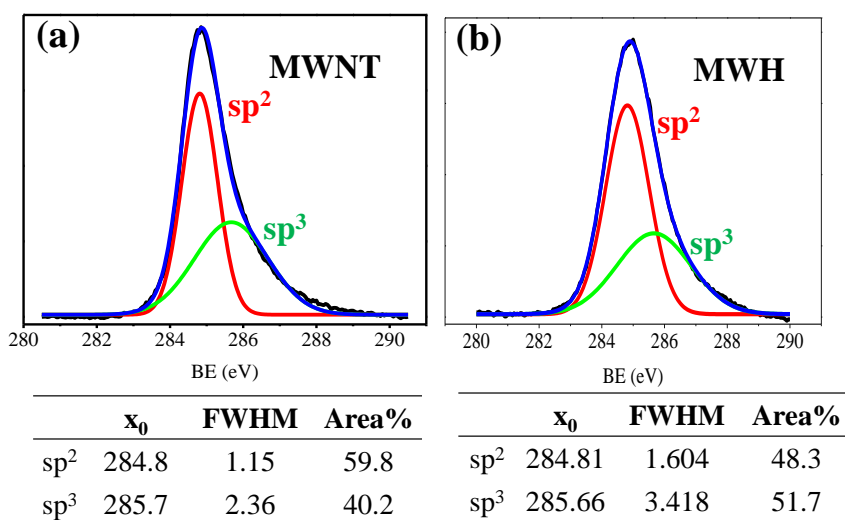


**Figure 3.** C 1s XPS spectra of (a) MWNT and (b) MWH. Table below each shows the peak positions, FWHM and % of area for contributions from sp<sup>2</sup> and sp<sup>3</sup> carbon.

Figure 3 shows the C-1s XPS spectra of MWNT and hydrogenated MWNT. The binding energy for sp<sup>2</sup> and sp<sup>3</sup> C atoms are ~ 284.8 and 285.7 eV, respectively. The carbon 1s XPS spectra of MWNT and MWH were de-convoluted to show the contributions due to the sp<sup>2</sup> and sp<sup>3</sup> carbon. While the peak positions in both the spectra remain the same, the

FWHM as well as the area of the peak due to sp<sup>3</sup> carbon increases significantly on hydrogenation. The % contribution each to the total area of the 1s-C is listed in tables below the XPS spectra. On hydrogenation the % of sp<sup>3</sup> carbon increases from 40.2% to 51.7% an increase of 28%. Assuming all the increase in sp<sup>3</sup> carbon arises from hydrogenation of MWNT the hydrogen wt% was calculated to be 2.12%. Having confirmed successful hydrogenation of MWNTs with upto 2 wt% of hydrogen content we looked at hydrogen release characteristics of MWH using a combination of GC and TGA analysis.

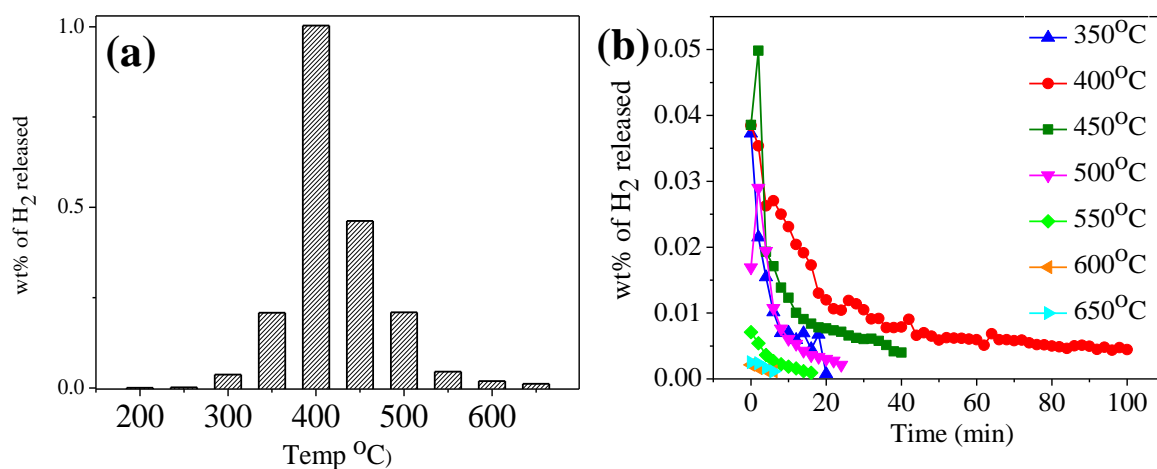


**Figure 4.** (a) Plot of H<sub>2</sub> released at different temperatures by MWH and (b) the release profile of the H<sub>2</sub> evolved by MWH was studied by gas chromatography.

The release of H<sub>2</sub> by MWH was studied by heating known quantity of sample in a steel tube under N<sub>2</sub> flow. The evolved gases were studied using a GC calibrated to measure H<sub>2</sub>-N<sub>2</sub> mixtures. On heating the sample from room temperature to 200°C we did not observe any evolution of H<sub>2</sub>. On heating beyond 200°C the sample starts evolving H<sub>2</sub> slowly with the evolution reaching maxima at 400°C as shown in Figure 4 (a). Figure 4(b) shows the H<sub>2</sub> release profile over various temperatures starting from 350°C to 650°C with the sample being maintained at a particular temperature till the H<sub>2</sub> evolution by the sample becomes negligible. On heating to 350°C the sample evolves about 0.04 wt% of H<sub>2</sub> in the first 5 mins (Figure 4(b)). H<sub>2</sub> evolution gradually decreases with time and becomes negligible in 20 mins (for 50 mg sample), with the total evolution being ~0.2 wt% at 350°C (Figure 4(a)). On heating further to 400°C the sample evolves about the

same wt% of H<sub>2</sub> initially, however the release at this temperature is more gradual and continues for more than 100 mins. Complete removal of all H<sub>2</sub> was possible by heating the sample to 650°C with a total of 2.15 wt% of H<sub>2</sub> released (calculated from total gas collected in the temperature range 25-650 °C). Temperature programmed TGA of MWH too shows a wt loss starting at 350°C and continuing all the way upto 650°C with total weight loss of 2.1 wt% (ignoring small weight loss due to water till 120°C). TGA of the sample initially heated to 700°C does not show any weight loss. We carried out detailed characterization of MWH after it was heated to 700°C in N<sub>2</sub> atmosphere for 3 hrs. IR spectra of the heated sample does not show any characteristic C-H stretching vibrations and the Raman D band to G band ratio decreases to 0.66 as shown in Figure 2. The elemental CHNS analysis of heated sample indicates a H wt% of 0.09, indicating that complete removal of H<sub>2</sub> from MWH was achieved. In order for MWNTs to act as good H<sub>2</sub> storage material the process of hydrogenation and removal of H<sub>2</sub> should be recyclable.

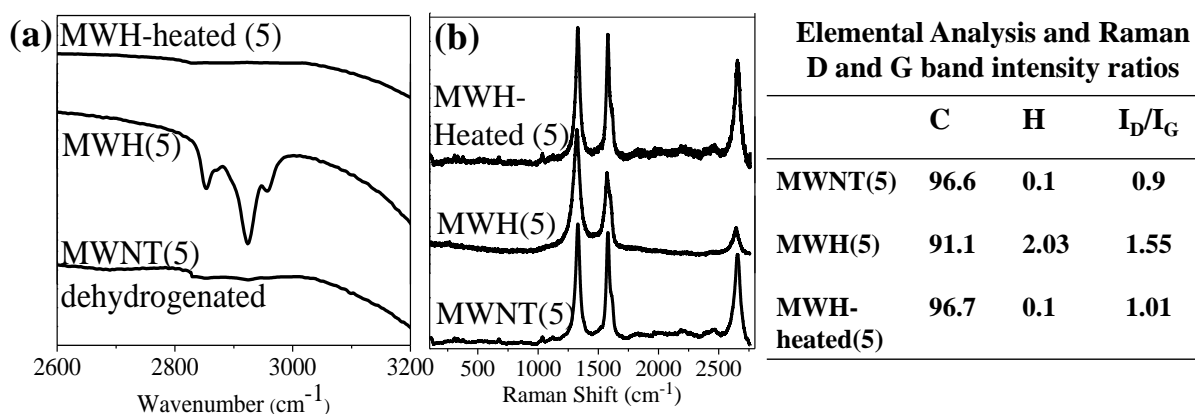


**Figure 5** (a) IR spectra and (b) Raman spectra of hydrogenated and de-hydrogenated nanotubes after 5 cycles of hydrogenation and de-hydrogenation. Table shows the C and H weight % and intensity ratios of D and G band as determined from elemental analysis and Raman spectroscopy.

We carried out five cycles of hydrogenation and de-hydrogenation of MWNTs and characterized the products. Even after five cycles of hydrogenation and de-hydrogenation MWNTs can store reversibly upto 2 wt% of H<sub>2</sub> as shown by elemental analysis. IR and Raman studies show increase in C-H stretching frequencies and in intensity of D band on hydrogenation and complete reversal to MWNT on heat treatment indicating the

cyclability of the process. Having found that Birch reduction of MWNTs is a suitable way to reversible chemical storage of H<sub>2</sub> we decided to study Birch reduction of DWNTs and SWNTs keeping in mind that DWNTs and SWNTs intrinsically possess more surface area than MWNTs.

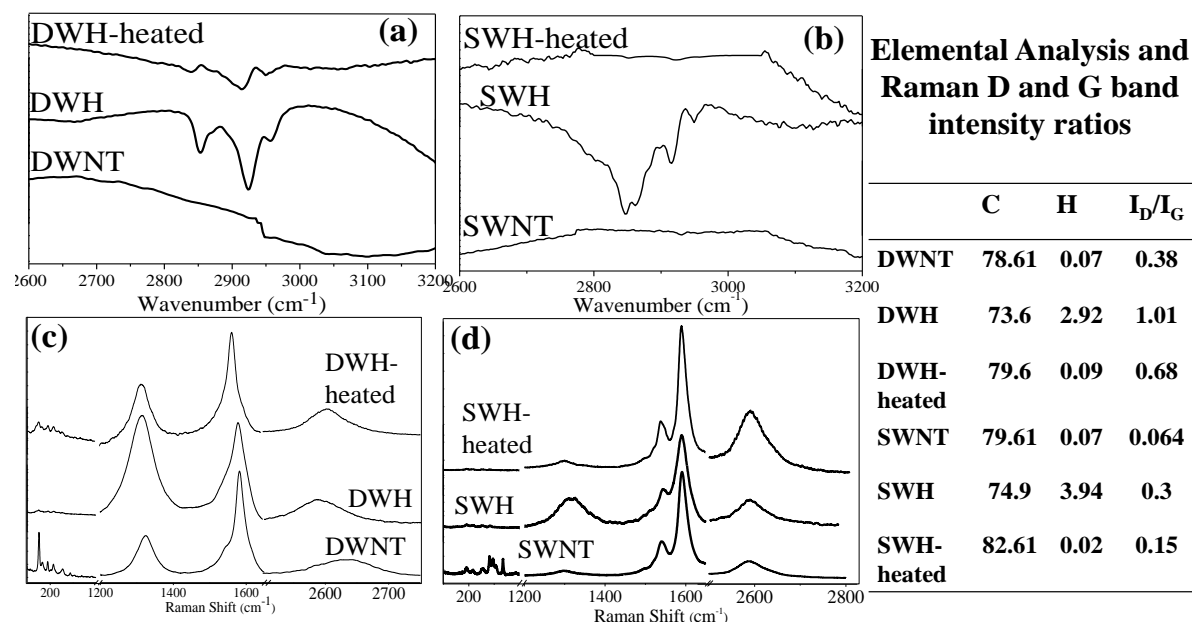


**Figure 6** (a) and (b) IR spectra and (c) and (d) Raman spectra of hydrogenated and dehydrogenated DWNTs and SWNTs, respectively. Table shows the C and H weight % and intensity ratios of D and G band as determined from elemental analysis and Raman spectroscopy.

DWNTs and SWNTs were hydrogenated in a manner similar to that of MWNTs. IR spectra of hydrogenated DWNTs and SWNTs (DWH and SWH) shows strong C-H stretching bands in the range 2850–2950 cm<sup>-1</sup> while DWNTs and SWNTs do not show any band in this region as shown in Figure 6(a) and (b), respectively. Presence of C-H stretching frequency clearly indicates successful hydrogenation in DWH and SWH. Elemental CHNS analysis of DWH and SWH indicates that the DWNTs and SWNTs can store up to 2.9 wt% and 3.9 wt% of H<sub>2</sub> respectively. XPS analysis of hydrogenated DWNT reveals an increase in area of sp<sup>3</sup> C from 20.4% to 34.8% corresponding to H content of 2.72%. Similarly the area for sp<sup>3</sup> C in SWH is increased to 40.5% from 19.8% in SWNTs, indicating H weight % of 4.16%. The Raman D band intensity increases on

hydrogenation such that the ratio of Raman D to G band intensities increases from 0.38 in DWNTs to 1.01 in case of DWH as shown in Figure 6 (a). Raman D band of pristine SWNTs is very weak with I<sub>D</sub> to I<sub>G</sub> ratio of only 0.064. Hydrogenated SWNTs on the other hand show strong D band, the I<sub>D</sub>/I<sub>G</sub> ratio being 0.3. The G band for SWNTs consist of two modes G<sup>+</sup> and G<sup>-</sup> at 1590 cm<sup>-1</sup> and 1540 cm<sup>-1</sup>, respectively arising from in-plane vibrations along the tube axis and circumferential directions. Interestingly, the ratio of G<sup>+</sup> to G<sup>-</sup> increases along with broadening of the G<sup>-</sup> band a probable reason for which will be discussed later.

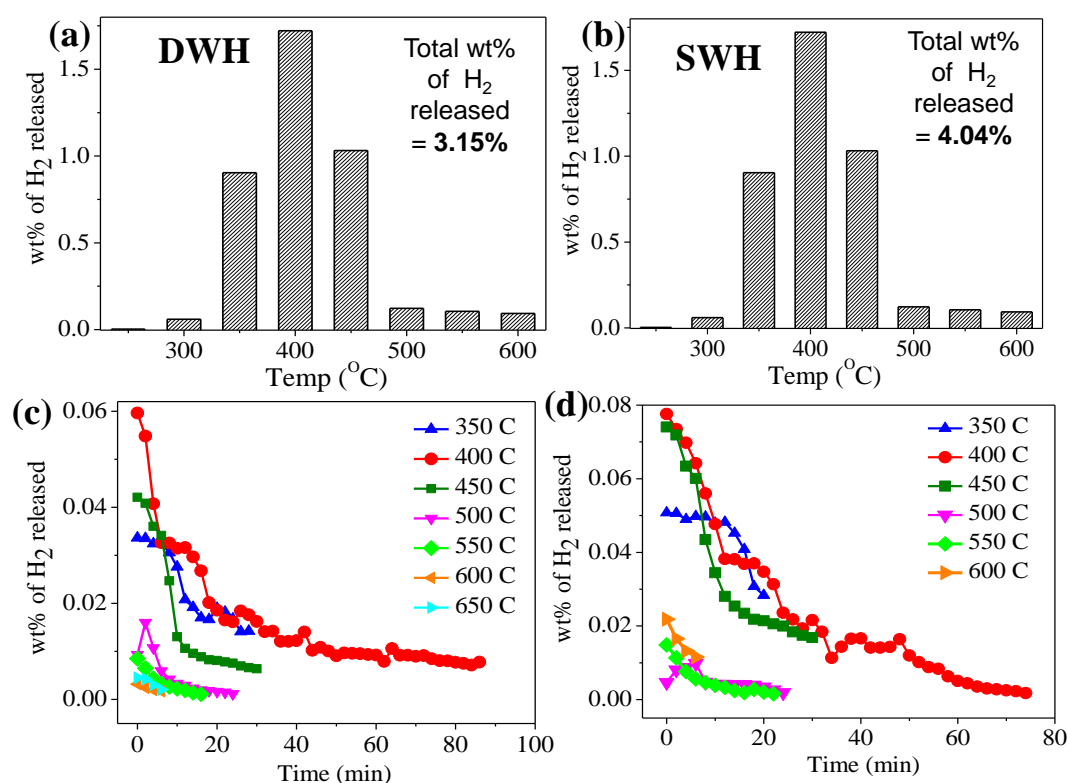


**Figure 7.** (a) and (b) Plot of H<sub>2</sub> released at different temperatures by DWH and SWH, respectively, (c) and (d) shows the release profile of the H<sub>2</sub> by DWH and SWH, respectively.

Thermal stability and desorption behavior of DWH and SWH were studied as described earlier. Both DWH and SWH are stable up to 250°C showing first sign of evolution only after heating the sample to 300°C. Figure 7 shows the amount of H<sub>2</sub> released and temperature dependent release profile of H<sub>2</sub> by the samples. As in case of hydrogenated

MWNTs, DWH and SWH too show maximum H<sub>2</sub> evolution at 400°C releasing almost 1.75 wt% of H<sub>2</sub> at this temperature. As observed earlier, both DWH and SWH release H<sub>2</sub> very slowly at an average rate of  $\sim 4.5 \text{ mL.g}^{-1}.\text{min}^{-1}$  over a period of 80 mins. Both the samples release all the H<sub>2</sub> stored by 650°C. On complete release of H<sub>2</sub> birch reduced SWNTs released a total of 4.04 w% of H<sub>2</sub> while DWNTs released 3.15 wt% of H<sub>2</sub>. The quantity of H<sub>2</sub> released was verified with temperature programmed TGA. IR-spectra of samples heated to 700°C in N<sub>2</sub> atmosphere do not show any signature due to C-H stretching frequency indicating complete loss of all the H<sub>2</sub> on heating. Raman spectra of the heated samples show a decrease of the I<sub>D</sub>/I<sub>G</sub> ratios as shown in table alongside Figure 6 (d), shows the I<sub>D</sub>/I<sub>G</sub> ratios of the heated sample are much greater than those of pristine DWNT and SWNT. This clearly indicates that even though heating removes all H<sub>2</sub> from the hydrogenated samples, the process of hydrogenation by birch reduction creates defects on DWNTs and SWNTs, an effect more pronounced in case of SWNTs than in case of DWNTs. Another aspect that is very evident from Raman analysis is that SWNTs after birch reduction followed by heat treatment do not show any radial breathing modes as shown in Figure 6(d).

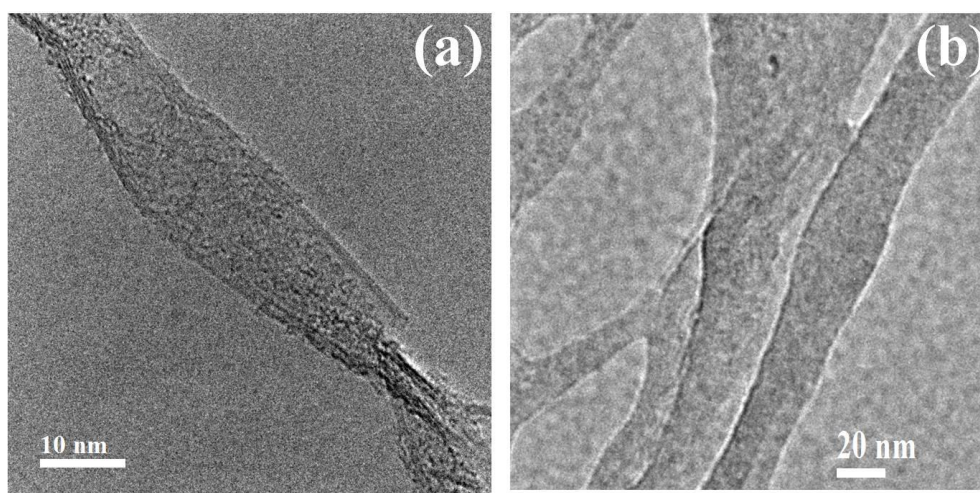


**Figure 8.** TEM images of (a) de-hydrogenated DWH and (b) de-hydrogenated SWH showing nanoribbons.

Radial breathing modes in nanotubes arise from radial expansion-contraction of the nanotubes. A loss in radial breathing mode signifies a loss of tube like feature. To probe into this further we carried out TEM analysis of DWH and SWH samples after dehydrogenation by heat treatment. The TEM images of de-hydrogenated SWH and DWH are shown in Figure 8. Interestingly, TEM images of the de-hydrogenated DWH and SWH samples reveal formation double layer and single layer graphene nanoribbons of width varying from 10-30 nm and several microns in length as shown in Figure 8 (a) and (b). During the method of birch reduction using Li in liquid NH<sub>3</sub>, it is possible that Li gets intercalated in between the tube walls. On addition of 2-methyl 1-propanol this intercalated Li reacts exothermically with alcohol creating enough energy to cut nanotubes at already created defect sites.

To check recyclability of DWNTs and SWNTs for use as potential hydrogen storage material we carried out 6 cycles of hydrogenation and de-hydrogenation on both DWNTs and SWNTs. Interestingly, in case of both the samples wt% of H<sub>2</sub> stored reduces drastically at the end of first cycle and remains constant thereafter. While DWNTs can store up to 2.9 wt% of H<sub>2</sub> repetitively from second cycle onwards SWNTs can store up to 3.2 wt% of H<sub>2</sub> as confirmed from elemental CHNS analysis. We assumed that drastic reduction in H<sub>2</sub> storage capacity at the end of first cycle could be an effect of conversion of nanotubes to graphene nanoribbons in the process of birch reduction. To further verify this we looked at H<sub>2</sub> storage properties of few-layer GNRs prepared by oxidative unzipping of MWNTs.

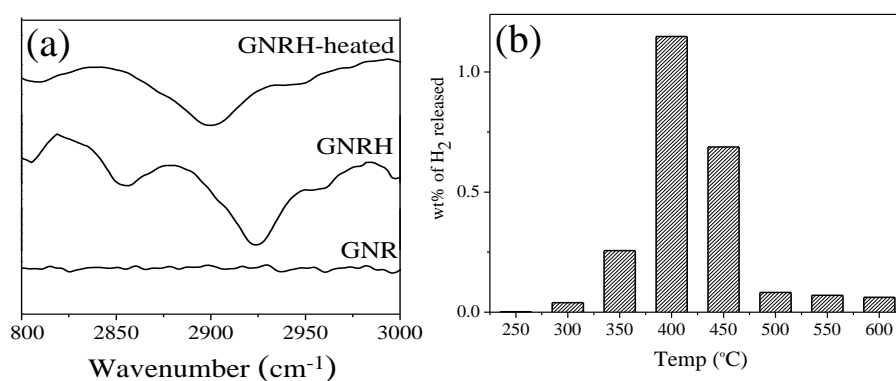


**Figure 9** (a) IR spectra and (b) temperature dependent de-hydrogenation behavior of GNRH



Figure 9(a) shows the IR spectra of birch reduced few-layer GNRs clearly revealing the appearance of strong C-H stretching vibrations. On heat treatment the sample loses almost all the peaks due to C-H stretching indicating removal of H<sub>2</sub>. Elemental CHNS analysis of the samples indicate that few-layer GNRs can store up to 2.85 wt% of H<sub>2</sub> reversibly close to that observed for DWNTs after first cycle. Thermal desorption behavior of the few-layer GNRs as studied by GC analysis shows GNRs too loose maximum H<sub>2</sub> at 400°C with de-hydrogenation starting at 250°C and complete de-hydrogenation by 650°C as shown in Figure 9 (b). On heating the sample loses a total of ~2.5 wt% H<sub>2</sub> as verified by GC analysis.

## 5. Conclusions

Present study demonstrates that carbon nanotubes are suitable candidates for chemical storage of H<sub>2</sub> by Birch reduction. Wt% of H<sub>2</sub> stored by different samples is presented in Table below. While MWNTs can store ~2 wt% of H<sub>2</sub> DWNTs and SWNTs can store a maximum of ~3 wt% and 4 wt% respectively. Chemically stored H<sub>2</sub> can be fully released by simply heating the sample in inert atmosphere. GC analysis of thermal stability and H<sub>2</sub> release behavior of the hydrogenated samples indicate that the samples are stable up to 250°C and start releasing H<sub>2</sub> only after heating the samples beyond 300°C. All samples release maximum H<sub>2</sub> at 400°C at a controlled rate of ~4.5 mL.g<sup>-1</sup>.min<sup>-1</sup> over a period of 80-100 mins for 50 mg of sample; allowing controlled release of H<sub>2</sub>. Interestingly, under Birch reduction conditions SWNTs and DWNTs get unzipped to form corresponding nanoribbons. Both nanoribbons obtained during Birch reduction and those prepared by oxidative unzipping of MWNTs also show good hydrogenation properties storing up to 2.5 wt% of H<sub>2</sub>.

**Table.** Comparison of wt% of H<sub>2</sub> stored in different samples by Birch reduction.

Sample	SWNT	DWNT	MWNT	3-4 layer GNR	3-4 layer Graphene
H <sub>2</sub> Wt%	4	3	2	2.5	5

## References

1. M. Gratzel. *Nature* **2001**, 414, 338-344.
2. M. A. de la Casa-Lillo, F. Lamari-Darkrim, D. Cazorla-Amors and A. Linares-Solano. *J. Phys. Chem. B* **2002**, 106, 10930-10934.
3. A. Peigney, C. Laurent, E. Flahaut, R. R. Bacsa and A. Rousset. *Carbon* **2001**, 39, 507-514.
4. C. N. R. Rao, A. K. Sood, R. Voggu and K. S. Subrahmanyam. *J. Phys. Chem. Lett.* **2010**, 1, 572-580.
5. S. K. Bhatia and A. L. Myers. *Langmuir* **2006**, 22, 1688-1700.
6. M. M. Calbi, M. W. Cole, S. M. Gatica, M. J. Bojan and G. Stan. *Rev. Mod. Phys* **2001**, 73, 857.
7. M. W. Cole, V. H. Crespi, G. Stan, C. Ebner, J. M. Hartman, S. Moroni and M. Boninsegni. *Phys. Rev. Lett.* **2000**, 84, 3883.
8. L. Schlapbach and A. Züttel. *Nature* **2001**, 414, 353-358.
9. P. Chen, X. Wu, J. Lin and K. L. Tan. *Science* **1999**, 285, 91-93.
10. R. T. Yang. *Carbon* **2000**, 38, 623-626.
11. F. E. Pinkerton, B. G. Wicke, C. H. Olk, G. G. Tibbetts, G. P. Meisner, M. S. Meyer and J. F. Herbst. *J. Phys. Chem. B* **2000**, 104, 9460-9467.
12. A. Reyhani, S. Z. Mortazavi, S. Mirershadi, A. Z. Moshfegh, P. Parvin and A. N. Golikand. *J. Phys. Chem. B* **2011**, 115, 6994-7001.
13. S. Dag, Y. Ozturk, S. Ciraci and T. Yildirim. *Phys. Rev. B* **2005**, 72, 155404.
14. J. Li, T. Furuta, H. Goto, T. Ohashi, Y. Fujiwara and S. Yip. *J. Phys. Chem.* **2003**, 119, 2376-2385.
15. S. Ryu, M. Y. Han, J. Maultzsch, T. F. Heinz, P. Kim, M. L. Steigerwald and L. E. Brus. *Nano Lett.* **2008**, 8, 4597-4602.
16. D. Haberer, D. V. Vyalikh, S. Taioli, B. Dora, M. Farjam, J. Fink, D. Marchenko, T. Pichler, K. Ziegler, S. Simonucci, M. S. Dresselhaus, M. Knupfer, B. Büchner and A. Grüneis. *Nano Lett.* **2010**, 10, 3360-3366.

17. D. C. Elias, R. R. Nair, T. M. G. Mohiuddin, S. V. Morozov, P. Blake, M. P. Halsall, A. C. Ferrari, D. W. Boukhvalov, M. I. Katsnelson, A. K. Geim and K. S. Novoselov. *Science* **2009**, 323, 610-613.
18. S. Pekker, J. P. Salvetat, E. Jakab, J. M. Bonard and L. Forr. *J. Phys. Chem. B* **2001**, 105, 7938-7943.
19. A. Nikitin, H. Ogasawara, D. Mann, R. Denecke, Z. Zhang, H. Dai, K. Cho and A. Nilsson. *Phys. Rev. Lett.* **2005**, 95, 225507.
20. A. V. Talyzin, S. Luzan, I. V. Anoshkin, A. G. Nasibulin, H. Jiang, E. I. Kauppinen, V. M. Mikoushkin, V. V. Shnitov, D. E. Marchenko and D. Norel•us. *ACS Nano* **2011**, 5, 5132-5140.
21. A. J. Birch. *J Chem. Soc.* **1944**, 430-436.
22. A. Govindaraj. *Curr Sci India* **1993**, 65, 868–870.
23. A. Govindaraj, A. Rathna, J. Chandrasekhar and C. N. R. Rao. *P Indian AS-Chem Sci* **1993**, 105, 303–309.
24. S. Park, D. Srivastava and K. Cho. *Nano Lett.* **2003**, 3, 1273-1277.
25. C. N. R. Rao and R. Sen. *Chem. Comm.* **1998**, 1525-1526.
26. Y. T. Lee, N. S. Kim, J. Park, J. B. Han, Y. S. Choi, H. Ryu and H. J. Lee. *Chem. Phys. Lett.* **2003**, 372, 853-859.
27. L. S. Panchakarla, A. Govindaraj and C. N. R. Rao. *ACS Nano* **2007**, 1, 494-500.
28. A. Govindaraj, B. C. Satishkumar, M. Nath and C. N. R. Rao. *Chem. Mater.* **1999**, 12, 202-205.

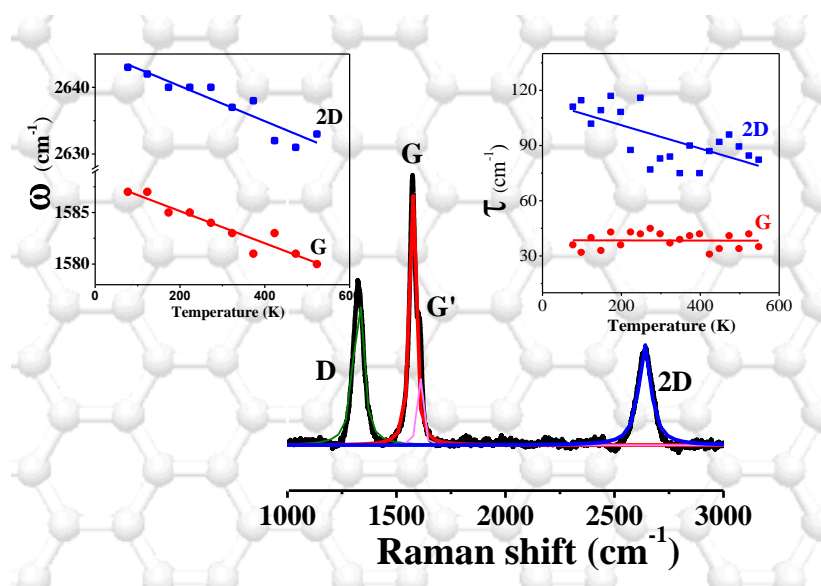


# Chapter II.4

## *Temperature effects on the Raman spectra of graphene and graphene nanoribbons*

### *Summary\**

*Temperature dependence of different modes of graphene has been studied and their temperature coefficients have been determined. The effect of number of layers, doping, functional groups, other defects on the temperature coefficients has been explored by using different types of graphene samples. Temperature coefficient of G band frequency is generally always negative and is strongly affected by number of layers, doping and the nature of graphene. While both G and 2D band frequencies and full width half maxima are sensitive to all the above, the defect induced D and D' bands are insensitive to them. The observed phenomena can be understood on the basis of electron-phonon coupling, anharmonic phonon-phonon interactions and negative thermal expansion of graphene.*



\* A paper based on this work has appeared in *J. Phys. Cond. Mater.*, 2011

## 1. Introduction

In the history of studies on graphene Raman spectroscopy has already emerged as an important structural characterization technique. Raman spectrum of graphene consist of three prominent features the D-band, G-band and the 2D band all of which can be explained based on the Brillouin Zone (BZ) of graphene and the effect of incident light on phohon modes as shown in Figure 1.

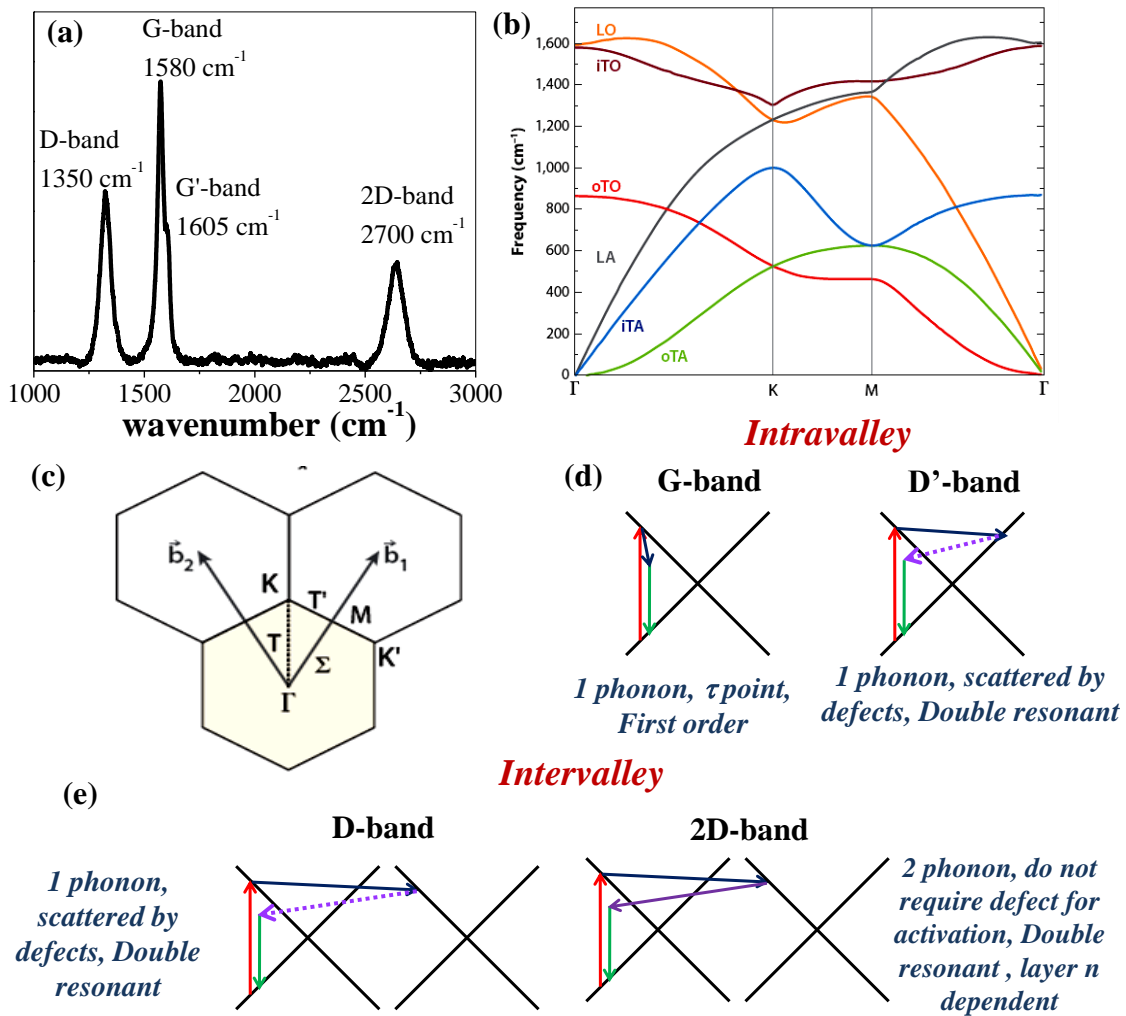


**Figure 1.** (a) Typical Raman spectrum of few-layer graphene (b) Phonon dispersion, (c) Brillouin Zone (d) the intravalley and (e) intervalley processes responsible for the origin of the Raman bands.

The G-band in graphite is the first order Raman mode corresponding to optical mode vibration of two neighbouring carbon atoms, the bond stretching of all pairs of  $sp^2$  carbons. G-band is the only first order Raman mode in graphite, the order of a scattering event being defined as its number in the sequence of the total scattering events. The Raman G band in graphite appears at  $1582\text{ cm}^{-1}$  while in case of single layer graphene it is upshifted by approximately  $5\text{ cm}^{-1}$ .<sup>1</sup> The upshift in frequency of G band was found to have  $1/n$  dependence on the number of layers  $n$  of graphene without a significant change in the line shape. This dependence has been used to characterize the number of layers in few-layer graphene samples. At  $\Gamma$  point the in-plane iTO and LO optic modes are degenerate (correspond to the vibrations of the sub-lattice A against the sublattice B) as shown in Figure 1(b). The degeneracy is lifted by applying an external stress to graphene.

The second important feature in the Raman spectrum of graphene is the D band  $\sim 1350\text{ cm}^{-1}$ , which is absent in pure graphite. The zone-boundary phonons in defect free graphite do not satisfy the Raman fundamental selection rule and are therefore not seen in the first order Raman spectra of defect free graphite. Edges and defects in single to few-layer graphene give rise to the second order, one phonon, double resonant D band, involving electronic states around two inequivalent K and K' points in the BZ of graphite. D-band is dispersive in nature i.e. the frequency of D band shifts with the energy of the incident laser.

The third most significant feature is the 2D band at  $2700\text{ cm}^{-1}$ . It is the second order Raman mode due to a double resonant process involving two phonons with opposite wave vectors. Since 2D band arises from process where momentum is conserved by two opposite wave vectors, no defects are required for their activation and are thus always present in graphene. Interesting aspect of 2D bands is that they are highly layer dependent. While, in single layer graphene the 2D band is composed of only one peak, the 2D band in graphite is composed of two distinct peaks  $2D_1$  and  $2D_2$ . For bilayer graphene the 2D band is composed of four peaks. The four double resonant process that gives rise to 2D band in bilayer graphene is demonstrated in Figure 2.

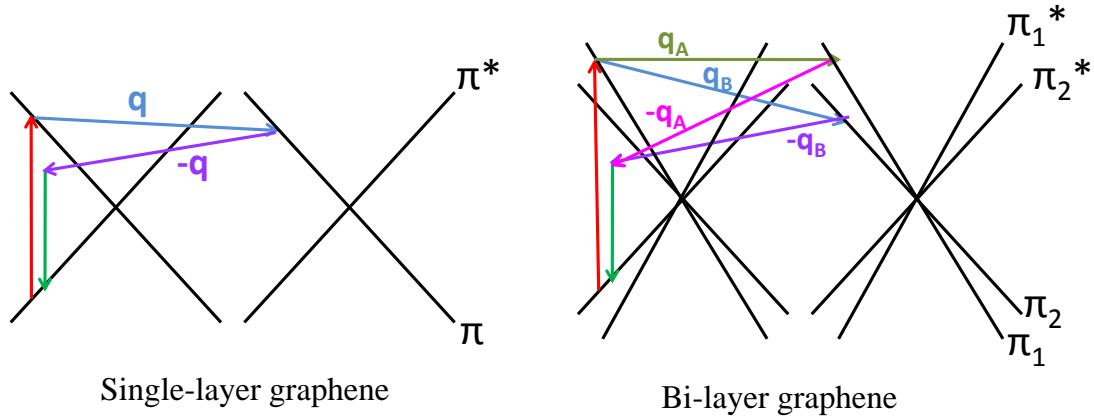


**Figure 2.** The Double resonant processes responsible for 2D band in single layer and bi-layer graphene.

In bi-layer graphene the interaction of the two graphene planes causes the  $\pi$  and  $\pi^*$  bands to divide into four bands with different splitting for electrons and holes as shown in Figure 2. The incident light generates an electron and hole pair with two possible transitions i.e.,  $\pi_1-\pi_1^*$  or  $\pi_2-\pi_2^*$  one of which is shown in Figure 2. In either case two phonons with slightly degenerate energies couple all the electron bands amongst them. The resulting four processes involve phonons with momenta  $q_{1A}$ ,  $q_{1B}$ ,  $q_{2A}$  and  $q_{2B}$  and correspondingly four different phonon frequencies due to strong phonon dispersion around  $\mathbf{K}$  induced by the electron phonon coupling, resulting in four different peaks in the Raman spectra. Thus depending on number of layers the line shape and width of the 2D band varies. As is also evident from Figure 2, the 2D band is highly dependent on laser energy showing almost a linear dependence.

Another conspicuous feature in the Raman spectrum of graphene is the D'-band at  $\sim 1605 \text{ cm}^{-1}$ . It has its origin in an intravalley double resonant process connecting two points belonging to the same cone around  $\mathbf{K}$ . Like D-band it is a single phonon process the phonon being scattered by a defect site.

Raman spectrum of graphene is not only sensitive to number of layers and defects, it is effective in determining charge carrier or molecular doping. When gate voltage is applied to move the Fermi energy of graphene into the conduction (or valence) band to dope graphene n-type (or p-type), the G-band frequency ( $\omega_G$ ) stiffens (softens) with increasing electron or hole doping.<sup>2</sup> The positive doping removes the electrons from



antibonding orbitals, and therefore a hardening of the G band is expected. On the other hand, negative doping adds electrons to the antibonding orbitals which should lead to a softening of the  $\omega_G$ . Both phonon energy renormalization and a change of the bond strength occur, and the two effects are superimposed in the analysis of the experimental data. For positive doping both effects lead to an upshift of the phonon frequency. However, for negative doping they have an opposite effect on the frequency shift.<sup>3</sup> This is consistent with the experimental results since a monotonic increase of the G band frequency was found at positive electrode potentials and a nonmonotonic change in frequency was observed for negative electrode potentials. Also, the observed shift never becomes as large for the negative potentials. The 2D peak however shows a different response to holes and electrons. The ratio of the intensities of the G and 2D peaks shows a strong dependence on doping, making it a sensitive parameter to monitor the doping.<sup>2</sup> Molecular charge transfer to or from graphene too significantly affect the  $\omega_G$ ,  $\omega_G$  decreases on interaction of graphene with electron donors and vice versa.<sup>4</sup> The Raman spectra can also show signature of effect of substrate and atmospheric adsorbates like humidity and other gases.<sup>5,6</sup>

## ***2. Scope of the present investigation***

As mentioned earlier the most important bands in the Raman spectra of graphene and are the G band ( $\sim 1580 \text{ cm}^{-1}$ ), the defect-related D band and D' bands ( $\sim 1350 \text{ cm}^{-1}$  and  $1610 \text{ cm}^{-1}$  respectively) and the 2D band ( $\sim 2700 \text{ cm}^{-1}$ ).<sup>7,8</sup> The effect of temperature on the Raman spectra of graphite and carbon nanotubes has been discussed in the literature.<sup>9-12</sup> There are a few reports on variable temperature Raman spectra of single-layer graphene prepared by mechanical exfoliation of graphite. These studies are by and large concerned with the temperature coefficient of Raman G band frequency. The temperature coefficient of the band width has been examined by two groups. There is limited information on the temperature effects with respect to the 2D and D' bands of graphene. Thus, Tan *et al.*<sup>11</sup> reported the temperature coefficient of the G mode of graphite  $\chi_G$ , to be  $-0.011 \text{ cm}^{-1}/^\circ\text{C}$  some time ago. Calizo *et al.*<sup>13</sup> have recently found  $\chi_G$  of single-layer graphene to be  $-0.016 \text{ cm}^{-1}/^\circ\text{C}$  and that of bi-layer graphene to be somewhat smaller ( $-0.015 \text{ cm}^{-1}/^\circ\text{C}$ ).

These results were taken to suggest that the temperature coefficient of the G band decreases with the increase in the number of layers. These workers do not report the dependence of the full-width-at-half-maximum (FWHM) of the G band. Malard *et al.*<sup>14</sup> find that both the G and 2D bands of SLG have negative temperature coefficients, but the temperature coefficients of the FWHMs ( $\tau$ ) of the bands show opposite slopes,  $\tau_{2D}$  being positive and  $\tau_G$  showing a small negative value. These workers observed differences in the  $\chi_G$  values measured during the heating and cooling cycles. Zhang *et al.*<sup>15</sup> report a  $\chi_G$  value of  $-0.019 \text{ cm}^{-1}/^\circ\text{C}$  for weakly doped graphene, a value slightly higher than that of SLG. Abdula *et al.*<sup>16</sup> have found the  $\chi_G$  of SLG to be  $-0.035 \text{ cm}^{-1}/^\circ\text{C}$  and  $\chi_{2D}$  to be  $-0.07 \text{ cm}^{-1}/^\circ\text{C}$  on impure graphene sample. The temperature coefficients of the FWHMs,  $\tau_G$  and  $\tau_{2D}$ , show opposite signs, the latter being positive.

Clearly, several aspects of the temperature effects on the Raman spectrum of graphene need to be fully examined. These include the effects of number of layers and doping on the temperature coefficients of the frequencies of G, 2D as well as the other Raman bands. It is also necessary to clearly determine the temperature coefficients of the FWHMs of the G and 2D bands. With this in view, we have investigated the effect of temperature on the Raman spectra of several graphene samples consisting of different number of layers as well as dopants over the 77 K- 573K range.

### **3. Experimental Section**

#### ***Synthesis of single and few-layer graphene and graphene nanoribbons:***

Single layer graphene (SLG) was prepared by mechanical exfoliation.<sup>17</sup> For this a thin sheets of graphite from highly oriented pyrolytic graphite was first deposited onto SiO<sub>2</sub> (300 nm)/Si substrates by using scotch tape followed by repeated peeling off the layers and washing with acetone to remove the glue from the tape. Thus deposited films were identified using optical microscope (attached with Raman spectrometer) and Raman spectrum.

For the preparation of single layer reduced graphene oxide (RGO), Graphite oxide (GO) was first prepared by Hummers method involving the oxidation of graphite with

strong oxidizing agents like  $\text{KMnO}_4$  and  $\text{NaNO}_3$  in  $\text{H}_2\text{SO}_4/\text{H}_3\text{PO}_4$ .<sup>18,19</sup> On oxidation, the interlayer spacing increases and exfoliation by sonication in water gives single-layer graphene oxide which was reduced with hydrazine monohydrate to give well dispersed single layer graphene sheets.<sup>20</sup>

Few-layer (5-6) exfoliated graphene (EG) was prepared by rapid heating of GO under inter atmosphere. On rapid heating decomposition rate of the epoxy and hydroxyl groups of GO exceeds the diffusion rate of the evolved gases resulting in pressures that exceed the van der Waals forces holding the graphene sheets together and exfoliation occurs. Exfoliated graphene sheets were highly wrinkled and had defects. As a result these sheets do not collapse back to graphite but remain as highly agglomerated graphene sheets.<sup>21,22</sup>

Arc evaporation (100 A, >50 V) of graphite in the presence of hydrogen ( $\text{H}_2$ : He = 70 torr : 500 torr) yielded 2-3 layered graphene (HG) having flake size of 100-200 nm. This procedure makes use of the knowledge that the presence of  $\text{H}_2$  during arc-discharge process terminates the dangling carbon bonds with hydrogen and prevents the formation of closed structures<sup>21,23,24</sup>. To prepare boron and nitrogen doped graphene (B-HG and N-HG) the discharge is carried out in the presence of  $\text{H}_2$  + diborane and  $\text{H}_2$  + (pyridine or ammonia) respectively.<sup>25,26</sup>

Few-layer and bi-layer graphene nanoribbons were prepared by longitudinal unzipping of carbon nanotubes by oxidative cutting of nanotubes using highly oxidizing mixture of conc.  $\text{H}_2\text{SO}_4:\text{H}_3\text{PO}_4$  and  $\text{KMnO}_4$  followed by treatment with dilute  $\text{H}_2\text{O}_2$ .<sup>27</sup>

### ***Raman Studies***

Raman spectra were recorded with a 632.8 nm laser in the back scattering geometry. All measurements were carried out in ambient air. As-prepared samples were taken on glass slides and heated or cooled on a heating-cooling stage fitted with a temperature sensor which could operate in the temperature range 77 K to 673 K. Low temperature measurements were carried out under flow of liquid  $\text{N}_2$  to the sample chamber such that the sample does not come in contact with liquid  $\text{N}_2$ . The temperature sensor was adjacent to the sample. All temperature coefficients were calculated from the data

collected after one cycle of cooling and heating as suggested by Mallard *et al.*<sup>14</sup> to ensure that the heating curves were completely reversible. We have used the Raman band nomenclature proposed by Ferrari *et al.*<sup>1</sup>

## **4. Results and Discussion**

We first examined the temperature effects on the Raman spectrum of SLG prepared by the mechanical exfoliation of graphite and compared the results with those reported by other workers.<sup>13-16</sup> We then studied variable temperature Raman spectra of single-layer RGO. While SLG is almost defect free, the surface of RGO has a substantial quantity of carbonyl and other oxygen functionalities. Few-layer thermally exfoliated graphene – EG, prepared from GO is comparable to single layer RGO in the context of possessing functional groups and other defects. This enabled us to determine the effect of number of layers on the nature and magnitude of the temperature effects. In order to substantiate these results, we have investigated the effect of temperature on the Raman spectra of 2-layer and 6-layer graphene nanoribbons prepared by the unzipping of carbon nanotubes. We have examined the effect of doping on the temperature effects by studying nitrogen- and boron-doped graphene in comparison with the undoped sample HG prepared by arc discharge of graphite in a hydrogen atmosphere, all containing 3-layers. Room temperature Raman spectrum of all the samples is shown in Figure 1 (a). As discussed earlier the Raman spectra of all graphene samples are composed of D, G and 2D bands, except for mechanically exfoliated SLG which does not show the D-band. Besides these prominent bands all graphene samples except SLG possess significant D'-band which as discussed has its origin in defects. The Raman D, G and D' bands are therefore deconvoluted as shown in Figure 1 (c-e) to determine their exact peak positions and peak widths, the peaks being fitted with Lorentzian function. The G-band in SLG is fitted with a single Lorentzian function. Raman spectra of all samples were collected in the temperature range 77 K -523 K and the Raman frequencies and FWHMs of each band were plotted as a function of temperature. The slope of the each plot gives the corresponding temperature coefficients. Temperature coefficients of various Raman features for different graphene samples were compared to gain an insight into the effect of defects, number of layers or dopants on the temperature coefficients.

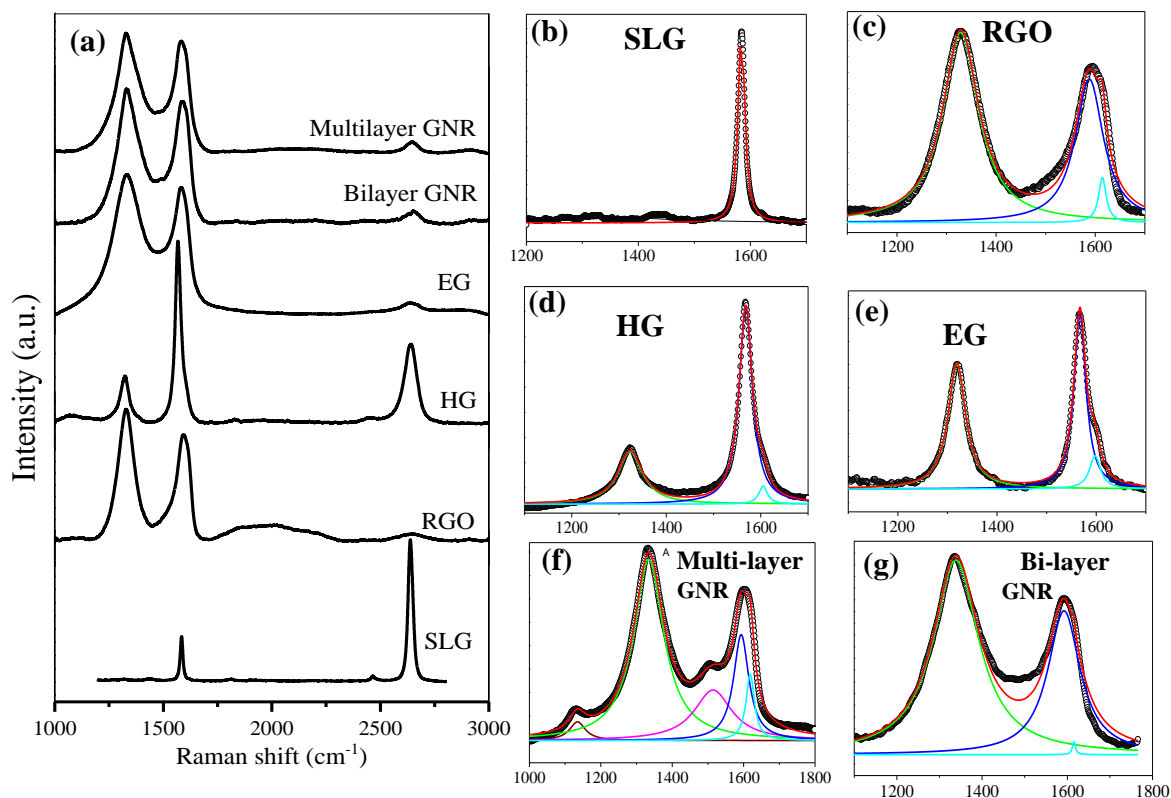


**Figure 3** Raman spectra of different graphene samples and the corresponding Lorentzian fits for the D, G and D' bands.

Single layer graphene, SLG, prepared by mechanical exfoliation of graphite shows the G band at  $1584\text{ cm}^{-1}$  and an intense 2D band at  $2635\text{ cm}^{-1}$  as can be seen from spectrum in Figure 1(a). It does not exhibit the defect-related D band as expected. The G and 2D bands vary linearly with temperature as shown in Figure 2 (a). The temperature coefficients of the frequencies of the G and the 2D bands of SLG are found to be  $-0.016\text{ cm}^{-1}/\text{K}$  and  $-0.026\text{ cm}^{-1}/\text{K}$ , respectively. The  $\chi_{\text{G}}$  value agrees with that of Calizo *et al.*<sup>13</sup> [9], but both the  $\chi_{\text{G}}$  and  $\chi_{\text{2D}}$  values are much smaller than those reported by Abdula *et al.*<sup>16</sup> who conducted several Ar annealing before determining the  $\chi$  values. Malard *et al.*<sup>14</sup> too report a comparable  $\chi_{\text{G}}$  value of  $-0.018\text{ cm}^{-1}/\text{K}$ . The temperature coefficient of the FWHM of the 2D band ( $\tau_{\text{2D}}$ ) is positive,  $+0.026\text{ cm}^{-1}/\text{K}$  as shown in inset of Figure 2(b), while that of G-band ( $\tau_{\text{G}}$ ) is slightly negative over the temperature range investigated. Figure 2(b) shows the variation of intensity ratio of 2D to G-band with temperature. The

ratio of the intensities of the 2D and G band varies little in this temperature range with very small negative slope of  $\sim -0.0034 \text{ K}^{-1}$ .

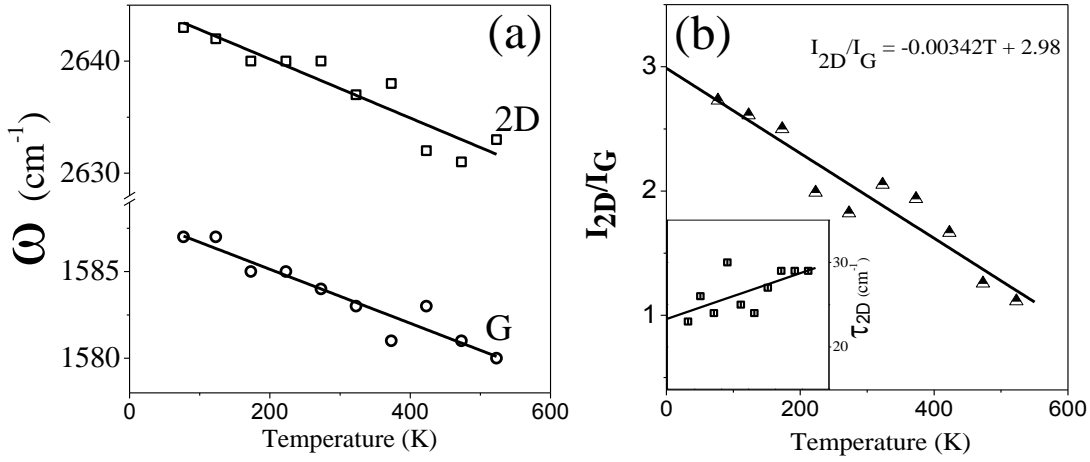


**Figure 4.** Temperature dependence of (a)  $\omega_G$  and  $\omega_{2D}$  and (b)  $I_{2D}/I_G$  for SLG. Inset in (b) shows the temperature dependence of  $\tau_G$ .

Single-layer RGO shows the G band at  $1591 \text{ cm}^{-1}$ , D band at  $1329 \text{ cm}^{-1}$  and a weak 2D band at  $2644 \text{ cm}^{-1}$  (see Figure 3(c)). RGO is known to exhibit such weak 2D band.<sup>28</sup> RGO also shows a very weak D' band at  $1610 \text{ cm}^{-1}$ . RGO exhibits a negative temperature coefficient for the G band frequency, the value being  $-0.029 \text{ cm}^{-1}/\text{K}$  (Figure 5 (a)), a value larger than that of clean SLG. The 2D band frequency on the other hand, does not vary much with temperature as can be seen from Figure 5 (a) (see Table 1.). Interestingly,  $\tau_G$  and  $\tau_{2D}$  are both positive as shown in Figure 5 (b), the slope of each being  $0.0051 \text{ cm}^{-1}/\text{K}$  and  $0.017 \text{ cm}^{-1}/\text{K}$ , respectively. Note that SLG also shows a positive  $\tau_{2D}$ , the temperature coefficient of  $\tau_{2D}$  for SLG being slightly greater than that for RGO. Both  $I_D/I_G$  and  $I_{2D}/I_G$  do not vary much with temperature, with very small negative slope. It is noteworthy that temperature coefficient of  $I_{2D}/I_G$  of SLGs too showed a small negative slope. Six-layer graphene (EG) prepared by thermal exfoliation of graphite oxide exhibits the G band at  $1583 \text{ cm}^{-1}$ , D band at  $1333 \text{ cm}^{-1}$ , D' band at  $1610 \text{ cm}^{-1}$  and the 2D band at  $2640 \text{ cm}^{-1}$  as shown in Figure 3. The six-layer EG also shows negative temperature coefficients for the G and 2D band frequencies (Figure 5(c)), but the  $\chi_G$  is considerably smaller than that of RGO (Table 1).

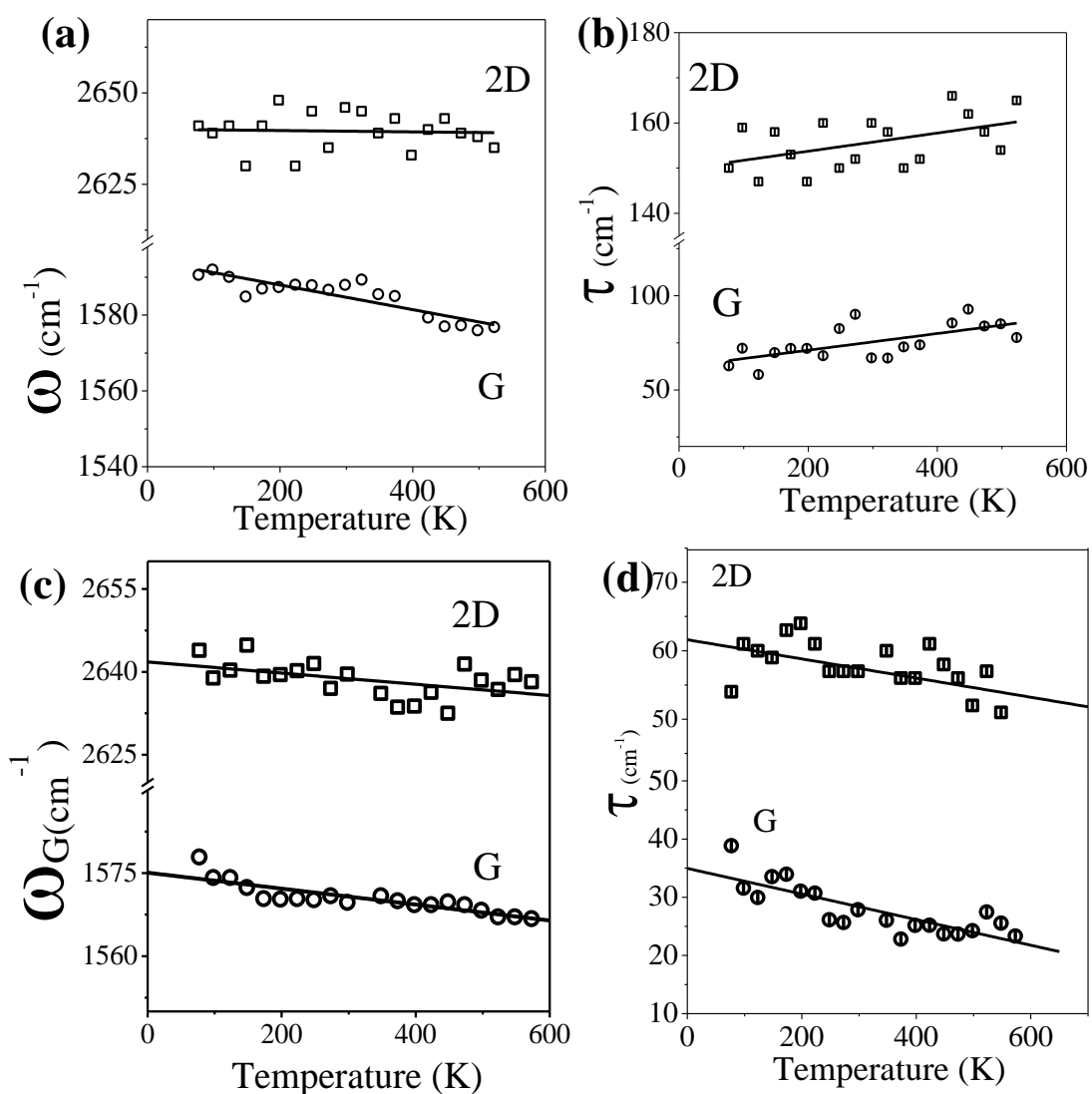


**Figure 5.** Temperature dependence of  $\omega$  and  $\tau$  of G and 2D bands of (a,b) RGO and (c, d) EG.

This is consistent with the suggestion that  $\chi_G$  decreases with the increase in the number of layers. The  $\chi_{2D}$  value becomes more negative compared to that of RGO. We find both  $\tau_G$  and  $\tau_{2D}$  to be negative (Figure 5(c)), temperature coefficient of  $\tau_G$  being greater than that of  $\tau_{2D}$ . Both  $\tau_G$  and  $\tau_{2D}$  tend to be positive in SLG and RGO samples. Furthermore,  $I_D/I_G$  and  $I_{2D}/I_G$  shows significant negative slope, the slopes being greater than single layer SLG and RGO.

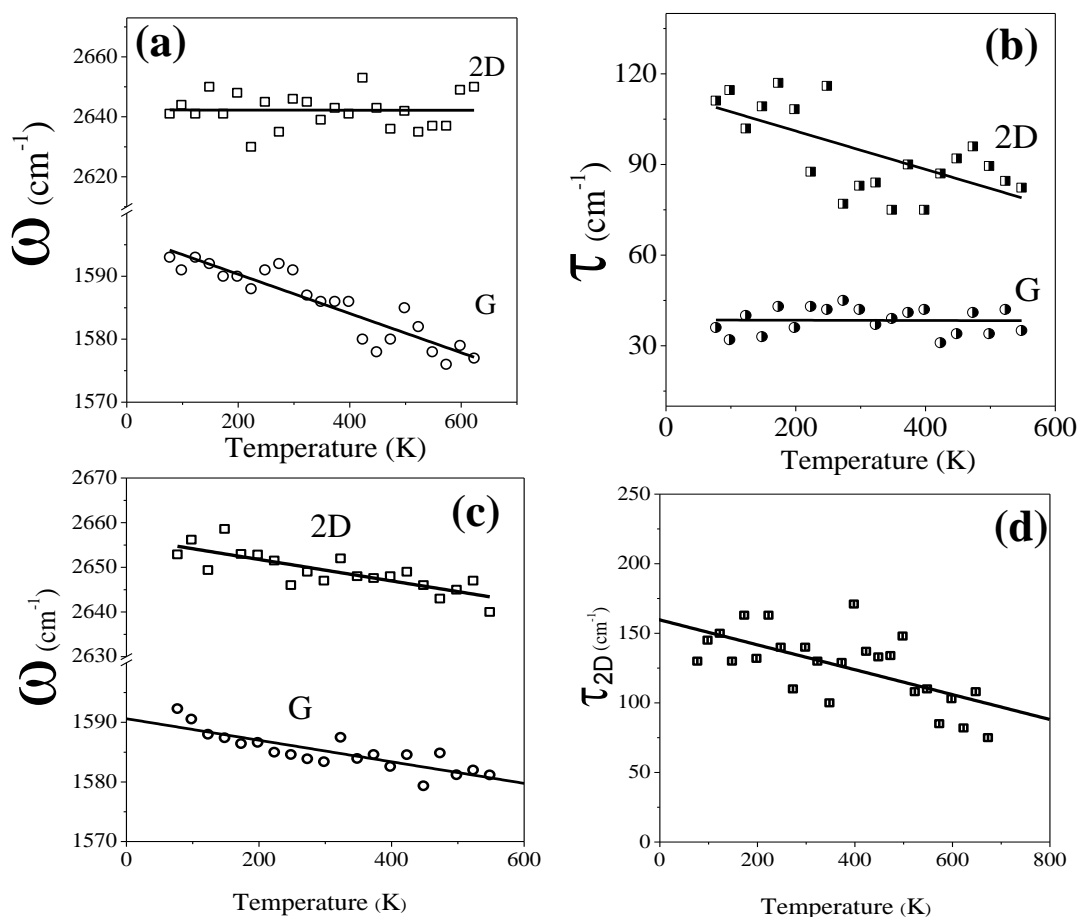


**Figure 6.** Temperature dependence of  $\omega$  and  $\tau$  of G and 2D bands of (a,b) Bi-layer and (c, d) multi-layer GNR

The bi- and multi-layer (5-6 layers) GNRs prepared by unzipping of double-walled and multi-walled nanotubes show the G band at  $1585\text{ cm}^{-1}$  and  $1581\text{ cm}^{-1}$  respectively and a D band around  $1329\text{ cm}^{-1}$  (Figure 3). Both the GNRs show a broad hump in the range  $1450\text{ cm}^{-1}$  to  $1500\text{ cm}^{-1}$ , the origin of which is not yet fully understood.<sup>29</sup> The defect related D'-band in multi-layer GNRs is stronger than in bi-layer GNR while both the samples have a very weak 2D band.<sup>30</sup> In Figure 6 we show the temperature variation of the various features of the 2-layer and multi-layer GNR. The  $\chi_G$  values for the 2-layer and multi-layer samples are  $-0.030\text{ cm}^{-1}/\text{K}$  and  $-0.018\text{ cm}^{-1}/\text{K}$  respectively, showing a decrease with the increasing number of layers. This is consistent with the trend observed with RGO and EG (Table 1). While the 2D-band in bi-layer GNR does not vary much with temperature (Figure 6(a)), the temperature coefficient of 2D band for



multi-layer GNR is  $-0.026 \text{ cm}^{-1}/\text{K}$  (see Figure 6(c) and Table 1). The temperature coefficient of 2D band frequency thus becomes more negative with increase in number of layers, a trend similar to that observed for RGO and EG. The temperature coefficients of FWHMs of the 2D bands of 2- and multi-layer samples are negative, just as in the case of EG (Figure 6(b) and (d)), but the values are larger in GNRs (Table 1).  $\tau_G$  in bi-layer GNR is almost independent of temperature with only a negligibly small positive slope (Figure 6(b)), while for multi-layer GNR it does not vary significantly with temperature. It is notable that temperature coefficients of FWHMs of single layer graphene samples, i.e. SLG and RGO were positive, while for 5-6 layer EG samples it was negative.  $\tau_G$  for GNR follows the trend though the temperature coefficients are much lower, while  $\tau_{2D}$  always has a negative slope for GNRs.

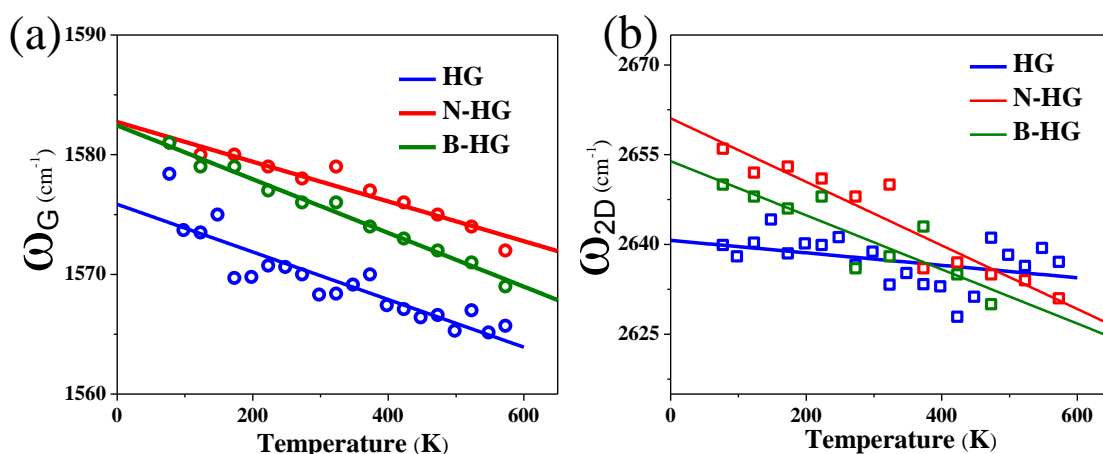


**Figure 7.** Temperature dependence of frequency of G and 2D bands of undoped and B, N doped HG.

Three-layer HG shows the G band at  $1577 \text{ cm}^{-1}$ , a weak D band at  $1333 \text{ cm}^{-1}$  and the 2D band at  $2652 \text{ cm}^{-1}$ . On N-doping ( $\sim 1$  atomic % of N) the G band shifts to  $1580 \text{ cm}^{-1}$  and the 2D band to  $2660 \text{ cm}^{-1}$ , with no change in the position of the D band. On B-doping ( $\sim 1$  atomic % of B) the G band occurs at  $1585 \text{ cm}^{-1}$ . Malard *et al.*<sup>14</sup> and Abdula *et al.*<sup>16</sup> mentioned that chemical doping affects the temperature dependence of Raman spectrum of graphene. However, in both these reports, doping was unintentional and the type of doping was not known. We have carried out temperature dependent studies on

N- and B-doped 3 layer graphene (HG). Figures 6 (a) and (b) show the comparison of temperature dependence of the G and 2D band frequencies of the undoped HG with B and N-doped samples. The undoped HG sample exhibits temperature effects somewhat comparable to those of EG with negative values of  $\chi_G$  and  $\chi_{2D}$  as well as  $\tau_G$  and  $\tau_{2D}$ . On doping with B and N, there is a small increase in the value of  $\chi_G$  to  $\sim -0.022 \text{ cm}^{-1}/\text{K}$  from the original value of  $-0.020 \text{ cm}^{-1}/\text{K}$  (Table 1). The value of  $\chi_{2D}$ , on the other hand, shows a large increase from  $-0.01 \text{ cm}^{-1}/\text{K}$  in HG to  $\sim -0.05 \text{ cm}^{-1}/\text{K}$  in the doped samples. The temperature coefficients of the FWHMs of both the G and 2D bands are positive in the case of N-doped HG, similar to that observed in case of the RGO (Table1).

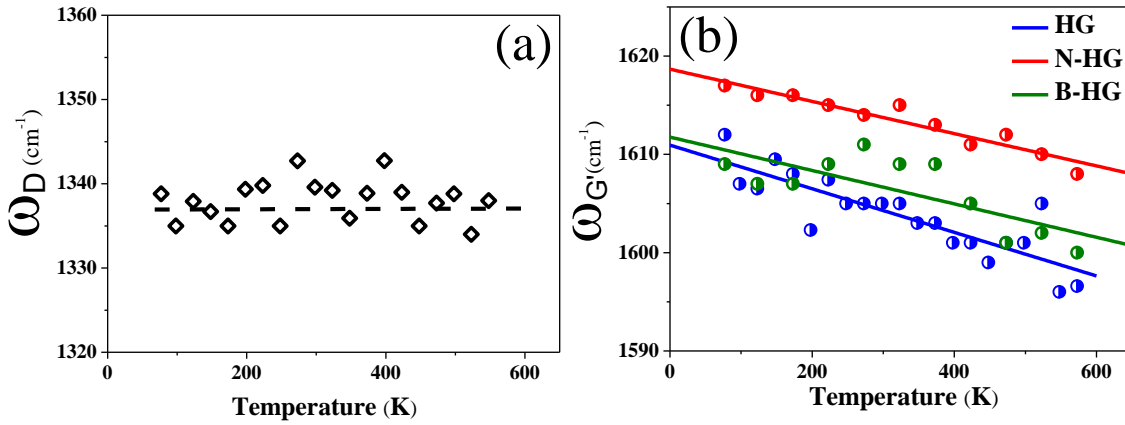


**Figure 8.** Temperature variation of (a) D band of undoped HG and (b) D' band of undoped and B, N doped HG.

The disorder-induced D band shows no temperature dependence in all the graphene samples studied by us. Figure 8 shows the variation of D band frequency of HG with temperature.  $\chi_D$  is almost zero for the sample as is for all graphene samples showing that defect induced D band undoped as well as doped graphene is temperature independent. On the other hand, the disorder-induced D' band shows a constant slope of around  $-0.02 \text{ cm}^{-1}/\text{K}$  in all the samples. Figure 8(b) shows the temperature dependence of D' band frequency of undoped and doped HG with temperature. While  $\chi_{D'}$  of undoped HG is  $-0.021 \text{ cm}^{-1}/\text{K}$  like all graphene samples, both N and B doped HG shows

slightly lesser temperature dependence with slope of  $-0.0164 \text{ cm}^{-1}/\text{K}$  and  $-0.017 \text{ cm}^{-1}/\text{K}$  respectively.

**Table 1.** Temperature coefficients of Raman features of Graphene

Material	$\chi_G$ ( $\text{cm}^{-1}/\text{K}$ )	$\chi_{2D}$ ( $\text{cm}^{-1}/\text{K}$ )	$\tau_G$ ( $\text{cm}^{-1}/\text{K}$ )	$\tau_{2D}$ ( $\text{cm}^{-1}/\text{K}$ )
SLG	-0.016	-0.026	<sup>(a)</sup> ~0	+0.026
1- layer RGO	-0.029	<sup>(a)</sup> ~0	+0.015	+0.017
6- layer EG	-0.014	-0.01	-0.022	-0.013
2- layer GNR	-0.030	<sup>(a)</sup> ~0	0.0	-0.063
6- layer GNR	-0.018	-0.026	0.0	-0.089
3- layer HG	-0.020	-0.01	-0.009	-0.009
N-doped HG	-0.022	-0.053	+0.003	+0.04
B-doped HG	-0.022	-0.045	0.0	0.0

<sup>(a)</sup> very small negative value

There are three factors that influence the temperature dependence of Raman spectra of graphene (i) electron-phonon coupling<sup>9,16,31</sup> (ii) thermal expansion which is negative in sign, and (iii) anharmonic phonon-phonon interactions.<sup>13</sup> We can use these factors to understand the observed trends in temperature dependence of Raman spectra of graphene with doping and number of layers. We note that the negative thermal expansion coefficient of graphene<sup>32,33</sup> cannot explain the sign of the thermal coefficient of the frequency of the G band. Our estimate of the coefficient  $\frac{\partial \omega_G}{\partial \epsilon}$  from first-principles calculations is about  $-3000 \text{ cm}^{-1}$ , where  $\epsilon$  is the strain in the  $ab$ -plane of SLG. Using the value of negative thermal expansion coefficient alone,<sup>32,33</sup> the contribution to thermal coefficient of the G band is positive with magnitude less than  $0.01 \text{ cm}^{-1}/\text{K}$ . The Grüneisen parameter of graphene is negative and can be used to calculate the volume dependence of the frequency of phonon modes. Since both the Grüneisen parameter and the thermal expansion coefficient of graphene are negative, the change in phonon frequency will turn out to have a negative sign.<sup>11</sup> Electron-phonon coupling could also be a contributing factor especially in the case of RGO which exhibits a more negative value of thermal coefficient of the G band frequency as compared to SLG. With weaker thermal contraction of multi-layer graphene than SLG, its effect on G band is expected to become weaker with the number of layers. At the same time, doping and wrinkling also become

weaker with number of layers. As a result, we expect an overall reduction in the magnitude of thermal coefficient of G band with  $n$ . A prominent D band in most of the samples studied here suggests the presence of residual groups such as carbonyl or oxygen, and also why it does not change much with temperature (similar to the mode in diamond reflecting  $sp^3$ -based bonds).

Presence of the 2D band in the Raman spectrum of graphene is a result of second order (in phonon) scattering, which depends sensitively on the features of electronic structure that facilitate a double resonant two-phonon scattering through conservation of energy and momentum.<sup>1</sup> Thus, the frequency and the resonant line-width depend on (a) the conical electronic band structure in the region near the K-point with its range determined by the energy of the radiation light used in the Raman measurement, and (b) phonon dispersion near the K-point, particularly of the highest optical branch with A1' mode at the K-point. The band-width increases with the number of layers as more electronic states are available for the resonant condition,<sup>34</sup> and the 2D band splits with uniaxial strain.<sup>35</sup> Temperature dependence of the frequency (the line-width) of the 2D band arises from the real (the imaginary) part of the self-energies associated with electron-phonon coupling and phonon-phonon anharmonic interactions. As the temperature increases, flexural modes (ripples) develop, which provide additional scattering of the near-K-phonons relevant to the 2D band,<sup>35</sup> arising from anharmonic phonon-phonon interaction. We believe this gives rise to the temperature-dependent softening of the 2D band and hence a negative temperature coefficient. Secondly, the frequency and the width of 2D band increase with  $n$ <sup>13,35</sup> due to additional states near the Fermi energy and a broader distribution of the occupation of states with electrons. Correspondingly, the temperature coefficient of the 2D frequency becomes more negative. A similar, even stronger, effect is expected for 2D bands of the B- and N-doped graphenes. Features of the electronic structure near the Fermi energy change noticeably upon doping with B and N substitution,<sup>26</sup> which alter the temperature coefficient of the frequency of 2D band drastically (Table 1). While the changes in frequency of the G band due to thermal expansion of B and N-doped graphene have opposite signs, the dominant dynamic corrections to the G band of both are of the same sign,<sup>26</sup> and as a result, corresponding temperature coefficients of the G band are similar.

The electronic structure of graphene nano-ribbons is quite different from that of graphene, particularly near the Dirac point because of fewer electronic states with wavevectors perpendicular to the axis of the ribbon. As a result, the 2D band is not strong. However, temperature effects through the Fermi-dirac distribution or smearing on electron-phonon coupling are significant, and manifest in the large temperature coefficients of the line-widths of 2D band. They appear to cancel the effects of thermal expansion and anharmonicity giving a weak temperature-dependence of the width of the G band.

## **5. Conclusions**

Based on the present experimental study, we are able to arrive at the following conclusions on the effect of number of layers and doping on the temperature dependence of various Raman-features of graphene. (i) The negative temperature coefficient of the G band frequency decreases with the increase in the number of layers. (ii) The temperature coefficient of the 2D band frequency is generally negative and becomes more negative with the increase in number of layers. (iii) Doping affects the temperature coefficients of frequencies of the G and the 2D band showing a large value. Note that the D band is known to be sensitive to doping as well as the number of layers. (iv) The temperature coefficients of FWHMs are near zero or positive in single-layer graphene and become negative with the increase in the number of layers. (v) The temperature coefficient of the defect related D' band is constant in all the samples studied ( $\sim -0.02 \text{ cm}^{-1}/\text{K}$ ) while that of the D band is zero. The observed phenomena can be understood on the basis of electron-phonon coupling, anharmonic phonon-phonon interactions and negative thermal expansion of graphene.

## References

1. A. C. Ferrari, J. C. Meyer, V. Scardaci, C. Casiraghi, M. Lazzeri, F. Mauri, S. Piscanec, D. Jiang, K. S. Novoselov, S. Roth and A. K. Geim. *Phys. Rev. Lett.* **2006**, 97, 187401.
2. A. Das, S. Pisana, B. Chakraborty, S. Piscanec, S. K. Saha, U. V. Waghmare, K. S. Novoselov, H. R. Krishnamurthy, A. K. Geim, A. C. Ferrari and A. K. Sood. *Nature Nanotechnol.* **2008**, 3, 210.
3. M. Kalbac, A. Reina-Cecco, H. Farhat, J. Kong, L. Kavan and M. S. Dresselhaus. *ACS Nano* **2010**, 4, 6055.
4. V. Rakesh, D. Barun, R. Chandra Sekhar and C. N. R. Rao. *J. Phys. Cond. Matter* **2008**, 20, 472204.
5. B. Claflin, J. Park, K. Eyink, D. Tomich and J. Albrecht. *Meeting Abstracts Electro. Chem. Soc.* **2009**, MA2009-01, 1301.
6. H. Komurasaki, T. Tsukamoto, K. Yamazaki and T. Ogino. *J. Phys. Chem. C* **2012**, 116, 10084.
7. M. S. Dresselhaus, A. Jorio and R. Saito. *Ann. Rev. Cond. Matt. Phys.* **2010**, 1, 89.
8. A. C. Ferrari. *Solid State Comm.* **2007**, 143, 47.
9. E. S. Zouboulis and M. Grimsditch. *Phys. Rev. B* **1991**, 43, 12490.
10. P. V. Huong, R. Cavagnat, P. M. Ajayan and O. Stephan. *Phys. Rev. B* **1995**, 51, 10048.
11. P. Tan, Y. Deng, Q. Zhao and W. Cheng. *Appl Phys. Lett.* **1999**, 74, 1818.
12. H. D. Li, K. T. Yue, Z. L. Lian, Y. Zhan, L. X. Zhou, S. L. Zhang, Z. J. Shi, Z. N. Gu, B. B. Liu, R. S. Yang, H. B. Yang, G. T. Zou, Y. Zhang and S. Iijima. *Appl. Phys. Lett.* **2000**, 76, 2053.
13. I. Calizo, A. A. Balandin, W. Bao, F. Miao and C. N. Lau. *Nano Lett.* **2007**, 7, 2645.
14. L. M. Malard, R. L. Moreira, D. C. Elias, F. Plentz, E. S. Alves and M. A. Pimenta. *J. Phys. Cond. Matt.* **2010**, 22, 334202.
15. L. Zhang, Z. Jia, L. Huang, S. O'Brien and Z. Yu. *J. Phys. Chem. C* **2008**, 112, 13893.

16. D. Abdula, T. Ozel, K. Kang, D. G. Cahill and M. Shim. *J. Phys. Chem. C* **2008**, 112, 20131.
17. K. S. Novoselov, A. K. Geim, S. V. Morozov, D. Jiang, Y. Zhang, S. V. Dubonos, I. V. Grigorieva and A. A. Firsov. *Science* **2004**, 306, 666.
18. W. S. Hummers and R. E. Offeman. *J. Am. Chem. Soc.* **1958**, 80, 1339.
19. D. C. Marcano, D. V. Kosynkin, J. M. Berlin, A. Sinitskii, Z. Sun, A. Slesarev, L. B. Alemany, W. Lu and J. M. Tour. *ACS Nano* **2010**, 4, 4806.
20. V. C. Tung, M. J. Allen, Y. Yang and R. B. Kaner. *Nature Nanotechnol.* **2009**, 4, 25.
21. C. N. R. Rao, U. Maitra and H. S. S. R. Matte *Synthesis, Characterization, and Selected Properties of Graphene; Wiley-VCH Verlag GmbH & Co. KGaA, 2012.*
22. C. N. R. Rao, A. K. Sood, K. S. Subrahmanyam and A. Govindaraj. *Angew. Chemie Int. Ed.* **2009**, 48, 7752.
23. C. N. R. Rao, K. S. Subrahmanyam, H. S. S. R. Matte, B. Abdulhakeem, A. Govindaraj, D. Barun, K. Prashant, G. Anupama and J. L. Dattatray. *Sc. Technol. Adv. Mater.* **2010**, 11, 054502.
24. K. S. Subrahmanyam, L. S. Panchakarla, A. Govindaraj and C. N. R. Rao. *J. Phys. Chem. C* **2009**, 113, 4257.
25. L. S. Panchakarla, A. Govindaraj and C. N. R. Rao. *Inorganica Chimica Acta* **2010**, 363, 4163.
26. L. S. Panchakarla, K. S. Subrahmanyam, S. K. Saha, A. Govindaraj, H. R. Krishnamurthy, U. V. Waghmare and C. N. R. Rao. *Adv. Mater.* **2009**, 21, 4726.
27. A. L. Higginbotham, D. V. Kosynkin, A. Sinitskii, Z. Sun and J. M. Tour. *ACS Nano* **2010**, 4, 2059.
28. S. Park, J. An, I. Jung, R. D. Piner, S. J. An, X. Li, A. Velamakanni and R. S. Ruoff. *Nano Lett.* **2009**, 9, 1593.
29. Z.-S. Wu, W. Ren, L. Gao, B. Liu, J. Zhao and H.-M. Cheng. *Nano Res* **2010**, 3, 16.
30. J. Campos-Delgado, J. M. Romo-Herrera, X. Jia, D. A. Cullen, H. Muramatsu, Y. A. Kim, T. Hayashi, Z. Ren, D. J. Smith, Y. Okuno, T. Ohba, H. Kanoh, K.

**Chapter II. 4 Temperature dependent Raman.....**

---

- Kaneko, M. Endo, H. Terrones, M. S. Dresselhaus and M. Terrones. *Nano Lett.* **2008**, 8, 2773.
31. C.-H. Park, F. Giustino, M. L. Cohen and S. G. Louie. *Nano Lett.* **2008**, 8, 4229.
32. N. Mounet and N. Marzari. *Phys. Rev. B* **2005**, 71, 205214.
33. S. Vibhor, S. Shamashis, S. S. Hari, D. Rohan, A. Adrien, D. Sajal, P. Prita and M. D. Mandar. *Nanotechnol* **2010**, 21, 165204.
34. A. Gupta, G. Chen, P. Joshi, S. Tadigadapa and Eklund. *Nano Lett.* **2006**, 6, 2667.
35. M. Huang, H. Yan, T. F. Heinz and J. Hone. *Nano Lett.* **2010**, 10, 4074.

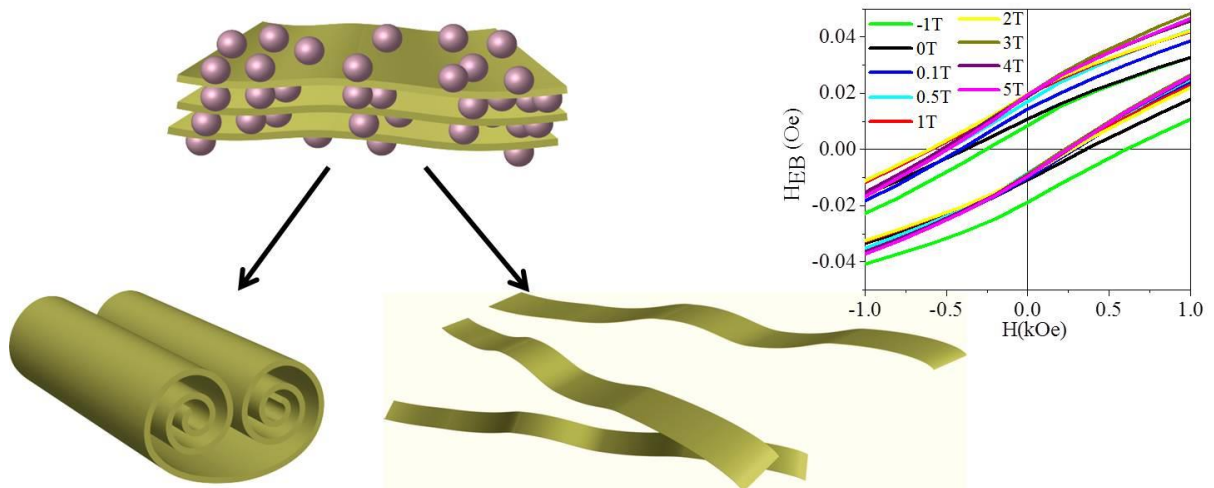


# Chapter II.5

## *Nanoribbons and nanoscrolls of Graphene and graphene analogues of BN and MoS<sub>2</sub>*

### *Summary*

*Pottassium intercalation between the layers of layered materials like graphite and its analogue BN and MoS<sub>2</sub> has been achieved by vapour phase Potassium intercalation. Exothermic reaction occurs on addition of ethanol to K-intercalated layered materials leading to exfoliation. K-intercalation and exfoliation of bulk powders of graphite, BN and MoS<sub>2</sub> yield nanoscrolls while that of their few-layer sheet like analogues give nanoribbons. All the nanoribbons possess both ferromagnetic and antiferromagnetic type interactions which manifests as exchange bias effect. MoS<sub>2</sub> nanoscrolls could also be obtained by allowing sudden expansion of liquid N<sub>2</sub> on the surface of bulk MoS<sub>2</sub> powders under the effect of microwave heating.*



## **1. Introduction**

Graphene with its intriguing properties have inspired exploration of its applications in electronic and photonic devices, sensors, detectors and several other applications. Because of its superior electronic, thermal and mechanical properties graphene is one of the most promising candidates for replacing Si in future electronic devices. However, while Si is a small band gap semiconductor, mono-layer graphene is a zero band gap semimetal. Being a semimetal graphene based FETs have a low on/off ratio and efforts have been devoted to opening the band gap in graphene while still retaining high mobility of charge carrier through it. Substrate induced<sup>1</sup> bilayer-graphene,<sup>2</sup> chemical doping,<sup>3</sup> controlled oxidation<sup>4</sup> and hydrogenation<sup>5</sup> are among them. Confinement of graphene to 0D or 1D also opens up band gap. While 0D confined graphene is called a graphene quantum dot, graphene confined to 1D is known as graphene nanoribbon. Confinement of graphene however curbs the superior electronic properties of graphene, like high carrier mobility. Graphene nanoribbons (GNR) on the other hand are linear strips of graphene which can in theory retain graphene like mobilities at least in one dimension.

Reducing 2D graphene to 1D GNRs can result in edges with three different edge structures namely, arm-chair, zigzag and chiral. The band gap of a GNR is governed by the ribbon width and the edge configuration.<sup>6,7</sup> GNRs with homogenous that arm chair or zigzag edges have been demonstrated to have energy gaps which decreases nearly linearly with increasing GNR width.<sup>6</sup> Edge structure and width of GNRs not only determines its band gap but also carrier mobilities. Due to edge/boundary scattering effects GNRs of width below 10 nm are predicted to possess exponentially decreasing carrier mobilities.<sup>8</sup> However, Lin et. al. achieved high mobility exceeding  $3000 \text{ cm}^2\text{V}^{-1}\text{s}^{-1}$ , along with small bandgap of 50-100 meV in ultraclean and ultra-smooth-edged GNRs.<sup>9</sup> Sub-10 nm wide graphene nanoribbon FETs have been demonstrated to have  $I_{\text{ON}}/I_{\text{OFF}}$  ratio of upto  $10^6$  with a carrier mobility of  $200 \text{ cm}^2\text{V}^{-1}\text{s}^{-1}$ . This has opened up path to all semiconducting devices having electronic properties comparable and even better than carbon nanotubes.<sup>10</sup> Not only do GNRs possess fascinating applications in electronics, quantum confinements and edge effects open up new realm of exciting properties. Semiconducting GNRs with width  $<10 \text{ nm}$  have been found to exhibit half-metallicity (one electron spin being insulating and the other being metallic) under the influence of

electric field.<sup>11</sup> This opens up possibilities of regulating spin polarized currents in low-dimensional systems.<sup>12</sup>

The unusual properties and remarkable applications of GNRs have aroused interest in nanoribbons of other layered materials, such as molybdenum sulfide and boron nitride. The hexagonal BN a structural analogue of graphene has attracted special interest due to its higher thermal and chemical stability and intrinsic electrical insulation. Though bulk BN and 2D BN nanosheets are insulators, BN nanoribbons (BNNR) exhibit semiconducting behavior due to edge effects. While, zigzag BNNRs are indirect band gap semiconductors with band gap decreasing monotonically with ribbon width, armchair BNNRs are direct band gap semiconductors. 2D hexagonal MoS<sub>2</sub> nanosheets has become a recent sensation because of its unique optical, electrical, sensing and catalytic properties. Theoretical calculations on nanoribbons of MoS<sub>2</sub> (MoS<sub>2</sub>NR) suggest magnetic spin states being concentrated at the edges of zigzag nanoribbons. While bulk and 2D MoS<sub>2</sub> are both small band gap semiconductors, zigzag MoS<sub>2</sub>NR is metallic and arm chair nanoribbons are semiconducting with the band gap converging to a constant value on increasing ribbon width. While theoretical study on nanoribbons of graphene and its analogues suggest many intriguing properties experimental studies of properties and applications have been limited due to difficulty in synthesis of these nanoribbons, especially those with particular width or edge type.

After the discovery of fullerenes in 1985,<sup>13</sup> it was soon recognized that inorganic layered materials such as MoS<sub>2</sub> and WS<sub>2</sub> can also form fullerene-like structures.<sup>14</sup> After the discovery of carbon nanotubes,<sup>15</sup> inorganic nanotubes analogous to carbon nanotubes were prepared and characterized, nanotubes of MoS<sub>2</sub> and WS<sub>2</sub> being examples.<sup>15</sup> The discovery and characterization of graphene, that is, two-dimensional nanocarbon, which has created great interest in last few years.<sup>16</sup> It led to the synthesis of graphene analogues of layered inorganic materials such as dichalcogenides of molybdenum and tungsten.<sup>17</sup> Scroll whiskers were first reported by Bacon in 1960.<sup>18</sup> Interest in graphene nanoscrolls is spurred by the fact that chirality dependence of carbon nanotubes can be eliminated in graphene nanoscrolls while still retaining beneficial properties like high conductivity for large scale use of 1D carbon nanostructures.<sup>19</sup> FETs of graphene nanoscrolls have been demonstrated to have maximum mobilities of the holes and electrons of 3117 cm<sup>2</sup>V<sup>-1</sup>s<sup>-1</sup>

and  $4595 \text{ cm}^2\text{V}^{-1}\text{s}^{-1}$ , respectively and a maximum current density upto  $7 \times 10^7 \text{ Acm}^{-2}$ . Moreover due to their self-encapsulated structures nanoscrolls unlike graphene are insensitive to external factors like substrate. Due to its unique morphology graphene nanoscrolls are predicted to possess unusual electronic and optical properties, i.e. unique from both graphene and carbon nanotubes.<sup>20</sup> Because of its special morphology nanoscrolls provide interlayer galleries that can be easily intercalated thereby increasing the inter layer spacing. Intercalation of graphene nanoscrolls is found to be energetically more favourable than that of multiwalled carbon nanotubes. Easy intercalation and de-intercalation properties could make nanoscrolls ideal for Li ion batteries and supercapacitors.<sup>21</sup> Large surface area and defined pore size along with curved surface makes them ideal candidate for H storage.<sup>22</sup> While synthesis and properties of nanoscrolls and nanoribbons of graphene have been reported, to the best of my knowledge nanoscrolls and nanoribbons of inorganic layered materials have not yet been reported.

First experimental study on high temperature ferromagnetism of graphite like materials was carried out by Kopelevich and Esquinazi.<sup>23</sup> Pyrolytic graphite showed highly anisotropic behaviour in magnetic field, with ferromagnetic behaviour when magnetic field was applied parallel to the graphite sheets and large diamagnetic signal when field was applied normal to the sheets. On raising the temperature to 800K in He atmosphere the ferromagnetic signal was enhanced.<sup>24</sup> Absence of correlation with impurity content implied that this was an intrinsic property of the pure carbon.<sup>25</sup> Later polymerised  $\text{C}_{60}$ , was shown to have long range ferromagnetic ordering.<sup>24</sup> Magnetic properties of nanographite were studied by Enoki *et al.*<sup>26</sup> followed by observation of magnetism in activated carbon fibres comprised of a disordered network of nanographites.<sup>27</sup> Antiferromagnetic interactions mediated by p-type carriers between the nanographites was predicted.<sup>27</sup> Ferromagnetism in highly oriented pyrolytic graphite (HOPG) and Kish graphite samples are considered to arise from topological defects and strong Coulomb interaction between electrons.<sup>28</sup> Partially reduced graphene oxide shows room temperature ferromagnetism and a long-range coupling of spin units, in this case defects has been proposed.<sup>29</sup> Magnetic properties of graphene samples prepared under different conditions and thus having different densities of defects and edges, bore signature of both antiferromagnetic and ferromagnetic interactions.<sup>30-32</sup> Single-atom

defects can induce ferromagnetism in graphene-based materials.<sup>33</sup> Vacancies, substitution atoms (e.g., B or N) and adatoms could also be responsible for the magnetism of graphene.<sup>34,35</sup> Zig-zag edges are often considered to be responsible for the magnetic properties of graphene.<sup>36</sup> Tensile strain along the zig-zag direction is often considered to enhance the ferromagnetic stability.<sup>37</sup> The presence of van Hove singularities can also lead to magnetism and such singularities are generated by the rotation between the stacked layers of graphene.<sup>38</sup>

Graphene nanoribbon can be thought of as a graphene lattice with finite termination along one of the directions leading to a confinement to one dimension. The long edge of the GNR determines its nomenclature as armchair, zig-zag or chiral. Theoretical calculations predict that GNRs have parallel spin alignments along each zig-zag edge, whereas the spin alignments in two edges are antiparallel to each other. Again the spins happen to be antiferromagnetically coupled within the nearest neighbour sites throughout the lattice with decay of spin moments towards the centre of the ribbon.<sup>12,39</sup> Band structure of GNRs is highly sensitive to the edge alignment and can be responsible for different magnetic properties of GNRs.<sup>40</sup> The width of the nanoribbon as well as impurities and defects play major role in determining magnetic properties of nanoribbons.<sup>41</sup> Magnetism of GNRs is also known to be affected by hydrogenation<sup>42</sup>, hydroxylation<sup>43</sup> and impurities.<sup>44</sup> Near-edge x-ray absorption fine structure and electron-spin resonance studies on few-layer GNRs synthesized by chemical vapour deposition confirm the existence of magnetic edge states that originate from open nanographene edges.<sup>45</sup> First-principles calculations predict half-metallicity in nanometre-scale graphene ribbons. Magnetic properties of GNRs have been controlled by application of electric fields across their zig-zag edges.<sup>46</sup> Tao *et al.*<sup>47</sup> have studied sub-nanometre-resolved scanning tunneling microscopy and spectroscopy on GNRs synthesized from unzipping of carbon nanotubes. The measurements reveal the presence of edge states, corroborating the theoretical calculations of GNRs of similar width and chirality. However, direct evidence of magnetism and the nature of magnetic interactions in GNRs are still lacking.

Magnetism has been observed in nanoforms of other layer materials like BN and MoS<sub>2</sub>. MoS<sub>2</sub> nanosheets exhibit weak magnetism and 2.5% magnetoresistance and this behaviour has been related to the presence of edge spins, where the terminating atoms are

unsaturated.<sup>48</sup> Spin-polarized density-functional theory (DFT) calculations on triangular shaped clusters show that magnetic states are present in clusters terminated by 100% Mo edge and 100% S edge.<sup>48</sup> Dev *et al.*<sup>49</sup> suggested that cation vacancies can induce long-range magnetic order in BN. Room temperature ferromagnetism has been observed in BN and the ferromagnetic ordering is suggested to arise from the conversion of  $sp^3$  C to  $sp^3$ - $sp^2$  hybridized C or from defects.<sup>50</sup> Layer and crystallite size dependence of magnetic properties of graphene analogues of  $MoS_2$ ,  $WS_2$ , and BN have been studied and exhibit an increase in the magnetic moment with the decreasing number of layers.<sup>51</sup> The importance of edge structure in determining the nature of magnetic interactions has however been borne out earlier.<sup>51</sup>

## **2. Scope of the present investigations**

Synthesis of graphene nanoribbons has been carried out by several techniques like lithographic patterning followed by plasma etching, sonochemical breaking of chemically functionalized graphene, metal-catalyzed or oxidative cutting of graphene, direct chemical synthesis, and unzipping of carbon nanotubes. GNRs of width 10-100 nm and 1-2  $\mu$ m were prepared for the first time by oxygen plasma etching of graphene sheets.<sup>52</sup> Negative tone e-beam resist, hydrogen silsesquioxane (HSQ) was used to protect the underlying graphene layer, while the unprotected layer got etched away by the oxygen plasma.<sup>53</sup> Tapasztó *et al.*<sup>54</sup> etched the desired geometrically and crystallographically oriented GNRs from graphene sheets by applying constant bias potential (significantly higher than that used for imaging) and simultaneously moving the STM tip with constant velocity over the surface. However these methods could not produce GNRs of widths less than 20 nm and had edge roughness of  $\sim$  5 nm. Li *et al.*<sup>55</sup> chemically prepared sub 10 nm width GNRs of varying lengths from thermally exfoliated graphite by dispersing it in a 1,2-dichloroethane (DCE) solution of poly(m-phenylenevinylene-co-2,5-dioctoxy-p-phenylenevinylene) (PmPV) by sonication and removing the larger pieces by centrifugation. Delgado *et al.*<sup>56</sup> prepared 20-300 nm few layered GNRs in bulk scale by chemical vapour deposition of ethanol with ferrocene and thiophene acting as catalysts. Longitudinal unzipping of carbon nanotubes (CNTs) has also been used for synthesis of

GNRs. While Kosynkin *et al.*<sup>57</sup> carried out oxidative unzipping using  $\text{KMnO}_4$ -  $\text{H}_2\text{SO}_4$  mixture, Higginbotham *et al.*<sup>58</sup> used a second acid like TFA or  $\text{H}_3\text{PO}_4$  to get more controlled oxidation yielding high quality GNRs with lesser holes. Jiao *et al.*<sup>59</sup> carried out mild gas phase oxidation to create defects on CNTs which were then dispersed in 1,2-dichloroethane (DCE) solution of poly(m-phenylenevinylene-co-2,5-dioctoxy-p-phenylenevinylene) (PmPV) by sonication and obtained high quality unzipped nanoribbons. Jiao *et al.*<sup>38</sup> carried out controlled unzipping of partially embedded CNTs in PMMA by Ar plasma etching. GNRs has also been obtained by sonochemical cutting of graphene sheets involving oxygen induced unzipping of graphene sheets.<sup>60,61</sup> Laser irradiation of undoped and doped multi-walled carbon nanotubes by an excimer laser (energy ~200–350 mJ) also yielded graphene nanoribbons.<sup>61</sup> GNRs have also been obtained by plasma-enhanced chemical vapor deposition on Pd nanowire templates. On removing the Pd nanowires tubular shaped graphene layer collapsed to yield edge closed nanoribbons while the graphene layers on the top part of the metal nanowire were selectively etched by  $\text{O}_2$  plasma to yield edge opened GNRs.<sup>62</sup> Wang *et al.*<sup>63</sup> prepared 20–30-nm-wide graphene nanoribbon arrays lithographically, and used the gas phase etching chemistry to narrow the ribbons down to <10 nm and thereby achieving a high on/off ratio up to  $\sim 10^4$ . Bottom up fabrication on the other hand provides precise control over topologies and widths of GNRs. Surface-assisted coupling of molecular precursors into linear polyphenylenes and their subsequent cyclo-dehydrogenation have been used to prepare GNRs with predefined edge structure and morphology.<sup>64</sup> Yang *et al.*<sup>65</sup> carried out Suzuki-Miyaura polymerization of the bis-boronic esters with diiodobenzenes to prepare polyphenylenes resembling GNRs.

It is evident that both chemical and physical methods have been applied to synthesize GNRs. While physical methods like lithographic patterning followed by plasma etching can generate nanoribbons of defined widths, they are inappropriate for large scale synthesis of nanoribbons. Bulk scale synthesis of GNRs involving chemical cutting methods like sonochemical cutting of functionalized graphene or oxidative unzipping of carbon nanotubes results in highly oxidized GNRs with large number of defects. Direct chemical synthesis is by far the best synthetic produre for GNRs yielding nanoribbons with defined and ultrasmooth edges and width. However, such synthesis method involves

large number of steps and is complex. Moreover, preparation of nanoribbons via chemical synthesis and other synthesis methods like oxidative unzipping of nanotubes can be utilized only for graphene and carbon based materials. Intercalation of alkali metal ions however happens in all layered materials like BN and MoS<sub>2</sub>. Cano-Márquez et al.<sup>66</sup> observed that MWNTs could be partially opened by intercalation of lithium and ammonia followed by exfoliation. Atomic radii of Li being very small, intercalation of Li does not increase the interlayer spacing between two walls of MWNTs much. Such a small increase in the interstitial distance does not provide enough strain to break the carbon-carbon bonds. Kosynkin *et al.*<sup>67</sup> successfully intercalated potassium in MWNTs by treating the MWNTs in K vapour. On quenching with ethanol the MWNTs split completely to yield GNRs that have electrical properties comparable to that of exfoliated graphene. K intercalation of graphite followed by exfoliation with ethanol on the other hand results in rolling of graphene sheets to form carbon nanoscrolls.<sup>68</sup> While K intercalation can cut MWNTs it is interesting that in case of graphite only rolling up of the sheets was found. Both MWNTs and graphite are composed of layers of graphene sheets bond to each other by van der waals forces of interaction, i.e. they are chemically same. The difference between the two being MWNTs are rolled up and being chemically synthesized bear defects in its tube walls, while graphite is composed of flat sheets of graphene with almost no defects. We thought it of interest to see the effect of K intercalation and exfoliation in few-layer graphene sheets. It would also be interesting to intercalate of K inorganic layered materials like BN and MoS<sub>2</sub>. Exfoliation of K intercalated BN and MoS<sub>2</sub> might open up possibilities of nanostructures of these materials with novel morphologies.

A variety of synthetic approaches have been explored to prepare graphene nanoscrolls. A 2D layer with ripples and dangling bonds at their edges is unstable. Rolling up of such a layer is thus thermodynamically favourable leading to reduction in dangling bonds. However, energy needs to be supplied to create single layers and destabilize them. Scrolls have also been prepared by slight perturbation applied to single layer graphene. Single layer graphene on SiO<sub>2</sub>/Si substrate can be easily scrolled into 1D structures by simply immersing the substrate containing single layer graphene in isopropyl alcohol. Functionalized Reduced graphene oxide nanosheets have been scrolled



by Langmuir-Blodgett technique. The above methods cannot be used to prepare nanoscrolls in larger quantities. All the above methods are chemically driven and are therefore specific to synthesis of nanoscrolls of graphene only. Recently, microwave spark assisted sudden expansion of liquid N<sub>2</sub> has been utilized for exfoliation and scrolling of graphene. The method being physically driven can be utilized to prepare nanoscrolls of all layered materials having van der Waals stacked layers. We considered it of interest to synthesize nanoscrolls of layered metal chalcogenides with the expectation that they have properties differing from layered MoS<sub>2</sub> and WS<sub>2</sub>.

Based on the knowledge that edges play an important role in determining the magnetic properties of graphene and graphene analogues, we felt that it would be interesting to study the magnetic properties of nanoribbons of graphene and graphene analogues, specially since nanoribbon is almost an all-edge material. In our curiosity to find the nature of interactions that exist in these nanoribbons we carried out exchange bias studies that give direct evidence of co-existence of both ferromagnetic and antiferromagnetic domains. A very dilute exchange bias effect has earlier been observed by Tour and co-workers in graphene nanoribbons prepared by K intercalation and exfoliation of carbon nanotubes.<sup>69</sup> Though, presence of antiferromagnetic interactions have been observed experimentally in nano-graphite and graphene, no evidence of antiferromagnetism has been observed in graphene analogues of MoS<sub>2</sub> or BN yet.

### **3. Experimental section**

#### ***Synthesis of graphene and graphene analogues of BN and MoS<sub>2</sub>***

Graphene was prepared by thermal exfoliation of graphite oxide. Graphene oxide was prepared by modified Hummers method.<sup>70</sup> For this 70 ml of concentrated H<sub>2</sub>SO<sub>4</sub> was added to a mixture of 1 g of graphite flakes and 1.5 g of NaNO<sub>3</sub> and the mixture was cooled to 0 °C. 9 g of KMnO<sub>4</sub> was slowly added always keeping the temperature of the reaction mixture well below 20 °C. the reaction mixture was then warmed to 35 °C and stirred for 7 h. Additional KMnO<sub>4</sub>(9.0 g) was then added and stirred at 35 °C for 12 h. The mixture was cooled by pouring onto ~ 400 ml of ice with 3 ml of 30% H<sub>2</sub>O<sub>2</sub>. GO was collected by centrifugation and washed with water. Thermally exfoliated graphene EG (3-

5 layers) was obtained from GO by sudden heating to 300°C in air. This process not only exfoliates the graphene but also retains some of the functional groups.

BN nanosheets were prepared by thermal decomposition of a mixture of Boric acid and urea. A mixture of boric acid and urea in the ratio 1:24 by weight were heated were heated at 900 °C for 5h in N<sub>2</sub> atmosphere, yielding white products. MoS<sub>2</sub> nanosheets were similarly prepared by heating a mixture of Molybdic acid and thiourea in the weight ratio 1:24 at 500900 °C for 5h in N<sub>2</sub> atmosphere.

### ***Potassium intercalation and exfoliation***

Potassium intercalation was carried out by treating the bulk crystals and nanosheets to K vapour. For this purpose 20 mg of required material and known quantity (20 mg, 70 mg, 150 mg or 300 mg) of K metal were taken in a pyrex glass tube and sealed under  $\sim 10^{-5}$  atm pressure. The reaction mixture was kept at 300°C for 12h during which the golden-bronze coloured intercalation compound is formed along with silver K metal.

Exfoliation was carried out in a mixture of ethyl ether and ethanol. Once the tube has cooled to room temperature the tube is broken and the contents were transferred to a beaker containing 20 mL ethanol. Reaction of K with ethanol is highly exothermic and proceeds with evolution of large amount of H<sub>2</sub> which is evident as bubbles of gas effuse out on addition of ethanol. The quenched product was collected by centrifugation followed by washing with water and ethanol.

### ***Synthesis of MoS<sub>2</sub> and WS<sub>2</sub> nanoscrolls by microwave irradiation***

50 mg of bulk MoS<sub>2</sub>/WS<sub>2</sub> powder (alfa aser) was placed in a 100 mL beaker and 40 mL of liquid nitrogen was added to the beaker. We allowed the liquid N<sub>2</sub> to boil off till it becomes 10 ml. Liquid N<sub>2</sub> boils off with vigorous bubble formation during which process MoS<sub>2</sub> gets well dispersed in liquid N<sub>2</sub>. When liquid nitrogen becomes 10 mL, the beaker was irradiated in a microwave oven at 600W for 1min followed by addition of 10 ml water and sonication. Time and power of microwave irradiation was varied from 30 sec to 5 min and from 150W to 900W. 600 W and 1 min gives the best result with maximum yeild. Solvents other than water like ethanol, iso-propanol, N-methyl pyrrolidone, tetrahydrofuran, dichloromethane and di-methyl formamide were used instead of water. For reasons yet unknown water gives maximum yield of nanoscrolls.

Sonication was first carried out in a probe sonicator for 2 min and then in a normal low power sonic bath for 15 min to form homogeneous suspension. The suspension was centrifuged at 1500 rpm for 15 min to separate bulk MoS<sub>2</sub>/WS<sub>2</sub> from the suspension of nanoscrolls which was retained in the supernatant. AFM image was taken by drop coating thoroughly cleaned Si substrate with a supernatant solution.

### ***Magnetic measurements***

Magnetic measurements were carried out in vibrating sample magnetometer. Approximately, 20 mg of dry powder was packed in diamagnetic tape and used for magnetic measurements. Diamagnetic contribution was subtracted for all M vs. H (moment vs. field) measurements. Field cooled (FC) and zero field cooled (ZFC) measurements were carried out at 500 Oe. For FC measurements, the sample was cooled under an applied field of 500 Oe followed by raising the temperature to 380 K under the applied field. For ZFC measurements, oscillating field was applied to reach 0 Oe so as to ensure complete removal of any remnant field. The sample was then cooled to 2K without application of any field and ZFC measurements were carried out at 500 Oe. For exchange bias measurements the sample was first cooled to 2K under a particular field called the cooling field ( $H_{cool}$ ). M vs. H measurements were then carried out by directly taking the sample to 10 kOe ( $H_M$ ) and hysteresis of the sample was studied in the range -10 kOe to 10 kOe. Dependence of exchange bias on field was probed by cooling the sample to 2K under different fields in the range -1T to 5T and M vs. H measurements were carried out at 2K. To look at temperature dependence of exchange bias effect the sample was first cooled to particular temperature under 1T field ( $= H_{cool}$ ) and hysteresis of the sample was studied at this temperature in the range -10 kOe to 10 kOe.

## ***4. Results and Discussion***

### ***A. Nanoribbons and nanoscrolls of Graphene and graphene analogues of BN and MoS<sub>2</sub> by potassium intercalation***

We have carried out K intercalation of both bulk powders of graphite, BN and MoS<sub>2</sub> and their chemically synthesized few-layer counter parts and compared the effects K

intercalation on the morphology of the final product. K intercalation was carried out with different graphite: K ratio (1:1, 1:3.5, 1:7.5 and 1:15 wt/wt) to determine the role of K in shaping the morphology. Figure 1 shows the TEM images of scrolls formed by the K intercalation and exfoliation of graphite. The samples are composed of  $\mu\text{m}$  large flakes of few nm thick graphene scrolled from the edges. Majority of the sample is composed of partially scrolled sheets. Only scrolls are formed by the process of vapour phase K intercalation followed by exfoliation with ethanol, irrespective of the amount of K metal used for intercalation. On increasing the ratio of K the length of graphene length of the graphene sheet that has scrolled up increases, i.e. greater amount of scrolled up regions are visible as compared to the flat graphene regions. Figure 1(c) shows the image of nanoscrolls formed on using graphite to K weight ratio of 1:15. Almost all the scrolls are fully formed with very little flat graphene regions. Higher amounts of K were not taken due to safety issues.

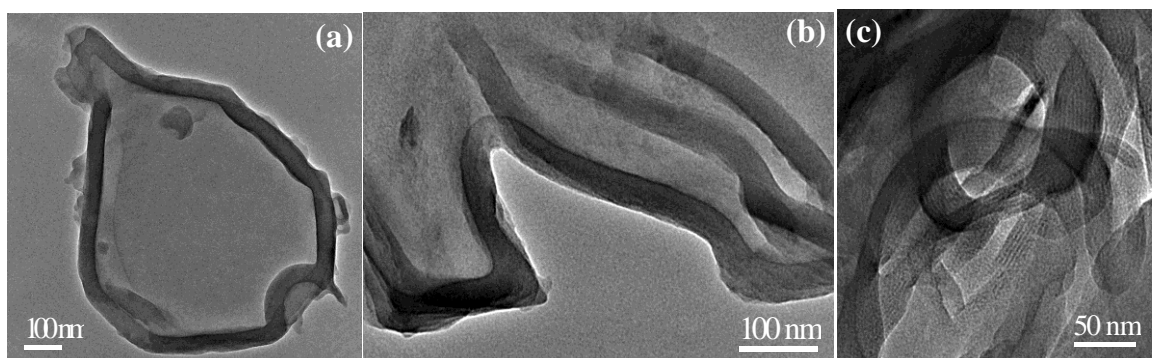


**Figure 1.** TEM image of scrolls formed by K intercalation and exfoliation of Graphite on using (a) 1:1, (b) 1:7.5 and (c) 1:15 wt/wt of Graphite:K.

When BN and MoS<sub>2</sub> powders were treated with K vapour followed by ethanol, we observe similar scrolls of BN and MoS<sub>2</sub> were formed. Figure 2 shows the partially formed nanoscrolls of BN and MoS<sub>2</sub> starting from with two different weight ratios of BN:K and MoS<sub>2</sub>:K (1:1 and 1:15). As in case of graphene higher the ratio of K is to BN or MoS<sub>2</sub> greater is the degree of scrolling. It is noteworthy that unlike Viculis et. al.<sup>68</sup> we do not get fully formed scrolls but rather  $\mu\text{m}$  size nanosheets scrolled up at the edges. It is significant that while Viculis et. al.<sup>68</sup> observed curling of exfoliated sheets into scrolls only on sonication, in our case scrolls were formed without any sonication.

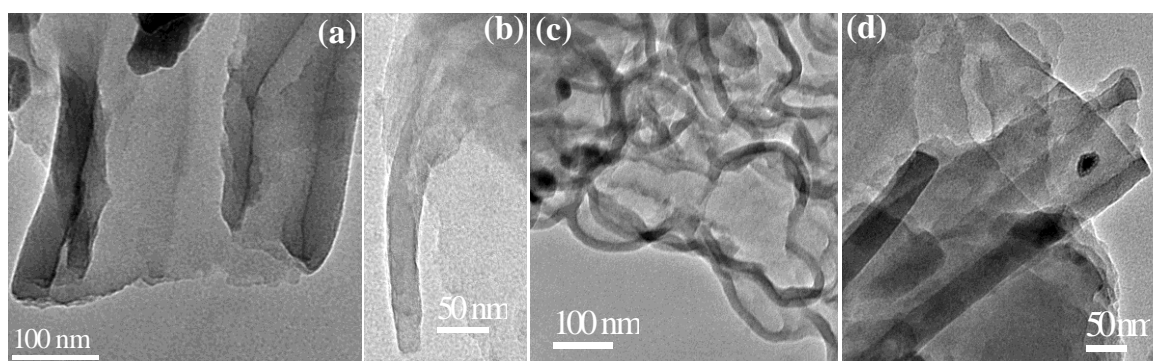
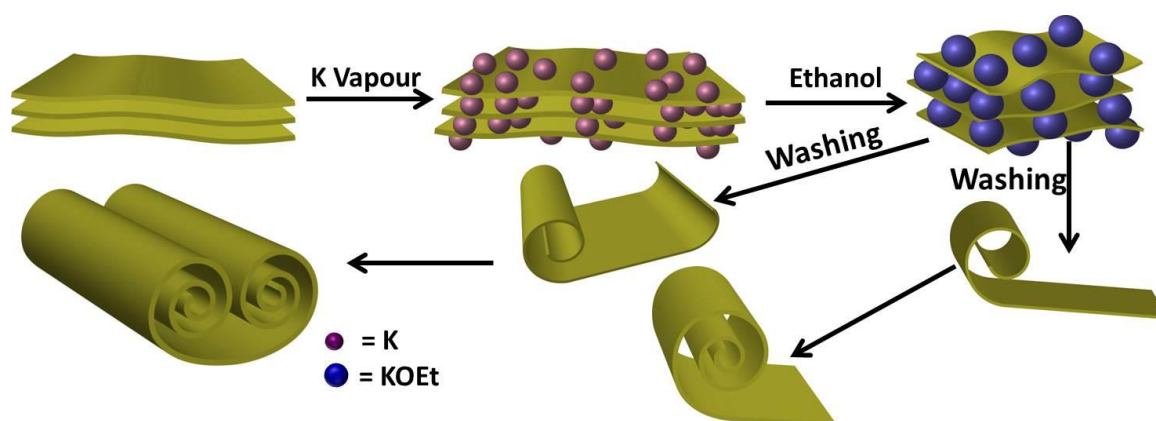


**Figure 2.** Partially formed nanoscrolls of BN (a & b) and MoS<sub>2</sub> (c & d) starting from (a) BN:K = 1:1, (b) BN:K = 1:15, (c) MoS<sub>2</sub>:K = 1:1 and (d) MoS<sub>2</sub>: K = 1:15 (wt/wt).

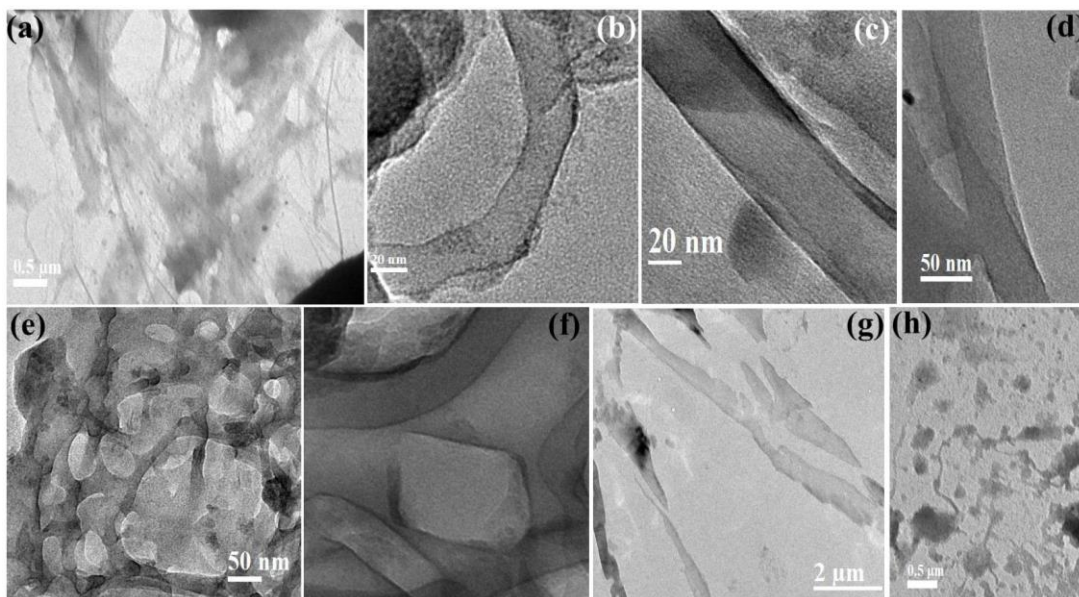


**Scheme 1.** Schematics of formation of scrolls by K intercalation and exfoliation in ethanol.

K intercalation results in increase in the interlayer spacing decreasing the stability of the system. On addition of ethanol K vigorously and exothermically converts to KOEt with release of H<sub>2</sub>. In the process it not only exfoliates the sheets but also bends it. Bending of a sheet decreases the stability. The stability of the system is regained by scrolling whereby the van der Waals interaction is regained in between two walls of the scroll. The exothermic reaction of K with ethanol provides energy for the transition from sheet to scroll.

The fact that nanoscrolls of graphene, BN and MoS<sub>2</sub> could be obtained by K intercalation and exfoliation, encouraged us to study the effect of the process on chemically prepared few-layer graphene, BN and MoS<sub>2</sub>. Few-layer graphene was prepared by thermal exfoliation of graphite oxide in air. The sample is composed of 3-6 layer graphene with flake widths of 0.5 to few  $\mu\text{m}$ . We carried out K intercalation with

graphene: K ratio of 1:1 and 1:15 followed by exfoliation in ethanol. Figure 3(a) shows the low resolution TEM image of sample prepared on using graphene: K ratio of 1:15 (wt/wt). Most of the sheets are cut into thin and long stripes few microns in length. The ribbons vary in width from about 10 nm to 200 nm with majority of them in the range 20-50 nm. TEM images of two such ribbons are shown in Figure 3(b, c) with widths 20 nm and 50 nm respective. K intercalation and exfoliation of BN too yields distinct ribbons like graphene with majority of ribbon widths in the 25 nm to 60 nm.



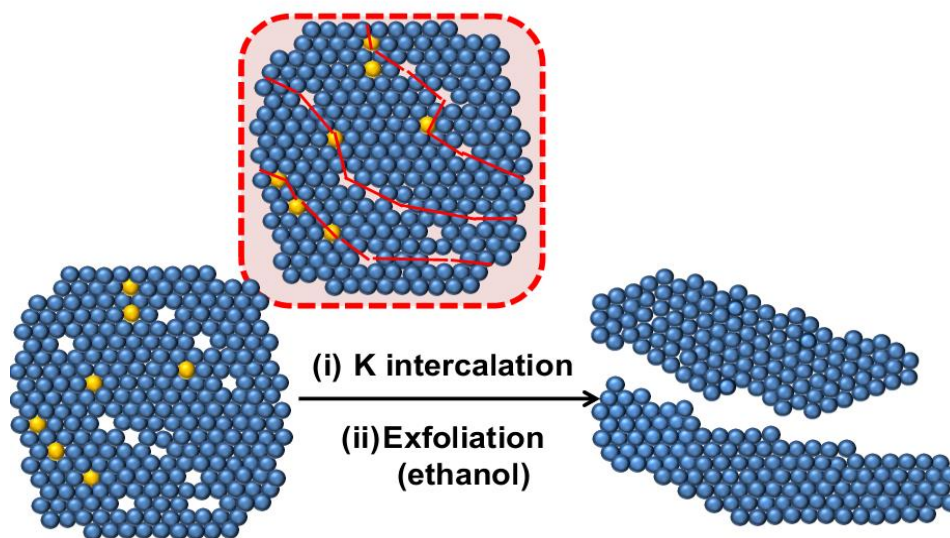
**Figure 3.** TEM images of nanoribbons formed by the reaction of K vapour followed by ethanol on few-layer graphene (a-c, f), BN (d) and MoS<sub>2</sub> (e). (a) shows the low resolution TEM image of graphene nanoribbons formed with graphene:K of 1: 15 while (b& c) shows the high resolution image for the same, (f) for sample prepared with graphene : K of 1: 1 (wt/wt), (g) with graphene: K of 1:1 when exfoliated in water instead of ethanol and (h) with graphene: K of 1:1 (wt/wt) when exfoliated in water.

Figure 3(d) shows the TEM image of typical BN nanoribbons formed by K intercalation and exfoliation. The ribbon has width of ~ 40 nm. Reducing large area sheets to ribbons increases the flexibility as a result of which ribbons generally fold and bend easily as can be seen in Figure 3(d). While GNRs and BNNRs are obtained on K intercalation and exfoliation of few-layer graphene and BN in ethanol, few-layer MoS<sub>2</sub> does not form well defined ribbons but rather thin stripes of interconnected network of

few-layer MoS<sub>2</sub>. It can be described as few-layer MoS<sub>2</sub> scised so as to generate interconnected network of ribbon like stripes as shown in Figure 3(e). Figure 3(f) shows the TEM image of few-layer graphene treated with K in the ratio 1:1 (wt/wt) and exfoliated in ethanol. Cuts and holes in graphene sheets are clearly visible. It is therefore evident that ribbon formation is driven by cutting of sheet induced by K vapour. Degree of cutting depends on the amount of K used, with 1:1 weight ratio of graphene: K giving partially cut graphene sheets with holes while higher ratio of K (1:15) giving completely cut ribbons. It is therefore probable that higher weight ratio of few-layer MoS<sub>2</sub> to K than 1:15 would result in fully formed nanoribbons of MoS<sub>2</sub>. We did not use greater amounts to K due to risk of pyrex tube reacting with K at higher pressures. The role of ethanol in determining the formation of ribbons is evaluated by replacing ethanol with water for exfoliation. Water reacts more exothermically with K with vigorous generation of H<sub>2</sub>. On using water for exfoliating of K intercalated few-layer graphene inhomogenously cut pointed ended flakes and flat-wedges are formed instead of ribbons for samples being prepared with 1:1 graphene:K. When greater amounts of K are used for the reaction (1:15) followed by exfoliation with water a multitude of fragmented nanostructures are formed as shown in Figure 3(h).

Thus, while bulk defect free graphite, BN or MoS<sub>2</sub> yield fully or partially formed nanoscrolls, their few-layer counterparts get cut into ribbons or smaller fragments depending on the amount of K intercalated or the exfoliation conditions. We believe that the morphology difference between the bulk and few-layer systems on K intercalation and exfoliation is a manifestation of few-layer samples having different defect sites while bulk sample is mostly defect free. When exposed to K vapours, K intercalates between the layers and forms a “blister” as observed by Kosynkin et.al.<sup>67</sup> using molecular dynamic simulations. Once a fissure is formed the unzipping propagates by joining defect sites with each other as shown in Scheme 2. Presence of line defects have earlier been reported in chemically synthesized graphene. This process of nanoribbon formation yields few-layer nanoribbons with lesser defects than those produced by oxidative unzipping.<sup>67</sup> Figure 4 (a) shows the IR spectra of GNR prepared with graphene:K of 1:15 followed by exfoliation in ethanol. The IR spectra is mainly composed of C related stretching and

bending frequencies with no C=O or C-O stretching visible indicating no oxidation related defects. Only small O-H stretching frequency is visible.



**Scheme 2.** Schematic representation of nanoribbon formation from few-layer graphene. Yellow and empty spaces represent different types of defect sites. Top in box - red lines are a guide for the eye from where graphene sheet gets cut.

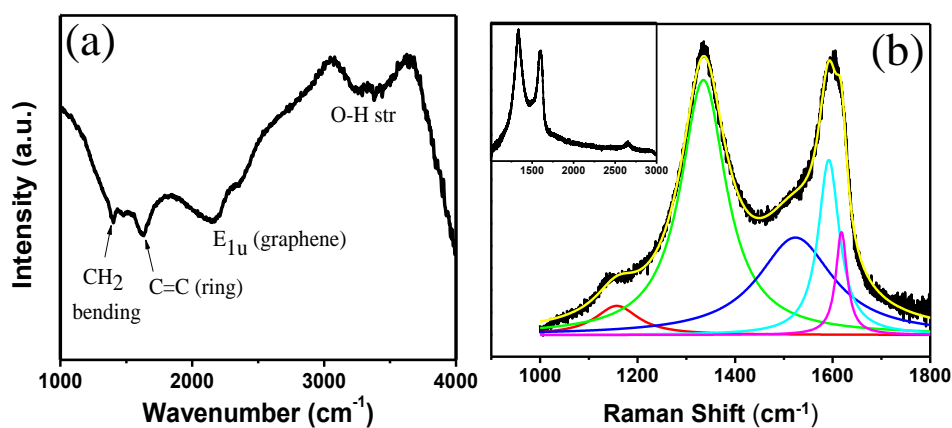


**Figure 4.** (a) IR spectrum, (b) Raman spectrum of GNRs prepared from K intercalation (1:15) followed by exfoliation in ethanol. (Inset in (b) shows the full spectrum while figure (b) shows the region of Raman D and G bands with Lorentzian fit for all the peaks.)

Raman spectrum of GNRs is shown in Figure 4 (b). The full spectrum ( $1000\text{ cm}^{-1}$  to  $3000\text{ cm}^{-1}$ ) is shown in the inset. The spectrum is composed of strong D and G bands with



an inconspicuous 2D band. Strong D and weak 2D band is attributed to significant contributions from edges of the few-layer sample, the  $I_D/I_G$  ratio being  $\sim 1.4$ . More importantly, two extra peaks at  $\sim 1140\text{ cm}^{-1}$  and  $1525\text{ cm}^{-1}$  are observed in the Raman spectrum which is otherwise absent in the Raman spectrum of starting few-layer graphene or in the scrolls formed by K intercalation and exfoliation of graphite. The origin of these two peaks is not clear, though it is worth mentioning that Wu et. al.<sup>60</sup> observed a Raman band at  $1530\text{ cm}^{-1}$  in GNRs prepared by ultrasonication induced cutting of highly oxidized artificial graphite.

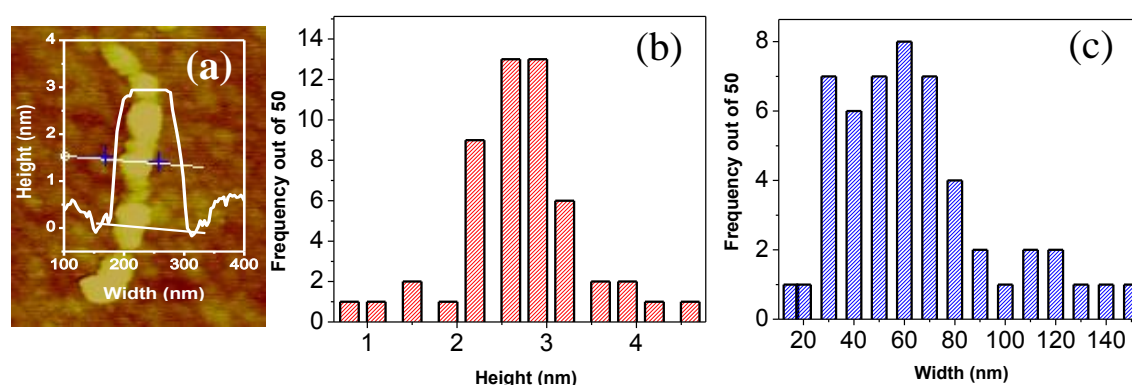


**Figure 5.** (a) AFM with height profile of GNRs prepared from K intercalation (1:15) followed by exfoliation in ethanol, (b) and (c) shows the height and width distribution of GNRs as determined from AFM measurements.

GNRs, BNNRs and nanoribbon like interconnected structures of  $\text{MoS}_2$  prepared by this method are composed of ribbons of different widths and height. While height of the ribbon is mainly determined by the starting few-layer samples, the width is determined by the amount of K taken for intercalation. AFM image of a typical GNR is given in Figure 5(a) showing a nanoribbon of typical width  $\sim 100\text{ nm}$ , height of  $\sim 2.9\text{ nm}$  corresponding to 6 layers and several microns in length. AFM measurements of over 50 samples revealed that the majority of the GNRs are in the range  $2.2\text{ nm} - 3.3\text{ nm}$  (Figure 5(b)) corresponding to sample with 3-7 layers, which is similar to the thickness distribution of the starting material i.e. few-layer graphene sample. The GNRs vary in width over a wide range from  $\sim 15\text{ nm}$  to about  $150\text{ nm}$ , with the majority of them lying in the range  $30-80\text{ nm}$  as shown in Figure 5(c). BNNRs too show comparable height and width distribution while  $\text{MoS}_2$

***Chapter II.5. Nanoribbons and nanoscrolls .....***

---

does not form complete cut nanoribbons but is rather like a sheet with large number of large holes and narrow stripes of inter-connected MoS<sub>2</sub>.

### ***B. Synthesis of MoS<sub>2</sub> and WS<sub>2</sub> nanoscrolls by sudden expansion of Liquid N<sub>2</sub> in microwave***

Microwave irradiation of a dispersion of MoS<sub>2</sub> followed by sonication yielded nanoscrolls of varying length and width. Figure 6 shows FESEM images of MoS<sub>2</sub> nanoscrolls. The nanoscrolls obtained after microwave irradiation of bulk MoS<sub>2</sub> and liquid nitrogen were separated from the bulk MoS<sub>2</sub> flakes by centrifugation at a low rpm of around 1500. The supernatant obtained after centrifugation was directly drop-coated on Si substrates and dried for viewing under FESEM. Tubular structures can be identified in all the cases along with small flakes. Interestingly, highest concentration of scrolls is seen along the edge of the substrate where the solvent dries the last. At the center of the substrate concentration of micron sized flakes is larger than that of scrolls. The scrolls formed are of varying size distribution ranging from few-microns to ~100 nm, though majority of the scrolls are smaller than 300 nm in length. In Figure 6 (c) and (d) we show high resolution FESEM images two of such long MoS<sub>2</sub> nanoscrolls. Rolling up of sheets can be clearly visualized on looking at their edges.

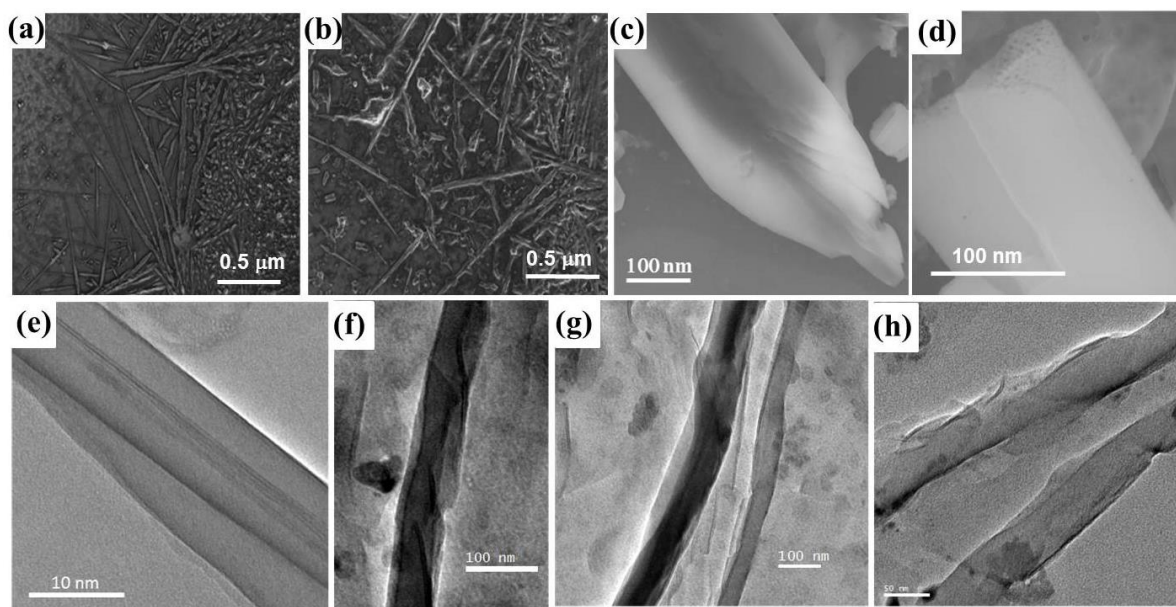


**Figure 6.** (a-d) FESEM images and (e-h) TEM images of nanoscrolls of MoS<sub>2</sub>

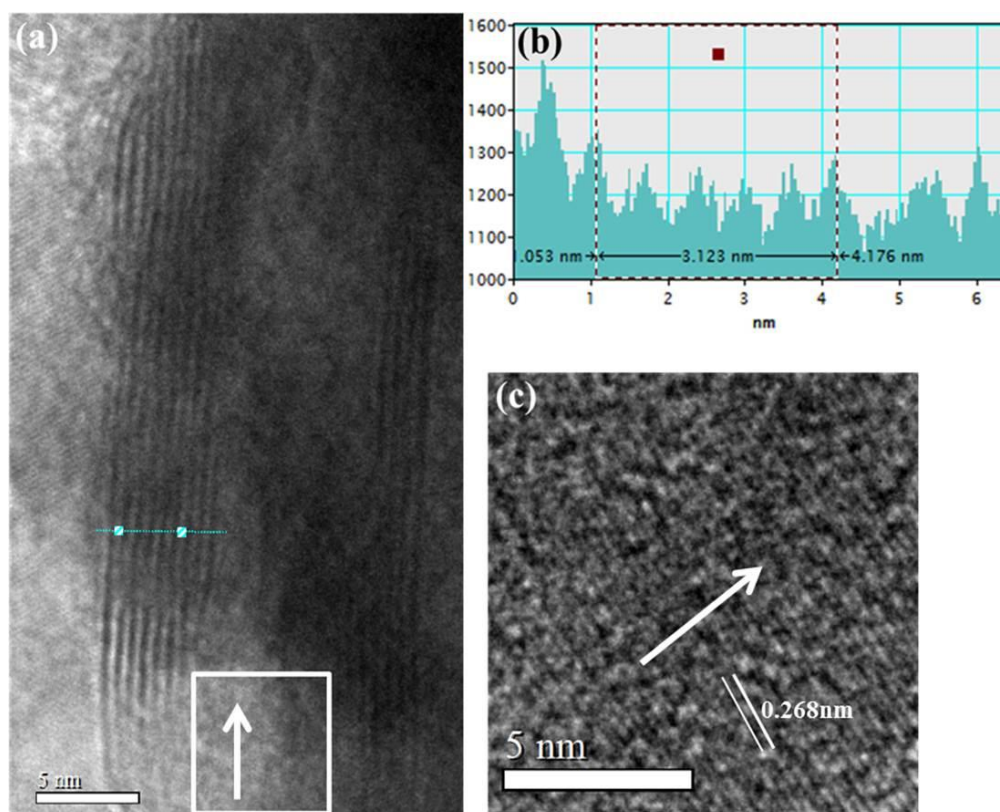
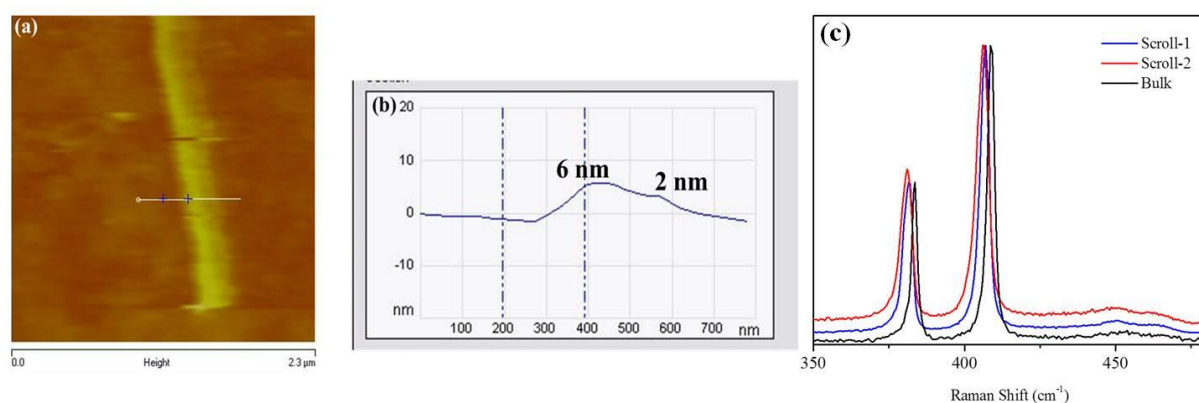


**Figure 7.** (a) High resolution TEM image of nanoscrolls, (b) Line profile showing interlayer spacing and (c) High resolution TEM image of the region highlighted in (a).

Figure 7 shows the TEM images of nanoscrolls of MoS<sub>2</sub>. Figure 7(a) shows a scroll formed by the rolling of few layers. Partially unfolded sheet along with rolled up portion is clearly visible. Figure 7(e-g) show images of one sided nanoscrolls with one side scrolled up while other side freely dangling. Figure 7(h) shows a two sided nanoscroll which is formed when the sheet rolls up from both the sides. Figure 7(a) shows HRTEM image recorded from a two sided nanoscroll. The line profile (Figure 7(b)) shows the interlayer spacing to be 0.63 nm which corresponds to the (002) distance of MoS<sub>2</sub> layered structures. The scroll thus represents a tightly packed scroll likes of which have been reported in case of carbon nanoscrolls formed from graphite flakes when treated with liquid nitrogen in microwave.<sup>71</sup> Figure 7(c) shows the magnified HRTEM image of the center connecting the two scrolls. The fringes parallel to the scrolling axis have inter planer separation of 0.27 nm corresponding to (101) plane, the basal plane for MoS<sub>2</sub>

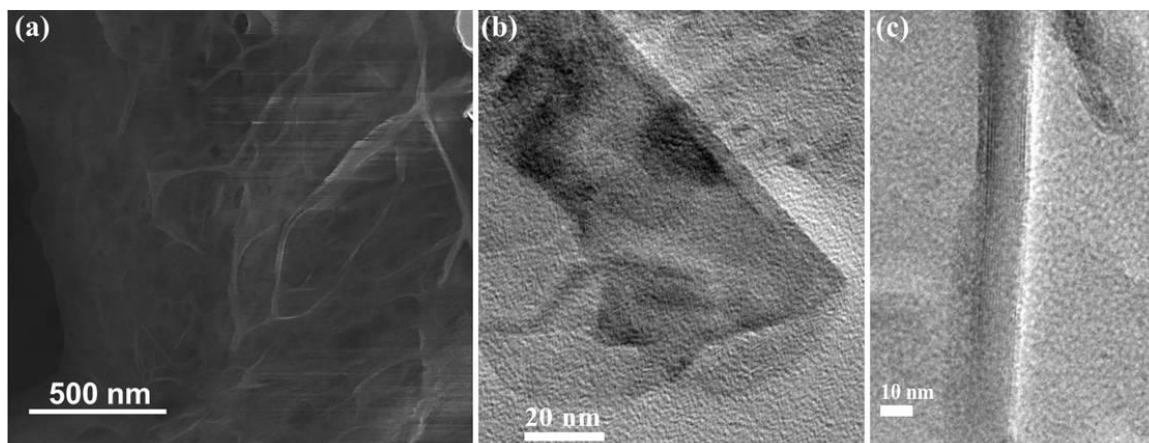
sheets. This confirms the fact that 2D nanosheet of MoS<sub>2</sub> rolled up to form this nanoscroll. Majority of scrolls are however formed from rolling up of few layers of MoS<sub>2</sub>.

Figure 8(a) shows the AFM image of a one sided nanoscrolls. Height profile is shown in Figure 8(b). The open side of the scroll has height of ~2 nm. Considering inter-layer spacing between MoS<sub>2</sub> nanosheets to be 0.65 nm, a height of 2 nm corresponds to 2-3 layers. The height on the scrolled side is more than three times that on the open side. Since the scrolled region is composed of two walls each composed of 2-layer MoS<sub>2</sub>, the distance between the two walls therefore is ~ 2nm. This scroll thus represents a tightly packed one sided scroll as formed when graphite flakes treated under similar conditions.<sup>71</sup>



**Figure 8.** (a) AFM image of a nanoscroll, (b) height profile of the same and (c) Raman spectra of nanoscrolls taken at two different places in comparison with that of bulk MoS<sub>2</sub>.

Raman characterization of nanoscrolls was carried out to understand bulk properties of these nanoscrolls. Figure 8(c) shows Raman spectra of the nanoscrolls taken at two different places along with that from bulk MoS<sub>2</sub>. Bulk MoS<sub>2</sub> shows two peaks at 383 cm<sup>-1</sup> and 408 cm<sup>-1</sup> corresponding to the in plane Mo-Mo and S-S stretching frequency ( $E_{2g}^1$ ) and the out of plane symmetric displacement of sulfur atoms ( $A_{1g}$ ). In case of nanoscrolls both the peaks due to in palne and out of plane modes broaden as well as soften. Brodening of Raman peaks is known to occur due to phonon confinement on going from bulk to nano.<sup>72-74</sup> FWHM for both the peaks increased from 1.2 cm<sup>-1</sup> in case of bulk MoS<sub>2</sub> to around 2cm<sup>-1</sup> for scrolls. The peaks also soften by around 2 cm<sup>-1</sup> from the bulk. Such softening of Raman modes are known to occur graphene when the system is subjected to strain.<sup>75</sup>



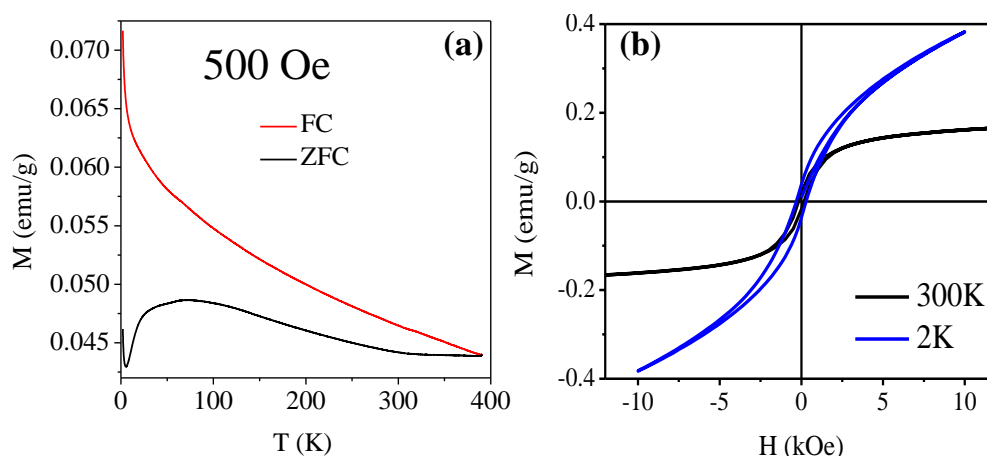
**Figure 9.** (a) FESEM and (b,c) TEM images of WS<sub>2</sub> nanoscrolls.

Figure 9 shows FESEM and TEM images of nanoscrolls of WS<sub>2</sub>. Figure 9(a) shows FESEM image of nanoscrolls of WS<sub>2</sub>. Large number of nanoscrolls bundled together can be clearly seen. Figure 9(b) shows TEM image of a one sided nanoscrolls with one side scrolled up while other side freely dangling similar to those observed in case of MoS<sub>2</sub> scrolls. Figure 9 shows TEM image of a tightly packed WS<sub>2</sub> nanoscroll. The inter-layer spacing for this scroll is 0.66 nm corresponding to the (002) stacking of WS<sub>2</sub>. We tried to prepare nanoscrolls in different solvents such as ethanol, isopropanol, dimethyl formamide, di-chloromethane and N-methyl pyrrolidone. For reasons not known yet, water turns out to be a good solvent for the formation of nanoscrolls of MoS<sub>2</sub> and WS<sub>2</sub> in good yield.

When irradiated by in microwave, the MoS<sub>2</sub> and WS<sub>2</sub> were heated to high temperature, resulting in an expansion in volume. At the same time, the layers coated on the surface of the bulk samples were cooled by the liquid nitrogen, resulting in their shrinkage. The resulting surface strain drives the rolling up of a layer to produce nanoscrolls, which is the energetically favorable state. Furthermore, the violent release of heat by contact of liquid nitrogen with MoS<sub>2</sub> and WS<sub>2</sub> resulted in a rapid boiling of the liquid nitrogen on the surface, which can also contribute to the rolling up of the layered metal chalcogenides. Such scrolling mechanism has been reported for synthesis of graphene scrolls from graphite flakes.<sup>71</sup>

### C. Magnetic properties of nanoribbons of graphene, BN and MoS<sub>2</sub> and observation of exchange bias effect

We first studied temperature dependence of magnetization of GNRs. Figure 10(b) shows the temperature dependence of magnetization under zero field cooled (ZFC) and field cooled (FC) conditions. The FC curve under 500 Oe cooling field does not indicate any magnetic anomaly. We see a divergence between the FC and ZFC data from 2K all the way upto 380K where it converges. Large divergence between the FC and ZFC curves indicate presence of large anisotropy in the sample that lasts even at room temperature. The divergence nearly disappears on application of higher field. This type of behavior has earlier been observed in few-layer graphene, BN and MoS<sub>2</sub> and is presumed to be an effect of spin glass like behaviour arising from random distribution of conflicting interactions (like ferromagnetic and antiferromagnetic interactions) in comparable frequencies.



**Figure 10.** (a) FC and ZFC curves of GNR under an applied field of 500 Oe and (b) Ferromagnetic hysteresis of GNR at room temperature and 2K.

The ZFC data shows a broad maximum around 70 K. The existence of maxima could be a consequence of two reasons i) presence of competing magnetic interactions or ii) presence of small super paramagnetic domains. However, since the sample retains magnetic interactions beyond room temperature, clearly, the blocking temperature is well above room temperature ruling out the possibility of superparamagnetism below 70 K. A

low temperature upturn is clearly visible in the FC and ZFC curves. This kind of upturn is often visible in case of nanoparticles and layered systems like graphene. This is often referred to in the literature as “Curie-like tail” and occurs at low temperatures where the effect of paramagnetic components arising from non-interacting defects becomes more prominent over the ferromagnetic or antiferromagnetic interactions. Nanographite like materials are known to exhibit Curie tail like behaviour.<sup>24</sup> The room temperature and low temperature magnetization of graphene nanoribbons prepared by K intercalation and exfoliation of few-layer graphene shown in Figure 10(a). The sample shows from 2K all the way upto room temperature with finite coercive field, supporting the large divergence between ZFC and FC curves. The ferromagnetic loop does not show saturation till 1T, implying a higher field would be required to reach saturation.

To probe into the existence of competing ferromagnetic and antiferromagnetic interactions,  $M$  vs.  $H$  measurements were carried out at 2K by applying a field of 1T during cooling ( $H_{cool}$ ). Figure 11(a) shows the isothermal magnetization curve at 2K with  $H_{cool} = 1T$  (black). A closer inspection revealed a shift of the hysteresis loop towards the negative field, an effect commonly known as exchange bias effect.

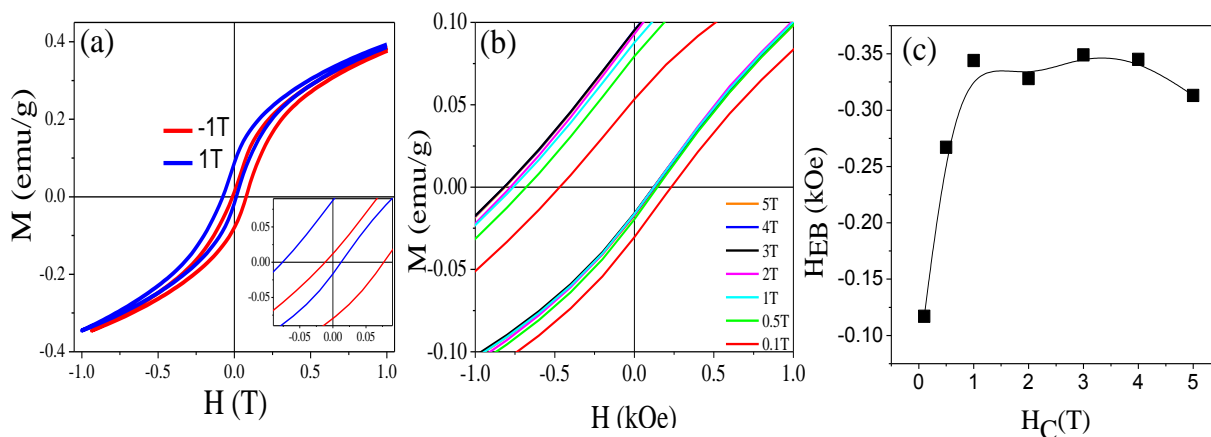


**Figure 11.** (a) Hysteresis loop at 2K on applying cooling field of 1T and -1T, (b) magnified portion of the hysteresis loop at 2K with  $H_{cool} = 0.1T, 0.5T, 1T, 2T, 3T, 4T$  and  $5T$  and (c) the variation of  $H_{EB}$  with  $H_{cool}$  at a constant temperature of 2K for few-layer GNRs. Inset in (a) shows the magnified part of the hysteresis loop showing the exchange bias effect in GNRs.



Exchange bias is a phenomenon known to occur in magnetic materials where ferromagnetic and antiferromagnetic layers or domains are strongly coupled to each other. In such strongly coupled systems, the ferromagnetic spins get pinned by the more anisotropic antiferromagnetic spins. When the field is reversed an extra energy is needed to overcome the pinning of the ferromagnetic spins and reverse it completely. This manifests as a shift in the hysteresis loop along the field axis. The loop shifts to positive or negative field direction depending on the polarity of the field applied during cooling. Since the interaction between the ferromagnetic and the antiferromagnetic regions is generally ferromagnetic type, a positive applied cooling field ( $H_{cool}$ ) generally shifts the loop towards negative field axis.

Exchange bias ( $H_{EB}$ ) is calculated according to the formula  $H_{EB} = (H_{cool1} + H_{cool2})/2$  where  $H_{cool1}$  and  $H_{cool2}$  are the positive and negative coercive fields respectively. GNRs show an exchange bias of -343 Oe on application of  $H_{cool} = 1T$ . On changing the polarity of the applied field ( $H_{cool} = -1T$ ) the  $H_{EB}$  changes its polarity, the  $H_{EB}$  at -1T being 346 Oe. Figure 11(b, c) shows the effect of variation of  $H_{cool}$  on  $H_{EB}$ . The exchange bias increases with increasing the applied cooling field from 0.1T to 1T and then saturates. The exchange bias not only varies with applied cooling field but also with cooling temperature. Figure 12(a, b) shows the effect of cooling temperature on exchange bias field at  $H_{cool} = 1T$ . The  $H_{EB}$  decreases with increasing cooling temperature and nearly vanishes beyond 50K. To see exchange bias effect it is necessary to cool the sample across  $T_N$  ( $T_N > T_C$ ) under an applied cooling field such that both ferromagnetic and anti-ferromagnetic spins get aligned. With increasing cooling temperature, thermal vibrations begin to play greater role and contribute to randomization. Thus, at higher cooling temperatures the exchange bias decreases. It is worth mentioning that GNRs prepared by K intercalation and exfoliation show  $H_{EB}$  of about 5-10 times greater than those reported earlier.<sup>69</sup> While strong exchange bias effect is observed in the case of few-layer GNRs no exchange bias effect was observed in few-layer graphene which is the starting material for synthesis of GNRs. Few-layer graphene however shows room temperature ferromagnetism as observed earlier.<sup>51</sup> Graphene nanoscrolls obtained by K intercalation of graphite under similar conditions as GNRs do not show significant ferromagnetic hysteresis.

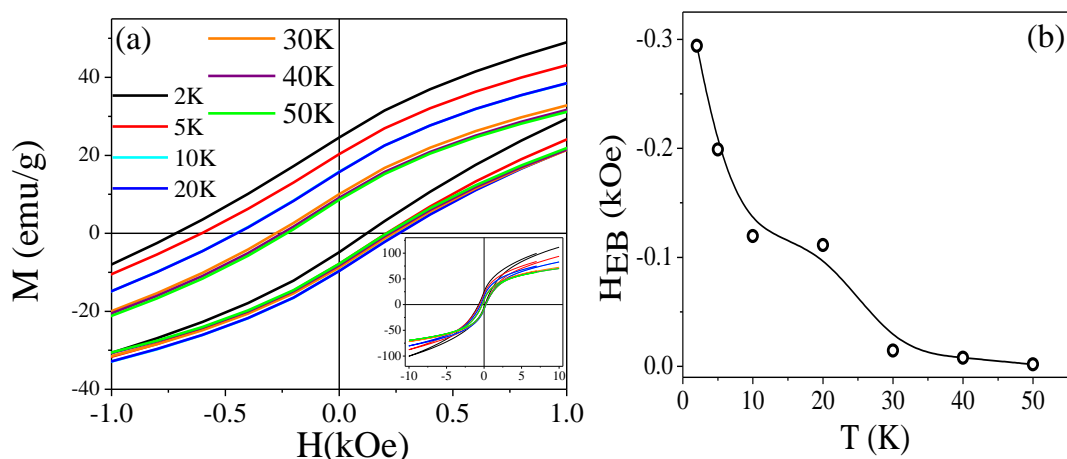


**Figure 12.** (a) Hysteresis loop at 1T on cooling to different temperatures from 50K to 2K and (b) variation of  $H_{EB}$  with cooling temperature at 1T field for few-layer GNRs. Inset in (a) shows the full hysteresis curve at different temperatures under a cooling field of 1T for GNRs.

Figure 13 shows the magnetic properties of  $\text{MoS}_2$  nanoribbons prepared by K intercalation and exfoliation of few-layer  $\text{MoS}_2$ . The FC and ZFC magnetizations are shown in Figure 13(a). A clear ferromagnetic type transition is visible in the FC curve at  $\sim 40$  K. Like graphene nanoribbons,  $\text{MoS}_2$  nanoribbons too show Curie like tail at lower temperatures, an effect of paramagnetic contributions being greater than the ferromagnetic. The perfect s-shaped ferromagnetic hysteresis loops for  $\text{MoS}_2$  nanoribbons are shown in the inset in Figure 13(a). It is interesting that the sample retains ferromagnetism even at room temperature. A divergence between ZFC and FC curves indicate highly anisotropic nature. Both FC and ZFC curves show a broad hump in the region 120K-150K. To look into the nature of interaction responsible for this hump we carried out exchange bias measurements at temperatures below and above this hump. While the sample does not show any exchange bias effect at 150K, it shows a considerable negative exchange bias of 55 Oe at 80K (Figure 13(b)). The observance of exchange bias at temperatures lower than the hump indicates paramagnetic to antiferromagnetic transition. Exchange bias measurements were carried out with varying cooling fields from  $H_{cool} = 5\text{T}$  to  $-1\text{T}$ . The  $\text{MoS}_2$  nanoribbons show significant exchange bias effect of  $H_{EB} = -750$  Oe at 1T.  $H_{EB}$  changes polarity on changing the polarity of the applied cooling field with  $H_{EB} = 768$  Oe at  $-1\text{T}$ . Figure 13(c) shows the effect of cooling

field on  $H_{EB}$  of  $MoS_2$  nanoribbons. Interestingly, the sample shows a distinct broad maxima in  $H_{EB}$  at a cooling field of  $H_{cool} = 1T$ .

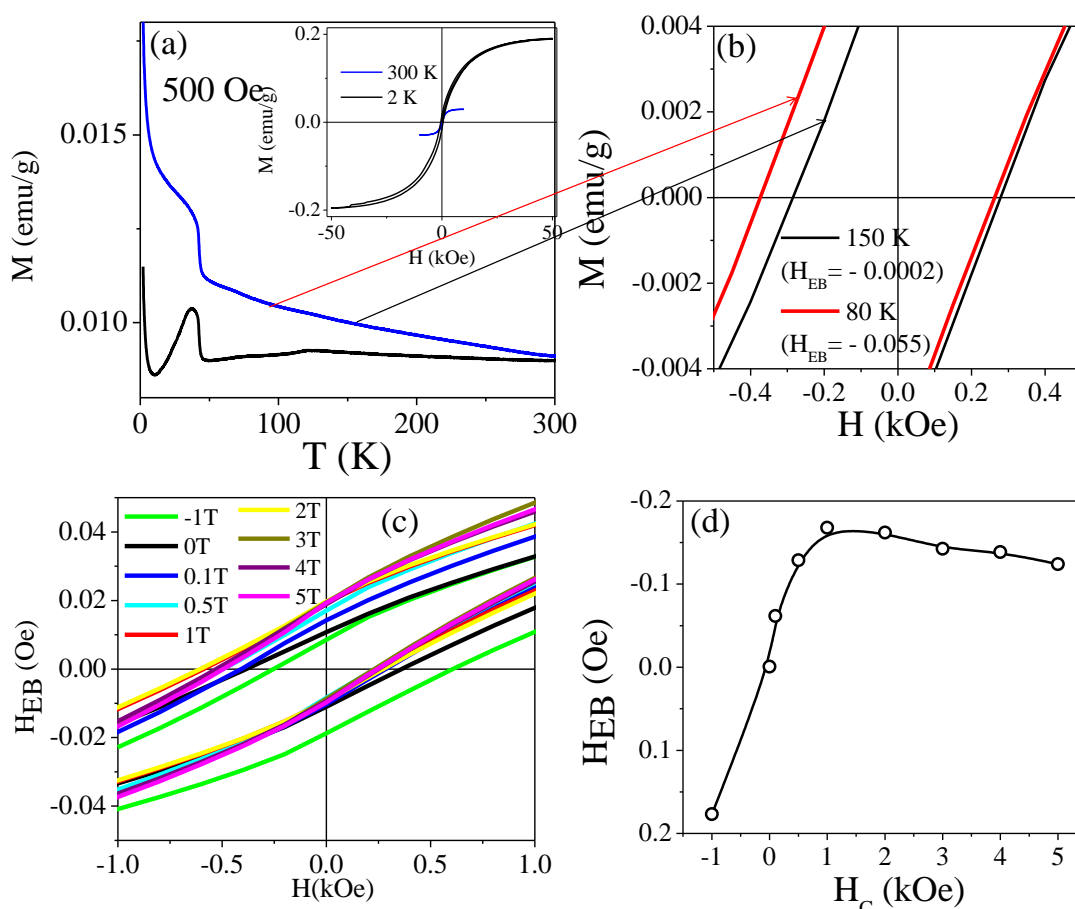


**Figure 13.** (a) FC and ZFC curves of GNR under an applied field of 500 Oe, (b) hysteresis loops at 150K and 80K with  $H_{cool} = 1T$ , (c) variation of hysteresis loops at 2K with  $H_{COOL} = -1T, 0.1T, 0.5T, 1T, 2T, 3T, 4T$  and  $5T$  and (d) the dependence of  $H_{EB}$  on  $H_{cool}$  at 2K for few-layer  $MoS_2$  nanoribbons. Ferromagnetic hysteresis loops at 2K and 300K for  $MoS_2$  nanoribbons are shown as inset in (a).

Bulk  $MoS_2$  and  $MoS_2$  nanoscrolls prepared by K intercalation and exfoliation do not show any ferromagnetism or exchange bias effect. However, it is to be noted that few-layer  $MoS_2$  does show very small exchange bias effect with an exchange bias field of - 20 Oe at cooling field of 1T (see Figure 14(a)) . This is about 35-40 times lesser than that observed in case of nanoribbons. Thus, both graphene nanoribbons and their analogues

MoS<sub>2</sub> nanoribbons show significant exchange bias effect confirming the existence of strongly coupled ferromagnetic and antiferromagnetic interactions.

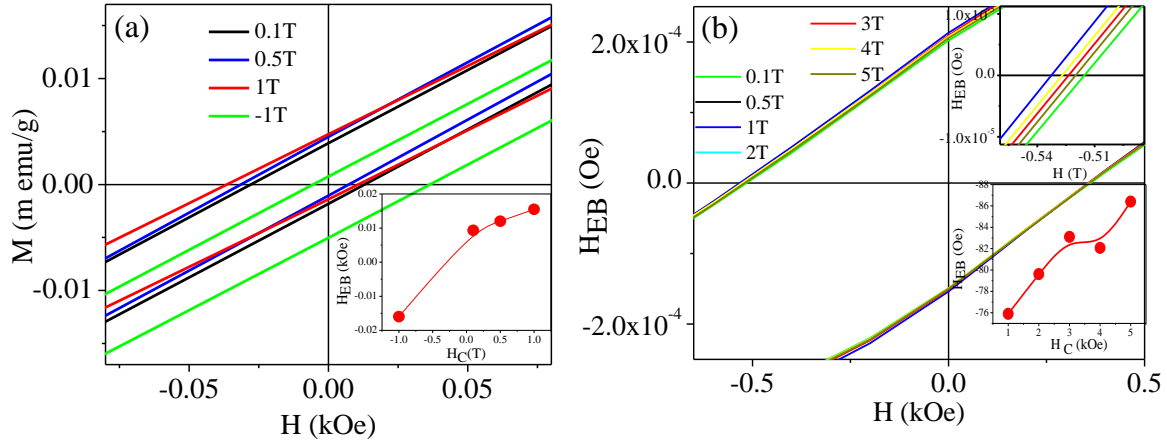


**Figure 14.** (a) Hysteresis loops of few-layer MoS<sub>2</sub> sheets at 2K with  $H_{cool} = -1T, 0.1T, 0.5T$  and  $1T$ . Inset in (a) shows the dependence of  $H_{EB}$  on  $H_{cool}$ . (b) Hysteresis loops of few-layer BNNRs at 2K with  $H_{COOL} = 0.1T, 0.5T, 1T, 2T, 3T, 4T$  and  $5T$ . Inset in (b, top) shows the magnified  $-ve$  field axis of the same and (b, bottom) shows the dependence of  $H_{EB}$  on  $H_{cool}$ .

To further generalize the fact that nanoribbons of layered materials do possess competing ferromagnetic and antiferromagnetic interactions that manifests itself as exchange bias effect, we studied field dependent exchange bias properties of few-layer BN nanoribbons (BNNRs) as shown in Figure 14(b). BNNRs also show exchange bias effect with  $H_{EB} = 87$  Oe on using a cooling field of  $5T$ . Unlike GNRs and MoS<sub>2</sub>NRs, BNNRs show much weaker exchange bias effect and the  $H_{EB}$  increase almost monotonically with increasing cooling field.

## 5. Conclusions

In conclusion, we have been able to obtain nanoribbons and nanoscrolls of graphene and graphene analogues of BN and MoS<sub>2</sub> by intercalation of K followed by exfoliation in ethanol. K intercalation was carried out by reaction of corresponding bulk or nanosheets with K vapour. Highly exothermic reaction of K metal with ethanol provides energy for exfoliation and drives the formation of nanoscrolls and nanoribbons. While

nanoscrolls are formed when bulk samples were intercalated and exfoliated, nanoribbons are formed when few-layered analogues were used as starting material. Defect sites on few-layer samples help the propagation of initially formed fissures in the layer resulting in cutting of the sheets. Defect free bulk samples on the other hand roll up using the energy supplied by the exothermic reaction of K with ethanol and form nanoscrolls, which are energetically more stable than individual bent sheets obtained by exfoliation.

Nanoscrolls of MoS<sub>2</sub> and WS<sub>2</sub> were also prepared by using microwave irradiation and liquid nitrogen. FESEM and TEM studies shows the synthesized MoS<sub>2</sub> and WS<sub>2</sub> nanoscrolls exhibit a tubular structure, with interlayer spacing corresponding to the (002) stacking of corresponding metal sulfides. Raman studies show softening and broadening of the in-plane and out of plane modes, clearly indicative of the fact that scrolls have macroscopic properties different from bulk.

Nanoribbons of graphene and graphene analogues of MoS<sub>2</sub> and BN show evidence both ferromagnetic and antiferromagnetic interactions. These two competing interactions are strongly coupled to each other and therefore manifest as exchange bias effect. MoS<sub>2</sub> nanoribbons show stronger exchange bias effect as compared to GNRs and BNNRs, with BNNRs showing only a very weak effect. Though, exchange bias effect is observable in few-layer 2D MoS<sub>2</sub>, it is 35-40 times weaker than that observed in the case of nanoribbons of few-layer MoS<sub>2</sub>. On reducing the dimensionalities from 2D to 1D ribbon like morphology the exchange bias effect enhances. Observation of exchange bias effect in nanoribbons of graphene and its analogues is a direct evidence of presence of both ferromagnetic and antiferromagnetic type interactions in these materials.

## References

1. S. Y. Zhou, G. H. Gweon, A. V. Fedorov, P. N. First, W. A. de Heer, D. H. Lee, F. Guinea, A. H. Castro Neto and A. Lanzara. *Nature Mater.* **2007**, 6, 770.
2. Y. Zhang, T.-T. Tang, C. Girit, Z. Hao, M. C. Martin, A. Zettl, M. F. Crommie, Y. R. Shen and F. Wang. *Nature* **2009**, 459, 820.
3. S. Y. Zhou, D. A. Siegel, A. V. Fedorov and A. Lanzara. *Phys. Rev. Lett.* **2008**, 101, 086402.
4. S. Wang, P.-J. Chia, L.-L. Chua, L.-H. Zhao, R.-Q. Png, S. Sivaramakrishnan, M. Zhou, R. G. S. Goh, R. H. Friend, A. T. S. Wee and P. K. H. Ho. *Adv Mater.* **2008**, 20, 3440.
5. D. C. Elias, R. R. Nair, T. M. G. Mohiuddin, S. V. Morozov, P. Blake, M. P. Halsall, A. C. Ferrari, D. W. Boukhvalov, M. I. Katsnelson, A. K. Geim and K. S. Novoselov. *Science* **2009**, 323, 610.
6. Y.-W. Son, M. L. Cohen and S. G. Louie. *Phys. Rev. Lett.* **2006**, 97, 216803.
7. V. Barone, O. Hod and G. E. Scuseria. *Nano Lett.* **2006**, 6, 2748.
8. B. Obradovic, R. Kotlyar, F. Heinz, P. Matagne, T. Rakshit, M. D. Giles, M. A. Stettler and D. E. Nikonov. *Appl. Phys. Lett.* **2006**, 88.
9. M.-W. Lin, C. Ling, L. A. Agapito, N. Kioussis, Y. Zhang, M. M.-C. Cheng, W. L. Wang, E. Kaxiras and Z. Zhou. *Phys. Rev. B* **2011**, 84, 125411.
10. X. Wang, Y. Ouyang, X. Li, H. Wang, J. Guo and H. Dai. *Phys. Rev. Lett.* **2008**, 100, 206803.
11. Y.-W. Son, M. L. Cohen and S. G. Louie. *Nature* **2006**, 444, 347.
12. S. Dutta and S. K. Pati. *J. Mater. Chem.* **2010**, 20, 8207.
13. H. W. Kroto, J. R. Heath, S. C. O. Brien, R. F. Curl and R. E. Smalley. *Nature* **1985**, 318, 162.
14. R. Tenne, L. Margulis, M. Genut and G. Hodes. *Nature* **1992**, 360, 444.
15. S. Iijima. *Nature* **1991**, 354, 56.
16. K. S. Novoselov, D. Jiang, F. Schedin, T. J. Booth, V. V. Khotkevich, S. V. Morozov and A. K. Geim. *Proc. Natl. Acad. Sc. USA* **2005**, 102, 10451.
17. H. S. S. Ramakrishna Matte, A. Gomathi, A. K. Manna, D. J. Late, R. Datta, S. K. Pati and C. N. R. Rao. *Angew. Chem. Int. Ed.* **2010**, 49, 4059.

18. R. Bacon. *J. Appl. Phys.* **1960**, 31, 283.
19. T. Sharifi, E. Gracia Espino, H. Reza Barzegar, X. Jia, F. Nitze, G. Hu, P. Nordblad, C.-W. Tai and T. Wagberg. *Nature Commun.* **2013**, 4, DOI: 10.1038/ncomms3319.
20. H. Pan, Y. Feng and J. Lin. *Phys. Rev. B* **2005**, 72, 085415.
21. S. F. Braga, V. R. Coluci, S. B. Legoas, R. Giro, D. S. Galvão and R. H. Baughman. *Nano Lett.* **2004**, 4, 881.
22. G. Mpourmpakis, E. Tylianakis and G. E. Froudakis. *Nano Lett.* **2007**, 7, 1893.
23. Y. Kopelevich and P. Esquinazi. *J. Low Temp. Phys.* **2007**, 146, 629.
24. T. L. Makarova, K. H. Han, P. Esquinazi, R. R. da Silva, Y. Kopelevich, I. B. Zakharova and B. Sundqvist. *Carbon* **2003**, 41, 1575.
25. P. Esquinazi, A. Setzer, R. Hoene, C. Semmelhack, Y. Kopelevich, D. Spemann, T. Butz, B. Kohlstrunk and M. Loesche. *Phys. Rev. B* **2002**, 66, 024429.
26. O. E. Andersson, B. L. V. Prasad, H. Sato, T. Enoki, Y. Hishiyama, Y. Kaburagi, M. Yoshikawa and S. Bandow. *Phys. Rev. B* **1998**, 58, 16387.
27. Y. Shibayama, H. Sato, T. Enoki and M. Endo. *Phys. Rev. Lett.* **2000**, 84, 1744.
28. P. Esquinazi, A. Setzer, ouml, R. hne, C. Semmelhack, Y. Kopelevich, D. Spemann, T. Butz, B. Kohlstrunk and M. sche. *Phys. Rev. B* **2002**, 66, 024429.
29. Y. Wang, Y. Huang, Y. Song, X. Y. Zhang, Y. F. Ma, J. J. Liang and Y. S. Chen. *Nano Lett.* **2009**, 9, 220.
30. C. N. R. Rao, K. S. Subrahmanyam, H. S. S. Ramakrishna Matte, B. Abdulhakeem, A. Govindaraj, B. Das, P. Kumar, A. Ghosh and D. J. Late. *Sci. Tech. Adv. Mater.* **2010**, 11, 054502.
31. C. N. R. Rao, A. K. Sood, K. S. Subrahmanyam and A. Govindaraj. *Angew. Chem. Int. Ed.* **2009**, 48, 7752.
32. H. S. S. R. Matte, K. S. Subrahmanyam and C. N. R. Rao. *J. Phys. Chem. C* **2009**, 113, 9982.
33. O. V. Yazyev. *Phys. Rev. Lett.* **2008**, 101, 037203.
34. R. Singh and P. Kroll. *J. Phys.-Condes. Matter* **2009**, 21, 196002.
35. M. M. Ugeda, I. Brihuega, F. Guinea and J. M. Gomez-Rodriguez. *Phys. Rev. Lett.* **2010**, 104, 096804.

36. S. Bhowmick and V. B. Shenoy. *J. Chem. Phys.* **2008**, 128, 244717.
37. L. Z. Kou, C. Tang, W. L. Guo and C. F. Chen. *Acs Nano* **2011**, 5, 1012.
38. L. Jiao, L. Zhang, X. Wang, G. Diankov and H. Dai. *Nature* **2009**, 458, 877.
39. O. V. Yazyev and M. I. Katsnelson. *Phys. Rev. Lett.* **2008**, 100, 047209.
40. B. Sahu, H. K. Min and S. K. Banerjee. *Phys. Rev. B* **2010**, 82, 7.
41. D. W. Boukhvalov and M. I. Katsnelson. *Nano Lett.* **2008**, 8, 4373.
42. H. Xiang, E. Kan, S.-H. Wei, M.-H. Whangbo and J. Yang. *Nano Lett.* **2009**, 9, 4025.
43. D. W. Boukhvalov. *Chem. Phys. Lett.* **2010**, 501, 396.
44. R. C. Longo, J. Carrete and L. J. Gallego. *J. Chem. Phys.* **2011**, 134, 024704.
45. V. L. J. Joly, M. Kiguchi, S.-J. Hao, K. Takai, T. Enoki, R. Sumii, K. Amemiya, H. Muramatsu, T. Hayashi, Y. A. Kim, M. Endo, J. Campos-Delgado, F. Lapez-Urias, A. Botello-Menendez, H. Terrones, M. Terrones and M. S. Dresselhaus. *Phys. Rev. B* **2010**, 81, 245428.
46. Y.-W. Son, M. L. Cohen and S. G. Louie. *Nature* **2006**, 444, 347.
47. C. Tao, L. Jiao, O. V. Yazyev, Y.-C. Chen, J. Feng, X. Zhang, R. B. Capaz, J. M. Tour, A. Zettl, S. G. Louie, H. Dai and M. F. Crommie. *Nature Phys.* **2011**, 7, 616.
48. J. Zhang, J. M. Soon, K. P. Loh, J. Yin, J. Ding, M. B. Sullivan and P. Wu. *Nano Lett.* **2007**, 7, 2370.
49. P. Dev, Y. Xue and P. Zhang. *Phys. Rev. Lett.* **2008**, 100, 117204.
50. B. Song, J. C. Han, J. K. Jian, H. Li, Y. C. Wang, H. Q. Bao, W. Y. Wang, H. B. Zuo, X. H. Zhang, S. H. Meng and X. L. Chen. *Phys. Rev. B* **2009**, 80, 153203.
51. C. N. R. Rao, H. S. S. R. Matte, K. S. Subrahmanyam and U. Maitra. *Chem. Sc.* **2012**, 3, 45.
52. M. Y. Han, B. Åzyilmaz, Y. Zhang and P. Kim. *Phys. Rev. Lett.* **2007**, 98, 206805.
53. Z. Chen, Y.-M. Lin, M. J. Rooks and P. Avouris. *Physica E* **2007**, 40, 228.
54. L. Tapaszto, G. Dobrik, P. Lambin and L. P. Biro. *Nature Nanotechnol.* **2008**, 3, 397.
55. X. Li, X. Wang, L. Zhang, S. Lee and H. Dai. *Science* **2008**, 319, 1229.



56. J. Campos-Delgado, J. M. Romo-Herrera, X. Jia, D. A. Cullen, H. Muramatsu, Y. A. Kim, T. Hayashi, Z. Ren, D. J. Smith, Y. Okuno, T. Ohba, H. Kanoh, K. Kaneko, M. Endo, H. Terrones, M. S. Dresselhaus and M. Terrones. *Nano Lett.* **2008**, 8, 2773.
57. D. V. Kosynkin, A. L. Higginbotham, A. Sinitskii, J. R. Lomeda, A. Dimiev, B. K. Price and J. M. Tour. *Nature* **2009**, 458, 872.
58. A. L. Higginbotham, D. V. Kosynkin, A. Sinitskii, Z. Sun and J. M. Tour. *ACS Nano* **2010**, 4, 2059.
59. JiaoLiyang, WangXinran, DiankovGeorgi, WangHailiang and DaiHongjie. *Nature Nanotechnol.* **2011**, 6, 132.
60. Z.-S. Wu, W. Ren, L. Gao, B. Liu, J. Zhao and H.-M. Cheng. *Nano Res.* **2010**, 3, 16.
61. P. Kumar, L. S. Panchakarla and C. N. R. Rao. *Nanoscale* **2011**, 3, 2127.
62. W. J. Yu, S. H. Chae, D. Perello, S. Y. Lee, G. H. Han, M. Yun and Y. H. Lee. *ACS Nano* **2010**, 4, 5480.
63. X. Wang and H. Dai. *Nature Chem.* **2010**, 2, 661.
64. J. Cai, P. Ruffieux, R. Jaafar, M. Bieri, T. Braun, S. Blankenburg, M. Muoth, A. P. Seitsonen, M. Saleh, X. Feng, K. Mullen and R. Fasel. *Nature* **2010**, 466, 470.
65. X. Yang, X. Dou, A. Rouhanipour, L. Zhi, H. J. Rader and K. Mullen. *J. Am. Chem. Soc.* **2008**, 130, 4216.
66. A. G. Cano-Maquez, F. J. Rodríguez-Macias, J. Campos-Delgado, C. G. Espinosa-González, F. Tristán-López, D. Ramírez-González, D. A. Cullen, D. J. Smith, M. Terrones and Y. I. Vega-Cantu. *Nano Lett.* **2009**, 9, 1527.
67. D. V. Kosynkin, W. Lu, A. Sinitskii, G. Pera, Z. Sun and J. M. Tour. *ACS Nano* **2011**, 5, 968.
68. L. M. Viculis, J. J. Mack and R. B. Kaner. *Science* **2003**, 299, 1361.
69. S. S. Rao, S. N. Jammalamadaka, A. Stesmans, V. V. Moshchalkov, J. v. Tol, D. V. Kosynkin, A. Higginbotham-Duque and J. M. Tour. *Nano Lett.* **2012**, 12, 1210.

**Chapter II.5. Nanoribbons and nanoscrolls .....**

---

70. D. C. Marcano, D. V. Kosynkin, J. M. Berlin, A. Sinitskii, Z. Sun, A. Slesarev, L. B. Alemany, W. Lu and J. M. Tour. *ACS Nano* **2010**, 4, 4806.
71. J. Zheng, H. Liu, B. Wu, Y. Guo, T. Wu, G. Yu, Y. Liu and D. Zhu. *Adv. Mater.* **2011**, 23, 2460.
72. D. Roy, E. Angeles-Tactay, R. J. C. Brown, S. J. Spencer, T. Fry, T. A. Dunton, T. Young and M. J. T. Milton. *Chem. Phys. Lett.* **2008**, 465, 254.
73. M. Viršek, A. Jesih, I. Milošević, M. Damjanović and M. Remškar. *Surf. Sci.* **2007**, 601, 2868.
74. H.-q. Zhou, C.-y. Qiu, H.-c. Yang, F. Yu, M.-j. Chen, L.-j. Hu, Y.-j. Guo and L.-f. Sun. *Chem. Phys. Lett.* **2011**, 501, 475.
75. M. Huang, H. Yan, C. Chen, D. Song, T. F. Heinz and J. Hone. *Proc. Natl. Acad. Sc. USA* **2009**, 106, 7304.

# ***PART III***

## ***Artificial photosynthesis to generate hydrogen and oxygen***

### ***Introduction***

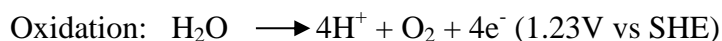
Energy and environmental issues constitute the biggest technological challenges today. The global energy demands are stipulated to rise from current level of 12 TW per day to 27 TW by 2050. The current sources of energy, primarily hydrocarbons, coal and petroleum are non-renewable and will not be able to sustain the increasing demands of energy. Burning of hydrocarbons emits CO<sub>2</sub>, the major greenhouse gas leading to alarming rate of environmental degradation and global warming. According to International energy agency the goal of limiting global warming to 2°C is becoming more difficult to maintain with each passing year and if action is not taken within 2020, all allowable CO<sub>2</sub> emissions would be locked. Alternative energy supplies are urgently needed to limit our dependence on fossil fuels. Solar energy is the most abundant and sustainable natural source of energy with the earth receiving about 120,000 TW each day, way higher than all our energy needs. Direct conversion of solar energy to electricity for direct use or storage in batteries can be achieved by photovoltaic cells. Direct conversion of solar energy to fuels involving storage of solar energy in the form of energy of chemical bonds is another way to harvest energy, also known as artificial photosynthesis. Solar fuels can be in the form of H<sub>2</sub>, produced from photoassisted water splitting or high-energy carbon compounds (CO, HCOOH, or CH<sub>3</sub>OH) that are produced by light-driven reduction of CO<sub>2</sub>. Hydrogen having the highest energy density per unit weight and being

## ***Artificial photosynthesis***

---

the cleanest source of energy (only byproduct of burning H<sub>2</sub> is water) has been advocated as the ultimate fuel for future. Electrolysis of water using solar cells, reforming biomass and photocatalytic or photoelectrochemical water splitting are the three approaches to Hydrogen. Photocatalytic water splitting being the simplest in design has been one of the most investigated field of research over the past several years.

In photocatalytic water splitting the energy of photons is converted to the chemical energy of H<sub>2</sub> by breaking the bonds in water. This process is accompanied by large positive Gibbs free energy of 238 kJ.mol<sup>-1</sup>. Just as in natural photosynthesis, this is an uphill reaction and is difficult to perform unlike photocatalytic degradation of organic compounds using oxygen which is a downhill reaction. Water splitting involves two redox reactions involving four electrons:



Plants perform this conversion through natural photosynthesis where CO<sub>2</sub> and water get converted to oxygen and carbohydrates. Photosynthesis occurs in two stages. In the first stage, water is oxidized to O<sub>2</sub> generating a proton which gets bound to NADP<sup>+</sup> to give the energy carrier, NADPH. In the second stage, NADPH is used to reduce CO<sub>2</sub> to glucose.

## ***Natural Photosynthesis***

In Figure 1, we show a schematic representation of natural photosynthesis. Solar energy is absorbed by chlorophyll and other pigments of PSII, which is the center for light-reaction in photosynthesis. P680 (containing chlorophyll a) or PSII absorbs a photon and loses an electron to pheophytin (a modified form of chlorophyll) generating P680<sup>+</sup>. The redox potential of P680 is highly oxidizing while that of pheophytin is -0.5V so that it is able to reduce H<sup>+</sup> to H<sub>2</sub>.<sup>1</sup> In order to reduce the probability of charge recombination the electron is transported from pheophytin, down, along a chain of molecules to photosystem I (PSI). This process of electron transfer down a chain of potential gradients ensures that the charge separation quantum efficiency of nearly 100% since the electron transfer processes happen on a femto-second time scale.

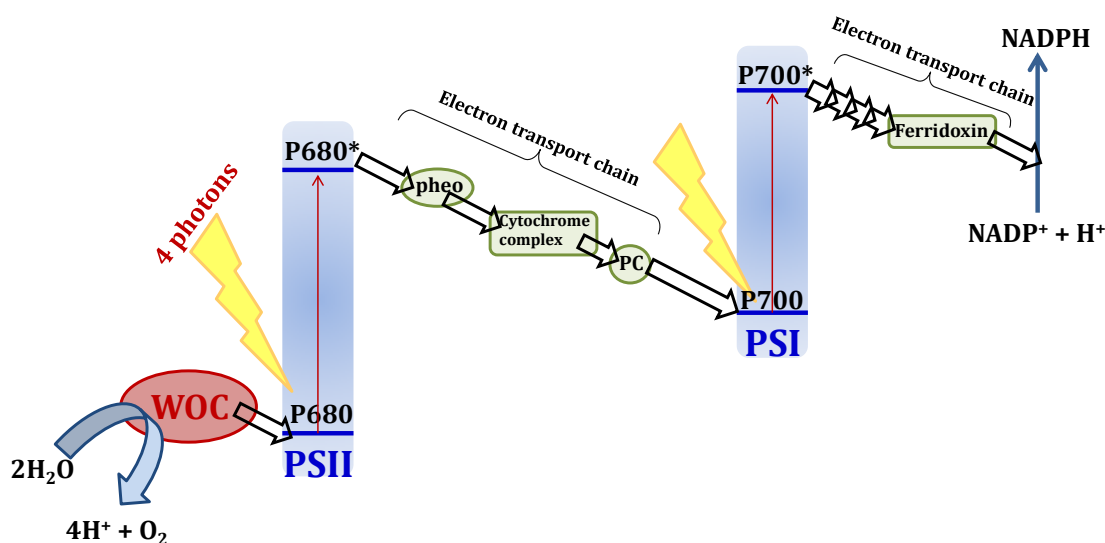


**Figure 1.** Z-scheme of photosynthesis. PSI and PSII are photosystems I and II respectively, also known as P680 and P700. (adapted from reference <sup>1</sup>)

The electrons ( $e^-$ ) and holes ( $h^+$ ) have life times of  $\mu\text{sec}$  before charge recombination.  $\text{P680}^+$  regains its electron from water thereby oxidizing it to  $\text{O}_2$  in a reaction catalyzed by the water oxidizing center (WOC) which is a cubic  $\text{Mn}_4\text{O}_5\text{Ca}$  cluster encapsulated in a protein environment. In the meantime, P700 or PSI absorbs light and loses an electron to reduce  $\text{H}^+$  and convert  $\text{NADP}^+$  to  $\text{NADPH}$  thereby generating  $\text{P700}^+$ . The electron that travels down the cascade of steps to PSI is used up by  $\text{P700}^+$ .<sup>1</sup> This electron transport chain is commonly referred to as the **Z-scheme** of photosynthesis. Generation of  $\text{O}_2$  from water is a 4 electron process as shown in reaction 1. PSII has to therefore absorb 4 photons to drive this half-reaction and PSI also has to absorb 4 photons for the subsequent reduction reaction. Absorption of two photons by the natural photosynthetic system generates one electron and one hole making the efficiency of this reaction almost 50%. However, considering that chlorophylls absorb nearly in the entire visible range and utilize only the red photons, the efficiency drops down to 20%. In actuality, natural photosynthesis in an agricultural crop is only 1% efficient over its entire life-cycle.<sup>2</sup>

### Artificial Photosynthesis

Artificial photosynthesis provides great efficiency and simplicity and employs principles derived from natural photosynthesis. Artificial photosynthesis primarily

## Artificial photosynthesis

involves a photon absorbing center and a catalytic center with an electron and hole transfer pathway joining the two. A single-step or a two-step process can be employed in artificial photosynthesis (Figure 2). In the single-step process, a photon absorber is directly attached to an electron donor on one side and/or an electron acceptor on the other. The photon absorber can be a semiconductor or a dye which absorbs light generating an electron-hole pair. The wavelength of light absorbed depends on the band gap of the semiconductor or the HOMO-LUMO gap of the dye as shown in Figure 2 (a). The semiconductor or dye is generally used in conjugation with an electron donor or an electron acceptor to enhance charge separation. An electron donor should have an energy level more negative than the excited state reduction potential of the semiconductor or the dye and at the same time more positive than the water oxidation potential. The electron acceptor would have an energy level more negative than the proton reduction potential and more positive than the excited state oxidation potential of the photon absorber. For swift electron transfer, acceptors and donors must be close to the photon absorber. Electron and hole transfer occurs directly from the energy levels of the semiconductor or the dye with only the electron donor or the electron acceptor or neither of them being used in the process of the reaction.

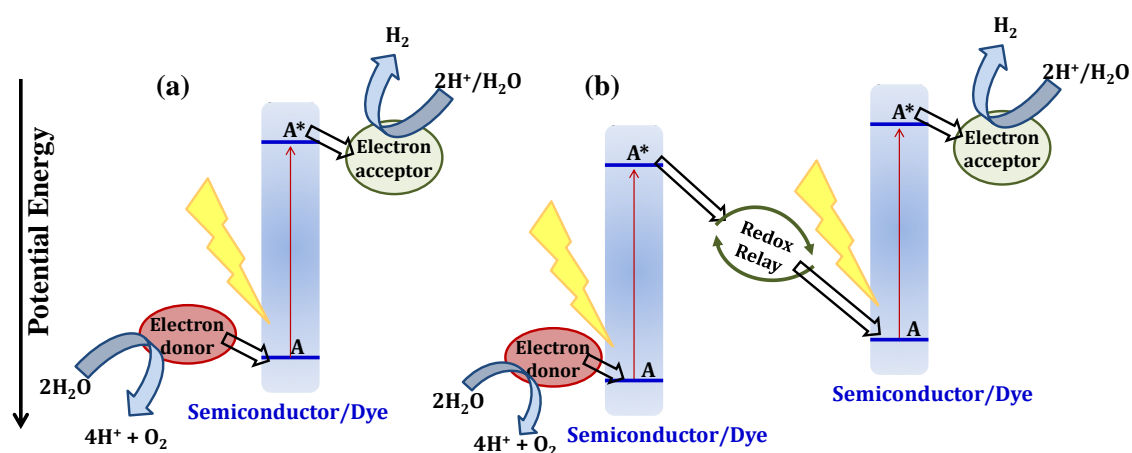


**Figure 2.** Artificial photosynthesis by (a) single- and (b) two-step processes. (adapted from reference <sup>1</sup>)

In the two-step process, two photon absorbers are connected to each other by an electron transfer-relay material, the rest of the principles being similar to that of the single step

process as shown in Figure 2 (b). A redox couple is used as the electron transfer relay. The two-step process is analogous to the Z-scheme of natural photosynthesis and utilizes two photons to generate one electron and one hole. In the case of the single-step process, on the other hand, the two components of the Z-scheme are combined into one. The single-step process is simple, but the disadvantage is that only a limited fraction of sunlight (<680 nm) can be used to initiate both the oxidation and reduction of water. The two-step process can be used for complete water splitting even with low excitation energy, as low as near-infrared wavelengths. This advantage is accompanied by the difficulty of maintaining the kinetics of the full electron-transfer process with minimal energy loss by charge recombination reactions. An ideal process of electron transfer is to have more than one electron acceptor or donor level closely spaced in energy as in natural photosynthesis. However, this increases the complexity of the system and is somewhat difficult to achieve. Good electron acceptors like fullerenes<sup>3,4</sup> have been coupled with chromophores to achieve upto 95% charge separation. A simpler but less effective strategy is to employ co-catalysts in semiconductor based light harvesters. Pt, NiO (for H<sub>2</sub>) and RuO<sub>2</sub>, IrO<sub>2</sub> (for O<sub>2</sub>) satisfy the required conditions for use as catalysts.

The mechanism of photosynthesis (artificial or natural) thus comprises three aspects: i) light-harvesting, ii) charge generation and separation and iii) catalytic reaction as shown in Figure 3 (a). The photosynthetic catalysts can be classified as:

- Semiconductor- based photocatalysts
- Catalysts used in photoelectrodes.
- Dye-sensitized catalysts

✓ *Semiconductor-based photocatalysts*

These are the simplest of all catalysts with all the three processes of photosynthesis occurring in a single system. The semiconductor absorbs a photon with energy greater than its band gap and generates an electron-hole pair, followed by the migration of the electrons and holes to the surface of the semiconductor which participate in surface chemical reactions with water or other sacrificial agents. Recombination of e<sup>-</sup> and h<sup>+</sup> competes with the process of charge separation reducing the efficiency of photocatalysis as illustrated in Figure 3 (a). Grain boundaries and defects in the semiconducting particles

## Artificial photosynthesis

act as charge recombination centers. Charge recombination can be minimized by decreasing the size of the particle down to a few nm.<sup>5</sup> The electrons and holes would then go to the surface and are used to reduce and oxidize water respectively. They can also be used up by a sacrificial electron or hole scavenger. A hole scavenger is a strong reducing agent such as an alcohol or a sulfide which gets oxidized by the photogenerated  $h^+$  instead of water and thereby enriches the system with electrons to be used for the reduction of water to generate  $H_2$ .  $Ag^+$  and  $Fe^{3+}$  have also been used as electron scavengers for water oxidation.<sup>5</sup> A sacrificial system eliminates back electron transfer and renders it feasible to examine only the oxidation or the reduction of water.

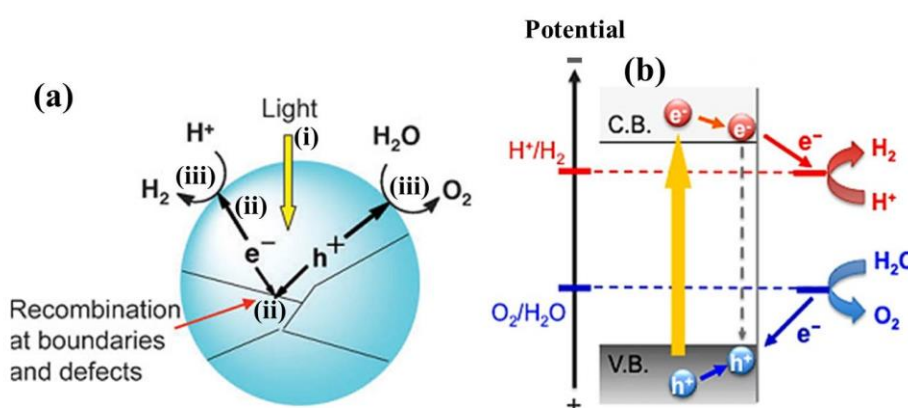


**Figure 3.** Schematic representations of (a) processes in photosynthesis and (b) of the energy level requirements in semiconductor photocatalysis. (from reference <sup>2,5</sup>)

For a semiconductor to act as a water-splitting catalyst, it must satisfy the following energy level conditions. The bottom of the conduction band must be more negative than the reduction potential of  $H^+/H_2$  (0 V vs. SHE), and the top of the valence band must be more positive than the oxidation potential of  $O_2/H_2O$  (1.23 V) as shown in Figure 3 (b), limiting the theoretical minimum band gap for water splitting to 1.23 eV. Based on the above criterion, several semiconductors have been identified for  $H_2$  evolution or oxygen evolution or both (Figure 4.). Semiconductors such as  $TiO_2$ ,  $SrTiO_3$ ,  $BaTiO_3$ ,  $FeTiO_3$ ,  $ZrO_2$  and  $ZnO$  whose conduction band potential lie above the proton reduction potential can reduce water to produce  $H_2$ . On the other hand, semiconductors such as  $Fe_2O_3$ ,  $SnO_2$ ,  $WO_3$  etc. can only oxidize water to  $H_2$ . Semiconductors like  $CdS$ ,  $CdSe$  and  $MoS_2$  are ideal for visible light photocatalytic  $H_2$  production by virtue of the sufficiently negative conduction band potential and small band gap (Figure 4.).



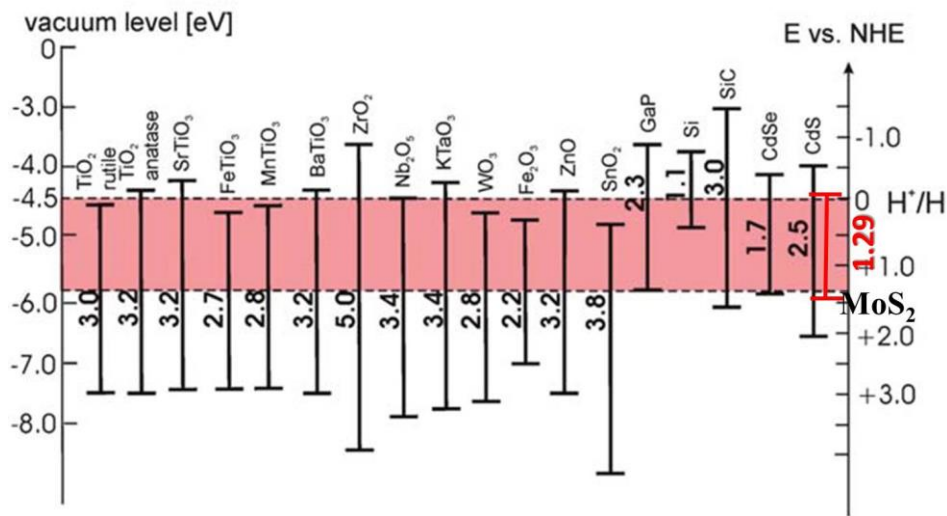


**Figure 4.** Some semiconductor photocatalysts and their corresponding band positions with respect to the water redox potential.[from reference <sup>6</sup>]

✓ *Catalysts used in photoelectrodes*

In photo-electrocatalytic systems, the semiconductor acts as one of the electrodes of an electrochemical cell and is connected to the counter electrode via an external circuit. On absorbing light, the semiconductor generates the electron-hole pair. In the case of an n-type semiconductor photoelectrode, the photoexcited electron is transferred to the counter electrode (mostly Pt) where it reduces  $H^+$  to  $H_2$ . The  $h^+$  oxidizes water at the semiconductor surface.

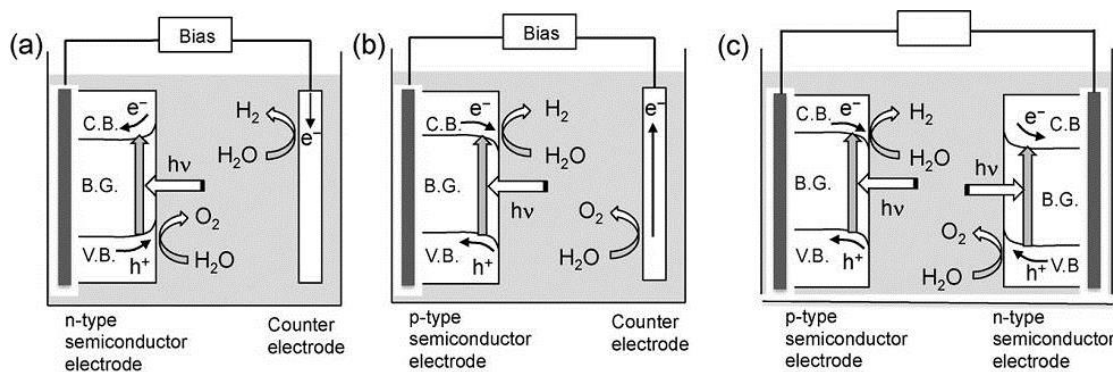


**Figure 5.** Schematic representation of the processes of photo-electrochemical water splitting. (From reference <sup>2</sup>)

## ***Artificial photosynthesis***

In the case of a p-type semiconductor photoelectrode, the photogenerated electrons reduce water at the surface of the semiconductor while an electron from the counter electrode balances the  $h^+$ , oxidizing water at the counter electrode. The process of photo-electrochemical water splitting is demonstrated in Figure 5. Photo-electrochemical cells with both the anode and the cathode composed of photon absorbers have been used. Even though the semiconductor possesses suitable CB/VB levels for the reduction/oxidation of water, an external bias or a pH difference (chemical bias) needs to be maintained to overcome the resistance between the two electrodes in solution and at the interface between the solution and the semiconductor electrode. Here, charge-recombination is inhibited by the bias leading to greater efficiency, with the quantum yield approaching unity and a power conversion efficiency of  $\sim 18\%$ .<sup>7</sup>

### ✓ ***Dye-sensitized catalysts***

Use of semiconductors as photocatalysts imposes a limitation on the band gap of the semiconductor. Semiconductors with a large band gap absorb light in the UV region neglecting the entire visible and near infrared regions of the solar spectrum. Dye sensitization permits the use of semiconductors with energy levels matched with the redox potential of water, without compromising with the range of energies absorbed. On illumination with visible light, the excited dye transfers an electron to the conduction band of the semiconductor provided the excited state oxidation potential of the dye is more negative than the conduction band of the semiconductor (Figure 6) and the dye itself gets oxidized.

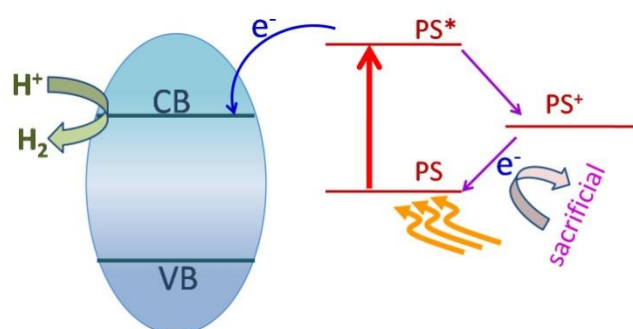


**Figure 6.** Schematic representation of dye-sensitized  $H_2$  evolution. (PS represents a photosensitizer/dye)

A sacrificial electron donor or a redox shuttle such as the  $I^{3-}/I^-$  pair is used to regenerate the photosensitizer and sustain the reaction cycle. Photosynthesis broadens the spectrum response range and increases the efficiency of charge transfer by spatial separation of the electron and the hole. Dye-sensitized photo-electrochemical cells having dye-sensitized photoelectrodes also work on similar principles with the reduction of water occurring at the counter electrode and the sacrificial agent getting oxidized at the photosensitized electrode. Dye sensitized  $TiO_2$  electrodes bearing  $IrO_2$  nanoparticles have been used for complete water splitting. On sensitization, the dye loses an  $e^-$  to  $TiO_2$  which transfers to the counter (Pt) electrode generating  $H_2$ . The  $IrO_2$  particles donate  $e^-$  to the oxidized dye to regenerate the photosensitizer.<sup>8</sup>

In the following two chapters we have dealt with understanding the process of water oxidation and hydrogen evolution separately. In natural systems water oxidation happens during the light-reaction of photosynthesis at PSII. The water oxidation center is composed of water oxidizing complex called the WOC. In order to develop efficient catalysts for water oxidation with earth abundant and cost effective elements much study has been conducted on understanding and mimicking the WOC. Several metal complexes, hybrids and inorganic oxides having structure and composition similar to the core of WOC have been studied. In the first chapter we have studied the principles behind water oxidation by inorganic transition metal oxides keeping in mind that oxidation state of the transition metal ion in WOC plays a crucial role in determining its catalytic properties. Proton reduction on the other hand is carried out naturally by hydrogenase an enzyme that catalyzes reduction of proton accompanied by oxidation of electron donors such as ferridoxin. Recently, it has become possible to anchor hydrogenase to an electrode surface,<sup>9</sup> and considerable progress has been made in the synthesis of compounds in solution resembling the hydrogenase active site and showing activity for hydrogen evolution.<sup>10,11</sup> More recently,  $MoS_2$  has been identified to have free energy for  $H_2$  evolution comparable to that of nitrogenase and hydrogenase with the edge structure of  $MoS_2$  sheets having close resemblance with the catalytically active sites of these enzymes. In the second chapter we have studied the photocatalytic properties of two polymorphs of  $MoS_2$  and their composites with graphene. To study the catalytic properties of inorganic transition metal oxides and  $MoS_2$  dye sensitization technique has been utilized with sacrificial electron donors and acceptors present in

solution. Since we were interested in getting an insight into the catalytic activity of the water oxidizing and reducing catalysts respectively, we have not used any co-catalyst during our study.

*In this part of the thesis following studies are presented:*

***Chapter III. 1*** Photochemical oxidation of water catalyzed by nanoparticles of Mn and Co oxides; the importance of  $e_g^1$  configuration.

***Chapter III. 2*** Highly efficient visible-light induced  $H_2$  generation by single-layer 1T-MoS<sub>2</sub> & nanocomposite of few-layer 2H-MoS<sub>2</sub> with heavily nitrogenated graphene

## References

1. Y. Tachibana, L. Vayssieres and J. R. Durrant. *Nat. Photon.* **2012**, *6*, 511.
2. R. Abe. *J. Photochem. Photobio. C* **2010**, *11*, 179.
3. D. González-Rodríguez, E. Carbonell, G. d. M. Rojas, C. A. Castellanos, D. M. Guldi and T. Torres. *J. Am. Chem. Soc.* **2010**, *132*, 16488.
4. G. Kodis, P. A. Liddell, A. L. Moore, T. A. Moore and D. Gust. *J. Phys. Org. Chem.* **2004**, *17*, 724.
5. A. Kudo and Y. Miseki. *Chem. Soc. Rev.* **2009**, *38*, 253.
6. M. Batzill. *Energy Environ. Sc.* **2011**, *4*, 3275.
7. E. R. Kleinfeld and G. S. Ferguson. *Science* **1994**, *265*, 370.
8. W. J. Youngblood, S.-H. A. Lee, K. Maeda and T. E. Mallouk. *Acc. Chem. Res.* **2009**, *42*, 1966.
9. S. E. Lamle, K. A. Vincent, L. M. Halliwell, S. P. J. Albracht and F. A. Armstrong. *Dalton Trans.* **2003**, 4152.
10. R. Mejia-Rodriguez, D. Chong, J. H. Reibenspies, M. P. Soriaga and M. Y. Darensbourg. *J. Am. Chem. Soc.* **2004**, *126*, 12004.
11. T. B. Rauchfuss. *Inorg. Chem.* **2003**, *43*, 14.

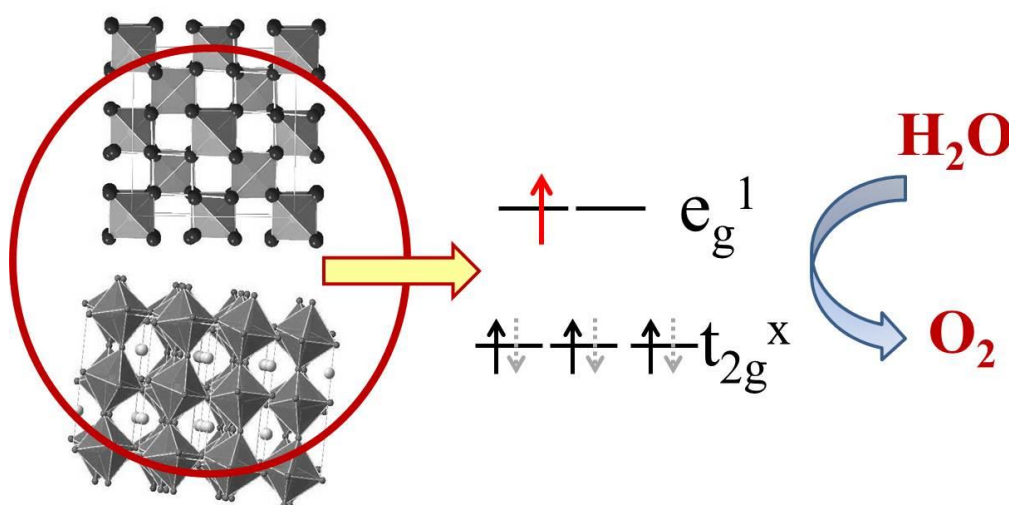


# Chapter III.1

## ***Photochemical oxidation of water catalyzed by nanoparticles of Mn and Co oxides; the importance of $e_g^1$ configuration***

### *Summary\**

*Electronic structure of the transition metal and not the structure of the oxide catalyst determines its activity for photo-catalytic water oxidation. All the transition metal oxides containing trivalent Co and Mn ions with single electron in the  $e_g$  orbital show good activity while samples with lesser or higher  $e_g$  occupancy do not show catalytic activity, irrespective of their structure. All the lanthanide manganites with the orthorhombic structure ( $t_{2g}^3 e_g^1$ ) show high catalytic activity while hexagonal manganites with  $e''^2 2e' a_1^0$  do not. Among all the perovskite and spinel oxides studied by us,  $\text{LaCoO}_3$  shows the highest activity.*



## **1. Introduction**

As discussed already, any strategy for solving the energy crisis would involve the generation of fuels through artificial photosynthesis, involving the sun as the only source of energy. In order to complete the solar cycle, water has to act as the source of electrons, either to generate liquid fuels by the reduction of CO<sub>2</sub> or to yield H<sub>2</sub> through a complete cycle of transfer of electrons. Photovoltaics have been used for production of H<sub>2</sub>, but cost of photovoltaic solar cells marginalizes the use of this route for the purpose. The challenge is to develop a water-splitting catalyst that is robust and composed of earth abundant non-toxic materials.

Oxidation of water, involving the transfer of 4 electrons is energy-intensive. One of the challenges with artificial photosynthesis is the development of cost effective catalysts made of earth abundant elements for the efficient oxidation of water to O<sub>2</sub>.<sup>1</sup> RuO<sub>2</sub> and IrO<sub>2</sub> are widely used as oxygen evolution catalysts although their availability is limited and expensive.<sup>2-5</sup> Natural system of water oxidation in plants occurs in the water oxidation complex (WOC) of the Photosystem II.<sup>6,7</sup> The WOC is a Mn<sub>4</sub>O<sub>5</sub>Ca cluster housed in protein environment. Mn is one of the most abundant transition metal found on earth while Ca is the fifth most abundant element on earth's crust. Understanding of the WOC therefore paves way to develop efficient water oxidation catalysts. Wide range techniques have been applied to probe the molecular mechanism and investigate the structure of the catalytic centre. X-ray absorption spectroscopy<sup>8</sup> and X-ray crystallography studies,<sup>9,10</sup> coupled with quantum mechanical analyses, have provided a refinement of the structure of the WOC<sup>11</sup> and given detailed schemes for the water-splitting chemistry leading to O – O bond formation<sup>10,12,13</sup>. These detailed investigations have revealed that WOC comprises of three Mn ions and a Ca ion forming a cubane-like structure with the four metal ions linked by oxo-bridges. A fourth Mn ion is linked to the cubane by two oxo-bridges and is adjacent to the Ca ion forming CaMn<sub>4</sub>O<sub>5</sub> cubical core cluster.<sup>14,15</sup> To study the principles governing photosynthesis, molecular systems with structures comparable to the Mn<sub>4</sub>O<sub>5</sub>Ca cluster having a [Mn<sub>4</sub>O<sub>4</sub>] core have been studied.<sup>16,17</sup>

Several simple Mn and other transition metal oxides with structures similar to the Mn<sub>4</sub>O<sub>4</sub> core have been studied to understand the process of natural photosynthesis utilizing simple inorganic oxides. Mn is not only an abundant element, but also occurs in



easily switchable oxidation states. Marokite type oxides,  $\text{CaMn}_2\text{O}_4$  and  $\text{CaMn}_2\text{O}_4 \cdot x\text{H}_2\text{O}$  exhibit good activity for water oxidation.<sup>18</sup> Based on X-ray spectroscopic studies, mixed valency of Mn (III/IV) was considered to be a criterion for good catalytic activity.<sup>19</sup> Electrochemical water oxidation by  $\text{Ca}_2\text{Mn}_3\text{O}_8$  which is structurally analogous to the  $\text{CaMn}_4\text{O}_5$  clusters has also been investigated.<sup>20</sup>  $[\text{Co}_4\text{O}_4]$  cubanes<sup>21,22</sup> nanocrystalline  $\text{Co}_3\text{O}_4$ <sup>23</sup> and  $\text{Mn}_2\text{O}_3$ <sup>24</sup> as well as “Co-Pi” and Co-Phosphates<sup>25,26</sup> have also been shown to be active for the oxygen evolution reactions(OER).

## **2. Scope of the present investigations**

In two interesting publications, Greenblatt, Dismukes and coworkers<sup>27,28</sup> have recently reported that nanoparticles of  $\lambda\text{-MnO}_2$  obtained by delithiation of  $\text{LiMn}_2\text{O}_4$  shows a much higher water oxidation catalytic activity with turnover frequency (TOF) of  $3 \times 10^{-5} \text{ s}^{-1}$  compared to the parent oxide. The extra flexibility of the  $[\text{Mn}_4\text{O}_4]$  cubic unit in  $\lambda\text{-MnO}_2$  was considered to be an important factor. Studies on nanoparticles of the  $\text{Li}_2\text{Co}_2\text{O}_4$  spinel containing the  $[\text{Co}_4\text{O}_4]$  cubic unit were also found by them to exhibit OER activity.<sup>28</sup>  $[\text{Co}_4\text{O}_4]$  cubic structural unit in  $\text{Li}_2\text{Co}_2\text{O}_4$  was demonstrated as the necessary criterion for catalytic activity. Its polymorph layered  $\text{LiCoO}_2$  does not show any activity for water oxidation. It is noteworthy that delithiation which was earlier deemed necessary to enable required flexibility was not needed in this case. It may be noted that Co in  $\text{Li}_2\text{Co}_2\text{O}_4$  exists as Co (III) whereas Mn in  $\lambda\text{-MnO}_2$  is primarily in the IV state. These workers did not report the properties of  $\text{LiCo}_2\text{O}_4$  where Co is mixed-valent. In order to understand the crucial factors responsible for catalytic oxidation of water and find a superior catalyst in the process, we have examined OER catalytic properties of nanoparticles of  $\text{LiMn}_2\text{O}_4$ ,  $\text{LiMnCoO}_4$ ,  $\text{LiCo}_2\text{O}_4$ ,  $\text{Li}_2\text{Co}_2\text{O}_4$  as well as few other Mn and Co oxides, specially  $\text{Mn}_2\text{O}_3$ ,  $\text{LaMnO}_3$ ,  $\text{MgMn}_2\text{O}_4$ ,  $\text{Li}_2\text{Co}_2\text{O}_4$  and  $\text{LaCoO}_3$  keeping in mind that strict comparisons of catalyst performance are best made on the basis of per mole of transition metal per unit surface area.

### 3. Experimental Section

#### Synthesis

**LiMn<sub>2-x</sub>A<sub>x</sub>O<sub>4</sub>:** All these materials were synthesized by citrate sol-gel method. For the synthesis of LiMn<sub>2-x</sub>A<sub>x</sub>O<sub>4</sub> nanoparticle, Mn(CH<sub>3</sub>COO)<sub>2</sub>.4H<sub>2</sub>O, Co(CH<sub>3</sub>COO)<sub>2</sub>.4H<sub>2</sub>O, Fe(NO<sub>3</sub>)<sub>3</sub>.9H<sub>2</sub>O, Cr(NO<sub>3</sub>)<sub>3</sub>.9H<sub>2</sub>O, Ni(NO<sub>3</sub>)<sub>2</sub>.6H<sub>2</sub>O, Li<sub>2</sub>CO<sub>3</sub>, anhydrous citric acid, urea and conc. HNO<sub>3</sub> (70%) were used as starting materials. A typical synthesis of LiMn<sub>2</sub>O<sub>4</sub> is described below. 10 mmoles (2.45 g) of Mn (CH<sub>3</sub>COO)<sub>2</sub>.4H<sub>2</sub>O, 2.5 mmoles (0.184 g) of Li<sub>2</sub>CO<sub>3</sub> (5 mmoles of Li ions), 30 mmoles (5.764 g) of anhydrous citric acid, 30 mmoles (1.8 g) of urea, were dissolved in 30 mL water in 250 ml beaker. To this 3 ml of conc. HNO<sub>3</sub> was added. Total metal ions: citric acid: urea mole ratio was maintained to 1:2:2. This solution was heated at 80 °C for 9 hours (until entire solvent was evaporated) while stirring. The resultant resin was kept in an electrical oven at 180 °C for 14 hours and a sponge like material with very high volume was obtained. This material was grinded well and heated in a furnace at 350 °C for 12 hours in air. The resultant compound was used for characterization. Similar procedure was followed for the synthesis of other materials also except the replacement of Mn(CH<sub>3</sub>COO)<sub>2</sub>.4H<sub>2</sub>O with required metal salts in an appropriate ratio.

**Delithiation of LiMn<sub>2</sub>O<sub>4</sub> nanoparticles:** To 100 mL dil HNO<sub>3</sub> (pH of the solution was kept at 1.2), 100 mg of LiMn<sub>2</sub>O<sub>4</sub> nanoparticles were added and sonicated for 10 min. The solution was stirred for 48 hours and centrifuged at 4000 rpm. The resultant material was washed with water and acetone respectively. The sample was dried under ambient atmosphere and it was named as λ - MnO<sub>2</sub>.

**LnMO<sub>3</sub>:** In a typical synthesis procedure, 5 mmoles of lanthanum nitrate and 5 mmoles of transition metal nitrate were dissolved in 30 mL of distilled water. To this solution, 50 mmoles of anhydrous citric acid was added and heated to 80 °C while stirring to form gel and maintained at this temperature till dryness (around 9 h). This gel was kept in an electrical oven at 200 °C for 12 h and a small part of this gel was heated at required temperatures after grinding. For preparing lanthanide manganites, precursor citrate-gel was heated at 800 °C for 5h with heating rate of 7 °C/min whereas for lanthanide ferrites and lanthanide nickelites heated at 700 °C for 5 h. In case of

orthorhombic lanthanide cobaltates, the heating temperature was varied with lanthanides. In case of La, Pr, Nd, Sm; gel was heated at 500 °C for 8 h, for Gd at 700 °C and for Dy at 800 °C about 5 h.

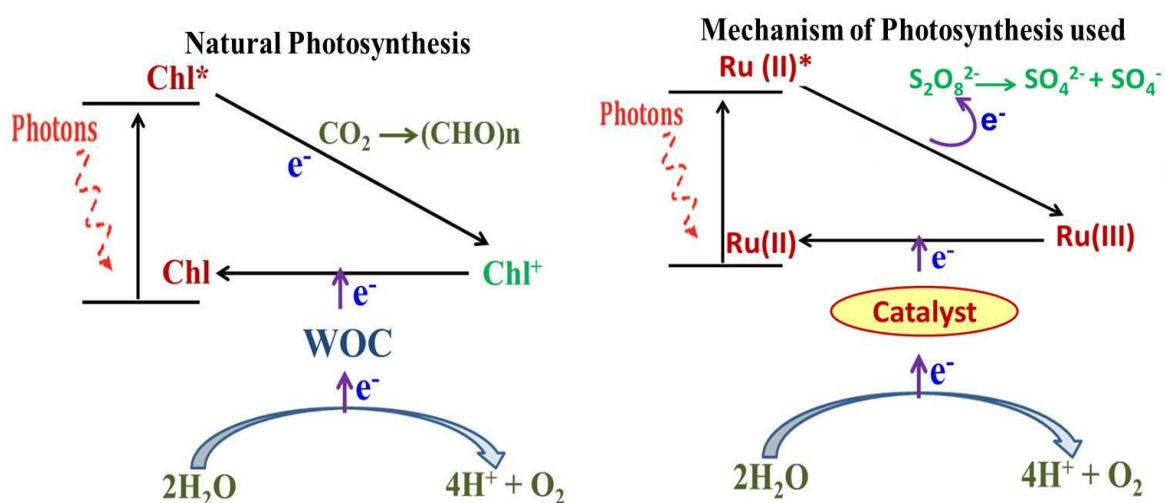
Other oxides were also prepared by similar citrate sol-gel method with minute variations in heating conditions. In case of Mn<sub>2</sub>O<sub>3</sub>, the gel was prepared with Mn(CH<sub>3</sub>COO)<sub>2</sub>:citric acid ratio of 1:2. The gel was baked at 200 °C for 12 h with final heating of 500 °C for 8 h in air. Zn(Mg)Mn<sub>2</sub>O<sub>4</sub> samples were prepared starting from corresponding metal acetates, with metal to citric acid ratio of 1:2 in the gel. Two step heating, first at 200 °C for 12 hours followed by 350 °C for 8 hrs in air was carried out to obtain pure nanoparticles of ZnMn<sub>2</sub>O<sub>4</sub> and MgMn<sub>2</sub>O<sub>4</sub>.

Details of characterization in Appendix.

**Oxygen evolution measurements:** Oxygen evolution measurements were carried out using oxygraph instrument, Hansatech Ltd, equipped with Clark type oxygen electrode. Calibration of the oxygen electrode was done with air saturated Millipore water and then deoxygenated by N<sub>2</sub> purging. Throughout all the measurements, temperature of the reaction chamber was maintained at 25 °C by using Julabo F 25 pump. In the reaction chamber, 0.022 M Na<sub>2</sub>SiF<sub>6</sub> and 0.028 M NaHCO<sub>3</sub> buffer, 1.5 mM [Ru(bpy)<sub>3</sub>]Cl<sub>2</sub>·6H<sub>2</sub>O, 20 mM Na<sub>2</sub>S<sub>2</sub>O<sub>8</sub> and 80 mM Na<sub>2</sub>SO<sub>4</sub> and 100 ppm catalyst was added. Total volume of the solution was 2 mL the solution was stirred continuously throughout the reaction with 100 rpm speed. The catalyst solution was sonicated for 5-10 min prior to adding into the reaction vessel. All the solutions were made freshly every day. This solution was purged with nitrogen till all the oxygen was purged out then the reaction chamber was closed with air tight plunger and waited till the oxygen level was constant. Then the reaction vessel was illuminated with 100W halogen lamp and small percentage of UV light was filtered with BG 38 filter. Light intensity was kept at 25,000 Lux. Oxygen evolution from these samples was further confirmed with Gas chromatograph (GC) by maintaining similar conditions for 50 ml reaction solution. Head space gas was analysed by using PerkinElmer Clarus 580 GC system.

## 4. Results and Discussion

Oxygen evolution property of the catalysts were studied under visible light in standard photoexcitation system<sup>29</sup> consisting of  $[\text{Ru}^{\text{III}}(\text{bpy})_3]^{2+}$  as photosensitizer and  $\text{Na}_2\text{S}_2\text{O}_8$  as sacrificial electron acceptor in a solution buffered at  $\text{pH} = 5.8$ . The singlet  $[\text{Ru}(\text{bpy})_3]^{2+}$  on photoexcitation goes to triplet state denoted as  $[\text{Ru}(\text{bpy})_3]^{2+*}$ . The species transfers its electrons to the sacrificial oxidant  $\text{S}_2\text{O}_8^{2-}$ . The resulting  $[\text{Ru}(\text{bpy})_3]^{3+}$  takes an electron from the metal oxide catalyst which in turn oxidizes water to molecular  $\text{O}_2$ , as demonstrated in Scheme below. The process used to study water oxidation was designed similar to natural photosynthesis as shown in the Scheme below. While chlorophyll acts as the photosensitizer in plants,  $[\text{Ru}^{\text{III}}(\text{bpy})_3]^{2+}$  was used in our processes and the photoexcited electron instead of being used up by  $\text{CO}_2$  is taken up irreversibly by  $\text{Na}_2\text{S}_2\text{O}_8$ . The catalyst thus plays the exact role as that of the WOC, donating electrons to regain the photosensitizer oxidizing water in the processes. Oxygen evolved was quantified both by Clark type electrode and gas chromatography.

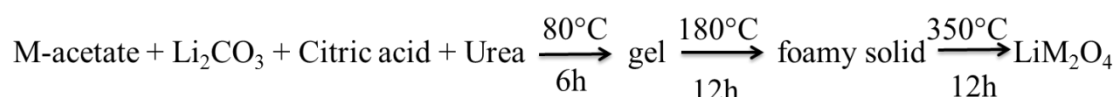


**Scheme 1.** Comparison the processes used for photosynthetic oxidation of water with that of natural photosynthesis.

In order to be able to strictly compare catalytic performance of the various oxide materials, we have measured the oxygen evolved per mole of transition metal and normalized it with respect to BET surface area of the catalyst. Turn over frequencies

(TOF) for each catalyst was calculated from the initial slope of O<sub>2</sub> evolved per mole of transition metal vs. time plot.

First we studied the catalytic properties of Li based spinel oxides of Mn, Co and other transition metals. All samples were prepared by citrate sol-gel method from their corresponding metal precursors.<sup>29</sup> For this calculated amounts of Li<sub>2</sub>CO<sub>3</sub> and metal acetate were mixed with thrice the amount of urea and citric acid and heated to form a foamy mass. This was then decomposed at 500 °C to get the spinel oxides as elucidated below,



M = Mn, Co, Ni, Cr, Fe

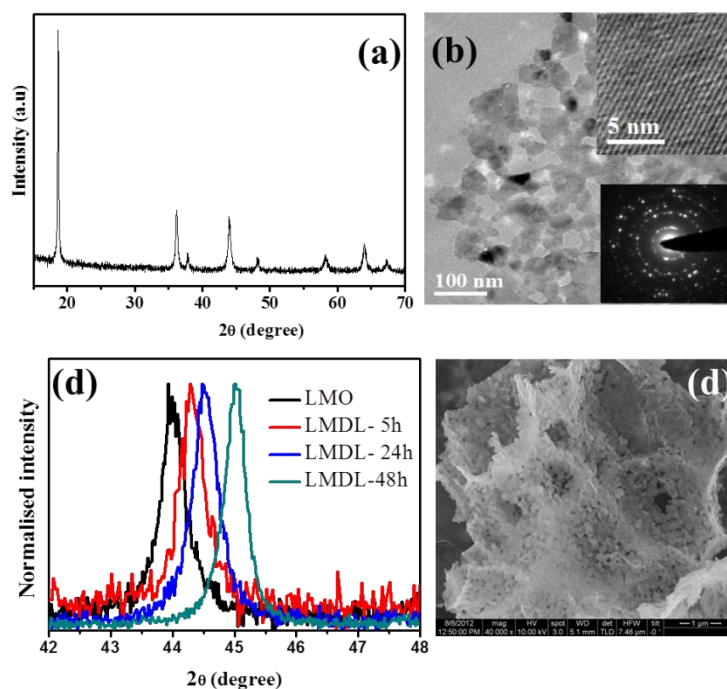


**Figure 1.** (a) XRD and (b) TEM of LiMn<sub>2</sub>O<sub>4</sub>, (c) Shift in XRD with delithiation duration and (d) FESEM of DILiMn<sub>2</sub>O<sub>4</sub> after 48h of delithiation. Inset in (b) shows the HRTEM of LiMn<sub>2</sub>O<sub>4</sub> (top) and electron diffraction pattern (bottom)

Powder x-ray diffraction (XRD) of LiMn<sub>2</sub>O<sub>4</sub> thus prepared (Figure 1 (a)) verifies the formation of pure spinel phase with no visible impurity. Average crystallite size as determined from DebyeScherer formula is 57 nm. Transmission electron microscopy (TEM) image of LiMn<sub>2</sub>O<sub>4</sub> shown in Figure 1 (b) shows particles of the size range of 40-

60 nm. High resolution TEM (HRTEM) image and electron diffraction pattern (Figure 1(b)) of the samples confirm its highly crystalline nature. Delithiation of  $\text{LiMn}_2\text{O}_4$  was carried out in dilute nitric acid. On delithiation the XRD pattern upshifts gradually depending on the duration of de-lithiation with a maximum of 1 degree after 48 h of dilute  $\text{HNO}_3$  treatment implying a decrease in the unit cell volume. (see Figure 1(c)). The Li content in the sample delithiated for 48h (DI- $\text{LiMn}_2\text{O}_4$ ) was estimated to be 0.01% from ICP analysis. The particles do not show any change in morphology on delithiation as seen from FESEM image in Figure 1(d). However average crystallite size decreases slightly manifested as slight increase in surface area from  $20 \text{ m}^2/\text{g}$  to  $55 \text{ m}^2/\text{g}$  (see Table1).

**Table 1.** Crystallite and particle size and surface area of different samples.

Compound	Average Crystallite size (nm) XRD	Particle size (nm) TEM	BET Surface Area ( $\text{m}^2/\text{g}$ ) $\text{N}_2$ adsorption
$\text{LiMn}_2\text{O}_4$	57	15-50	20
DI- $\text{MnO}_2$	46	15-50	55
$\text{LiMnCoO}_4$	16	15-40	22
$\text{LiMnCrO}_4$	25	20-40	41
$\text{LiMnFeO}_4$	29	25-50	22
$\text{LiMn}_{1.5}\text{Ni}_{0.5}\text{O}_4$	38	20-60	19
$\text{Li}_{1.1}\text{Co}_2\text{O}_4$	17	15-25	27
$\text{Li}_2\text{Co}_2\text{O}_4$	23	20-40	23
$\text{Mn}_2\text{O}_3$	36	25-55	17
$\text{LaCoO}_3$	17	15-50	14
$\text{LaMnO}_3$	18	15-55	24
$\text{ZnMn}_2\text{O}_4$	17	15-25	26
$\text{MgMn}_2\text{O}_4$	19	15-25	22

As opposed to earlier reported literature<sup>27</sup>  $\text{LiMn}_2\text{O}_4$  nanoparticles showed reasonable catalytic activity as shown in Figure 2(a). The average crystallite size of the de-lithiated sample (DI- $\text{LiMn}_2\text{O}_4$ ) was 46 nm. Delithiation seemed to result in a slight improvement in the catalytic activity. However,  $\text{O}_2$  evolved per mole of Mn per unit surface area of the catalyst showed this not to be so (see inset of Figure 2 (a)). The

delithiated catalyst had a very small proportion of Mn (III), if any. We have plotted the rate of oxygen evolved per mole per unit time in Figure 2(b).

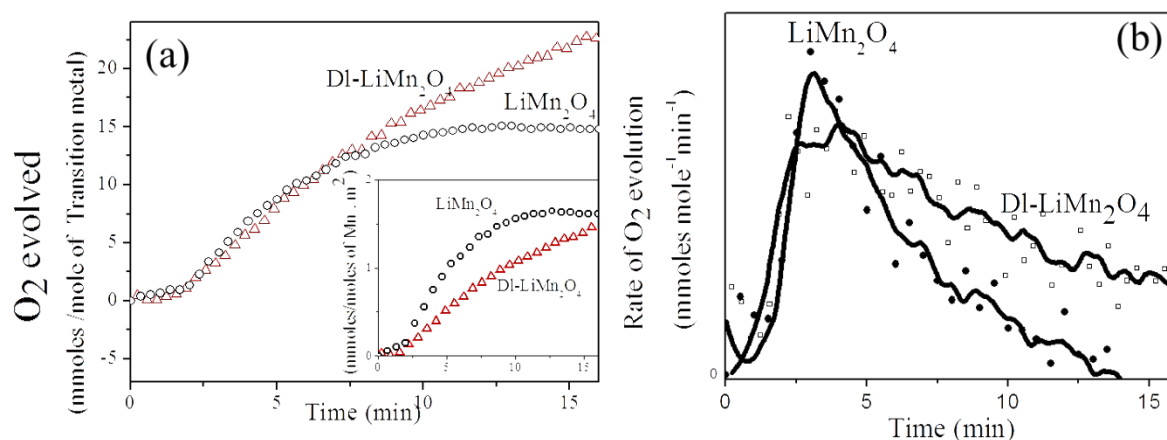


**Figure 2.**(a) Amount of oxygen evolved per mole of Mn by LiMn<sub>2</sub>O<sub>4</sub> and Dl-LiMn<sub>2</sub>O<sub>4</sub> and (b) Rate of oxygen evolved per mole of Mn per unit time by the same. Inset in (a) shows amount of oxygen evolved per mole of transition metal per unit surface area of catalyst.

In case of both the catalysts, the rate of oxygen evolution increases initially almost equally and then decreases slowly. Thus, both the catalysts have a TOF of  $2.2 \times 10^{-5} \text{ s}^{-1}$  catalyst, the rate of oxygen evolution increases after the reaction has proceeded for  $\sim 3$  min plausibly because, as the reaction proceeds it takes electrons from water generating Mn(III). The results suggested that the presence of Mn in its +3 state was essential for the activity of the catalyst. Accordingly, we prepared nanoparticles of ZnMn<sub>2</sub>O<sub>4</sub> and MgMn<sub>2</sub>O<sub>4</sub> which crystallize in tetragonal spinel structure and tested their photocatalytic O<sub>2</sub> evolution activity. Figure 3(a) shows XRD pattern of MgMn<sub>2</sub>O<sub>4</sub> and ZnMn<sub>2</sub>O<sub>4</sub> is characteristic of corresponding tetragonal spinel structure with average crystallite size as calculated using Deby-Scherrer formula to be 10-12 nm for both. TEM studies show average particle size of 10-15 nm in accordance with XRD (Figure 3 (b-c)). High resolution TEM (HRTEM) image and electron diffraction patterns confirm the highly crystalline nature of the sample. ZnMn<sub>2</sub>O<sub>4</sub> and MgMn<sub>2</sub>O<sub>4</sub> exhibit good catalytic properties for water oxidation as shown in Figure 3(c). For example, MgMn<sub>2</sub>O<sub>4</sub> particles show high O<sub>2</sub> evolution with TOF of  $8.2 \times 10^{-5} \text{ s}^{-1}$ . We shall discuss the catalytic activity of other Mn (III) oxides later in the article.

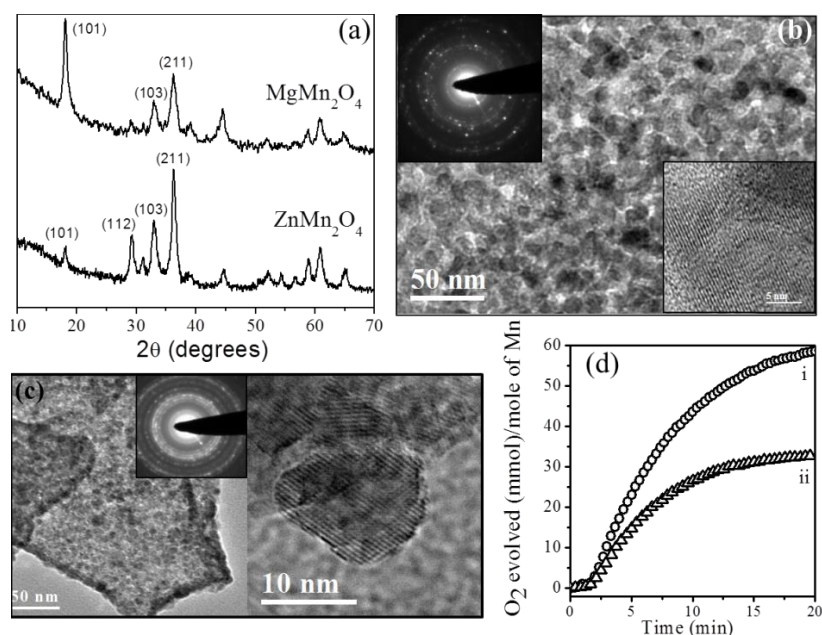


**Figure 3.** (a) XRD of  $\text{MgMn}_2\text{O}_4$  and  $\text{ZnMn}_2\text{O}_4$ , TEM, HRTEM and electron diffraction of (b)  $\text{MgMn}_2\text{O}_4$  and (c)  $\text{ZnMn}_2\text{O}_4$ , (d) Amount of oxygen evolved per mole of Mn (i)  $\text{MgMn}_2\text{O}_4$  and (ii)  $\text{ZnMn}_2\text{O}_4$ .

In order to understand the role of the transition metal ion and its oxidation state on catalytic water oxidation, we examined the catalytic activity by substituting one mole of Mn in  $\text{LiMn}_2\text{O}_4$  with Cr, Fe, Co and Ni, all of which crystallize in the spinel structure (see Figure 4(a)). In the case of Ni substitution,  $\text{LiMnNiO}_4$  could not be prepared, but we did obtain  $\text{LiMn}_{1.5}\text{Ni}_{0.5}\text{O}_4$ . Though prepared under similar conditions the average crystallite sizes of the samples vary as is evident from the FWHM of XRD patterns, with  $\text{LiMnCoO}_4$  having smallest crystallite size and  $\text{LiMn}_{1.5}\text{Ni}_{0.5}\text{O}_4$  the largest among them. BET surface areas and crystallite sizes of these oxides are listed in table 1. Of these oxides,  $\text{LiMnCoO}_4$  shows maximum activity with a TOF of  $8.3 \times 10^{-5} \text{ s}^{-1}$ . The overall order of activity is  $\text{Co} > \text{Ni} > \text{Cr} > \text{Mn} > \text{Fe}$  as shown in Figure 4(a). Since the samples vary in particle size a strict comparison of their catalytic activity can only be made considering the surface area available for catalysis. On normalizing the oxygen evolved per mole of transition metal by surface area the order of activity was found to be  $\text{Co} > \text{Ni} > \text{Mn} > \text{Cr} > \text{Fe}$  as shown in Figure 4(b). This trend can be rationalized in terms of the electronic configurations of the trivalent transition metal ions.<sup>30-33</sup> While poor catalysts like those containing Cr(III) and Fe(III) have electronic configuration  $t_{2g}^3 e_g^0$  and  $t_{2g}^3 e_g^2$ , respectively; those showing good



catalytic activity like Mn(III), Co(III) and Ni(III) have electronic configuration  $t_{2g}^3 e_g^1$  (HS),  $t_{2g}^5 e_g^1$  (IS) and  $t_{2g}^6 e_g^1$  (LS) respectively. The commonality between the good catalysts being presence of only one electron in the antibonding  $e_g$  orbital. In the case of Co (III), we have considered the intermediate spin state, an aspect that will be discussed later. Mn(III) and Ni(III) exist in high spin and low spin states, respectively.

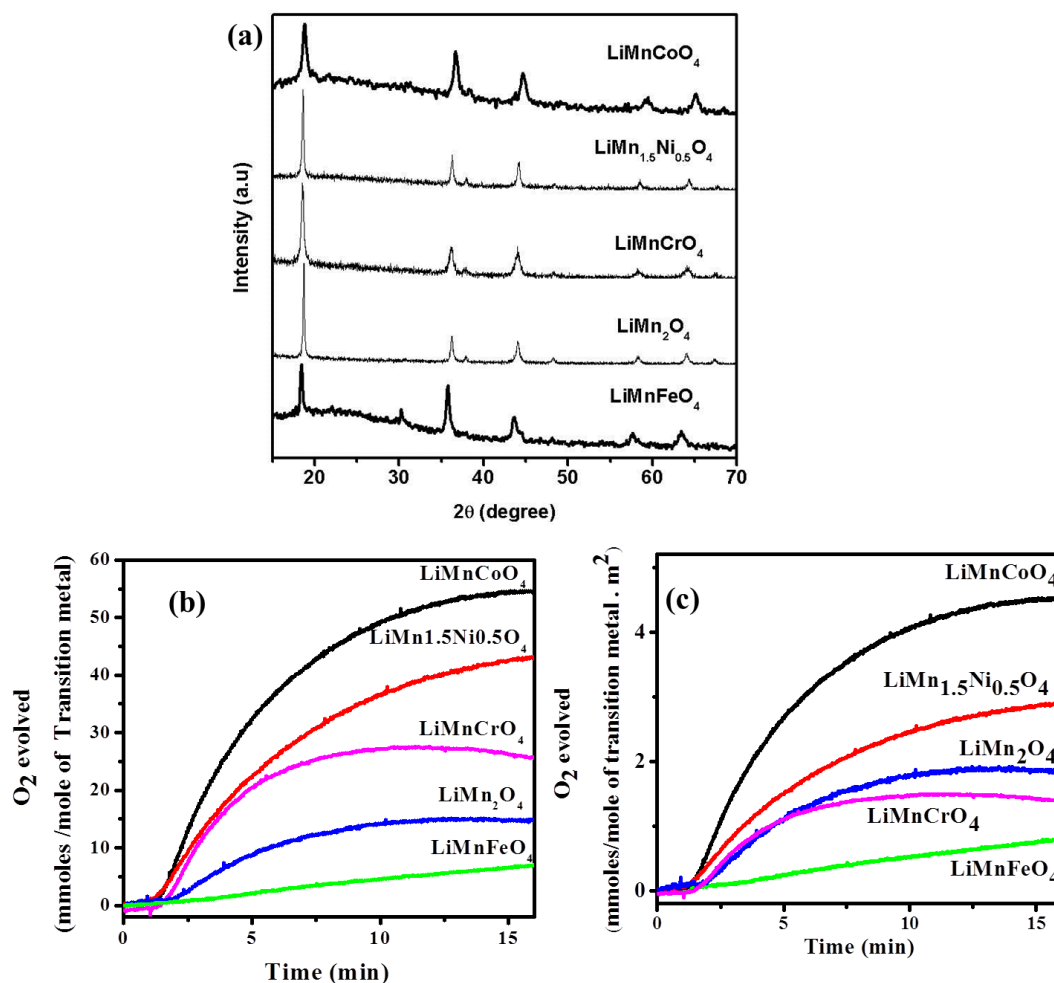


**Figure 4.**(a)XRD of  $\text{LiMn}_{1-x}\text{A}_x\text{O}_4$  ( $\text{A} = \text{Co}, \text{Ni}, \text{Cr}, \text{Mn}, \text{Fe}$  ;  $x = 1$  and  $0.5$ ) and the amount of  $\text{O}_2$  evolved by the same (b) per mole of transition metal and (c) per mole of transition metal per unit surface area.

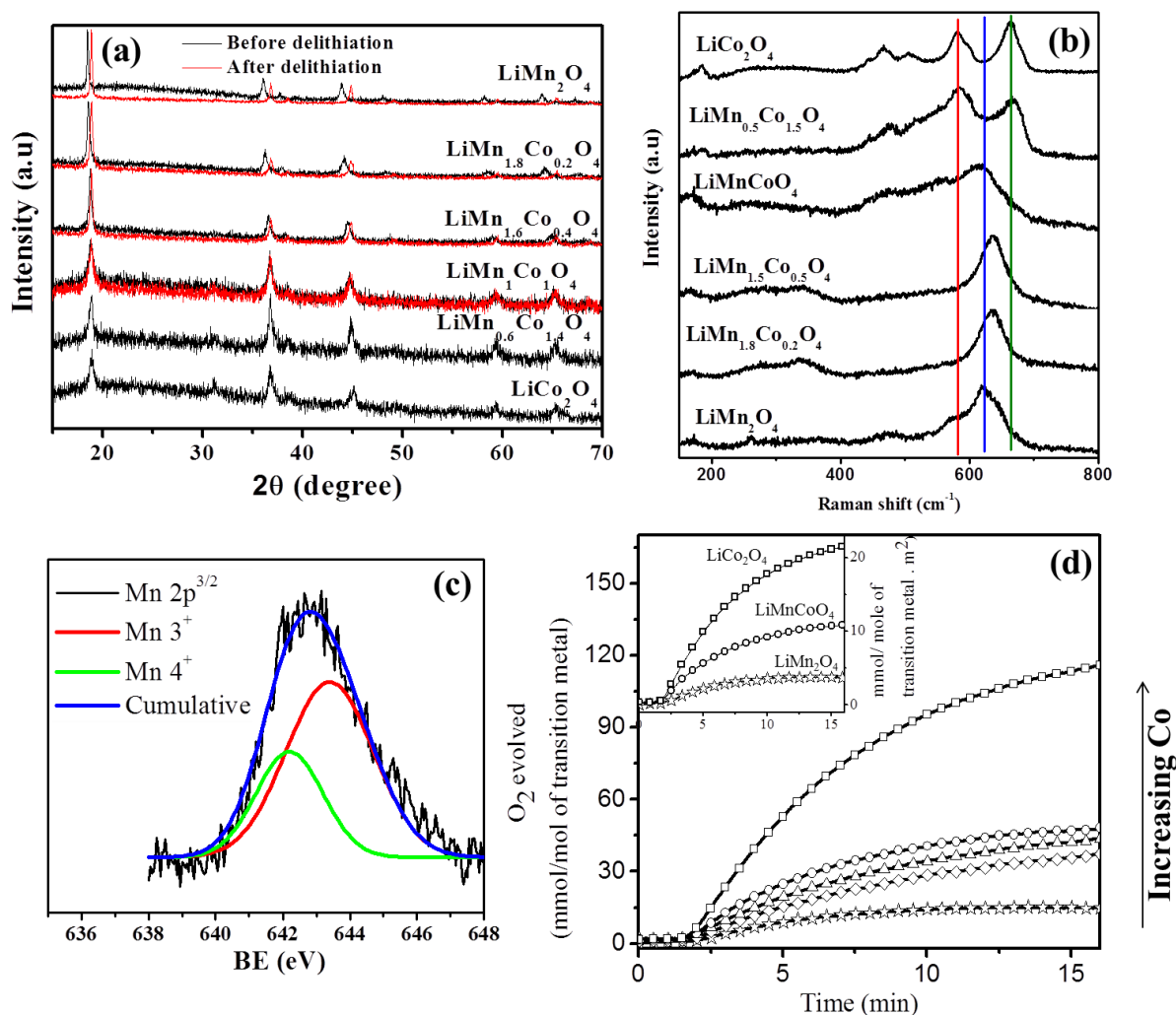


**Figure 5.** (a) XRD and (b) Raman spectra of  $\text{LiMn}_x\text{Co}_{2-x}\text{O}_4$  (where  $x = 0.2, 0.5, 1, 2$ ).  $580\text{ cm}^{-1}$  (red)  $\text{Mn}^{4+}\text{O}_6$  and  $\text{Co}^{4+}\text{O}_6$  octahedra,  $620\text{ cm}^{-1}$  (blue) tetragonally distorted  $\text{Mn}^{3+}\text{O}_6$  octahedra  $660\text{ cm}^{-1}$  (green) tetragonally distorted  $\text{Co}^{3+}\text{O}_6$  octahedra (c) XPS of  $\text{LiMnCoO}_4$  showing peaks corresponding to 2p level of Mn and (d) The amount of  $\text{O}_2$  evolved per mole of transition metal by  $\text{LiMn}_{2-x}\text{Co}_x\text{O}_4$  with increasing Co content. Inset in (d) shows the amount of  $\text{O}_2$  evolved per mole of transition metal per unit surface area.

Encouraged by the performance of  $\text{LiMnCoO}_4$ , we prepared nanoparticles of the composition  $\text{LiMn}_{2-x}\text{Co}_x\text{O}_4$  (where  $x = 0.2, 0.5, 1, \text{ and } 2$ ) all of which crystallize in the spinel structure, with a small gradual decrease in unit cell dimensions with increasing Co content (see Figure 5(a)). Nitrogen adsorption measurements reveal no discernable change in surface area and TEM studies indicate no change in morphology and particle size. Raman spectrum of  $\text{LiMn}_2\text{O}_4$  has contributions from  $\text{Mn}^{4+}\text{O}_6$  octahedra and tetragonally distorted  $\text{Mn}^{3+}\text{O}_6$  octahedra at  $575\text{ cm}^{-1}$  (red) and  $620\text{ cm}^{-1}$  (blue),

respectively as shown in Figure 5(b). Raman spectra of the samples show the gradual evolution of Co (III) and Co (IV) states from Mn(III) and Mn(IV) states with increasing Co content. While the band due to  $\text{Co}^{4+}\text{O}_6$  octahedra do not shift much from that of  $\text{Mn}^{4+}\text{O}_6$  octahedra (similar ionic radii, see the red line), the band due to tetragonally distorted  $\text{Mn}^{3+}\text{O}_6$  octahedra (blue) gradually shifts to  $660\text{ cm}^{-1}$  (green) corresponding to vibrations due to tetragonally distorted  $\text{Co}^{3+}\text{O}_6$  octahedra. XPS analysis of  $\text{LiMnCoO}_4$  indicates Mn(III): Mn(IV) ratio of  $\sim 0.6$  ( $\text{Co(III)} > \text{Co(IV)}$ ). XPS peaks corresponding to 2p level of Mn in  $\text{LiMnCoO}_4$  is shown in figure 5(c). Oxygen evolution activity of these catalysts increases with the increase in Co content (figure 5(d)),  $\text{Li}_{1.1}\text{Co}_2\text{O}_4$  showing the highest activity (TOF of  $1.6 \times 10^{-4}\text{ s}^{-1}$ ). The amount of oxygen evolved per mole of transition metal per unit surface area of the catalyst also follows the same order (inset in Figure 5(d)). The increase in the catalytic activity on Co substitution in  $\text{LiMn}_2\text{O}_4$  can arise from the higher oxidation potential of Co (III) as compared to Mn (III). It is also worth mentioning that increasing Co content not only increases the ratio of Co:Mn in the catalyst but also increases the ratio of Co(III) to Co(IV). XPS analysis suggests that the ratio of Co(III):Co(IV) is greater than 1, both in  $\text{LiMnCoO}_4$  and  $\text{Li}_{1.1}\text{Co}_2\text{O}_4$ . As already discussed, Co(III) in intermediate spin state with  $e_g^1$  electronic configuration shows very good catalytic activity for water oxidation. It is noteworthy that all these oxides show good catalytic activity even without de-lithiation.

$\text{Li}_{1.1}\text{Co}_2\text{O}_4$  has Co in both +3 and +4 states and it is therefore difficult to pin down the role of the oxidation state of Co on catalytic activity. To understand the role of the electronic configuration of Co on the ability of the catalyst to catalyse water to  $\text{O}_2$ , we investigated the catalytic activities of nanoparticles of  $\text{Li}_x\text{Co}_2\text{O}_4$  with varying Li content with  $x = 0.5, 1.1, 1.5$  and 2. Increasing Li content implies increase in Co (III) content. All  $\text{Li}_x\text{Co}_2\text{O}_4$  samples crystallize in spinel structure (see Figure 6(a)). With increasing Li content the lattice contracts by a maximum of  $2\theta = 0.4$  degrees as shown in Figure 6(b).  $\text{N}_2$  adsorption measurements revealed no appreciable difference in the surface area though the crystallite size showed a slight increase with increasing Li content. Raman spectroscopic studies indicate increase in proportion of Co (III) with increasing Li content. The Raman bands at  $580\text{ cm}^{-1}$  (red) and  $660\text{ cm}^{-1}$  (blue) correspond to  $\text{Co}^{4+}\text{O}_6$  octahedra and tetragonally distorted  $\text{Co}^{3+}\text{O}_6$ , respectively (see Figure 6(c)). The ratio of

intensities of Raman bands due to  $\text{Co}^{4+}\text{O}_6$  to  $\text{Co}^{3+}\text{O}_6$  decreases with increasing Li content. Raman spectrum of  $\text{Li}_2\text{Co}_2\text{O}_4$  has negligible contributions from  $\text{Co}^{4+}\text{O}_6$  octahedra. XPS analysis on  $\text{Li}_{1.1}\text{Co}_2\text{O}_4$  and  $\text{Li}_2\text{Co}_2\text{O}_4$  also confirm increasing proportion of Co(III) with increasing Li content (see figure 6(d-e)).  $\text{Li}_{1.1}\text{Co}_2\text{O}_4$  has almost equal proportions of Co in +3 and +4 states the ratio of Co(III) to Co(IV) being  $\sim 1.2$ .  $\text{Li}_2\text{Co}_2\text{O}_4$  on the other hand has negligible amount of Co (IV) with Co(III) to Co(IV) ratio being  $\sim 13.3$ .

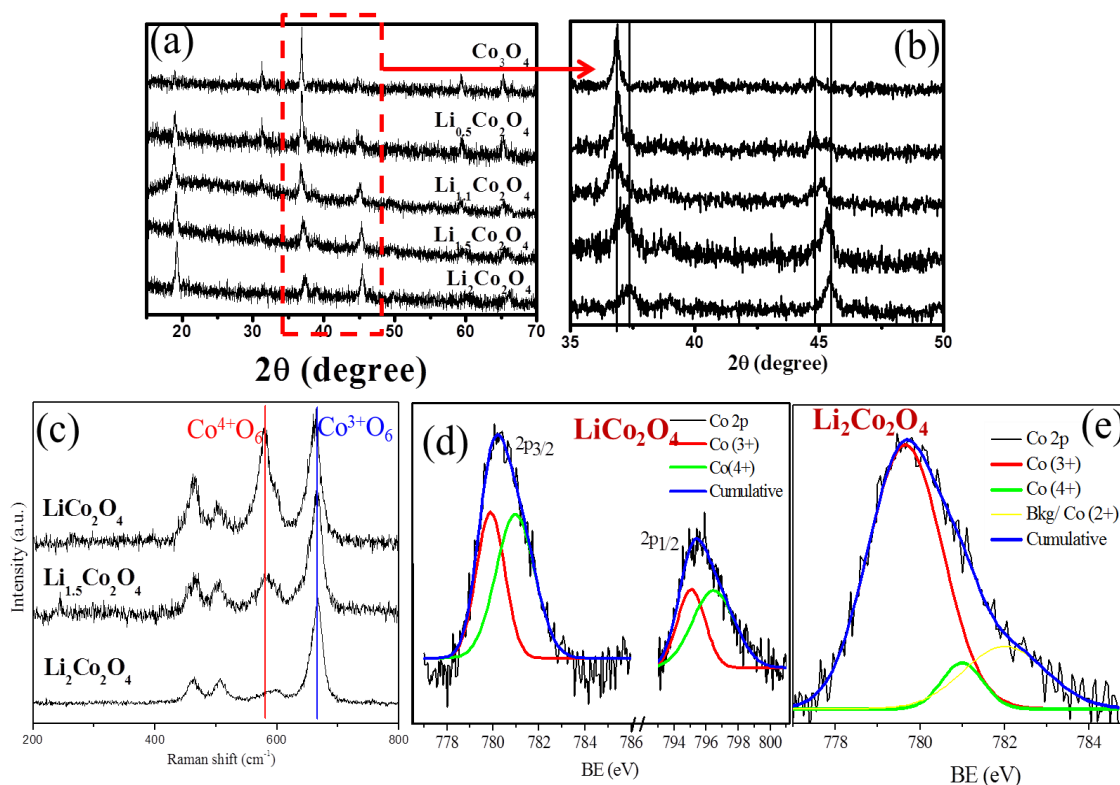


**Figure 6.** (a) XRD of  $\text{Li}_x\text{Co}_2\text{O}_4$  ( $x = 0, 0.5, 1, 1.5, 2$ ), (b) Magnified view of the region marked in red in (a). (c) Raman spectra of  $\text{Li}_x\text{Co}_2\text{O}_4$  showing the Raman bands due to  $\text{Co}^{4+}\text{O}_6$  (red) and  $\text{Co}^{3+}\text{O}_6$  (blue). XPS spectra of (d)  $\text{LiCo}_2\text{O}_4$  and (e)  $\text{Li}_2\text{Co}_2\text{O}_4$  showing the Co 2p level.

We found the catalytic activity to increase with increasing Li content (Figure 7(a)), with  $\text{Li}_2\text{Co}_2\text{O}_4$  showing the highest  $\text{O}_2$  evolution, slightly higher than that reported earlier.<sup>28</sup> This is in contrary to that observed by Gardner *et. al.*<sup>28</sup> where de-lithiated sample ( $\lambda\text{-MnO}_2$ ) shows higher activity than  $\text{LiMn}_2\text{O}_4$ . Even after taking the surface area of the catalysts into consideration  $\text{Li}_2\text{Co}_2\text{O}_4$  turns out to be a better catalyst than  $\text{Li}_{1.1}\text{Co}_2\text{O}_4$ . In  $\text{Li}_2\text{Co}_2\text{O}_4$ , Co exists in +3 state, again suggesting the importance of trivalency of Co in water oxidation catalysis. We carried out magnetic measurements on

$\text{Li}_2\text{Co}_2\text{O}_4$  samples to determine the electronic configuration of Co in it (Figure 7(b)). The  $\chi_M$  values suggest presence of 2 unpaired electrons indicating intermediate-spin of Co(III) with  $t_{2g}^5 e_g^1$  configuration.

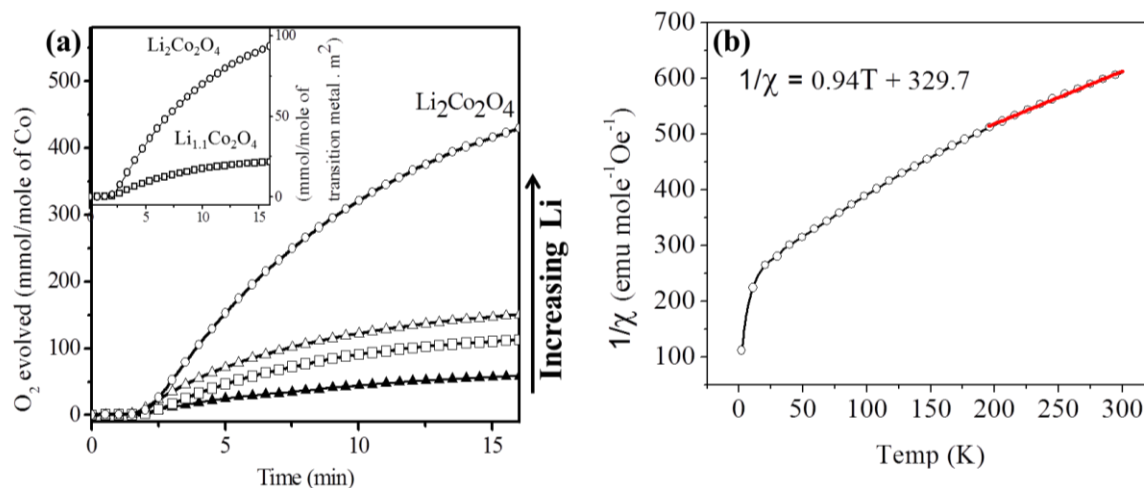


**Figure 7.** The amount of  $\text{O}_2$  evolved per mole of transition metal by  $\text{Li}_x\text{Co}_2\text{O}_4$  Inset in (a) shows the amount of  $\text{O}_2$  evolved per mole of transition metal per unit surface area, (b) susceptibility vs temperature for  $\text{Li}_2\text{Co}_2\text{O}_4$  at 500 Oe.

Based on the above results, we felt that the presence of the  $e_g^1$  electron could play a significant role in determining catalytic activity for oxidation of water. In order to investigate importance of  $e_g^1$  electrons and rule out the effect of structure of oxides in water oxidation we further prepared Co and Mn oxides of different structure but with electronic configuration of the transition metal ion being  $t_{2g}^x e_g^1$  ( $x = 5$  and  $3$  respectively). For this purpose we prepared  $\text{Mn}_2\text{O}_3$ ,  $\text{LaMnO}_3$  and  $\text{LaCoO}_3$  all of which crystallize in different structures but have 1 electron in the antibonding  $e_g$  orbital of the transition metal. While  $\text{Mn}_2\text{O}_3$  crystallizes in bixbyte structure  $\text{LaMnO}_3$  and  $\text{LaCoO}_3$  are perovskite as shown in Figure 8(a). Though water oxidation catalysis has earlier been reported for  $\text{LaCoO}_3$ <sup>34</sup> and  $\text{Mn}_2\text{O}_3$ <sup>24</sup> we decided to study the water oxidation properties of these oxides since the available information in the literature could not be used for proper comparisons. Furthermore, it was necessary to measure the catalytic properties of these oxides under similar conditions as those of the other oxide systems studied by us.  $\text{LaCoO}_3$  shows remarkably high catalytic activity for the oxidation of water and is even superior to  $\text{Li}_2\text{Co}_2\text{O}_4$  in performance (Figure 8(b)). The TOF for

LaCoO<sub>3</sub> is  $1.4 \times 10^{-3} \text{ s}^{-1}$  while that for Li<sub>2</sub>Co<sub>2</sub>O<sub>4</sub> it is  $9 \times 10^{-4} \text{ s}^{-1}$ . The commonality between these two oxides is that Co (III) in both these oxides is in the intermediate  $t_{2g}^5 e_g^1$  state. Higher activity of LaCoO<sub>3</sub> as compared to Li<sub>2</sub>Co<sub>2</sub>O<sub>4</sub> can be attributed to the fact that LaCoO<sub>3</sub> has all Co in +3 while in case of Li<sub>2</sub>Co<sub>2</sub>O<sub>4</sub> the ratio of Co(III) to Co(IV) is 13.3. LaMnO<sub>3</sub> which is a perovskite with Mn (III) shows good catalytic activity, only slightly lower than Mn<sub>2</sub>O<sub>3</sub> as shown in Figure 8(c), the TOF values being  $4.8 \times 10^{-4} \text{ s}^{-1}$  and  $5 \times 10^{-4} \text{ s}^{-1}$ , respectively. Even after taking the surface area of the catalysts into consideration, the OER catalytic activity follows the order, LaCoO<sub>3</sub>>Li<sub>2</sub>Co<sub>2</sub>O<sub>4</sub>>Mn<sub>2</sub>O<sub>3</sub>~LaMnO<sub>3</sub> as shown in Figure 8(c). The electronic configuration of the transition metal as opposed to crystal structure of catalyst appears to be the important factor in determining the OER catalytic.

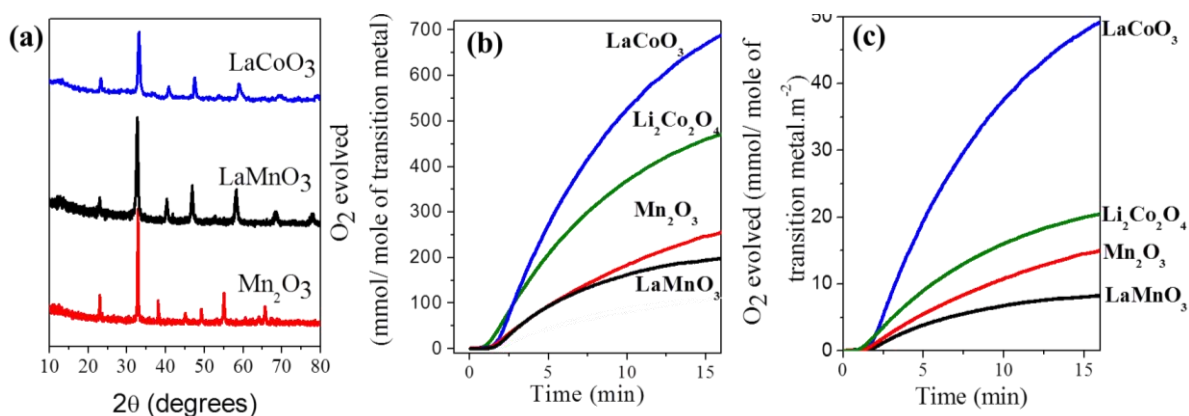


**Figure 8.** (a) XRD of LaCoO<sub>3</sub>, LaMnO<sub>3</sub> showing perovskite structure and Mn<sub>2</sub>O<sub>3</sub> showing bixbyite structure. Amount of O<sub>2</sub> evolved (b) per mole of transition metal and (c) per mole of transition metal per unit surface area by LaCoO<sub>3</sub>, Li<sub>2</sub>Co<sub>2</sub>O<sub>4</sub>, Mn<sub>2</sub>O<sub>3</sub> and LaMnO<sub>3</sub>.

Having found the important role of  $e_g^1$  electron in water oxidation catalysis and extraordinarily high catalytic activity of LaCoO<sub>3</sub>, we felt it necessary to study the family of perovskite oxides for water oxidation. We first examined the photochemical catalytic activity of lanthanum perovskites of the formula LaMO<sub>3</sub> (M= Cr, Mn, Fe, Co and Ni). All these lanthanum transition metal oxides crystallize in rhombohedral diffraction patterns as well as their BET surface areas are listed in Table.2.

**Table.2.** Calcination conditions, crystallite size calculated from XRD, BET surface area measured by N<sub>2</sub> absorption at 77K, O<sub>2</sub> evolved per mole of catalyst per unit surface area of LnMO<sub>3</sub> (Ln= rare earth, M = Mn, Co, Ni, Fe)

Sample name	Calcination temperature (°C) and duration (h)	Crystallite size (nm)	BET Surface area (m <sup>2</sup> /g)	O <sub>2</sub> evolved (mmol/mol of catalyst. m <sup>2</sup> & )
<sup>@</sup> LaMnO <sub>3</sub>	800, 5h	18	24	8.2
<sup>@</sup> LaFeO <sub>3</sub>	700, 5h	19	29	1.7
<sup>@</sup> LaCoO <sub>3</sub>	500, 8h	16	14	49
<sup>@</sup> LaNiO <sub>3</sub>	700, 5h	14	12	6.3
NdMnO <sub>3</sub>	800, 5h	26	12	10.9
SmMnO <sub>3</sub>	800, 5h	32	11	10.3
GdMnO <sub>3</sub>	800, 5h	35	9	11.9
DyMnO <sub>3</sub>	800, 5h	33	13	8.9
<sup>#</sup> YMnO <sub>3</sub>	800, 5h	23	20	1.9
<sup>#</sup> YbMnO <sub>3</sub>	800, 5h	27	15	3.9
PrCoO <sub>3</sub>	500, 8h	23	14	38
NdCoO <sub>3</sub>	500, 8h	24	12	34.5
SmCoO <sub>3</sub>	500, 8h	29	16	31.2
GdCoO <sub>3</sub>	700, 8h	47	8	34.1
DyCoO <sub>3</sub>	800, 8h	67	3	38
<sup>!</sup> (Dy <sub>2</sub> O <sub>3</sub> ) (Co <sub>2</sub> O <sub>3</sub> )	500, 8h		13	36.2
<sup>!</sup> (Y <sub>2</sub> O <sub>3</sub> ) (Co <sub>2</sub> O <sub>3</sub> )	500, 8h		24	19.5
<sup>!</sup> (Er <sub>2</sub> O <sub>3</sub> ) (Co <sub>2</sub> O <sub>3</sub> )	500, 8h		16	39.6
<sup>!</sup> (Yb <sub>2</sub> O <sub>3</sub> ) (Co <sub>2</sub> O <sub>3</sub> )	500, 8h		14	41.6

<sup>@</sup> Rhombohedral/cubic Perovskite, <sup>#</sup> Hexagonal Perovskite, <sup>!</sup>Cubic (solid solution), Rest all are Orthorhombic Perovskites, & After 15 min of illumination.

Oxygen evolution properties of these materials per mole of transition metal are shown in Figure 9 (b). LaCoO<sub>3</sub> shows the best water oxidation activity with a TOF of 1.4×10<sup>-3</sup> s<sup>-1</sup> followed by LaMnO<sub>3</sub> (4.8×10<sup>-4</sup>s<sup>-1</sup>). LaNiO<sub>3</sub> (1.2×10<sup>-4</sup> s<sup>-1</sup>) and LaFeO<sub>3</sub> (8.9×10<sup>-5</sup> s<sup>-1</sup>) show poor activity. LaCrO<sub>3</sub> does not show any oxygen evolution catalytic activity under similar conditions. The results again prove that catalysts containing Co(III) Mn(III) with e<sub>g</sub><sup>1</sup> electronic configuration show good catalytic activity as compared to those with Cr(III) and Fe(III) with e<sub>g</sub><sup>0</sup> and e<sub>g</sub><sup>2</sup> configuration. Even though Ni(III) in (LS) state has e<sub>g</sub><sup>1</sup>

configuration,  $\text{LaNiO}_3$  being metallic the electrons are delocalized and do not show as good catalytic activity, an aspect that will be discussed later.

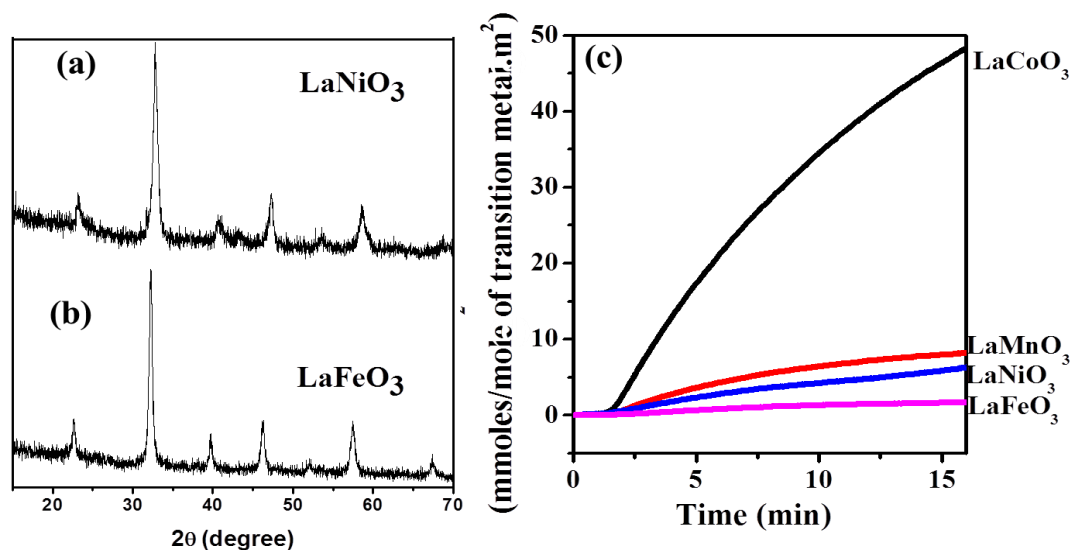


**Figure 9.** (a), (b) XRD patterns of  $\text{LaNiO}_3$ ,  $\text{LaFeO}_3$  respectively and (c)  $\text{O}_2$  evolved by  $\text{LaMO}_3$  (M: Mn, Fe, Co and Ni) per mole of transition metal per unit surface area

Rare earth manganese perovskites of the formula  $\text{LnMnO}_3$  (Ln = Nd, Sm, Gd, Dy, Y and Yb) are known to crystallize in two different crystal structures orthogonal and hexagonal phases while  $\text{LaMnO}_3$  exists as a rhombohedral phase. For further validation of the role of  $e_g^1$  electron in water oxidation catalysis we studied catalytic properties of the family of rare earth manganese perovskites. The manganites of Nd, Sm, Gd and Dy crystallize in the orthorhombic structure (space group Pbnm) whereas those of yttrium and ytterbium crystallize in the hexagonal structure (space group P63cm).  $\text{LaMnO}_3$  crystallizes in rhombohedral phase. The XRD patterns of the manganites are given in Figure 10 (a, b). TEM images showed that the oxide materials were composed of crystalline nanoparticles. The crystallite size calculated from XRD patterns and the BET surface areas obtained from  $\text{N}_2$  absorption at 77K are listed in Table.2. Among the manganites,  $\text{LaMnO}_3$  shows the highest catalytic activity with a TOF of  $4.8 \times 10^{-4} \text{ s}^{-1}$ . All the other orthorhombic manganites (Ln= Nd, Sm, Gd and Dy) have comparable catalytic activities with a TOF between  $2.4 \times 10^{-4} \text{ s}^{-1}$  and  $2.1 \times 10^{-4} \text{ s}^{-1}$  corresponding to  $10 \pm 1.8$  mmol of  $\text{O}_2$ /mole of Mn. $\text{m}^2$  after 15 min of illumination (Figure 10 (c)). The hexagonal manganites (Ln= Y and Yb), on the other hand, show much lower  $\text{O}_2$  yield of  $2.9 \pm 1$  mmol/mole of Mn. $\text{m}^2$  after 15 min of illumination with a TOF of  $5.2 \times 10^{-5} \text{ s}^{-1}$



for  $\text{YMnO}_3$  and  $9.2 \times 10^{-5} \text{ s}^{-1}$  for  $\text{YbMnO}_3$  (Figure 10 (c)). Clearly, orthorhombic perovskite manganites show better catalytic activity as compared to hexagonal perovskites for photocatalytic water oxidation. It must be noted that in all these oxides, Mn is in +3 oxidation state. The difference in the oxygen evolution catalytic activity between the orthorhombic and hexagonal manganites is considered to depend on the electronic configuration of  $\text{Mn}^{3+}$  ( $d^4$ ) ion which is determined by the nature of coordination. In the orthorhombic and rhombohedral manganites, Mn(III) exists in octahedral coordination and the electronic configuration is  $t_{2g}^3 e_g^1$  which causes Jahn-Teller distortion of the octahedra.<sup>35</sup> In hexagonal manganites, Mn(III) exists in trigonal bipyramidal symmetry ( $\text{MnO}_5$ ), the electronic configuration being  $e''^2 2e' a_1'^0$ .<sup>35-37</sup>

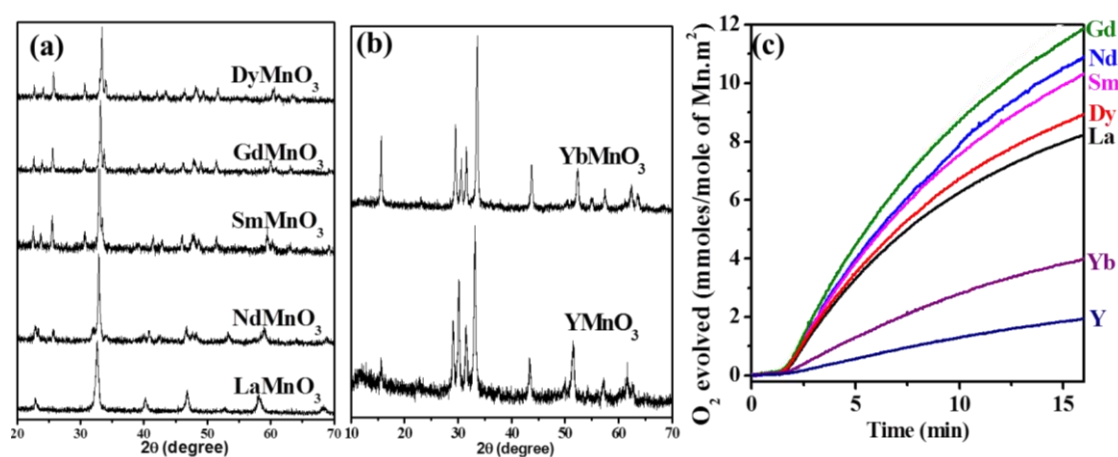


**Figure 10.** XRD patterns of (a) orthorhombic and (b) hexagonal  $\text{LnMnO}_3$  and their corresponding  $\text{O}_2$  evolution activity per mole of catalyst per unit surface area.

Similarly, we prepared rare earth cobaltites,  $\text{LnCoO}_3$  ( $\text{Ln} = \text{Pr, Nd, Sm, Gd and Dy}$ ) with the orthorhombic crystal structure and  $\text{LaCoO}_3$  with rhombohedral structure, and examined their photocatalytic water oxidation properties. The XRD patterns of the cobaltites are shown in Figure 11(a), and their crystallite size and BET surface areas listed in Table.2. With decreasing size of the lanthanum metal clear lattice contraction is observed as shown in Figure 11 (b). However unlike the manganites all rare earth the oxygen evolved by these orthorhombic cobaltites per mole of Co per unit surface are presented in Figure 11(b).  $\text{LaCoO}_3$  exhibits the best oxygen evolution catalytic activity with a TOF of  $1.4 \times 10^{-3} \text{ s}^{-1}$ . All the other cobaltites show comparable catalytic activity with TOF  $\sim 7 \times 10^{-4} \text{ s}^{-1}$ .  $\text{O}_2$  evolution activity per unit surface area of  $\text{LaCoO}_3$  (Rhombohedral,

$\bar{R}\bar{3}C$ ) is the highest 49 mmoles/mole of  $\text{Co.m}^2$  while all orthorhombic cobaltites show comparable activities with a yield of  $34.6\pm 3.4$  mmoles/mole of  $\text{Co.m}^2$  as shown in Figure 11(c).

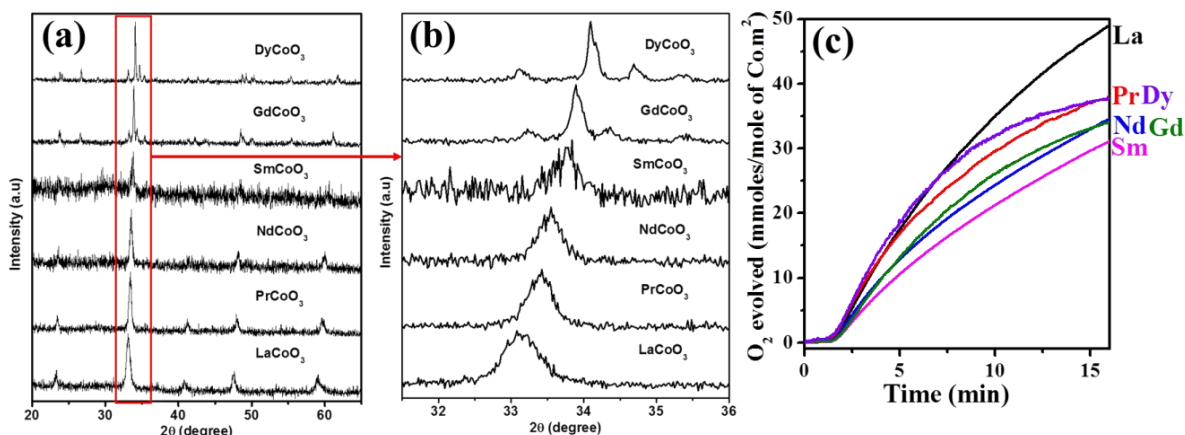


**Figure 11.** (a) XRD patterns of orthorhombic  $\text{LnCoO}_3$  (Ln:La, Pr, Nd, Sm, Gd and Dy), (b) XRD pattern showing only the region marked in red and (c)  $\text{O}_2$  evolved per mole of Mn per unit surface area

It is reported that monophasic orthorhombic  $\text{YbCoO}_3$  cannot be prepared on heating the citrate gel even to high temperatures.<sup>38</sup> What one gets instead is a solid solution of  $\text{Co}_2\text{O}_3$  in  $\text{Yb}_2\text{O}_3$  in the cubic rare earth oxide structure, with the cobalt in the 3+ state. We prepared the solid solutions of the formula  $(\text{Ln}_2\text{O}_3)(\text{Co}_2\text{O}_3)$ , (Ln = Dy, Y, Er and Yb) with the cubic structure by heating the citrate gels to  $700^\circ\text{C}$  or lower as shown in Figure 12 (a). All the cubic solid solutions of  $\text{Co}_2\text{O}_3$  with  $\text{Ln}_2\text{O}_3$  (Ln = Dy, Y, Er and Yb) show excellent catalytic activity with TOF values between  $7.9\times 10^{-4}$  and  $1.3\times 10^{-3} \text{ s}^{-1}$  (Figure 12 (b)). Having found good catalytic activity in solid solutions of  $\text{Co}_2\text{O}_3$  and  $\text{Ln}_2\text{O}_3$ , we examined the electronic configuration of Co in these oxides by carrying out magnetic susceptibility measurements of the solid solution of  $\text{Y}_2\text{O}_3$  and  $\text{Co}_2\text{O}_3$ . The plot of inverse magnetic susceptibility as function of temperature gives a magnetic momentum  $2.41 \mu\text{B}$  Co atom, indicating that cobalt in the intermediate-spin state,  $t_{2g}^5 e_g^1$ . Interestingly, the yield of  $\text{O}_2$  evolved by these solid solutions per mole of Co per unit surface area ( $38.9\pm 2.7$  mmoles/mole of  $\text{Co.m}^2$ ) is comparable to that of orthorhombic perovskite  $\text{LnCoO}_3$  ( $34.6\pm 3.4$  mmoles/mole of  $\text{Co.m}^2$ ), the only commonality between the two being the electronic configuration of Co ( $t_{2g}^5 e_g^1$ ).

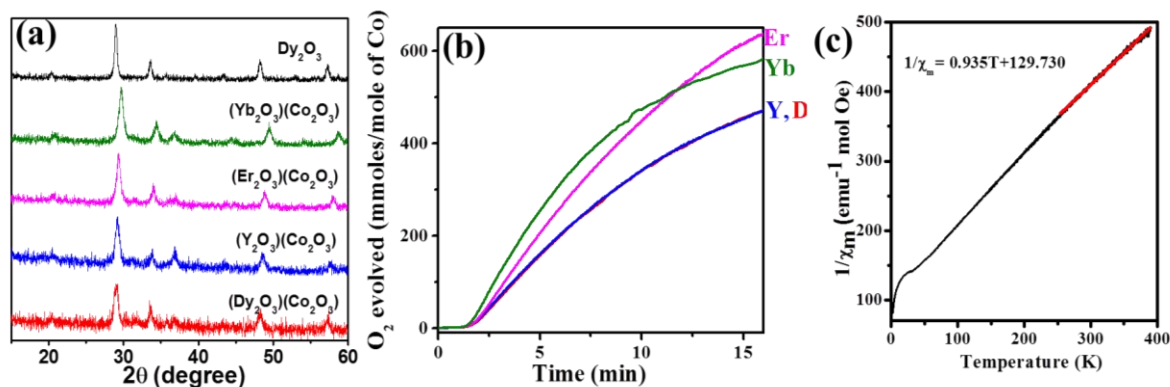


**Figure 12.** (a) XRD patterns of  $(\text{Ln}_2\text{O}_3)(\text{Co}_2\text{O}_3)$  (Ln: Dy, Y, Er, Yb) solid solutions and  $\text{Dy}_2\text{O}_3$  prepared at 700 °C and (b)  $\text{O}_2$  evolved per mole of Co by the same and (c) Temperature dependence of inverse susceptibility of  $(\text{Y}_2\text{O}_3)(\text{Co}_2\text{O}_3)$ .

In the foregoing paragraphs we discuss our studies with several transition metal oxides with different transition metal oxidation states, possessing in different structures to understand the crucial factor determining catalytic activity for water oxidation. Our present study shows that amongst the manganese oxides,  $\text{Mn}_2\text{O}_3$  with the bixbyite structure and  $\text{LaMnO}_3$  with the perovskite structure as well as  $\text{MgMn}_2\text{O}_4$  with the spinel structure containing  $\text{Mn}^{3+}(t_{2g}^3 e_g^1)$  ions show high catalytic activity. Orthorhombic rare earth manganites  $\text{LnMnO}_3$  (Ln= La, Nd, Sm, Gd and Dy) with the perovskite structure exhibit fairly good photocatalytic properties for the oxidation of water while the hexagonal manganites,  $\text{YbMnO}_3$  and  $\text{YMnO}_3$  do not. The presence of  $\text{Mn}^{3+}$  ions in the distorted octahedral environment in the orthorhombic manganites with electronic configuration of  $(t_{2g}^3 e_g^1)$  is clearly an important factor. Among several cobalt oxides, the spinel  $\text{Li}_2\text{Co}_2\text{O}_4$  and the perovskite  $\text{LaCoO}_3$ , both containing  $\text{Co}^{3+}$  ions in the intermediate spin state  $(t_{2g}^5 e_g^1)$  are good catalysts for water oxidation. In the rare earth cobaltites of perovskite structure,  $\text{LaCoO}_3$  (Rhombohedral,  $\bar{R}3\bar{C}$ ) shows the highest catalytic activity, while the other orthorhombic cobaltites  $\text{LnCoO}_3$  (Ln= Pr, Nd, Sm, Gd and Dy) show comparable activity, although little lower than that of  $\text{LaCoO}_3$ . The heavier rare earths (Dy, Er, Yb and Y) do not form orthorhombic perovskites readily and remain in the form of cubic solid solutions of  $\text{Co}^{3+}$  in  $\text{Ln}_2\text{O}_3$  when prepared around 700°C or lower. These solid solutions with the cubic C-type rare earth oxide structure

containing  $\text{Co}^{3+}$  present in the intermediate-spin configuration ( $t_{2g}^5 e_g^1$ ) just as in  $\text{LaCoO}_3$ , interestingly exhibit catalytic activity for the oxidation of water comparable to  $\text{LaCoO}_3$ . The commonality between these Co and Mn oxides is that they have Jahn-Teller distorted metal-oxygen octahedra due to the presence of  $e_g^1$  electrons. Our study of Mn and Co oxides of spinel and perovskite structures indicate that trivalency and the electronic configuration of the B site transition metal cation to be important factors in determining photocatalytic OER activity. Trivalency ensures easy electron transfer from the metal ion. In particular, we observe that oxides with B-site cation having  $d^4$  and  $d^6$  configurations with one electron in the antibonding  $e_g$  orbital, show high activity for oxygen evolution irrespective of the crystallographic structure of the catalyst.

3d electron number of the B-site ions both in  $\text{ABO}_3$  and  $\text{A}_2\text{B}_2\text{O}_4$  represent the antibonding electron occupation of the B-O bond which is known to represent the strength of B-O<sub>2</sub> binding interaction.<sup>39</sup> It has earlier been shown that electrochemical ORR and OER activity of perovskite oxides depends on the number of d electrons with a M shaped relationship, with maxima at  $d^4$  and  $d^7$  configuration.<sup>40,41</sup> It has been explained by molecular orbital approach based on the fact that  $e_g$  orbitals of transition metal ions can form  $\sigma$ -bond with the adsorbate and therefore its occupancy can influence the binding of oxygen related intermediate species for OER and ORR. The shape of the antibonding  $e_g$  orbital is such that it points towards the surface O atom. Thus,  $\sigma$ -bonding  $e_g$  orbital has greater overlap with the O  $2p\sigma$  orbital of the oxygen related adsorbate than the  $\pi$ -bonding  $t_{2g}$  orbital, thereby allowing easy electron transfer between the surface cation and the adsorbed oxygen related intermediates. Again, oxygen evolution will depend on the strength of binding of the reaction intermediates to the oxide catalyst. Too little filling of the  $e_g$  orbital ( $e_g^0$ ) can result in too strong interaction, while too much  $e_g$  filling ( $e_g^2$ ) can lead to a very weak interaction. It is also important to note that even though  $\text{LaNiO}_3$  in low spin state has  $e_g^1$  configuration, it does not show good catalytic activity for water oxidation. A probable reason for that could be the fact that  $\text{LaNiO}_3$  is metallic with delocalized electrons and only a localized electron in the  $\sigma^* - e_g$  orbital can be readily available for donation.

## 5. Conclusions

The present study highlights the importance of  $e_g^1$  electronic configuration of the transition metal in water oxidation photo-catalysis using  $[\text{Ru}(\text{bpy})_3]^{2+}$  as the photosensitizer. We find that  $\text{LaCoO}_3$ ,  $\text{Li}_2\text{Co}_2\text{O}_4$  and solid solutions of  $\text{Co}^{3+}$  in  $\text{Ln}_2\text{O}_3$  all show very high and comparable catalytic activity. All these samples exist in different crystal structure but has Co in +3 oxidation state with  $t_{2g}^5 e_g^1$  configuration. Similarly,  $\text{Mn}_2\text{O}_3$ ,  $\text{LaMnO}_3$  and  $\text{MgMn}_2\text{O}_4$  all containing Mn in +3 state with  $t_{2g}^3 e_g^1$  configuration show comparable and good catalytic activity even though all of them exist in different crystal structure. While samples like  $\text{LaCrO}_3$ ,  $\text{LaFeO}_3$  or other spinel oxides containing Cr(III) and Fe(III) show very poor or negligible catalytic activity even though they have same crystal structure like perovskite  $\text{LaCoO}_3$  or spinel  $\text{Li}_2\text{Co}_2\text{O}_4$ . Again, hexagonal perovskite manganites containing  $\text{Mn}^{+3}$  do not show good catalytic activity, the Mn in these oxides having electronic configuration of  $e''^2 2e' a_1'$ . Based on these experimental observations we propose that the presence of single electron in the  $e_g$  orbital is an important factor determining photo-catalytic water oxidation. Suntivich et. al.<sup>40,41</sup> observed the relation between  $e_g$  electron occupancy close to unity and high electrochemical OER and ORR activity, and explained it based on molecular orbital approach.  $\sigma$ -bonding  $e_g$  orbital is expected to form bonds with anion adsorbates and influence the binding of oxygen-related intermediate species while single electron in the  $e_g$  orbital is likely to yield just the appropriate strength of interaction between  $\text{O}_2$  and the catalyst for  $\text{O}_2$  evolution photo-catalysis.

## References

1. R. J. Pace. in *Artificial Photosynthesis* 13-34 (Wiley-VCH Verlag GmbH & Co. KGaA, 2005).
2. Y. Lee, B.-U. Ye, H. k. Yu, J.-L. Lee, M. H. Kim and J. M. Baik. *J. Phys. Chem. C* **2011**, 115, 4611-4615.
3. A. T. Marshall and R. G. Haverkamp. *Electrochim. Acta* **2010**, 55, 1978-1984.
4. Y. Lee, J. Suntivich, K. J. May, E. E. Perry and Y. Shao-Horn. *J. Phys. C. Lett* **2012**, 3, 399-404.
5. A. Di Blasi, C. D'Urso, V. Baglio, V. Antonucci, A. S. Arico', R. Ornelas, F. Matteucci, G. Orozco, D. Beltran, Y. Meas and L. G. Arriaga. *J. Appl. Chem.* **2009**, 39, 191-196.
6. V. Yachandra, V. DeRose, M. Latimer, I. Mukerji, K. Sauer and M. Klein. *Science* **1993**, 260, 675-679.
7. J. Penner-Hahn. in *Metal Sites in Proteins and Models Redox Centres* Vol. 90 *Structure & Bonding* (eds H. A. O. Hill, P. J. Sadler, & A. J. Thomson) Ch. 1, 1-36 (Springer Berlin Heidelberg, 1998).
8. J. Yano, J. Kern, K. Sauer, M. J. Latimer, Y. Pushkar, J. Biesiadka, B. Loll, W. Saenger, J. Messinger, A. Zouni and V. K. Yachandra. *Science* **2006**, 314, 821-825.
9. Z. Athina, W. Horst-Tobias, K. Jan, F. Petra, K. Norbert, S. Wolfram and O. Peter. *Nature* **2001**, 409, 739-743.
10. K. N. Ferreira, T. M. Iverson, K. Maghlaoui, J. Barber and S. Iwata. *Science* **2004**, 303, 1831-1838.
11. E. M. Sproviero, J. A. Gascón, J. P. McEvoy, G. W. Brudvig and V. S. Batista. *J. Am. Chem. Soc.* **2008**, 130, 3428-3442.
12. J. P. McEvoy and G. W. Brudvig. *Chem Rev* **2006**, 106, 4455-4483.
13. P. E. M. Siegbahn. *Chem Eur. J.* **2006**, 12, 9217-9227.
14. Y. Umena, K. Kawakami, J.-R. Shen and N. Kamiya. *Nature* **2011**, 473, 55-U65.
15. K. Kawakami, Y. Umena, N. Kamiya and J.-R. Shen. *J. Photochem. Photobio. B* **2011**, 104, 9-18.
16. G. C. Dismukes, R. Brimblecombe, G. A. N. Felton, R. S. Pryadun, J. E. Sheats, L. Spiccia and G. F. Swiegers. *Acc. Chem. Res.* **2009**, 42, 1935-1943.

17. R. Brimblecombe, A. Koo, G. C. Dismukes, G. F. Swiegers and L. Spiccia. *J. Am. Chem. Soc.* **2010**, 132, 2892-2894.
18. M. M. Najafpour, T. Ehrenberg, M. Wiechen and P. Kurz. *Angew. Chem. Int. Ed.* **2010**, 49, 2233-2237.
19. I. Zaharieva, M. M. Najafpour, M. Wiechen, M. Haumann, P. Kurz and H. Dau. *Energy Environ. Sc.* **2011**, 4, 2400-2408.
20. A. Ramírez, P. Bogdanoff, D. Friedrich and S. Fiechter. *Nano Energy* **2012**, 1, 282-289.
21. N. S. McCool, D. M. Robinson, J. E. Sheats and G. C. Dismukes. *J. Am. Chem. Soc.* **2011**, 133, 11446-11449.
22. M. D. Symes, D. A. Lutterman, T. S. Teets, B. L. Anderson, J. J. Breen and D. G. Nocera. *Chem. Sus. Chem* **2013**, 6, 65-69.
23. F. Jiao and H. Frei. *Angew. Chem. Int. Ed.* **2009**, 48, 1841-1844.
24. F. Jiao and H. Frei. *Chem. Comm.* **2010**, 46, 2920-2922.
25. M. W. Kanan, J. Yano, Y. Surendranath, M. Dincă, V. K. Yachandra and D. G. Nocera. *J. Am. Chem. Soc.* **2010**, 132, 13692-13701.
26. D. K. Zhong and D. R. Gamelin. *J. Am. Chem. Soc.* **2010**, 132, 4202-4207.
27. D. M. Robinson, Y. B. Go, M. Greenblatt and G. C. Dismukes. *J. Am. Chem. Soc.* **2010**, 132, 11467-11469.
28. G. P. Gardner, Y. B. Go, D. M. Robinson, P. F. Smith, J. Hadermann, A. Abakumov, M. Greenblatt and G. C. Dismukes. *Angew. Chem. Int. Ed.* **2012**, 51, 1616-1619.
29. D. M. Robinson, Y. B. Go, M. Greenblatt and G. C. Dismukes. *Journal of the American Chemical Society* **2010**, 132, 11467-11469.
30. M. Bose, A. Ghoshray, A. Basu and C. N. R. Rao. *Phys. Rev. B* **1982**, 26, 4871-4882.
31. M. A. Korotin, S. Y. Ezhov, I. V. Solovyev, V. I. Anisimov, D. I. Khomskii and G. A. Sawatzky. *Phys. Rev. B* **1996**, 54, 5309-5316.
32. C. N. R. Rao, M. M. Seikh and C. Narayana. in *Spin Crossover in Transition Metal Compounds II* Vol. 234 *Topics in Current Chemistry* Ch. 1, 1-21 (*Springer Berlin Heidelberg, 2004*).

33. M. Gibert, P. Zubko, R. Scherwitzl, J. Iniguez and J.-M. Triscone. *Nature Mater.* **2012**, 11, 195-198.
34. Y. Yamada, K. Yano, D. Hong and S. Fukuzumi. *Phys. Chem. Chem. Phys.* **2012**, 14, 5753-5760.
35. J. S. Zhou, J. B. Goodenough, J. M. Gallardo-Amores, E. Morán, M. A. Alario-Franco and R. Caudillo. *Phys. Rev. B* **2006**, 74, 014422.
36. T. A. Betley, Y. Surendranath, M. V. Childress, G. E. Alliger, R. Fu, C. C. Cummins and D. G. Nocera. *Phi Trans. R. Soc. B* **2008**, 363, 1293-1303.
37. A. Filippetti and N. A. Hill. *J Magn Magn Mater* **2001**, 236, 176-189.
38. L. B. Farhat, M. Amami, E. K. Hlil and R. B. Hassen. *J. Alloy. Compd* **2009**, 485, 701-705.
39. J. O. M. Bockris and T. Otagawa. *J Electrochem. Soc.* **1984**, 131, 290-302.
40. J. Suntivich, H. A. Gasteiger, N. Yabuuchi, H. Nakanishi, J. B. Goodenough and Y. Shao-Horn. *Nature Chem.* **2011**, 3, 647-647.
41. J. Suntivich, K. J. May, H. A. Gasteiger, J. B. Goodenough and Y. Shao-Horn. *Science* **2011**, 334, 1383-1385.

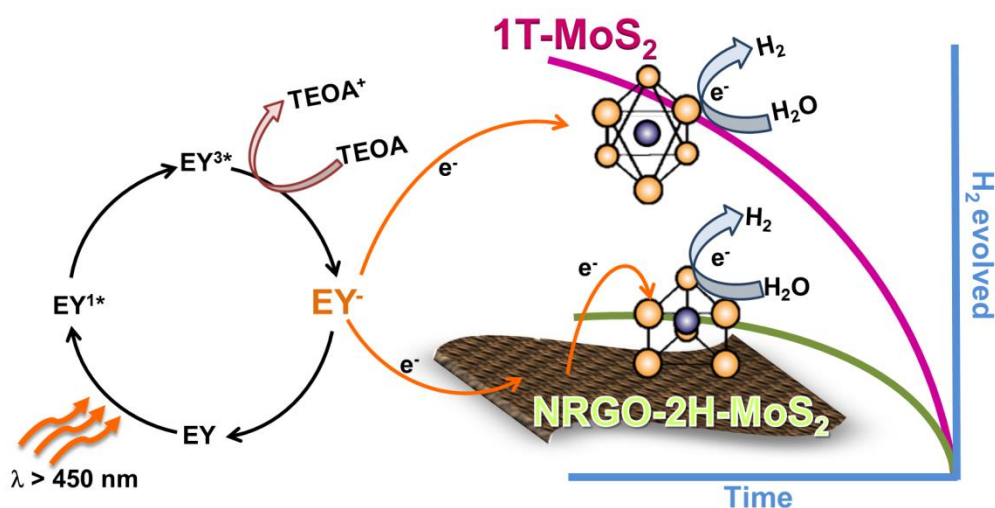


# Chapter III.2

## *Highly efficient visible-light induced H<sub>2</sub> generation by single layer 1T-MoS<sub>2</sub> and the nanocomposite of few-layer 2H-MoS<sub>2</sub> with heavily nitrogenated graphene*

### *Summary\**

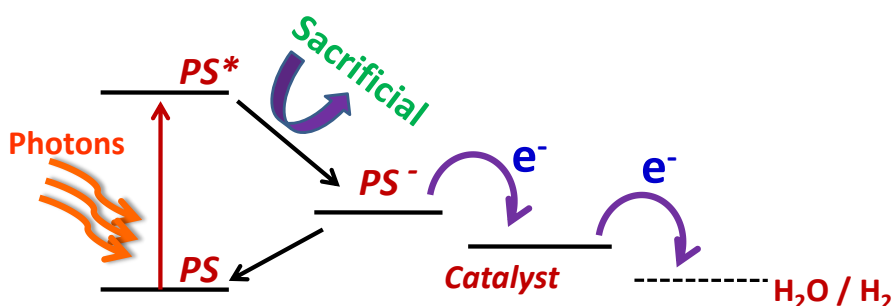
*In our endeavour to optimize MoS<sub>2</sub> based catalysts for dye (Eosin Y) sensitized photocatalytic H<sub>2</sub> evolution, we have found that increasing the ability of the catalyst to transfer photogenerated electrons from sensitized dye to the active sites of catalyst is the key to superior catalytic activity. Composite of MoS<sub>2</sub> with heavily nitrogen doped graphene show very high catalytic activity with N-doped graphene being n-type acts as a better electron donor to p-type MoS<sub>2</sub> than graphene. In the same lines making MoS<sub>2</sub> itself metallic improves the catalytic activity manifold.*



\* A paper based on this work has appeared in *Angew. Chemi. Int. Ed.*, 2013.

## 1. Introduction

Since the discovery of the Honda–Fujishima effect in TiO<sub>2</sub> in 1972,<sup>1</sup> semiconducting have been studied to great details as water splitting catalysts. Oxides are highly robust both mechanically and chemically and do not undergoes photodegradation or corrosion during photocatalytic reactions. In 1980 Scaife<sup>2</sup> noted that it is intrinsically difficult to develop an oxide semiconductor photocatalyst satisfies both the conditions of having sufficiently negative conduction band for H<sub>2</sub> production and a sufficiently narrow band gap for visible light absorption. This is because of the highly positive valance bands (+3.0 V vs. NHE) in oxides formed of the O 2p orbital. Non-oxide semiconductors like sulfides and nitrides possess appropriate band levels for visible light induced H<sub>2</sub> evolution. However they are generally unstable and get deactivated by photocorrosion or self-oxidation. Dye sensitization allows the use of semiconductors with energy levels matched with redox potential of water while still retaining tenability of absorption of light in the entire visible region. The process of dye sensitization involves electron transfer from the sensitized dye to the catalyst directly or indirectly. For a material to act as dye sensitized proton reduction catalyst the material must have its conduction band or an energy level more positive than the oxidation potential of the dye but more negative than the reduction potential of water as demonstrated below.



**Scheme 1.** Schematic representation of dye-sensitized catalysts for reduction of water.

Dye sensitization of many wide band gap semiconductors like TiO<sub>2</sub> has thus been used for H<sub>2</sub> evolution.<sup>3</sup> Despite several decades of research solar hydrogen generation via

photo-catalytic water splitting is still a challenging problem because of the fact that it is thermodynamically uphill reaction while the charge recombination reactions are energetically more favourable and are much faster than the multi electron processes of proton reduction. Organization of molecules into assemblies that promote long-lived charge separation<sup>3</sup> and use of electron acceptors and transporters like graphene<sup>4</sup> and nanoparticle catalysts promoting the opposite half-cell reaction of water oxidation<sup>5,6</sup> has been advocated as remedy to the above problem. A simpler approach to enhance H<sub>2</sub> evolution would be to use catalysts with better proton reduction ability than TiO<sub>2</sub>. Traditionally, H<sub>2</sub> is generated from water using Pt electrodes, and several catalysts have been used for electrocatalytic, photocatalytic or photoelectrocatalytic production of hydrogen<sup>7,8</sup>. In natural systems proton reduction is catalyzed by hydrogenase and nitrogenase, enzymes catalytic centre of which is mainly composed of earth abundant non-noble metal elements like Fe, Ni, Mo. Recent DFT calculations have revealed that free energy of hydrogen evolution on MoS<sub>2</sub> is comparable to hydrogenase, nitrogenase as well as Pt. The free energy was calculated based on the consideration that a catalyst should bind atomic H with just the appropriate strength (not too strong and not too weak) such that both binding and release of hydrogen is equally feasible. Based on this consideration the necessary condition for a catalyst to act as a good proton reduction catalyst is that the free energy of adsorbed H is close to that of the reactant and product i.e. the  $\Delta G^0 \approx 0$ .<sup>9</sup> It was also found that the edge structure of MoS<sub>2</sub> sheets have close resemblance with the catalytically active sites of nitrogenase and hydrogenase. MoS<sub>2</sub> has proven to be a good catalyst for electrochemical as well as photochemical hydrogen evolution reaction (HER)<sup>10-12</sup>.

## ***2. Scope of the present investigations***

Theoretical and experimental studies indicate that the edges of MoS<sub>2</sub> are catalytically active while the basal plane remains inert<sup>9,13</sup>. Nanoparticles of MoS<sub>2</sub> with single-layered truncated triangular morphology with exposed Mo edges,<sup>13,14</sup> or those grown on highly ordered pyrolytic graphite<sup>15</sup> or graphitic carbon<sup>16</sup> are catalytically active. Electrochemical HER carried out with nanoparticles of MoS<sub>2</sub> supported on carbon<sup>17</sup> and fluorine-doped tin

oxide electrodes<sup>18</sup> show higher yields of H<sub>2</sub>. Hydrogen evolution appears to be further enhanced by using graphene<sup>19</sup> or carbon nanotubes<sup>10</sup> to support nanocrystalline MoS<sub>2</sub>, the favorable conductivity of the nanocarbons ensuring efficient electron transfer to the electrodes. Good photo-electrocatalytic activity of MoS<sub>2</sub> has been reported, with MoS<sub>2</sub> possessing the double gyroid structure with a large number of interconnected pores showing the highest efficiency.<sup>20</sup>

While electrochemical HER by MoS<sub>2</sub> has been studied in detail, photocatalytic HER by MoS<sub>2</sub> has received less attention. Bulk MoS<sub>2</sub> being an indirect band gap (1.29eV) semiconductor does not absorb the solar spectrum efficiently. On sensitization with Ru(bpy)<sub>3</sub><sup>2+</sup>, colloidal MoS<sub>2</sub> nanoparticles show photocatalytic HER activity with a turn over number (TON) of 93. The method utilizes a three component system with ascorbic acid as the reductive quencher for excited state Ru(bpy)<sub>3</sub><sup>2+</sup> which in turn transfers electrons to MoS<sub>2</sub>.<sup>21</sup> MoS<sub>2</sub> loaded on TiO<sub>2</sub><sup>22</sup>, CdSe<sup>23</sup> and CdS<sup>24</sup> has been investigated for H<sub>2</sub> evolution where TiO<sub>2</sub> and CdS acting as both light absorbers and catalysts. Recently, few-layer MoS<sub>2</sub> loaded reduced graphene oxide (RGO) has been studied for photocatalytic HER with Eosin Y as the sensitizer showing higher H<sub>2</sub> evolution as compared to both MoS<sub>2</sub> as well as its physical mixture with RGO.<sup>25</sup> RGO is claimed to act in two ways i) as a substrate for growing highly dispersed MoS<sub>2</sub> with high density of catalytically active edges and ii) as conductive substrate for the efficient transfer of the photogenerated electrons to MoS<sub>2</sub>, thereby increasing the lifetime of photogenerated electrons.

Since graphene acts as a channel for transferring electrons to MoS<sub>2</sub> in graphene-MoS<sub>2</sub> composites we have carried out investigations on visible-light driven H<sub>2</sub> generation by few-layer 2H-MoS<sub>2</sub> and its composites with nitrogen-doped graphene. Nitrogen incorporation in graphene is expected to improve the catalytic activity of the composite with 2H-MoS<sub>2</sub> layers since it enhances the electron donating ability of the graphene. We have been able to prepare a MoS<sub>2</sub> composite with heavily nitrogenated RGO (%N ~ 15) which shows excellent HER activity. Heavily nitrogenated graphene (NRGO) being electron rich is thus n-type in nature, while MoS<sub>2</sub> is known to be p-type. Presumably NRGO and MoS<sub>2</sub> can interact strongly, thereby leading to greater probability of electron transfer to the MoS<sub>2</sub>. On analogous principles Meng et. al.<sup>26</sup> have demonstrated

enhancement in electrocatalytic activity due to the formation of a p-n junction in composites of n-type N-doped graphene with p-type MoS<sub>2</sub>.

The reaction involved in dye sensitized water splitting with MoS<sub>2</sub> involves photosensitization of the dye EY to generate reactive species EY<sup>-</sup>, which then can donate one electron to the catalyst.<sup>25</sup> So, though the overall reaction is photocatalytic generation of H<sub>2</sub> the electrons that are involved in the reduction of H<sub>2</sub>O are not photocatalytically generated on MoS<sub>2</sub>, rather transferred from photogenerated species EY<sup>-</sup> to MoS<sub>2</sub>. It therefore occurred to us that it would be more rewarding if the MoS<sub>2</sub> layer itself can be rendered more conducting. The edge sites in MoS<sub>2</sub> have been predicted to be metallic in nature.<sup>14,27</sup> Jramillo et. al.<sup>13</sup> carried out extensive study on nanoparticulate MoS<sub>2</sub> grown on Au by first atomically resolving the surface and edges of the catalyst and then measuring their electrochemical activity in solution and found the exchange current density to directly correlate with the MoS<sub>2</sub> edge length. Since only edges of MoS<sub>2</sub> are catalytically active and not the basal plane it is evident that greater the efficiency of electron transport to catalytically active site of MoS<sub>2</sub> higher the efficiency of photocatalytic hydrogen evolution. Several quantum mechanical calculations and experimental evidences have revealed a direct correlation between the catalytic activity and metallic character of MoS<sub>2</sub> edges.<sup>14,15,27</sup> 2H MoS<sub>2</sub> is semiconducting with an indirect band gap of 1.2 eV its polytype 1T MoS<sub>2</sub> crystallizes in octahedral geometry and is known to be metallic.<sup>28-32</sup> Prompted by our earlier results we expected metallic 1T-MoS<sub>2</sub> to act as an efficient H<sub>2</sub> evolution catalyst by virtue of both its metallic conductivity and as predicted high catalytic activity.

### ***3. Experimental Section***

#### **Synthesis:**

**MoS<sub>2</sub> :** MoS<sub>2</sub> samples were prepared both by hydrothermal and solid state route.<sup>33</sup> Solid state synthesis of MoS<sub>2</sub> involved heating a mixture of (NH<sub>4</sub>)<sub>6</sub>Mo<sub>7</sub>O<sub>24</sub>·4H<sub>2</sub>O and thiourea (in the ratio 1:10 by weight) at 500°C for 3 hrs in N<sub>2</sub> atmosphere. To prepare nanosheets of MoS<sub>2</sub> hydrothermally 60 mg of (NH<sub>4</sub>)<sub>6</sub>Mo<sub>7</sub>O<sub>24</sub>·4H<sub>2</sub>O and 60 mg of thiourea were

dissolved in 10 ml water and heated at 220°C for 72 hours followed by washing with water and ethanol.

**Graphene oxide (GO):** Graphene oxide was prepared by modified Hummers method.<sup>34</sup> For this 70 ml of concentrated H<sub>2</sub>SO<sub>4</sub> was added to a mixture of 1 g of graphite flakes and 1.5 g of NaNO<sub>3</sub> and the mixture was cooled to 0 °C. 9 g of KMnO<sub>4</sub> was slowly added always keeping the temperature of the reaction mixture well below 20 °C. the reaction mixture was then warmed to 35 °C and stirred for 7 h. Additional KMnO<sub>4</sub>(9.0 g) was then added and stirred at 35°C for 12 h. The mixture was cooled by pouring onto ~400 ml of ice with 3 ml of 30% H<sub>2</sub>O<sub>2</sub>. GO was collected by centrifugation and washed with water.

**Reduced graphene oxide (RGO):** 250mg of GO was dispersed in 100ml of water by sonication for 3 hours. 32ml 5% w/v solution of sodium carbonate was added to make pH ~10 and refluxed for 12 hours at 90°C and then 50 ml of 0.1 mol NaBH<sub>4</sub> was then added and stirred for 5 hours at 80°C.<sup>35</sup>

**Exfoliated Graphene (EG):** Thermally exfoliated graphene EG (3-5 layers) was obtained from GO by sudden heating to 300°C in air. This process not only exfoliates the graphene but also retains some of the functional groups.

**Nitrogen doped graphene (NEG):** N-doped EG (NEG) was prepared by heating mixture of 100 mg of EG and 1g urea 600 °C for 1hr in a N<sub>2</sub> atmosphere.<sup>36</sup> Heating graphene at high temperatures results in loss of functional groups. Further functionalization of NEG was needed to create a sufficient density of functional groups so as to get optimum adhesion of MoS<sub>2</sub> to its surface.<sup>37,38</sup> 50mg of graphene was dispersed in 8ml of nitric acid and 2ml of sulphuric acid mixture for half an hour. The mixture was transferred in a microwave bomb and 10 ml water was added to it. It was then microwaved for 10mins (3+3+4) at 600W.

**Highly N-doped GO - MoS<sub>2</sub> composite (NRGO-MoS<sub>2</sub>):** 30 mg GO and 60 mg of (NH<sub>4</sub>)<sub>6</sub>Mo<sub>7</sub>O<sub>24</sub>·4H<sub>2</sub>O was dispersed in 10 ml water followed by addition of 120 mg of thiourea. The mixture was heated in a Teflon lined autoclave 220°C for 72 hours.

**1T-MoS<sub>2</sub>:** 1T-MoS<sub>2</sub> was prepared by Li-intercalation of bulk MoS<sub>2</sub> with n-butyl lithium followed by exfoliation in water as reported earlier.<sup>39</sup> For a typical synthesis 300 mg of MoS<sub>2</sub> (alfa aser) was taken in a round bottom flask with a gas tight septum. Under inert

conditions 5 ml n-butyl lithium (sigma) was added to it and allowed to stir for 48 hrs. The sample was filtered and washed with n-hexane under inert atmosphere. To obtain single layer MoS<sub>2</sub> the sample was quickly poured into ice cold water and sonicated for 30 mins maintaining the temperature of the bath sonicator <5°C. This leads to sudden de-intercalation of Li and exfoliation of the layers. The sample was washed with water and dialyzed to remove all Li and used for characterization and H<sub>2</sub> evolution studies. The sample was stored as dispersion in water below 10°C.

To obtain dry sample, the dispersion was lyophilized. To obtain corresponding 2H-analogue the sample was dried by lyophilization and annealed at 300°C for 1 hr in N<sub>2</sub> atmosphere.

**Characterization:** All samples were characterized by XRD, FESEM and TEM to ensure the formation of pure phase and determine the morphology. CHNS analysis and XPS measurements were carried out to determine the percentage of doping. Carbon peak at 284.8eV and 286.15eV forms the part of the graphene sheet related to sp<sup>2</sup> carbon peak and C-N bond. The 289 eV was for –COOH group on the surface. 398.1 eV and 402.1eV were mapped to pyridinic and quaternary nitrogen respectively. The pyridinic matrix forms the part of the graphene matrix. Mo 3d<sup>3/2</sup> and 3d<sup>5/2</sup> were at 233 eV and 2229.5eV respectively. Mo 3p<sup>3/2</sup> at 395.5 eV merged with N 1 s spectra and was thus deconvoluted. CHNS analysis, EDAX and XPS measurements gave an insight into the % of MoS<sub>2</sub> in the graphene-MoS<sub>2</sub> composites. 1T MoS<sub>2</sub> was identified by TEM diffraction and HRTEM in a FEI TITAN cubed double aberration corrected 80-300 keV microscope. Negative Cs imaging technique was used (Cs ~ -35-40 μm, Δf ~ + 8 nm) to image atom with white contrast and direct interpretation. Raman spectrum was collected for all MoS<sub>2</sub> samples and composites to gain an insight into the interaction of MoS<sub>2</sub> with graphene. The concentration of the dispersion of 1T-MoS<sub>2</sub> was determined by ICPES analysis.

Details of characterization techniques are given in Appendix.

**Photocatalytic measurements:** 2mg of the catalyst was dispersed in 40ml of water and 15% v/v (8ml) of triethanolamine as sacrificial agent in a quartz vessel. The vessel was thoroughly purged with N<sub>2</sub>. 0.15mM Eosin Y was used as the sensitizer. The vessel was irradiated under 100W halogen lamp (flux of ~300 W/m<sup>2</sup>) with constant stirring of the

mixture. 1 ml of evolved gases were manually collected from the headspace of the vessel and analyzed in Perkin Elmer Clarus ARNEL 580 gas chromatograph. For better comparison with the literature photocatalysis was also carried out under 400W Xe lamp, Newport 69920 with flux of  $\sim 2500\text{W/m}^2$ . Turn over frequency (TOF) for each catalyst was calculated per mole of MoS<sub>2</sub> present in each catalyst, considering the fact that H<sub>2</sub> evolution happens on MoS<sub>2</sub> only. Number of moles of MoS<sub>2</sub> in per mg of catalyst was determined from XPS and CHNS analysis.

## 4. Results and Discussion

We first studied the photocatalytic properties of EG-MoS<sub>2</sub>(2H) prepared by solid state method and compared it with that of MoS<sub>2</sub> alone. XRD of MoS<sub>2</sub> shows all characteristic reflections of MoS<sub>2</sub> except the reflection corresponding to (002) plane of MoS<sub>2</sub> indicating lesser stacking along c direction (Figure 1(a)) and HRTEM image indicates the sample is mainly composed of flakes with 2-4 layers.

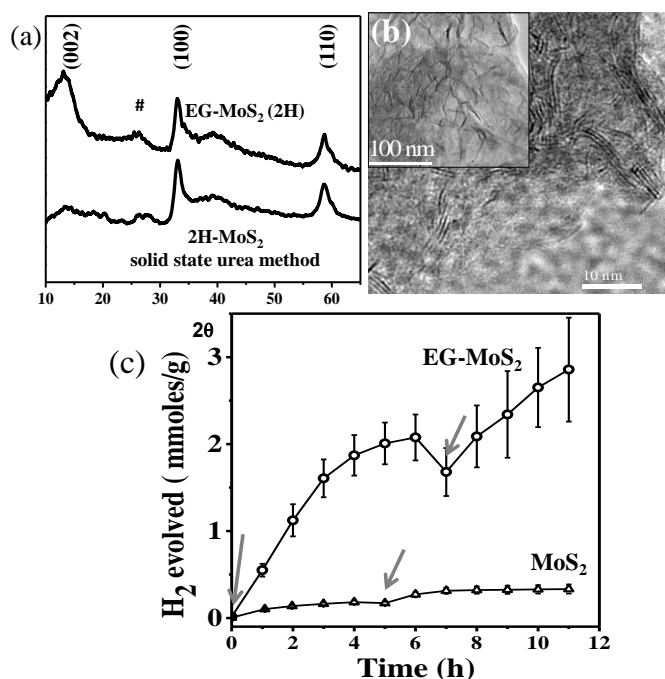


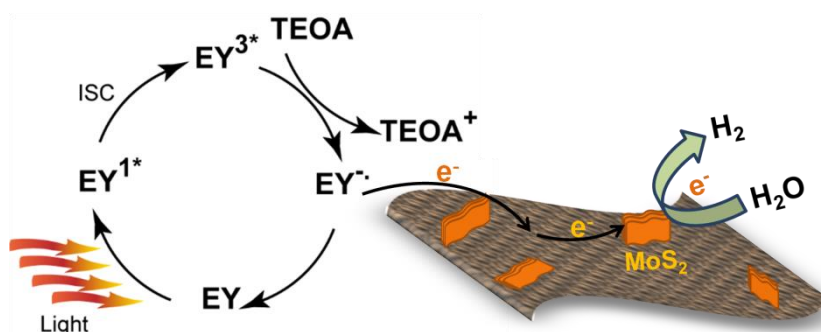
**Figure 1.** (a) XRD MoS<sub>2</sub> and EG-MoS<sub>2</sub> composite,(b) TEM and HRTEM showing MoS<sub>2</sub> flakes growing on grapheme sheets, (c) photo-catalytic H<sub>2</sub> evolution by MoS<sub>2</sub> and EG-MoS<sub>2</sub>. Arrow indicates the time of re-addition of dye.



EG-MoS<sub>2</sub> composites prepared under similar conditions were characterized using XRD, XPS, Raman and TEM studies indicating formation pure MoS<sub>2</sub> on graphene. TEM image of the sample in inset in Figure 1 (b) shows MoS<sub>2</sub> flakes growing on graphene. Stripes of MoS<sub>2</sub> are seen on graphene, most of them with their edges almost perpendicular to the graphene surface so as to expose their edges. HRTEM image (Figure 1(b)) shows MoS<sub>2</sub> flakes are mostly composed of 2-4 layers and are highly dispersed on graphene covering almost 50% of the graphene surface. XRD of the sample shows very weak and broad reflection due to (002) plane of MoS<sub>2</sub> indicating very less stacking along c axis as shown in Figure 1(a), consistent with the TEM studies. XPS studies indicate with Mo content of around ~ 5 atomic% in the sample.

Photocatalytic H<sub>2</sub> evolution studies were carried out on all the samples with Eosin Y (EY) as the sensitizer and triethanol amine (TEOA) as the sacrificial electron donor as described above. Initial concentration of EY was kept at 0.15mM. Figure 1(c) shows the time course of H<sub>2</sub> evolution catalyzed by MoS<sub>2</sub>. EY sensitized MoS<sub>2</sub> alone showed very little catalytic activity with initial slope of 0.05 mmole g<sup>-1</sup>h<sup>-1</sup> with a maximum 0.18 mmole/g at 4 hrs after which it decreases slightly. Rate of H<sub>2</sub> evolution is regained on further addition of EY. No H<sub>2</sub> was evolved by MoS<sub>2</sub> in absence of the sensitizer indicating that electron transfer from photosensitized EY to MoS<sub>2</sub> is necessary for MoS<sub>2</sub> to show catalytic activity and photogenerated electrons of MoS<sub>2</sub> play negligible role in H<sub>2</sub> evolution.<sup>21,25</sup> Transfer of electrons from photosensitized dye to MoS<sub>2</sub> can be considerably increased by using graphene as support for MoS<sub>2</sub>. Yield of H<sub>2</sub> evolved increased by almost 10 times for EG-MoS<sub>2</sub> with yield of 0.54 mmole.g<sup>-1</sup>.h<sup>-1</sup>. The rate of H<sub>2</sub> evolved decreased after 8 hrs and could be regained on addition of EY. The mechanism of EY sensitized H<sub>2</sub> evolution is represented in scheme 1. EY absorbs light and produces singlet excited state of EY<sup>1\*</sup> followed by a low lying triplet excited state EY<sup>3\*</sup>. In the presence of sacrificial acceptor TEOA this EY<sup>3\*</sup> subsequently forms EY<sup>-</sup>. EY<sup>-</sup> is highly reductive species and in absence of any electron acceptor recombines rapidly with the oxidative donor (TEOA<sup>+</sup>) or dye species resulting in quenching of the dye. In presence of MoS<sub>2</sub> EY<sup>-</sup> transfers one electron to MoS<sub>2</sub> reversing back to EY. This electron on MoS<sub>2</sub> then catalyzes reduction of water. Since electron transfer efficiency from EY<sup>-</sup> to MoS<sub>2</sub> is low, we observe rapid quenching of the dye. Graphene is not only an

efficient electron acceptor but can act as an effective electron channel to transfer electrons from the reductive species EY<sup>-</sup> to MoS<sub>2</sub>. Also EY being a planer molecule interacts with p conjugated graphene and thereby transfers its electrons to graphene easily. Graphene therefore prolongs the lifetime of the EY<sup>-</sup> and acts as an electron collector and transports the photogenerated electrons from highly reductive species EY<sup>-</sup> to catalytically active sites of 2H-MoS<sub>2</sub>. This directional electron transfer has been explained based on energy levels of the components, reductive potential of EY<sup>-</sup> being -0.8 V vs NHE while that of graphene and MoS<sub>2</sub> are roughly 0.16 V vs NHE and 0.2 V vs NHE respectively.



**Scheme 2.** EY sensitized water reduction over graphene-MoS<sub>2</sub>.

Based on the above mechanism it is clear that enhancing the electron transport to MoS<sub>2</sub> will enhance the photocatalytic yield. Doping of N in graphene makes it electron rich, while MoS<sub>2</sub> is intrinsically p-type in nature. In a composite of N-doped graphene with MoS<sub>2</sub> a heterojunction is thus formed, increasing the probability of electron transfer from graphene to MoS<sub>2</sub>. We therefore studied the effect of N-doping of graphene on photocatalytic H<sub>2</sub> evolution by the composite.

Like EG-MoS<sub>2</sub> composites NEG-MoS<sub>2</sub> too is composed of mostly vertically aligned MoS<sub>2</sub> with 2-4 layers (see HRTEM image in Figure 2(a)). Vertical alignment of MoS<sub>2</sub> sheets on graphene not only ensures high density of catalytically active edges but also better electron transfer from graphene to MoS<sub>2</sub>. Lesser stacking of MoS<sub>2</sub> along (002) direction is evident from XRD of the composites. Interestingly, all the composites show characteristic (002) reflection of graphene though very weak and broad, indicating very little stacking of graphene layers. XPS studies indicate N content of ~5 atomic% in the composites with Mo content of 3 atom%. Figure 2(c) shows the comparison of the H<sub>2</sub> evolution activity of NEG-MoS<sub>2</sub> in comparison with EG-MoS<sub>2</sub>. The rate of H<sub>2</sub> evolution

increased significantly to 0.83 mmole g<sup>-1</sup>h<sup>-1</sup> for NEG-MoS<sub>2</sub> attaining a value of ~5.2 mmoles g<sup>-1</sup> after 12 hrs of exposure to light. Thus, NEG-MoS<sub>2</sub>(2H) shows a TOF of 0.45 h<sup>-1</sup> which it is 2.1 times higher than that with EG-MoS<sub>2</sub> and 57 times higher than with MoS<sub>2</sub> alone.

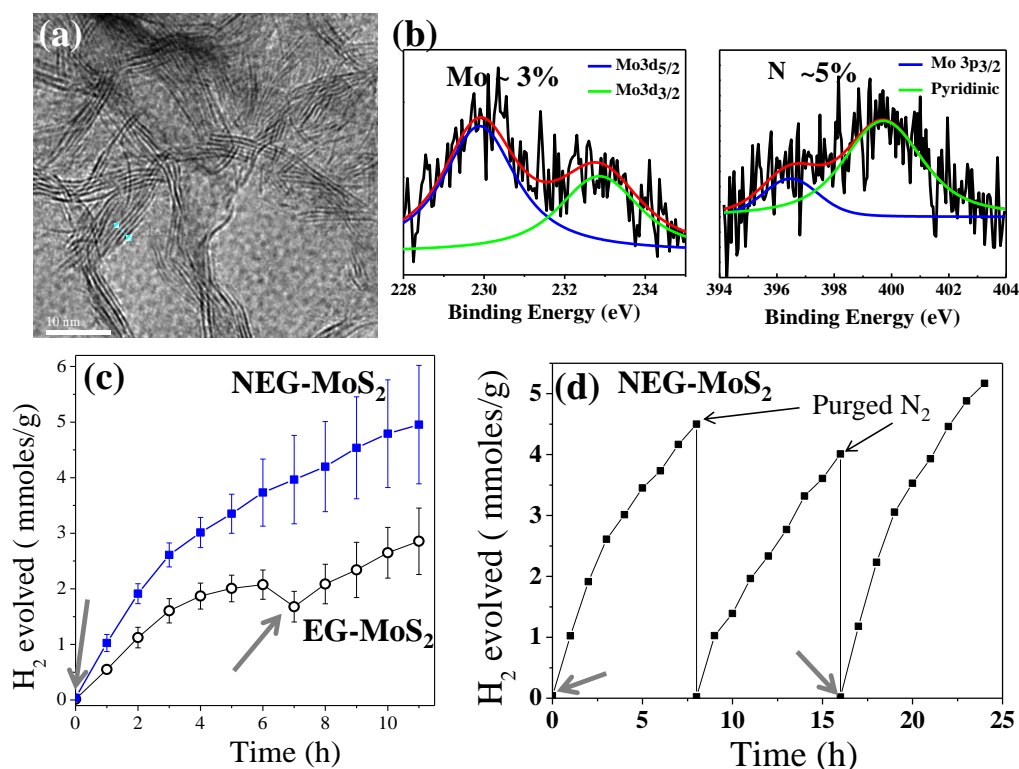


**Figure 2.** (a) HRTEM image of NEG-MoS<sub>2</sub> showing MoS<sub>2</sub> flakes on NEG, (b) XPS spectra of NEG-MoS<sub>2</sub> showing N 1s and Mo 3d spectra, (c) photocatalytic H<sub>2</sub> evolved by NEG-MoS<sub>2</sub> in comparison to EG-MoS<sub>2</sub> and (d) time course of photocatalytic H<sub>2</sub> evolution showing recyclability of the sample. Arrows indicate point of addition of dye.

Since TOF is independent of amount of MoS<sub>2</sub> present in a catalyst, an increased TOF for NEG-MoS<sub>2</sub> is a clear indication of the enhanced activity of NEG-MoS<sub>2</sub>. Interestingly, we do not observe in visible quenching of the dye upto 12 hrs of reaction, though the rate of reaction reduces slowly with increasing time. Figure 2(d) shows the time course of H<sub>2</sub> evolved by NEG-MoS<sub>2</sub> for 24 hrs with purging of the vessel with N<sub>2</sub> after every 8 hrs, showing the stability of the catalyst. The rate of H<sub>2</sub> evolution decreases slightly in the second cycle and was regained in third cycle by addition of 0.075 mM EY to the solution.

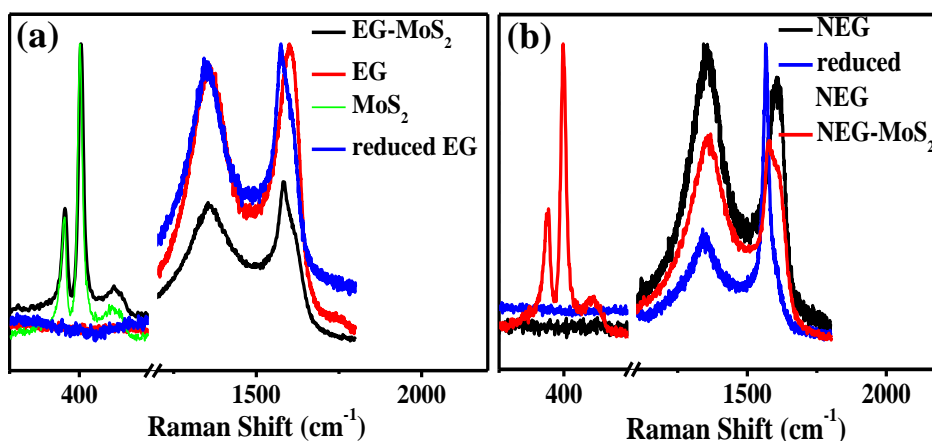


**Figure 3.** Comparison of Raman spectra of (a) EG-MoS<sub>2</sub> with EG, EG treated with thiourea and MoS<sub>2</sub> and (b) NEG-MoS<sub>2</sub> with that of NEG and NEG treated with thiourea.

Raman spectroscopic studies were carried out on all MoS<sub>2</sub> and graphene-MoS<sub>2</sub> composites to clearly understand the role of graphene in this charge transfer. MoS<sub>2</sub> shows characteristic A<sub>1g</sub> and E<sub>2g</sub> modes at around 378 and 402 cm<sup>-1</sup>.<sup>33</sup> Though the A<sub>1g</sub> and E<sub>2g</sub> modes of MoS<sub>2</sub> do not show significant shift in case of composites, the characteristic D and G bands of graphene shift considerably (Figure 3). Oxidation of graphene to graphene oxide is known to stiffen the G band. Therefore, for appropriate comparison graphene samples were reduced under similar conditions as during preparation of the graphene-MoS<sub>2</sub> composites. As expected reduction softens the G band (see table 1). Molecular charge transfer from an electron donor to graphene is known to soften the G band while charge transfer from graphene to an electron acceptor stiffens the G band.<sup>40</sup> The G band stiffens by 8 cm<sup>-1</sup> in EG-MoS<sub>2</sub> when compared to reduced EG, indicating charge transfer from EG to MoS<sub>2</sub>. On the other hand electrochemical doping of both holes and electrons is known to sharpen and stiffen the G band<sup>41</sup> N-doped EG therefore shows strongly blue shifted G band as compared to EG. G band in NEG-MoS<sub>2</sub> stiffens by 11 cm<sup>-1</sup> when compared to reduced NEG implying charge transfer from n-type NEG to p-type MoS<sub>2</sub>.

To further verify that the observed trend of activity arises from the role of N-doped graphene and graphene and is not an extrinsic effect, we decided to prepare MoS<sub>2</sub> and its composite with EG and NEG by hydrothermal method and check its H<sub>2</sub> evolution activity. Hydrothermally prepared samples show stronger (002) reflections than those

prepared by solid state method, implying larger number of layers in each MoS<sub>2</sub> stack. TEM analysis confirms the formation 10-20 layered thick of MoS<sub>2</sub> growing on graphene as shown in Figure 4 (a). Some MoS<sub>2</sub> flakes are seen growing outside graphene too. XPS and CHNS analysis shows greater MoS<sub>2</sub> content of 10-15 atomic% in these samples. Raman studies indicate presence of both graphene and MoS<sub>2</sub> in the sample. As discussed earlier Raman study also indicated clear charge transfer from graphene to MoS<sub>2</sub> in EG-MoS<sub>2</sub> and NEG-MoS<sub>2</sub>.

**Table 1.** Raman frequencies and intensity ratios of various catalysts

Samples	Peak Position (cm <sup>-1</sup> )				I <sub>D</sub> /I <sub>G</sub> <sup>b</sup>
	E <sub>2g</sub> <sup>a</sup>	A <sub>1g</sub> <sup>a</sup>	D-band <sup>b</sup>	G-band <sup>b</sup>	
EG	-	-	1357	1595	0.912
EG-reduced	-	-	1354	1575	0.91
<sup>+</sup> MoS <sub>2</sub>	378	400	-	-	-
<sup>+</sup> EG-MoS <sub>2</sub>	379	402	1358	1583	1.041
NEG	-	-	1355	1603	1.12
NEG-reduced	-	-	1350	1565	0.34
<sup>+</sup> NEG-MoS <sub>2</sub>	378	400	1354	1576	1
RGO	-	-	1353	1578	1.02
RGO-MoS <sub>2</sub>	378	403	1354	1584	1.32
NRGO-MoS <sub>2</sub>	376	401	1353	1590	0.43

<sup>+</sup> MoS<sub>2</sub> prepared using thiourea by solid state method

<sup>a</sup> Raman modes of MoS<sub>2</sub>

<sup>b</sup> Raman modes of graphene

Figure 4 (b) shows the time course of H<sub>2</sub> evolution by these samples. Even though the yield of H<sub>2</sub> evolved by hydrothermally prepared samples were found to be lesser than those prepared by solid state method, it follows the same trend *i.e.* NEG-MoS<sub>2</sub>> EG-MoS<sub>2</sub>> MoS<sub>2</sub> (Table 2). This unmistakably highlights the role of graphene as a charge carrier independent of the method of preparation of the MoS<sub>2</sub> composite. Also, it is clear that N-doping of graphene facilitates charge transfer to MoS<sub>2</sub> thereby increasing the catalytic yield of H<sub>2</sub>. There could be two possible reasons for lower photocatalytic H<sub>2</sub> yield by hydrothermally prepared MoS<sub>2</sub>, (i) larger number of layers in each stack of MoS<sub>2</sub> and (ii) lesser percent of MoS<sub>2</sub> sticking on graphene. To address the later

graphene with greater density of functional groups was used as a substrate for growing MoS<sub>2</sub>.

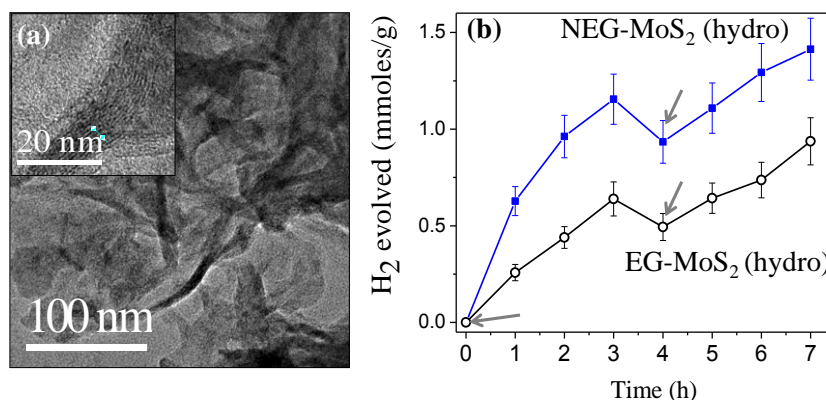


**Figure 4.** (a) TEM and HRTEM images of EG-MoS<sub>2</sub> prepared by hydrothermal method and (b) Time course of H<sub>2</sub> evolution by hydrothermally prepared composite of MoS<sub>2</sub> with EG and NEG.

Hydrothermally synthesized RGO-MoS<sub>2</sub> composites have earlier been reported to show high yield of H<sub>2</sub>.<sup>25</sup> However, the catalyst had not been characterized properly in terms of amount of MoS<sub>2</sub> present or the TOF. We carried out detailed characterization of the RGO-MoS<sub>2</sub> composite and determined its activity per mole of the active constituent of the composite. Both hydrothermally prepared MoS<sub>2</sub> and its composite with RGO show broad but strong (002) reflections corresponding to stacking of MoS<sub>2</sub> sheets along the c-axis, indicating significant stacking along the c-axis (Figure 5(a)). TEM image in Figure 5 (b) shows stacks of MoS<sub>2</sub> flakes growing on graphene sheets while HRTEM shows MoS<sub>2</sub> stacks containing 10-30 layers. XPS and CHNS analysis of RGO-MoS<sub>2</sub> indicate MoS<sub>2</sub> content of 15 atom%. Raman studies show large stiffening of the G band by around 6 cm<sup>-1</sup> in the composite as compared to RGO alone (Figure 5 (f)). This indicates a strong electronic coupling between RGO and MoS<sub>2</sub> with graphene donating electrons to p-type MoS<sub>2</sub>. The catalyst shows high H<sub>2</sub> evolution rate of 3 mmoleg<sup>-1</sup>h<sup>-1</sup> which is about 67 ml g<sup>-1</sup>h<sup>-1</sup> (see Figure 5 (g)). The TOF of RGO-MoS<sub>2</sub> was calculated to be 0.68 h<sup>-1</sup>, about 85 times greater than MoS<sub>2</sub> and three times of that of EG-MoS<sub>2</sub>. Hydrothermally prepared MoS<sub>2</sub> on the other hand shows activity comparable to that prepared by solid state method, both being 2H-MoS<sub>2</sub>. This implies that rate of H<sub>2</sub> evolution can be increased by increasing amount of MoS<sub>2</sub> growing on graphene.

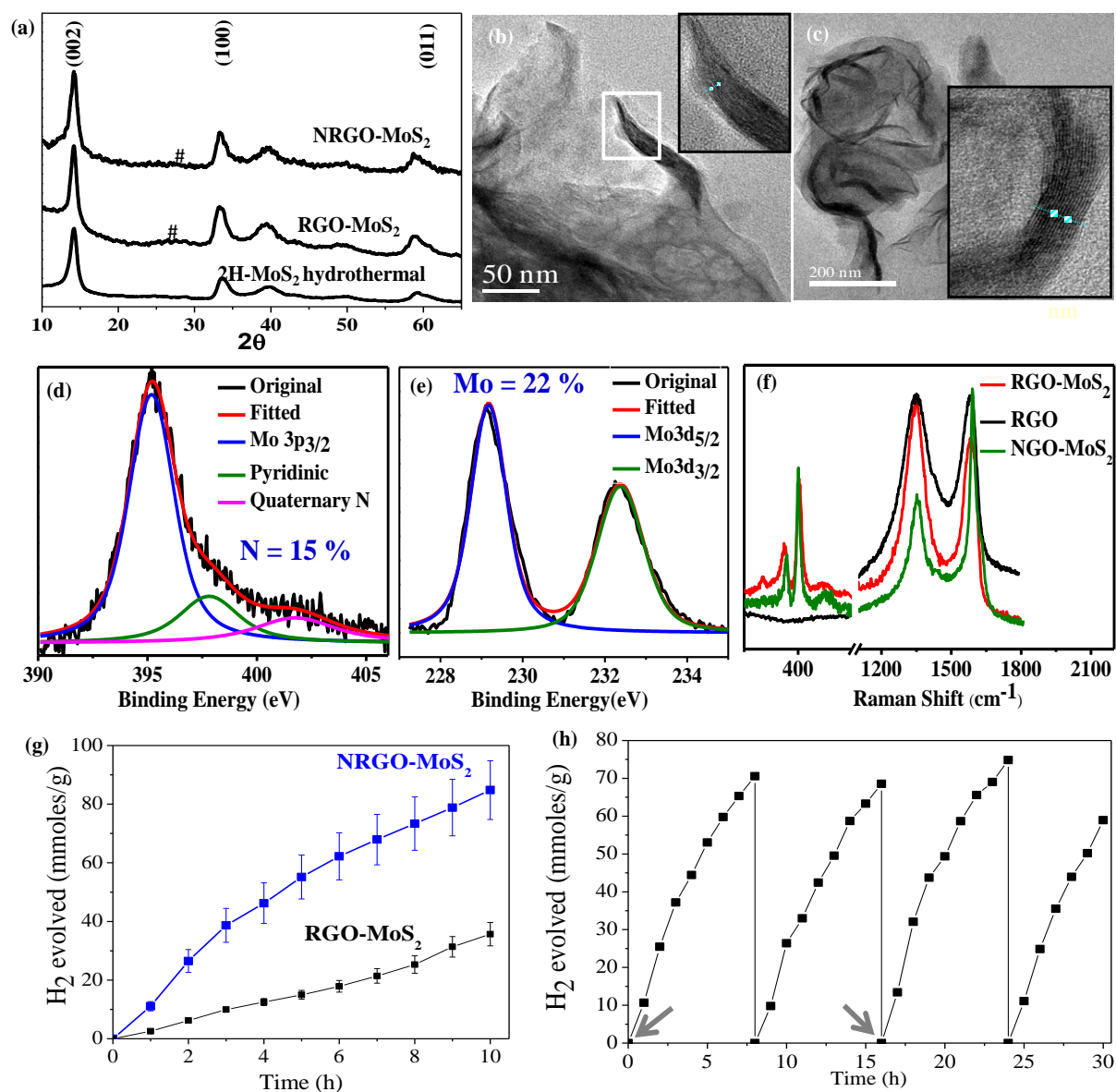


**Figure 5.** (a) XRD of MoS<sub>2</sub>, RGO-MoS<sub>2</sub> and NRGO-MoS<sub>2</sub> prepared hydrothermally, TEM and HRTEM images of MoS<sub>2</sub> composites of (b) RGO and (c) NRGO, Core level d) N1s, Mo3p and (e) Mo3d XPS spectra of NRGO-MoS<sub>2</sub>, (f) comparison of Raman spectra of NRGO-MoS<sub>2</sub> with RGO and RGO-MoS<sub>2</sub>, (g) Comparison of H<sub>2</sub> evolution by NRGO-MoS<sub>2</sub> and RGO-MoS<sub>2</sub> and (d) Time course of H<sub>2</sub> evolution by NRGO-MoS<sub>2</sub> over a period of 30 hrs with the reaction vessel being purged with N<sub>2</sub> after every 8hrs. The arrow indicates the time of addition of EY.

Since our studies showed the yield of H<sub>2</sub> production to depend on the degree of N-doping in graphene as well as the MoS<sub>2</sub> content, we prepared composites of few-layer-

2H-MoS<sub>2</sub> with heavily nitrogenated RGO, designated NRGO. XRD of NRGO-MoS<sub>2</sub> shows broad peaks due to MoS<sub>2</sub> and a small broad hump due to graphene (Figure 5(a)). N content was determined from core level N1s XPS spectra %N being calculated from the peak due to pyridinic N at 399 eV (Figure 5 (d)). %N in NRGO-MoS<sub>2</sub> was calculated to be 15% from XPS which is consistent with the CHNS analysis. Atomic % of MoS<sub>2</sub> was determined to be ~22% both from CHNS and core level Mo3d XPS (Figure 5 (e)). TEM and HRTEM images of the composite shows 10-30 layer thick flakes of MoS<sub>2</sub> growing on graphene (Figure 5 (c)). Raman spectrum of NRGO shows G band to be stiffened by about 12 cm<sup>-1</sup> as compared to both RGO as shown in Figure 5(f) and table 1. Large stiffening of the G band of NRGO in the composite is an effect of doping and interaction with MoS<sub>2</sub>. This clearly indicates a strong electronic coupling between N-doped graphene and MoS<sub>2</sub>, with the N-doped graphene donating electrons to MoS<sub>2</sub>. In Figure 5 (g), we show the time course of H<sub>2</sub> evolved by NRGO-MoS<sub>2</sub> (atomic % of Mo =22%) in comparison with that of RGO-MoS<sub>2</sub> (atomic % of Mo =24%). NRGO-MoS<sub>2</sub> evolves about 10.8 mmoles H<sub>2</sub> per g of the catalyst per hr, with a high TOF of 2.9 h<sup>-1</sup>. The yield of H<sub>2</sub> is nearly 3.5 times higher than that found with RGO-MoS<sub>2</sub> (3 mmoles g<sup>-1</sup>h<sup>-1</sup> as shown in Figure 5 (g)) and about 200 times higher than MoS<sub>2</sub> alone. N-doping makes graphene electron rich. MoS<sub>2</sub> being p-type accepts electrons more readily from electron rich NRGO than from RGO. The present results are consistent with the electrochemical measurements on N-doped RGO-p-type MoS<sub>2</sub> electrodes.<sup>26</sup> The morphology of MoS<sub>2</sub> on the graphene surface could also play a role in producing such high TOF. It is documented in the literature that only the edge sites of 2H-MoS<sub>2</sub> are catalytically active.<sup>9,42,43</sup> TEM images of composite (Figure 5 (c)) shows curling of the sheets to expose the catalytically active edges. Charge transfer to the edges is better with MoS<sub>2</sub> growing vertically on graphene. Table 2 shows a comparison of photocatalytic yields and TOF values of various MoS<sub>2</sub> based catalysts. Figure 5 (h) shows the time course of H<sub>2</sub> evolution by NRGO-MoS<sub>2</sub> over a period of 30 hrs. The catalyst retains similar activity even after 4 cycles of 8hrs each, with 0.075 mmoles of dye being replenished after 16hrs. For proper comparison with earlier reported values, experiments were carried out with a 400W Xe lamp as well. Under such conditions, NRGO-MoS<sub>2</sub> nanocomposite gave an yield of 42 mmole g<sup>-1</sup>h<sup>-1</sup> which is about 940 ml g<sup>-1</sup>h<sup>-1</sup>, the TOF value being 11.5h<sup>-1</sup> which is highest value reported so far (Table 2.).



**Table 2.** Activity of catalyst in terms of yield of H<sub>2</sub> evolved and TOF

Photocatalyst	Light Source	Activity (mmoles g <sup>-1</sup> h <sup>-1</sup> )	TOF <sup>c</sup> (h <sup>-1</sup> )
Colloidal MoS <sub>2</sub> <sup>21</sup>	300W Xe lamp, ( $\lambda > 420$ nm)	-	6
MoS <sub>2</sub> /CdS <sup>24</sup>	300W Xe lamp, ( $\lambda > 420$ nm)	5.3	~ 0.7
CdSe-MoS <sub>2</sub> <sup>23</sup>	300W Xe lamp, ( $\lambda > 420$ nm)	0.8	~ 0.15
MoS <sub>2</sub> /SiO <sub>2</sub> <sup>44</sup>	Hg Lamp	0.86	~ 0.14
MoS <sub>2</sub> /TiO <sub>2</sub> <sup>45</sup>	300W Xe lamp	0.03	~ 0.005
TiO <sub>2</sub> /MoS <sub>2</sub> /graphene <sup>22</sup>	300W Xe lamp	2.1	~ 0.35
MoS <sub>x</sub> Cy <sup>46</sup>	300W Xe lamp, ( $\lambda > 420$ nm)	19	~ 3
RGO-MoS <sub>2</sub> <sup>25</sup>	300W Xe lamp, ( $\lambda > 420$ nm)	2	-
<b>MoS<sub>2</sub></b>	<b>100W halogen, (<math>\lambda &gt; 420</math> nm)</b>	<b>0.05#, 0.05</b>	<b>0.008#, 0.008</b>
<b>EG-MoS<sub>2</sub></b>	<b>100W halogen, (<math>\lambda &gt; 420</math> nm)</b>	<b>0.54#, 0.21</b>	<b>0.21 #, 0.06</b>
<b>NEG-MoS<sub>2</sub></b>	<b>100W halogen, (<math>\lambda &gt; 420</math> nm)</b>	<b>0.83#, 0.54</b>	<b>0.45#, 0.144</b>
<b>BEG-MoS<sub>2</sub></b>	<b>100W halogen, (<math>\lambda &gt; 420</math> nm)</b>	<b>0.07#, 0.06</b>	<b>0.016#, 0.013</b>
<b>RGO-MoS<sub>2</sub></b>	<b>100W halogen, (<math>\lambda &gt; 420</math> nm)</b>	<b>3</b>	<b>0.68</b>
<b>NRGO-MoS<sub>2</sub></b>	<b>100W halogen, (<math>\lambda &gt; 420</math> nm)</b>	<b>10.8</b>	<b>2.9</b>
	<b>400W halogen, (<math>\lambda &gt; 450</math> nm)</b>	<b>42</b>	<b>11.5*</b>

#Values for MoS<sub>2</sub> prepared using thiourea by solid state method

<sup>c</sup> TOF calculated per mole of catalytically active material (Graphene and SiO<sub>2</sub> considered as catalytically inactive)

Since graphene plays a seminal role as an electron transporter to MoS<sub>2</sub> it seemed to us that increasing the conductivity of MoS<sub>2</sub> itself would favour HER. It was also noticed that higher yield of H<sub>2</sub> could be obtained with MoS<sub>2</sub> sheets vertically aligned on the electron transporting substrate. The edge sites in MoS<sub>2</sub> have been predicted to be metallic in nature.<sup>14,27</sup> Several quantum mechanical calculations and experimental evidences have revealed a direct correlation between the catalytic activity and metallic character of MoS<sub>2</sub> edges.<sup>14,15,27</sup> While few-layer 2H-MoS<sub>2</sub> is semiconducting with an indirect band gap of 1.2 eV, the 1T polytype of MoS<sub>2</sub> is metallic.<sup>29-32</sup> Prompted by our earlier results we expected metallic 1T-MoS<sub>2</sub> to act as an efficient H<sub>2</sub> evolution catalyst by virtue of both its metallic conductivity and as predicted high catalytic activity. Single-layer 1T-MoS<sub>2</sub> was prepared by Li-intercalation of bulk MoS<sub>2</sub> followed by exfoliation in water.<sup>39</sup> 1T-polytype is thermodynamically unstable phase and readily converts to its more stable 2H-polytype

on stacking. 1T-MoS<sub>2</sub> thus remains stable only as dispersion in water. We characterized 1T-MoS<sub>2</sub> by electron diffraction and HRTEM analysis.

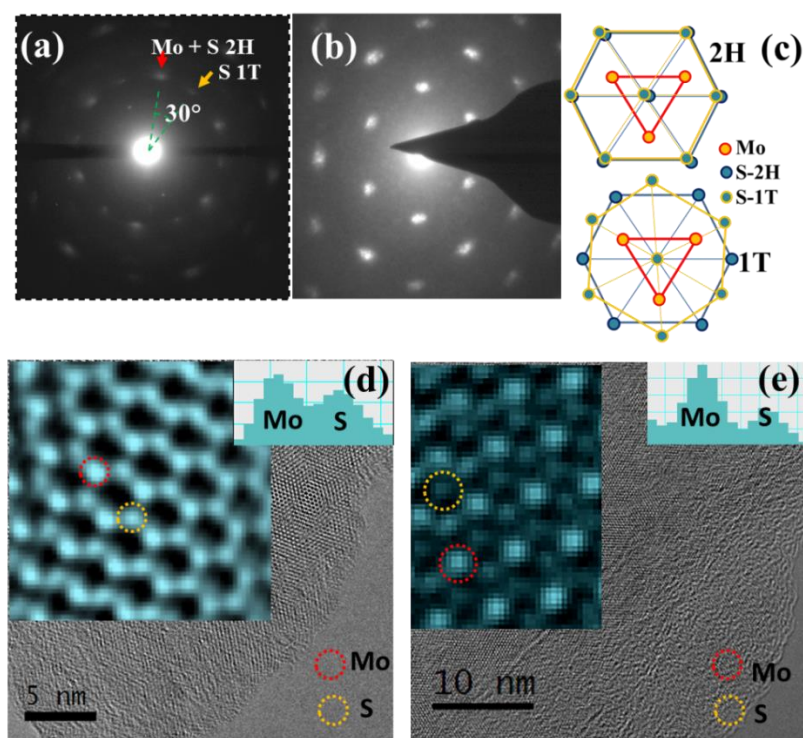


**Figure 6.** ED pattern from single layer MoS<sub>2</sub> with (a) 2H and (b) 1T structure, (c) the schematic structural model corresponding to 2H and 1T structures. HRTEM images from MoS<sub>2</sub> (d) 2H and (e) 1T structures respectively. Inset in (d and e) shows magnified images of Mo and S atomic arrangement both in 2H and 1T structures as well as intensity line scan through Mo and S atoms.

The electron diffraction pattern and the HRTEM images of 2H and 1T MoS<sub>2</sub> are given in Figure 6. The electron diffraction pattern of 2H-MoS<sub>2</sub> shows the usual hexagonal spot pattern (Figure 6 (a)), but 1T-MoS<sub>2</sub> shows an extra hexagonal spot at 30° angular spacing in between the hexagonal spots of the 2H structure (Figure 6(b)). Figure 6(c) shows the schematic representation of 2H- and 1T-MoS<sub>2</sub> structures. 2H-MoS<sub>2</sub> has trigonal prismatic co-ordination of Mo and S atoms with the S atoms in the lower layer lying directly below those of the upper layer. In 1T-MoS<sub>2</sub>, on the other hand, the S atoms in the upper and lower planes are off-set from each other by 30° such that the Mo atoms lie in the octahedral holes of the S layers. The extra spot in electron diffraction arises from this rotation of one of the S atomic layers with respect to another. Figures 6 (d) and (e) shows

the HRTEM images for single layer of 2H- and 1T-MoS<sub>2</sub>. In case of 2H-MoS<sub>2</sub> three S atoms surrounds one Mo atom whereas for the 1T structure six S atoms can be seen surrounding one Mo atom. Intensity line scans through Mo and S atoms show a higher intensity difference for the 1T structure (one S atom in projection) compared to the 2H structure (2 S atoms together in projection). This difference in contrast is related to the corresponding phase shift (related to the net atomic number) under negative C<sub>s</sub> imaging conditions.<sup>47</sup> It is to be pointed out that the sample prepared by Li-intercalation and exfoliation is not composed of entirely 1T- phase but is a mixture of 1T and 2H states as revealed by TEM analysis. 1T-phase being unstable on stacking or drying we were unable to characterize the ratio of 1T/2H phases in the sample.

Photocatalytic activities of 1T-MoS<sub>2</sub> were studied by taking 2 ml of the dispersion of the sample in 50 ml 10% TEOA/water. The concentration of MoS<sub>2</sub> in the dispersion was determined from ICPES analysis. The concentration varied between 0.5 mg/ml to 2 mg/ml. We show the time course of H<sub>2</sub> evolution of single-layer 1T-MoS<sub>2</sub> in Figure 7(a). This catalyst evolved almost 30 mmol g<sup>-1</sup>h<sup>-1</sup> of H<sub>2</sub>, 600 times higher than few-layer 2H-MoS<sub>2</sub>. Even under 100W irradiation, the TOF of the catalyst is estimated to be 6.2 h<sup>-1</sup>, higher than any MoS<sub>2</sub> based system reported so far. The highest TOF reported thus far is 6 h<sup>-1</sup>(under 300W Xe lamp) for [Ru(bpy)<sub>3</sub>]<sup>2+</sup> sensitized colloidal MoS<sub>2</sub> nanoparticles (see Table 1). 1T-MoS<sub>2</sub> evolves around 250 mmol of H<sub>2</sub> corresponding to about 5.6 L of H<sub>2</sub> per g of MoS<sub>2</sub> for 10 hrs. The activity of the 1T-MoS<sub>2</sub> samples prepared by us varies from sample to sample depending on the amount of 1T phase present in the sample. Coexistence of metallic 1T-phase and semiconducting 2H-phases within chemically homogeneous nanosheets is known to occur in single-layer MoS<sub>2</sub> prepared by Li-intercalation and exfoliation.<sup>48</sup> Figure 7(a) shows the time course of H<sub>2</sub> evolution by the sample showing the least yield among 10 experiments on different samples carried out by us, while Figure 7 (b) shows that for the sample with the highest yield. The sample showing the highest yield evolved ~55 mmol g<sup>-1</sup>h<sup>-1</sup> with a TOF of ~ 11 h<sup>-1</sup>. Figure 7 (b) shows the time course of H<sub>2</sub> evolution by 1T-MoS<sub>2</sub> over a period of 30 hrs, with the sample being purged after every 6hrs. The catalytic activity slowly degrades over the period from 55 mmol g<sup>-1</sup>h<sup>-1</sup> to 30 mmol g<sup>-1</sup>h<sup>-1</sup>. This could probably be because of the slow degradation of the 1T phase under the effect of heat from the light source. However,

no significant quenching of the dye was observed even after 30 hrs of reaction indicating that photogenerated species EY<sup>-</sup> does transfer its electrons to 1T-MoS<sub>2</sub> efficiently.

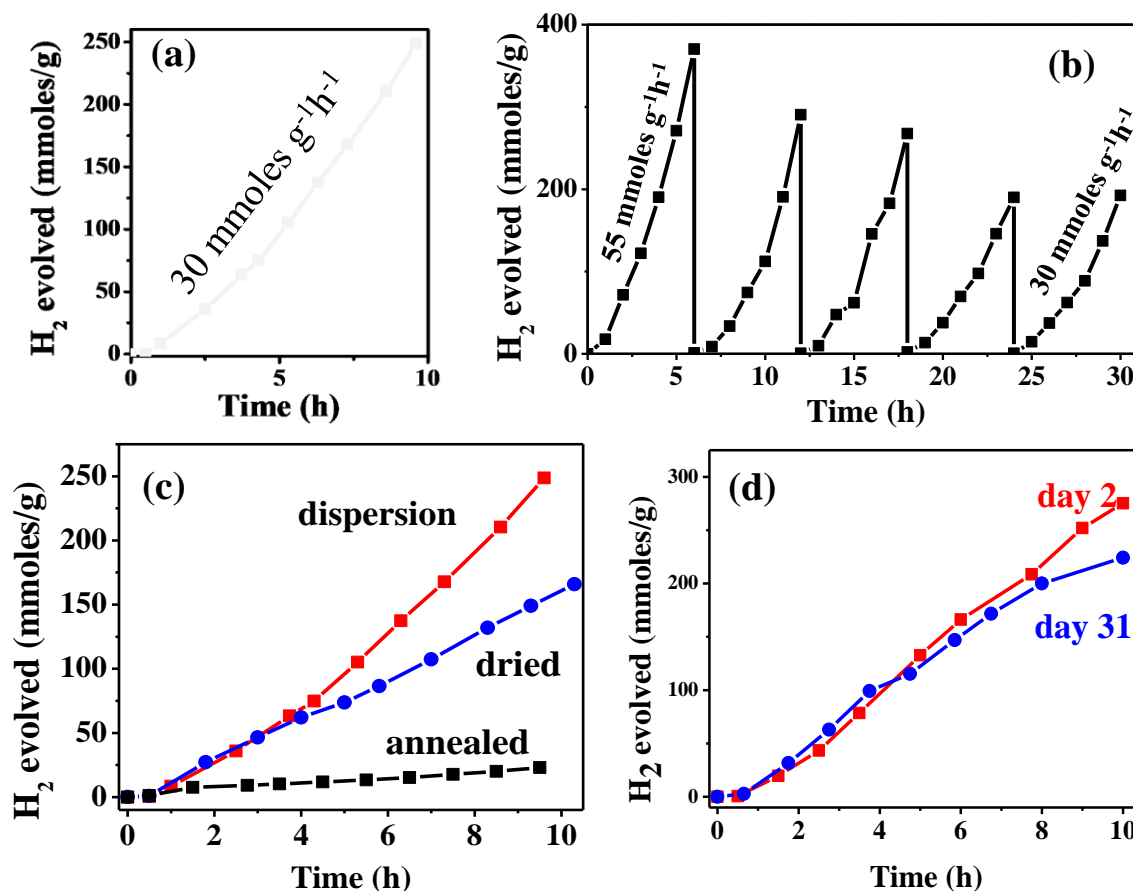


**Figure 7.** Time course of H<sub>2</sub> evolution by 1T-MoS<sub>2</sub> - (a) sample showing the lowest yield of H<sub>2</sub>, (b) sample showing the highest yield of H<sub>2</sub> shown over a period of 30 hrs with purging after every 6 hrs, (c) as prepared dispersion, dried by liophylization and annealed at 300°C for 1 hr and (d) as prepared dispersion ,dispersion stored for 30 days.

To confirm that the high catalytic activity of MoS<sub>2</sub> prepared by Li-intercalation and exfoliation arises from 1T phase and is not a result of better dispersion and other such extrinsic factors we carried out control experiments with 2H-MoS<sub>2</sub> obtained directly from the 1T-MoS<sub>2</sub>. 1T-MoS<sub>2</sub> is reported to get converted to the 2H analogue on annealing under inert atmosphere.<sup>39</sup> We dried the dispersion by liophylization to obtain fluffy mass of 1T MoS<sub>2</sub>. Since liophylization is carried out at low temperatures 1T-phase of MoS<sub>2</sub> is retained after liophylization. We carried Raman studies to see if 1T phase is retained even after liophylization. Raman spectra of single layer restacked MoS<sub>2</sub> or 1T-MoS<sub>2</sub> is known to have strong peaks at 156 cm<sup>-1</sup> (J<sub>1</sub>), 226 cm<sup>-1</sup> (J<sub>2</sub>) and 330 cm<sup>-1</sup> (J<sub>3</sub>) corresponding to the

frequencies at the M point of the Brillion zone of MoS<sub>2</sub>.<sup>49</sup> The appearance of J<sub>1</sub>, J<sub>2</sub> and J<sub>3</sub> modes in the Raman spectra of MoS<sub>2</sub> samples dispersed in water confirms the presence of 1T phase. Similarly, Raman spectra of the lyophilized sample when taken after 15 min of lyophilization show J<sub>1</sub>, J<sub>2</sub> and J<sub>3</sub> modes. The same sample after being stored for 1 day does not show any evidence of J<sub>1</sub>, J<sub>2</sub> and J<sub>3</sub> modes. Freshly, lyophilized sample thus retains 1T phase. On studying the H<sub>2</sub> evolution activity of the freshly lyophilized sample catalytic activity was found to reduce only slightly from 30 mmoles g<sup>-1</sup>h<sup>-1</sup> to 24 mmoles g<sup>-1</sup>h<sup>-1</sup> (Figure 7 (c)).

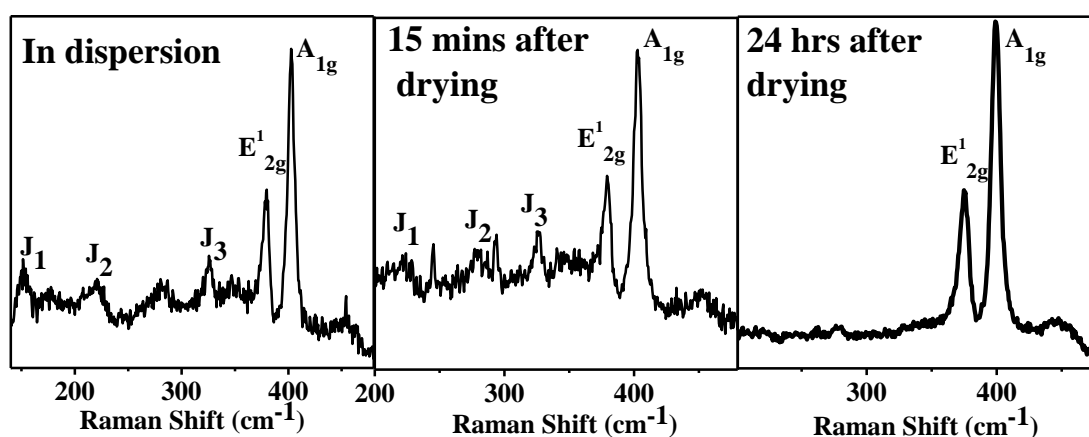


**Figure 8.** Raman spectra of as prepared 1T-MoS<sub>2</sub>, 15 min and 24h after lyophilization.

The lyophilized sample was annealed at 300°C for 1h to obtain the 2H analogue. We observe a drastic reduction in the catalytic activity of the annealed sample with rate of H<sub>2</sub> evolved being only 2.5 mmoles g<sup>-1</sup>h<sup>-1</sup> a value closer to that found with 2H-MoS<sub>2</sub> (Figure 7 (c)). The 1T phase, of MoS<sub>2</sub> being the metastable polytype of MoS<sub>2</sub>, is known to readily undergo transition to more stable 2H-polytype with time.<sup>39</sup> We therefore carried out photocatalytic H<sub>2</sub> evolution studies on fresh and 1 month old samples. The rate of H<sub>2</sub> evolution reduced only slightly over this period from 30 mmoles g<sup>-1</sup>h<sup>-1</sup> to 26 mmoles g<sup>-1</sup>h<sup>-1</sup> (Figure 7(d)).

MoS<sub>2</sub> and its composites have since long been used as a catalyst for electrochemical or photocatalytic H<sub>2</sub> evolution from water. We have been able to optimize MoS<sub>2</sub> based catalysts to obtain highest yield of H<sub>2</sub> reported thus far. Two strategies have been used to

improve the yield of H<sub>2</sub>: (i) increasing the density of catalytically active sites and (ii) promote electron transport to catalytically active sites. Of the two well know phases of MoS<sub>2</sub> the hexagonal polytype, 2H-MoS<sub>2</sub> is the more stable phase. Edges of a 2H-MoS<sub>2</sub> sheet have been identified as the catalytically active site for water reduction while the basal plane is inactive. We have attempted two approaches to increase the density of active sites in the catalyst: (i) making few-layer nanoflakes of MoS<sub>2</sub> with very small basal plane and greater density of edges<sup>25,26</sup> and (ii) making 1T-MoS<sub>2</sub>, an aspect that will be discussed later in this section. To enhance electron transfer to the active sites MoS<sub>2</sub> has been grown on metallic like support- graphene.<sup>19</sup> Graphene acts as an electron channel to transport electrons from the photosensitized dye, EY<sup>-</sup> to MoS<sub>2</sub>.<sup>25</sup> An optimized charge transport from graphene to MoS<sub>2</sub> can be obtained again by two means: (i) enhancement of electron donating ability of graphene and (ii) enhancement of electron transfer in MoS<sub>2</sub> to its edges. Electron donating ability of graphene is improved by making it electron rich, i. e. by nitrogen doping. N-doping makes graphene n-type while MoS<sub>2</sub> is known to be p-type in nature, enabling the formation of p-n heterojunction at the interface of MoS<sub>2</sub> and graphene.<sup>26</sup> The heterojunction not only increases the electron transfer from electron rich graphene to electron rich MoS<sub>2</sub> but also suppresses the probability of charge recombination. To increase the conductivity of electrons in MoS<sub>2</sub>, MoS<sub>2</sub> sheets have been grown vertically on graphene.<sup>10</sup> The electronic conductivity between adjacent layers of MoS<sub>2</sub> is very low while the basal plane is much more conducting. Vertical alignment of MoS<sub>2</sub> on graphene ensures transfer of electrons from graphene directly to each layer ensuring more efficient electron transfer to the edges, the conductivity of each layer being far better than along the perpendicular direction. It is also to be noted that, for a graphene-MoS<sub>2</sub> catalyst to show high catalytic yield of H<sub>2</sub> the amount of MoS<sub>2</sub> growing on graphene also needs to be optimized. Consequently the optimized catalyst, NRGO-MoS<sub>2</sub>, a composite of N-doped graphene containing 22 atom% of MoS<sub>2</sub>, with the MoS<sub>2</sub> flakes growing vertically on NRGO shows the highest yield of H<sub>2</sub> about 200 times greater than that of MoS<sub>2</sub> nanoflakes. Since increasing conductivity of electrons to the active sites is one of the key issues determining catalytic activity it seemed most plausible that making MoS<sub>2</sub> itself metallic would increase the catalytic activity manifold. 1T-polytype of MoS<sub>2</sub> is metallic at room temperature and was found to show the best photocatalytic activity

with a H<sub>2</sub> evolution rate of 600-1000 times that of few-layered 2H-MoS<sub>2</sub> as is clear from Figure 10.

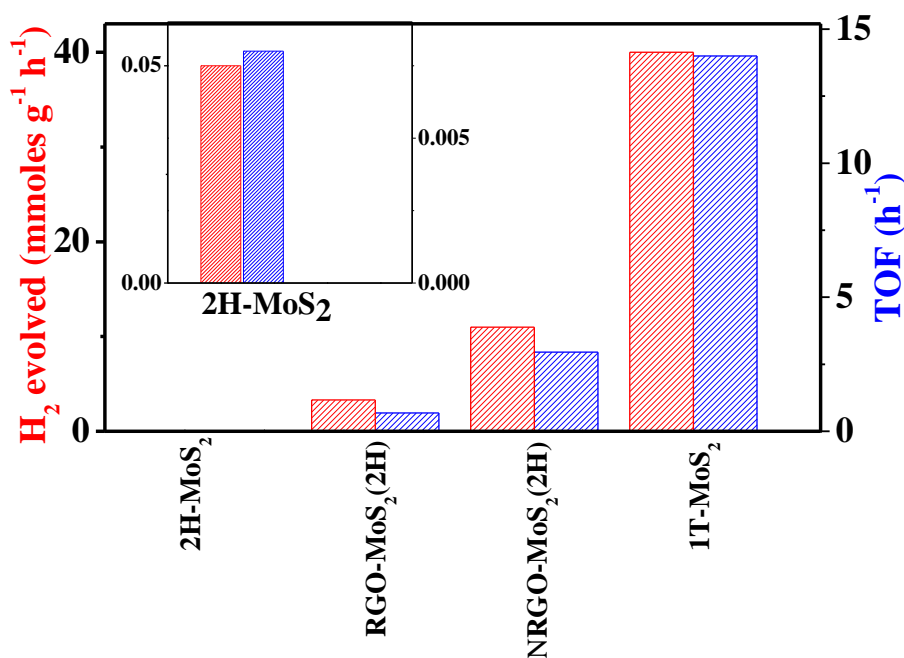


**Figure 10.** Comparison of activity of different catalysts used in the present study.

High catalytic activity of 1T-MoS<sub>2</sub> is not solely a consequence of its metallic nature. High catalytic of 1T-MoS<sub>2</sub> can be explained considering the crystal field splitting of Mo d orbitals in octahedral geometry as demonstrated in the Figure 11. As illustrated by Tenne *et al.*,<sup>32</sup> in case of 2H MoS<sub>2</sub> the valence band (VB) is composed of S3p which is below the Fermi level by ~3.5 eV. The conduction band (CB) composed of Mo 4d states that lie just above the Fermi level leading to a narrow band gap. In terms of crystal field theory it can be described as being composed of hexagonal ( $D_{3h}$ ) symmetry induced splitting Mo 4d orbitals into three orbitals of closely spaced energies – one  $4d_z^2$  and four doubly degenerate orbitals composed of ( $4d_{xy}, x^2 - y^2$ ) and ( $4d_{xz}, yz$ ) as shown in Figure 11. The Mo  $4d_z^2$  is completely occupied and spin paired forming the VB while other four orbitals form the empty CB. As in 2H-MoS<sub>2</sub>, VB of 1T-MoS<sub>2</sub> is composed of S 3p which lies 3 eV below the Fermi level while the Mo 4d hosts the Fermi level making it metallic. Crystal Field splitting of Mo 4d under octahedral  $O_h$  field in case of 1T MoS<sub>2</sub> leads to three triply degenerate orbitals  $4d_{xy, xz, yz}$  containing two unpaired electron and two empty doubly degenerate orbital  $4d_{x^2 - y^2, z^2}$ .

The incompletely filled  $4d_{xy, xz, yz}$  gives rise to metallic property of 1T-MoS<sub>2</sub>.<sup>32</sup> It is possible that easy transfer of electrons from photogenerated species EY<sup>-</sup> to H<sub>2</sub>O happens through the partially filled  $4d_{xy, xz, yz}$  in 1T-MoS<sub>2</sub>( as shown in Figure 11), which is otherwise hindered in case of completely occupied Mo  $4d_z^2$  orbital of 2H-MoS<sub>2</sub>.

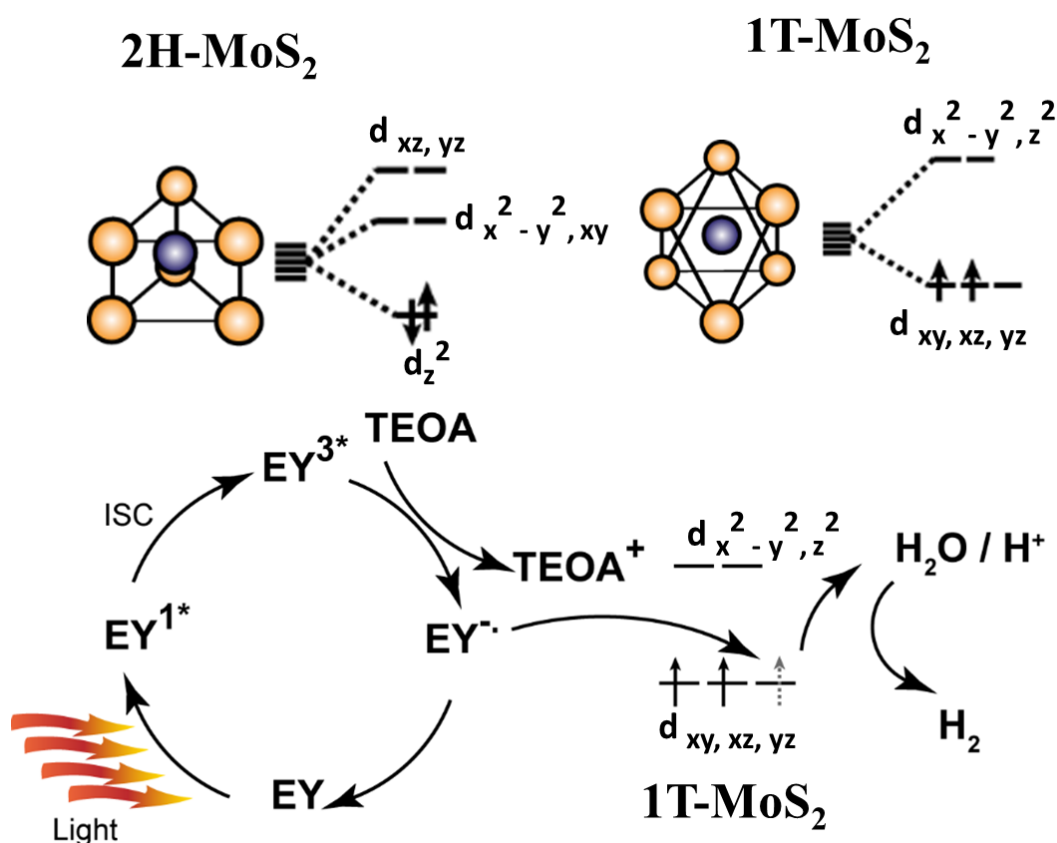


Figure 11. Proposed mechanism of catalytic activity in 1T-MoS<sub>2</sub>

Both theoretical and experimental evidences in literature support that even in the case of 2H-MoS<sub>2</sub>, it is the metallic edge states that are catalytically active and not the 2H- type basal plane.<sup>13,43,50</sup> Further investigation to clearly understand the mechanism of catalytic H<sub>2</sub> evolution by 1T-MoS<sub>2</sub> is being carried out. These results are in accordance with electrochemical measurements of Lukowski et. al.<sup>51</sup> and Voiry et.al.<sup>52</sup> for metallic 1T polytypes of MoS<sub>2</sub> and WS<sub>2</sub>. Since first-principles calculations suggest that as for MoS<sub>2</sub>, the conduction band minima of MoSe<sub>2</sub> too lie well above the water reduction



potential.<sup>53,54</sup> MoSe<sub>2</sub> was predicted to be a viable catalyst of H<sub>2</sub> evolution. Studies of 2H and 1T MoSe<sub>2</sub> indicated that MoSe<sub>2</sub> is a better catalyst than MoS<sub>2</sub> with 1T-MoSe<sub>2</sub> being the best catalyst by far.

## **5. Conclusions**

In conclusion, we were able to optimize the MoS<sub>2</sub> based catalysts to obtain the highest photocatalytic H<sub>2</sub> evolution rate in any MoS<sub>2</sub> based system reported thus far. Nanoflakes of MoS<sub>2</sub> with a high density of catalytically active edges, grown on heavily N-doped graphene, give the best yield among all 2H-polytypes of MoS<sub>2</sub>. N-doping of graphene not only improved the electron-donating ability of graphene but also created a p-n junction that suppresses charge recombination. More importantly, we find that the metallic 1T-polytype of MoS<sub>2</sub> shows extraordinary HER activity by virtue of its metallic nature and intrinsic high catalytic activity. Catalytic activity of 1T-MoS<sub>2</sub> is about 600-1000 times that of 2H-MoS<sub>2</sub>. Likewise, 1T-MoSe<sub>2</sub> shows extraordinarily high catalytic activity, being the best catalyst by far.

## References:

1. A. Fujishima and K. Honda. *Nature* **1972**, 238, 37.
2. D. E. Scaife. *Solar Energy* **1980**, 25, 41.
3. W. J. Youngblood, S.-H. A. Lee, K. Maeda and T. E. Mallouk. *Acc. Chem. Res.* **2009**, 42, 1966.
4. G. Xie, K. Zhang, B. Guo, Q. Liu, L. Fang and J. R. Gong. *Adv Mater* **2013**, 25, 3820.
5. T. Nakagawa, C. A. Beasley and R. W. Murray. *J. Phys. Chem. C* **2009**, 113, 12958.
6. W. J. Youngblood, S.-H. A. Lee, Y. Kobayashi, E. A. Hernandez-Pagan, P. G. Hoertz, T. A. Moore, A. L. Moore, D. Gust and T. E. Mallouk. *J. Am. Chem. Soc.* **2009**, 131, 926.
7. J. Barber. *Chem. Soc. Rev.* **2009**, 38, 185.
8. A. Kudo and Y. Miseki. *Chem. Soc. Rev.* **2009**, 38, 253.
9. B. Hinnemann, P. G. Moses, J. Bonde, K. P. Jørgensen, J. H. Nielsen, S. Horch, I. Chorkendorff and J. K. Nørskov. *J. Am. Chem. Soc.* **2005**, 127, 5308.
10. A. B. Laursen, S. Kegnaes, S. Dahl and I. Chorkendorff. *Energy Environ. Sc.* **2012**, 5, 5577.
11. H. Tributsch and J. C. Bennett. *J. Electroanal. Chem. Interfac. Electrochem* **1977**, 81, 97.
12. K. Sakamaki, K. Hinokuma and A. Fujishima. *J. Vacuum Sc. & Technol. B* **1991**, 9, 944.
13. T. F. Jaramillo, K. P. Jørgensen, J. Bonde, J. H. Nielsen, S. Horch and I. Chorkendorff. *Science* **2007**, 317, 100.
14. S. Helveg, J. V. Lauritsen, E. Lægsgaard, I. Stensgaard, J. K. Nørskov, B. S. Clausen, H. Topsøe and F. Besenbacher. *Phys. Rev. Lett.* **2000**, 84, 951.
15. J. Kibsgaard, J. V. Lauritsen, E. Lægsgaard, B. S. Clausen, H. Topsøe and F. Besenbacher. *J. Am. Chem. Soc.* **2006**, 128, 13950.
16. M. Brorson, A. Carlsson and H. Topsøe. *Catal Today* **2007**, 123, 31.
17. J. Bonde, P. G. Moses, T. F. Jaramillo, J. K. Nørskov and I. Chorkendorff. *Faraday Dis.* **2009**, 140, 219.

18. D. Merki, S. Fierro, H. Vrubel and X. Hu. *Chem. Sc.* **2011**, 2, 1262.
19. Y. Li, H. Wang, L. Xie, Y. Liang, G. Hong and H. Dai. *J. Am. Chem. Soc.* **2011**, 133, 7296.
20. Z. Chen, J. Kibsgaard and T. F. Jaramillo. *Proc. SPIE 7770* **2010**, 77700K.
21. X. Zong, Y. Na, F. Wen, G. Ma, J. Yang, D. Wang, Y. Ma, M. Wang, L. Sun and C. Li. *Chem. Comm.* **2009**, 0, 4536.
22. Q. Xiang, J. Yu and M. Jaroniec. *J. Am. Chem. Soc.* **2012**, 134, 6575.
23. F. A. Frame and F. E. Osterloh. *The Journal of Physical Chemistry C* **2010**, 114, 10628.
24. X. Zong, H. Yan, G. Wu, G. Ma, F. Wen, L. Wang and C. Li. *J. Am. Chem. Soc.* **2008**, 130, 7176.
25. S. Min and G. Lu. *J Phys. Chem. C* **2012**, 116, 25415.
26. F. Meng, J. Li, S. K. Cushing, M. Zhi and N. Wu. *J. Am. Chem. Soc.* **2013**, 135, 10286.
27. M. V. Bollinger, J. V. Lauritsen, K. W. Jacobsen, J. K. Nørskov, S. Helveg and F. Besenbacher. *Phys. Rev. Lett.* **2001**, 87, 196803.
28. F. Wypych and R. Schollhorn. *J. Chem. Soc. Chem. Comm.* **1992**, 1386.
29. V. Alexiev, R. Prins and T. Weber. *Phys. Chem. Chem. Phys.* **2000**, 2, 1815.
30. K. E. Dungey, M. D. Curtis and J. E. Penner-Hahn. *Chem. Mater.* **1998**, 10, 2152.
31. F. Wypych and R. Schollhorn. *J. Chem. Soc. Chem. Commun.* **1992**, 0, 1386.
32. A. N. Enyashin, L. Yadgarov, L. Houben, I. Popov, M. Weidenbach, R. Tenne, M. Bar-Sadan and G. Seifert. *J. Phys. Chem. C* **2011**, 115, 24586.
33. H. S. S. Ramakrishna Matte, A. Gomathi, A. K. Manna, D. J. Late, R. Datta, S. K. Pati and C. N. R. Rao. *Angew. Chemie Int. Ed.* **2010**, 49, 4059.
34. D. C. Marcano, D. V. Kosynkin, J. M. Berlin, A. Sinitskii, Z. Sun, A. Slesarev, L. B. Alemany, W. Lu and J. M. Tour. *ACS Nano* **2010**, 4, 4806.
35. W. Gao, L. B. Alemany, L. Ci and P. M. Ajayan. *Nature Chem* **2009**, 1, 403.
36. L. Xin-jing, Y. Xin-xin, L. Jin-yang, F. Xiao-dong, Z. Kun, C. Hong-bing, P. Nan and W. Xiao-ping. *Chin. J. Chem. Phys.* **2012**, 25, 325.

37. C. N. R. Rao, K. S. Subrahmanyam, H. S. S. R. Matte, B. Abdulhakeem, A. Govindaraj, B. Das, P. Kumar, A. Ghosh and D. J. Late. *Sc. Technol. Adv. Mater.* **2010**, 11, 054502.
38. K. S. Subrahmanyam, A. Ghosh, A. Gomathi, A. Govindaraj and C. N. R. Rao. *Nanosc. Nanotechnol. Lett.* **2009**, 1, 28.
39. G. Eda, H. Yamaguchi, D. Voiry, T. Fujita, M. Chen and M. Chhowalla. *Nano Lett.* **2011**, 11, 5111.
40. V. Rakesh, D. Barun, R. Chandra Sekhar and C. N. R. Rao. *J. Phys. Cond. Matter* **2008**, 20, 472204.
41. A. Das, S. Pisana, B. Chakraborty, S. Piscanec, S. K. Saha, U. V. Waghmare, K. S. Novoselov, H. R. Krishnamurthy, A. K. Geim, A. C. Ferrari and A. K. Sood. *Nat. Nanotechnol.* **2008**, 3, 210.
42. B. Hinnemann, J. K. Nørskov and H. Topsøe. *J. Phys. Chem. B* **2004**, 109, 2245.
43. J. Kibsgaard, Z. Chen, B. N. Reinecke and T. F. Jaramillo. *Nature Mater.* **2012**, 11, 963.
44. A. Sobczynski. *J. Catal.* **1991**, 131, 156.
45. S. Kanda, T. Akita, M. Fujishima and H. Tada. *J. Colloid Interface Sc.* **2011**, 354, 607.
46. J. Djamil, S. A. Segler, A. Dabrowski, W. Bensch, A. Lotnyk, U. Schurmann, L. Kienle, S. Hansen and T. Beweries. *Dalton Trans.* **2013**, 42, 1287.
47. C. L. Jia, M. Lentzen and K. Urban. *Science* **2003**, 299, 870.
48. G. Eda, T. Fujita, H. Yamaguchi, D. Voiry, M. Chen and M. Chhowalla. *ACS Nano* **2012**, 6, 7311.
49. D. Yang, S. J. Sandoval, W. M. R. Divigalpitiya, J. C. Irwin and R. F. Frindt. *Phys. Rev. B* **1991**, 43, 12053.
50. L. P. Hansen, Q. M. Ramasse, C. Kisielowski, M. Brorson, E. Johnson, H. Topsøe and S. Helveg. *Angew. Chem. Int. Ed.* **2011**, 50, 10153.
51. M. A. Lukowski, A. S. Daniel, F. Meng, A. Forticaux, L. Li and S. Jin. *J. Am. Chem. Soc.* **2013**, 135, 10274.

52. D. Voiry, H. Yamaguchi, J. Li, R. Silva, D. C. B. Alves, T. Fujita, M. Chen, T. Asefa, V. B. Shenoy, G. Eda and M. Chhowalla. *Nature Mater.* **2013**, DOI: 10.1038/nmat3700.
53. H. Jiang. *J Phys. Chem. C* **2012**, 116, 7664.
54. J. Kang, S. Tongay, J. Zhou, J. Li and J. Wu. *Appl. Phys. Lett.* **2013**, 102, 012111.



# Appendix

---

## *Instrumentation and Techniques for characterization*

**Powder X-ray diffraction (XRD)** – Recorded with Bruker D8 Advance diffractometer using Cu K $\alpha$  radiation. Around 5 mg of sample was mixed with one or two drops of methanol, grinded well and made a thin film on glass slide. This film was allowed to dry under ambient conditions prior to loading in XRD machine. The average crystallite size was calculated by using Debye-Scherrer formula

$$t = 0.9 \lambda / (\beta \cos \theta) ,$$

where,  $\beta$  is the full width at half maxima in radians,  $\lambda$  is the wavelength of X-rays,  $\theta$  is the Bragg angle.

**Small Angle X-ray Scattering** - SAXS measurements were carried out in Bruker-AXS NANOSTAR instrument. The instrument has X-ray tube (Cu K $\alpha$  radiation, operated at 45 kV/35 mA), cross-coupled Göbel mirrors, three pinhole collimation, evacuated beam path, and a 2D gas-detector (HI-STAR). SAXS data were recorded in the  $q$  range of 0.007 to 0.21  $\text{\AA}^{-1}$  (i.e,  $2\theta = 1-3^\circ$ ).

**Dynamic light scattering Experiments** - DLS measurements were carried out using a NanoZS (Malvern UK) employing a 532 nm laser at a back scattering angle of  $173^\circ$ .

**X-ray Photoelectron Spectroscopy-** High resolution core level XPS spectra of samples were recorded with Omicron nanotechnology spectrometer. Samples were prepared by drop-coating dispersions of sample on Si substrates.

**Raman spectroscopy** - Recorded with a Horiba-Jobin Yvon Lab RAM HR high-resolution Raman spectrometer using Ar laser ( $\lambda = 514.5$  nm or 632 nm) with D1 filter.

**Infrared spectroscopy-** IR spectra were recorded using Bruker IFS 66v/S spectrometer. Minute amounts of sample was mixed with dry KBr and pelletized for recording spectra. Dry KBr pellets were used for determining the background.

**Uv-Vis absorption spectroscopy** – Spectra was recorded in Perkin-Elmer Lambda 900 UV/VIS/NIR spectrometer

**Photoluminescence and Life Time** – PL and fluorescence decay was recorded in a time-correlated single-photon-counting spectrometer of Horiba-Jobin Yvon. Fluorescence data was analysed using DAS6 analysis package provided by Jobin Yvon IBH manufacturer.

**Inductively coupled plasma optical emission spectroscopy** - ICP–OES measurements were carried out using a Perkin-Elmer Optima 7000 DV instrument. Nanoparticles were digested in conc.  $\text{HNO}_3$  and one drop of conc. HCl and diluted with Millipore water for the measurements.

**Transmission electron microscopy** - Images obtained with a JEOL JEM 3010 operating at an accelerating voltage of 300 KV. Samples for TEM analysis are prepared by dispersing the sample in ethanol/water and drying one drop of the dispersion on holy carbon Cu grid.

**Field Emission Scanning Electron Microscopy-** Images were obtained using a FEI NOVA NANOSEM 600. A drop of dispersions of the sample was dried over



aluminium stub for imaging. For polymer nanocomposites the films were re-dissolved in respective solvents and were drop coated on the aluminum stub and imaging was carried out in low vacuum mode. Energy dispersive x-ray spectra (EDAX) was recorded in the same instrument.

**Confocal microscopy** - Imaging was done at room temperature using a Zeiss LSM 510 META laser scanning confocal microscope. The microscope objective of 63X(NA 1.4) and 20X (NA 0.5) was employed. The sample was prepared by sealing the solution between two glass plates.

**Differential scanning calorimetry** - DSC measurements were carried out in the 50 °–250 °C range with samples 10 mg at a scan rate of 0.16 K/s, using a Mettler-Toledo DSC equipment.

**Thermogravimetric analysis** - TGA was carried out on a Mettler-Toledo-TG-850 instrument. 20-30 mg of sample was loaded on a small alumina boat for the measurement.

**Magnetic measurements** - Carried out in physical property measurement system Quantum design, USA. 10-20 mg of sample was pelletized for the measurement.

**<sup>1</sup>H Nuclear Magnetic Resonance** – NMR was recorded on Bruker AVANCE-400 MHz spectrometer at room temperature.

**Nanoindentation** - Nanoindentation experiments were performed using a Hysitron triboin-denter with a Berkovich tip (a 3-sided pyramidal diamond tip) to determine the hardness and the elastic modulus. Ten indentations were made in each case, and the average value was taken as the property of the composite. A maximum load of 1 mN was used at loading and unloading rates of 0.1 mN/s with a hold time of 10 s at the peak load. In all of the cases, care was taken that the penetration depth was 1000 nm. Hardness and elastic modulus were determined by the Oliver-Pharr method.